ANEXO II

UNIVERSIDAD DE LAS PALMAS DE GRAN CANARIA
Departamento de Física

IOCAG
Instituto de Oceanografía y Cambio Global

- PROGRAMA DE DOCTORADO EN OCENOGRAFÍA -

Facultad de Ciencias del Mar

Diapycnal Mixing Processes and Vertical Velocities within Mesoscale Structures

(Procesos de Mezcla Diapicna y Velocidades Vertical en Estructuras de Mesoescala)

FACULTAD
DE CIENCIAS
DEL MAR

UNIVERSIDAD DE LAS PALMAS
DE GRAN CANARIA

Tesis doctoral presentada por Dª Sheila Natalí Estrada Allis para obtener el grado de Doctor por la Universidad de Las Palmas de Gran Canaria.

Dirigida por el Dr. Ángel Rodríguez Santana y el Dr. Pablo Sangrà Inciarte.

El Director El Director La Doctoranda

Las Palmas de Gran Canaria a 16 de Noviembre de 2015

A mi pilar, mi Familia y mis niños ...

– "Usted ama el mar, capitán.
– Sí, lo amo. El mar lo es todo. Cubre siete décimas partes del globo terrestre. Su aliento es puro y sano. Es el inmenso desierto en el que el hombre nunca está solo, pues siente latir la vida a su alrededor. El mar es el vehículo de una existencia prodigiosa y sobrenatural. Es movimiento y amor, es el infinito hecho vida, como dijo uno de sus poetas."

Julio Verne. Veinte mil leguas de viaje submarino.

Agradecimientos

Para la realización de esta tesis no solamente han hecho falta datos, programación, modelos numéricos, gran cantidad de horas de lectura y muchas más horas de comprensión de la misma, sino que también ha sido necesaria la ayuda de instituciones y su personal participando en su elaboración.

Quisiera en primer lugar agradecer al programa de becas propias de la Universidad de Las Palmas de Gran Canaria por la subvención disfrutada durante estos cuatro años de tesis doctoral. A la facultad de Ciencias del Mar y al Doctorado en Oceanografía Física por dotarme con las herramientas necesarias para que esta tesis diera sus frutos. y a la ayuda complementaria del Programa de Formación de Personal Investigador de la ULPGC. Al personal administrativo de Tercer Ciclo y Becas del rectorado de la ULPGC, especialmente a Inmaculada por facilitar la gestión académica en estos años. A la comunidad universitaria en general, especialmente a la Biblioteca Carlos Bass y al personal administrativo de Facultad de Ciencias del Mar. Al Departamento de Física, mediante el cual pude exponer mi proyecto de fin de carrera que plantaría la semilla de la investigación gracias al Dr. Ángel Rodríguez Santana del grupo Oceanografía Física y Aplicada (OFyGA), ayudando a que germinen con mis estudios de máster y finalmente este doctorado.

Los datos necesarios para la elaboración de esta tesis fueron obtenidos gracias a dos campañas oceanográficas englobadas dentro de proyectos en los que he tenido el privilegio de haber participado: proyectos PROMECA-2010 (CTM2009-06993-448 E/MAR), PROMECA (CTM2008-04057) y PUMP (CTM2012-3335). Igual de útil ha sido poder utilizar las salidas del modelo numérico del Dr. Evan Mason, al que agradezco su predisposición y consejos siempre que lo he necesitado. A los que conforman el núcleo de InvestigAdHoc, Dr. Francisco Machín y Dr. Evan Mason, cuyas correcciones del inglés financiadas por el proyecto PUMP, ayudaron a realzar este trabajo. Los inicios y aprendizaje con modelos numéricos de alta resolución fueron gracias al Dr. Rui Caldeira, dentro del marco del proyecto RAIA (BI/0313_RAIA_1_E/2009-016) y su financiación durante el periodo en el que cursaba el Máster Oficial en Oceanografía.

En las estancias de investigación pude disfrutar de diferentes puntos de vista, otras formas de trabajo y enriquecerme a ambos niveles tanto científico como personal. Gracias al Dr. Rui Caldeira de la Universidad de Madeira y al Dr. Xavier Couvelard del *Laboratoire de Physique des Oceans* (LPO) por guiar mis pasos en los primeros estadios de esta tesis. Al Dr. Alberto Garabato debo agradecer su dedicación y compromiso durante mi estancia en el *National Oceanographic Center of Southampton* (NOCS), junto con el Dr. Christian Buckinham, ha sido todo un honor.

Mi camino, aunque enfocado a la investigación, tenía otro rumbo. Sin embargo, mi camino fue derivando hacia Ciencias del Mar. Camino un tanto extraño había elegido esta andina del sur que solamente veía el mar quince días al año y que parecía estar bastante perdida entre buceadores, nadadores y navegantes. Fue el hecho de comprender que esa gran masa azul se encontraba estratificada, insignificante y obvio para la mayoría, lo que revolucionó mi forma de ver el océano. A partir de ese momento cada día fue un descubrimiento. En mi lista habían dos grandes sistemas incomprendidos por su naturaleza abstracta y caótica, el espacio y la mente humana. Desde hace ya varios años se añadió el océano, del cual intento comprender su carácter turbulento, sus escalas y sus interacciones, observando aunque sea desde lejos su compleja inmensidad. Por eso, y disculpen la informalidad, esta tesis va también dedicada a «él».

Una tesis requiere de esfuerzo continuo con interminables horas en una impasible posición delante del ordenador. Sin embargo, también requiere una gran inteligencia emocional. Este último punto es también tan importante como el primero y que a mi parecer solamente puede ser conseguido con el apoyo de las personas que te rodean.

Quiero así agradecer especialmente a mis padres, Susana y Quique, porque dando un vuelco a nuestras vidas hicieron que hoy esta tesis sea una realidad. A mi mami por estar siempre presente pese a la distancia, por ser un ejemplo de lucha y superación constante cuya energía es capaz de viajar miles de kilómetros. A mi papi, por ser un luchador nato, al cual le debo el poder de soñar libremente. A ellos que sorteando grandes dificultades me enseñaron que caer era imprescindible para levantarse aún más alto. A mi hermano Yael, mi pilar y a la vez mi faro, mi mejor amigo, el que mejor entiende mi ser y sabe más que yo como guiarlo, gracias por perturbar mi sistema para hacer que vuelva al equilibrio cuando me he perdido. A Ruymán, por aceptarme y caminar siempre a mi lado incluso cuando yo no lo sabía. Por ser el chófer y secretario de esta mente divergente, a vos que viviste cada segundo de todo este proceso. A ustedes, que creyeron más en mí que yo misma, gracias.

En dos personas encontré más que una guía. Gracias a mis directores de tesis El Dr. Ángel Rodríguez Santana y el Dr. Pablo Sangrà Inciarte, por ser verdaderos padres de ciencia para mi y por otorgarme con infinita paciencia su tiempo y conocimiento. A Ángel, por enseñarme tras largas horas de clases magistrales el borde del conocimiento y no temer a ello. A Pablo, por tener esa capacidad extraordinaria de hacer que mis ideas no diverjan libremente ayudándome a que confluyan a un mismo fin sin casi darme cuenta. Me llevo mucho más que teorías y parametrizaciones. Espero haber estado a la altura.

No se puede olvidar uno de lo comienzos, por eso quiero agradecer especialmente al Dr. Rui Caldeira, por hacerme ver el bosque en lugar del árbol, por enseñarme que una tesis se hace tesis al caminar.

Entre de las paredes del F-212 (y laboratorios aledaños), encontré personas de un amplio espectro de escalas, maravillosas por eso y con las que a su vez he podido compartir un único idioma. A Borja por tener siempre un consejo a mano y al cual admiro, a Mónica por su templanza y siempre presente sonrisa, a Charles y Davinia en quienes encontré el sabor de lo vegetariano y de la amistad, a Bàrbara con su mente inquieta y contagiosa locura salsera, a Iria por ser una artista! y a Marc por esas risas mientras fuertes olas golpeaban la popa del Ziphius. A Patri por su arte y porque no podría reír más con vos. También a Fede por alegrarnos los días con sus chistes, no siempre buenos, a Jaramillo, Nati e Igor, Mar y muchos otros, todos con una calidad tanto en la ciencia como en lo personal que admiro sinceramente. Sin duda hicieron que todo fuera más fácil y con diferencia mucho más divertido. No podría olvidarme de vos Caro, caminando juntas porque el universo (el nuestro xx) pensó que los aires del sur eran una buena combinación, gracias por compartir risas, lágrimas y locuras, eras sin duda la persona ideal para acompañarme en este último tramo. A Mire, por interminables charlas que siempre se resumen a un mismo punto turbulento, a un mismo doctor experimental, con las cuales nos sentíamos curiosamente en armonía. A todos ellos gracias por los momentos que surgían de las anécdotas de besos inesperados, «woks» y sentimientos que me hicieron evolucionar como persona.

Varios fueron mis mentores, a cada uno les agradezco su dedicación y paciencia. No por diferenciar pero si por destacar quisiera especialmente agradecer a aquellos que trazaron de varias maneras mi camino, tanto el científico como el personal. Gracias por los consejos y conocimiento doctores (y a la vez grandes profesores): Ángeles M., Miriam P, Rafael R., Luis C., Carmen G. y Diana G. A usted profesor Guillermo R., por enseñarme que era la vida de la ciencia. A los que me ayudaron a dar mis primeros pasos en la oceanografía física, en el arte a veces casi abstracto de la modelización en ROMS, Xavier y Rui, por hacer además que me sintiera en familia entre levadas, poncha y espetadas. La programación con el viejo compañero de camino Matlab no podría haber dado sus frutos de no ser por Francis, es un privilegio poder haber aprendido de un grande. A Avelina por su trabajo, muchas veces anónimo, haciéndonos la vida académica más fácil y a Jorge Pop por estar siempre dispuesto a «echar un cable» (muchas veces literalmente) y a luchar con incomprensibles particiones en RAID.

Empezamos juntos y no podría pedir mentes más brillantes que las de mis compañeros de carrera de Ciencias del Mar, Samuel (Sha), Violant, Guillem, Myriam, Raúl, Ángel, Lola, y todos los que pasaron por esas aulas, por el hecho de hacer que me esforzara cada día más solo por no desmerecer. En especial a mi Anna, amiga incondicional que te transmite momento con solo verla trabajar. A Javi, oceanógrafo por convicción y *gaiano* nato, no podría haber aprendido más sobre el arte del argumento. Gracias por esas acampadas y aguantar tediosas charlas «filosóficas» y no tan existenciales.

En las campañas oceanográficas, descubrí la pasión por la navegación y se debe en gran medida a todas las personas embarcadas en ellas. A ustedes que ayudaron en la recogida de datos y maniobra (muchas veces peliaguda) del TurboMAP. De cada una me llevo inmejorables momentos que siempre me han servido para evolucionar tanto personal como científicamente. Disculpen no poder nombrarlos a todos! Un enorme GRACIAS va para todos ustedes, tripulación, técnicos, biólogos, químicos, geólogos y físicos, pero sin duda gente de mar, de los buques García del Cid, Ángeles Alvariño, velero Ziphius, Atlantic Explorer, Hespérides. En especial a Dulce y Carmen, que ganas de volver a la mar junto a ustedes.

Tengo la fortuna de haber sentido el apoyo incondicional de aquellos que están lejos, mi abuela Paca, tío Gustavo, abuelo Jorge, tía Nancy y mis primos. El recuerdo de los que ya no están pero cuyos consejos y enseñanzas sigo recordando como si fuera hoy, abuela Nelly. También a mi abuelo José, soy lo que soy en parte por vos abuelo que con tu particular manera me enseñaste tanto. Se que ahora ambos forman parte de mi y de este mundo por fin.

Caminando por el mundo también encontré personas que me hicieron ver que a la familia también se la elige. Gracias Gisela y Emannuel, que entre mates y risas saben como hacer que mi mente entrara en resonancia gracias al poder de las «súper nenas». Gracias también a todas aquellas personas que han hecho este camino más divertido, a Aida por ser nuestra rubia que nos contagia alegría al instante y a los chicos del «eco-volley» por obrar el milagro de que me moviera haciendo ejercicio.

Desde el cielo argento he de agradecer el apoyo de mis hermanas por decisión, Magui y Dani, a la distancia sabemos que estamos unidas por un *éter* especial. Saber que están a mi lado me hace más fuerte. A Gabriel, Daniel y todos los chicos del «bule», ricos mates y asados volveremos pronto a compartir guitarra en mano. Por aires canarios encontré mi otro rincón en el mundo, el cual ha sido más confortable gracias a mi Flaca (Guaci), gracias por regalarme un poquito de tu manera de ver el mundo. A Mariana, por hacerme sentir de nuevo libre. Gracias Marisol y Andrés por dejarme entrar en sus vidas y disfrutar de tan rica comida canaria. Otras personas, aunque en tiempos tempranos de mi carrera, también lo hicieron posible, gracias Nicolás y Esther porque alimentaron mis ganas de ir siempre un poco más allá conociendo nuevos mundos y otros puntos de vista gracias a la lectura. A Mariana y mi linda Gara, gracias por regalarme tu sonrisa.

A ellos, muchas veces mi razón de felicidad, *mis niños* Bruno y Darwin, que dicha más grande poder haber disfrutado de una compañía tan pura y libre.

Imagen de la portada: Modelo numérico de inestabilidades de Kelvin-Helmholtz.
Fuente: https://en.wikipedia.org/wiki/File:Kelvin-Helmholtz_Instability.ogv

Abstract

An understanding of the main factors that affect upper ocean layer dynamics and vertical transport is crucial for the marine ecosystem and climate system. Diapycnal mixing processes such as diapycnal entrainment (w_e), by which fluid less turbulent from pycnocline is incorporated within the mixed layer, significantly control such systems and their effects can be amplified within mesoscale structures such as eddies and upwelling filaments. Despite the progress made in recent decades, the study of turbulent mixing and vertical transport processes is still a challenge in oceanography, partly due to the inherent intermittent nature of turbulence and the difficulty in taking measurements at fine- and micro-scales. This thesis examines the sources of turbulent kinetic energy (TKE) through the entrainment process, as well as the forcing components that dominate the vertical velocity (w) field within two mesoscale structures of the North Atlantic.

The TKE dissipation rates (ε_o) and vertical current shear (Sh^2) at the base of the mixed layer (h_ρ), are not usually included in the unidimensional balance of TKE of mixed layer models. The results presented here show an increase of both ε_o and Sh^2 at the base of h_ρ, within waters influenced by the upwelling filament of Cape Ghir. In this filament area, the mixing layer depth (h_ε) is deeper than h_ρ, resulting in positive entrainment zones (Δh). This indicates optimal conditions for the occurrence of entrainment. These results not only highlight the relation between filament waters and diapycnal mixing process, but also support the formulation of a modified w_e parameterization. The novel parameterization includes the effect of Sh^2, buoyancy fluxes at the surface and interface, $\Delta h > 0$ and ε_o observed through measures of a microstructure profiler taken for first time in this region.

The w_e returned by previous entrainment parameterizations are explored in terms of micro-scale turbulent microstructure profiles sampled quasi-synoptically over an intrathermocline anticyclonic eddy originated in the lee of the island of Tenerife. As in the case of the upwelling filament, we observe $h_\varepsilon > h_\rho$ crossing the eddy, which allows the development of a region of active mixing ($\Delta h > 0$). At the eddy periphery, an increase of w_e is accompanied by enhanced diapycnal diffusivity coefficients (K_ε) as a results of Sh^2 at the base of h_ρ, wind stress peaks and changes in the surface buoyancy fluxes. In deeper layers of the eddy core, the enhancement ε_o coincides with high levels of Sh^2, near-critical gradient Richardson numbers, and increased K_ε, supporting the theory that enhancement of diapycnal mixing is a consequence of trapped near-inertial waves inside anticyclonic eddies of the Canary Eddy Corridor, as suggested by a previous study.

Entrainment velocities however, cannot give us *per se* a general view of the total vertical transport at the mesoscale. Through a high resolution oceanic model previously validated, the main components of the w field and the role that the diapycnal mixing plays inside mesoscale anticyclonic eddies of the Canary Eddy Corridor are explored. Vertical mixing contributes indirectly to the surface w field by influencing the dominant ageostrophic components. Below the h_ρ, the surface wave-like spiral pattern of w is replaced by a dipole of upwelling/downwelling cells as a result of an imbalance between the ageostrophic and stretching terms. These dipoles are also observed when the w field is diagnosed from a generalized omega equation, and their changes in intensity may be linked to variations in vortex axisymmetrization and modulation by the presence of Vortex Rossby Waves.

Resumen

Comprender cuáles son los principales factores que afectan a la dinámica de la capa superficial del océano y el transporte vertical es crucial para el ecosistema marino y el sistema climático. A menudo, los procesos de mezcla diapicna, como el fenómeno de intrusión o *entrainment* (w_e) mediante el cual fluido menos turbulento de la picnoclina es incorporadas dentro de la capa de mezcla, ejercen un importante control sobre tales sistemas y sus efectos pueden verse amplificados dentro de estructuras de mesoescala como remolinos y filamentos de afloramiento. Sin embargo, el estudio de la mezcla turbulenta y los procesos de transporte vertical aún representan un desafío para la oceanografía, en gran parte debido a la inherente naturaleza intermitente de la turbulencia y a la dificultad en las medidas a fina y micro escala. La presente tesis trata con el estudio de las fuentes de energía cinética turbulenta (ECT), así como con los componentes que fuerzan el campo de velocidades verticales (w) dentro de dos estructuras de mesoescala del Atlántico norte.

Las tasas de disipación de ECT (ε_o) y la cizalla vertical inducida por la corriente (Sh^2) en la base de la capa de mezcla (h_ρ) no suelen estar incluidas dentro del balance de ECT unidimensional en modelos de capa de mezcla. Los resultados aquí expuestos muestran un aumento de ambos ε_o y Sh^2 en la base de h_ρ en aguas influenciadas por el filamento de afloramiento de Cabo Ghir. En estas zonas de filamento, las capas de mezcla activa (h_ε) son más profundas que h_ρ, resultando en zonas de *entrainment* (Δh) positivas. Las consecuencias son la creación de condiciones óptimas para que el fenómeno de *entrainment* tenga lugar. Además de la relación entre las aguas de filamento y los fenómenos de mezcla diapicna, estos resultados apoyan la formulación de una modificada parametrización de w_e, donde se incluye el efecto de Sh^2, flujos de flotabilidad en superficie e interfase, $\Delta h > 0$ y ε_o observadas a través de medidas de un perfilador de microestructura turbulenta, tomadas por vez primera en esta región.

Las w_e dadas por la previa parametrización son exploradas a través de perfiles de microestructura medidos a escalas casi sinópticas en un remolino anticiclónico intratermoclina al sur de la isla de Tenerife. De forma similar al caso del filamento, se observa que $h_\varepsilon > h_\rho$ a lo largo de la sección meridional del remolino permitiendo el desarrollo de una región de mezcla activa ($\Delta h > 0$). En la periferia del remolino, se observa un aumento de w_e acompañado por un incremento de los coeficientes de difusividad diapicna

(K_ε), resultado del aumento de Sh^2 en la base de h_ρ, picos de la tensión del viento y cambios en los flujos de flotabilidad superficiales. En las capas más profundas del núcleo del remolino, un incremento de ε_o coincide con altos niveles de Sh^2, números de Richardson de gradiente subcríticos y elevados valores de K_ε. Estos resultados apoyan la teoría de que el aumento de mezcla diapicna profunda es una consecuencia de ondas cuasi-inerciales atrapadas dentro de remolinos anticiclónicos del corredor de remolinos de canarias, en acuerdo con estudios previos.

Sin embargo, las velocidades w_e no pueden darnos *per se* una visión general del transporte vertical total de la mesoescala. A través de un modelo numérico de alta resolución previamente validado, se exploran los principales forzamientos del campo de w y el papel que juega la mezcla diapicna dentro de remolinos anticiclónicos de mesoescala del corredor de remolinos canario. La mezcla vertical contribuye indirectamente al campo de velocidades verticales mediante su influencia en el término dominante ageostrófico. Debajo de h_ρ, el patrón de onda en forma de espiral observado en el campo de w superficial, es reemplazado por un dipolo donde se alternan dos celdas de hundimiento y afloramiento en el núcleo de los remolinos de todo el dominio numérico. Esta estructura de la velocidad vertical es el resultado de un desequilibrio entre ambos forzamientos dominantes ageostróficos y de estiramiento. Los dipolos son también observados cuando el campo de w es diagnosticado a partir de una ecuación omega generalizada. Los cambios en intensidad de dicha estructura podrían además estar ligados a las variaciones de la axisimetrización del vórtice y verse moduladas por la presencia de ondas de vórtice de Rossby.

Thesis Preview

This thesis, entitled as "*Diapycnal Mixing Processes and Vertical Velocities within Mesoscale Structures*", was carried out within the research group Oceanografía Física y Geofísica Aplicada (OFYGA), Department of Physics of the University of Las Palmas de Gran Canaria (ULPGC). The work was carried out the framework of projects PROMECA-2010 (CTM2009-06993-448 E/MAR), PROMECA (CTM2008-04057) and PUMP (CTM2012-3335), and has been possible thanks to a PhD grant from the ULPGC in agreement with the "Estatuto de personal investigador en formación" (Real Decreto 63/2006) in the scope of Programa Propio de la ULPGC.

Dr. Ángel Rodríguez-Santana, director of OFYGA (ULPGC), together with Dr. Pablo Sangrà Inciarte from the Grupo de Oceanografía Física of the Instituto de Oceanografía y Cambio Global (IOCAG; ULPGC) have supervised this research thesis.

This thesis comprises an introductory part in Chapter 1 to set the theoretic context of the research study, followed by a short description of the main objectives and organization of the manuscript in Chapter 2. A description of the study area and materials and methods used are included in Chapter 3. In the subsequent three chapters research studies dealing with each research objective are addressed. These sections represent the core of the thesis. At the time of writing, two chapter of this PhD manuscript, Chapter 4 and Chapter 5, have been submitted for publication in indexed research journals; the first is undergoing a second round of revision at the Journal of Geophysical Research. The last research study of Chapter 6 is in preparation and is close submission. The final Chapter 7 presents the general conclusions resulting from this work and includes a list of future research objectives that have arisen from this thesis. Appendices are found at the end of the manuscript. In order to fulfill the demands of the Reglamento de Elaboración, Tribunal, Defensa y Evaluación de Tesis Doctorales de la Universidad de Las Palmas de Gran Canaria (BOULPGC. ART. 2 Cap. 1, 5 de Noviembre de 2008), a summary of this thesis is written in Spanish in Chapter 8.

Presentación de la Tesis

Esta tesis, titulada como "*Procesos de Mezcla Diapicna y Velocidades Verticales en Estructuras de Mesoescala*", fue llevada a cabo en el grupo de investigación de Oceanografía Física y Geofísica Aplicada (OFYGA), del Departamento de Física de la Universidad de Las Palmas de Gran Canaria (ULPGC). Los trabajos incluidos en esta tesis han sido desarrollados en el marco de los projectos PROMECA-2010 (CTM2009-06993-448 E/MAR), PROMECA (CTM2008-04057) y PUMP (CTM2012-3335), y han sido posibles gracias a una beca de doctorado de la ULPGC en acuerdo con el Estatuto de personal investigador en formación (Real Decreto 63/2006) como parte del Programa Propio de la ULPGC.

El Dr. Ángel Rodríguez-Santana, director de OFYGA (ULPGC), junto con el Dr. Pablo Sangrà Inciarte del Grupo de Oceanografía Física del Instituto de Oceanografía y Cambio Global (IOCAG; ULPGC) han supervisado esta tesis de investigación.

La estructura de esta tesis comprende una parte introductoria abordada en el Capítulo 1, estableciendo así el contexto teórico, seguido por una corta descripción de los principales objetivos y organización del manuscrito en el Capítulo 2. La descripción del área de estudio, material y métodos utilizados son incluidos en el Capítulo 3. En los siguientes tres capítulos se exponen tres artíulos de investigación que tratan con cada uno de los objetivos del Capítulo 2 conformando el núcleo de esta tesis. Al tiempo en que se escribe esta tesis, dos de esos capítulos, Capítulo 4 y 5, han sido enviados a revistas de alto impacto, el primero se encuentra en la segunda fase de revisión de la revista Journal of Geophysical Research. El último estudio del Capítulo 6 se encuentra en fase de preparación próximo a ser enviado. El posterior Capítulo 7 presenta las conclusiones generales derivadas de esta tesis e incluye una lista de líneas futuras de investigación que surgen de estos trabajos. Los apéndices y la bibliografía son encontrados al final del documento. En cumplimento de las demandas del Reglamento de Elaboración, Tribunal, Defensa y Evaluación de Tesis Doctorales de la Universidad de Las Palmas de Gran Canaria (BOULPGC. ART. 2 Cap. 1, 5 de Noviembre de 2008), se adjunta en el Capítulo 8 un resumen de esta tesis escrita en español.

Contents

List of Figures xvii

List of Tables xxxiii

1 Introduction 1

1.1 The scales of the ocean 1

1.2 Mixing processes at small-scales 3

1.3 The turbulent entrainment process 5

1.3.1 The Role of w_e in the TKE balance 6

1.3.2 Determination of w_e using a Richardson number dependent argument 10

1.4 Vertical velocity at the mesoscale 11

1.5 Mesoscale structures: Filaments and eddies in the Canary Basin 13

1.5.1 Mesoscale upwelling filaments 14

1.5.2 Mesoscale anticyclonic eddies 16

2 Objectives and Organization 19

2.1 Motivation 19

2.2 Thesis organization 20

3 Material and Methods 23

3.1 Data collection 23

3.1.1 CTD, XBT, ADCP data 23

3.1.2 Meteorological-related quantities and surface fluxes 25

3.1.3 Microstructure data processing 26

3.2 Satellite data: SST, chlorophyll and altimetric products 27

3.3 The numerical model solution: ROMS 31
3.3.1 Lagrangian Passive Tracers: Roff 31

4 Diapycnal Entrainment in an Eastern-Boundary Upwelling Filament 33

4.1 Introduction 33
4.2 Case study: Cape Ghir upwelling filament 35
4.2.1 Entrainment parameterizations 35
4.3 Results 39
4.3.1 Hydrographic background of the filament 39
4.3.2 Meteorological conditions 43
4.3.3 Active mixing in filament waters 46
4.4 Discussion 52
4.4.1 Vertical Current Shear as Mixing Forcing 53
4.4.2 New entrainment approach 55
4.4.3 2D Submesoscale processes 58
4.4.4 Accuracy of parameterized ε_p 60
4.5 Conclusions 61

5 Turbulent Diapycnal Mixing within an Intrathermocline Anticyclonic Eddy 65

5.1 Introduction 65
5.2 Case study: the PUMP intrathermocline eddy 68
5.3 Air-sea fluxes and diapycnal mixing 69
5.4 Mixed and mixing layer depths 72
5.5 Mixing at the entrainment zone 74
5.5.1 Sources of TKE for entrainment 74
5.5.2 Entrainment rates, $w_e^{\Delta h}$ 75
5.6 Deep enhanced diapycnal mixing 78
5.7 Diapycnal diffusivity coefficients 79
5.7.1 Surface K_ε 79
5.7.2 Deep K_ε 80
5.7.3 K_ε versus K_{kpp} 81
5.8 Concluding remarks 84

6 Vertical Velocities in Mesoscale Eddies: A Numerical Experiment 85

6.1 Introduction 85

6.2 Model outputs and selected eddies 88

6.3 Forcing mechanisms of the w-field 90

6.3.1 Decomposition of the vertical velocity field 90

6.3.2 Influence of eddy-wind interaction and nonlinear Ekman effects . 95

6.3.3 Influence of vortex Rossby waves 99

6.4 Surface role of diapycnal mixing in w 103

6.5 Sub-surface w-dipole 105

6.5.1 Temporal w-dipole evolution 106

6.5.1.1 Lagrangian release of passive tracers 108

6.6 A Comparison with the generalized omega equation 111

6.7 Summary and discussion 114

6.7.1 The role of diapycnal mixing in surface w 114

6.7.2 The subsurface w-dipole 115

6.7.3 Influence of VRWs on the total w field 115

7 Conclusions and Future Research 117

7.1 Main conclusions 117

7.2 Future research 120

8 Resumen en Español 123

8.1 Capítulo 1: Introducción 123

8.1.1 Proceso de intrusión (*entrainment*) diapicno turbulento 124

8.1.2 Velocidades verticales en la mesoescala 126

8.2 Capítulo 2: Motivación y Objetivos 126

8.3 Capítulo 3: Material y Metodología 128

8.3.1 Datos *in situ* 128

8.3.2 Cantidades meteorológicas y flujos superficiales 129

8.3.3 Procesamiento de datos de microestructura 130

8.3.4 Datos de satélite 131

8.3.5 Modelo numérico: ROMS 131

8.4 Capítulo 4: Velocidades de *Entrainment* en un Filamento de Afloramiento de Margen Este 133

8.4.1 Introducción 133
8.4.2 Caso estudio: Filamento de afloramiento de Cabo Ghir 134
8.4.3 Parametrizaciones de *entrainment* diapicno 134
8.4.4 Hidrografía del filamento 136
8.4.5 Condiciones meteorológicas 139
8.4.6 Mezcla activa en aguas de filamento 139
8.4.7 Cizalla vertical como forzamiento de w_e 142
8.4.8 Nuevo enfoque del *entrainment* diapicno 144
8.4.9 Parametrización de ε_p 145
8.4.10 Conclusiones 146
8.5 Capítulo 5: Mezcla Turbulenta Diapicna en un Remolino Intratermoclino Anticiclónico 148
8.5.1 Introducción 148
8.5.2 Caso estudio: Remolino intratermoclina PUMP 150
8.5.3 Capas de mezcla activa y de mezcla 150
8.5.4 Mezcla en la zona de *entrainment* diapicno 153
8.5.5 Aumento de mezcla diapicna profunda 154
8.5.6 Conclusiones 154
8.6 Capítulo 6: Velocidades Verticales en Remolinos Mesoescalares (Experimento Numérico) 156
8.6.1 Introducción 156
8.6.2 Descomposición del campo de w 158
8.6.3 Influencia de la interacción remolino-viento y de los efectos no lineales de Ekman 162
8.6.4 Influencia de las ondas de vórtice de Rossby 163
8.6.5 Papel de la mezcla diapicna en el campo superficial de w 165
8.6.6 Dipolo subsuperficial de w 167
8.6.7 Comparación con la ecuación omega generalizada 171
8.6.8 Discusión y conclusiones 173
8.7 Capítulo 7: Conclusiones Finales y Líneas Futuras 175
8.7.1 Líneas futuras de investigación 178

Appendix A Parameterization of ε_p **181**

Appendix B Local dispersion relation for vortex Rossby waves 185

References 187

List of Figures

1.1 Scheme illustrating the relevant time and space scales in which occur several physical and biological processes crucial for the oceanic and climate systems. From large-scale movements that comprises the climate global change $\mathcal{O}(10.000 \text{ km})$ over tens of years to micro-scales acting at $\mathcal{O}(0.1 \text{ m})$ in only few minutes but with important implications in the meridional overturning circulation. Scheme adapted from Chelton (2001). 2

1.2 Scheme of the main mixing processes acting into the ocean at many time and spatial scales. Some of them remain poorly understood. Adapted from Moum et al. (2003). 4

1.3 Simplified scheme of the turbulent diapycnal entrainment phenomenon for a potential density profile (ρ_θ). Three layers are considered: a well mixed surface layer (h_1), an interfacial layer (Δh) and a more stratified layer below pycnocline (h_2). Upward arrows indicate the jump from pycnocline to surface layers of buoyancy (δb), density ($\delta \rho$) and velocity (δV). Sources of TKE driving entrainment are depicted as: (1) mechanical stirring by wind driving by friction velocity (u_*), (2) convective mixing by free convection velocity scale (w_*) and (3) velocity jump (δV) across the interface as a result of vertical shear by horizontal current. . 9

1.4 EKE map (m^2 s^{-2}) derived from AVISO altimeter products. The snapshot correspond to the date of January 01 for 2014. White dashed boxes denote the oceanic study areas comprised in this thesis, where the uppermost box shows the Cape Ghir filament region studied in PROMECA project of Chapter 4, and lowermost box delimits the onset of the Canary Eddy Corridor (Sangrà et al., 2009) as part of the PUMP project, examined in both Chapters 5 and 6. 13

3.1 Shear power spectral density, $\psi(k)$ (red solid line), for first profile of station 24 from PROMECA-cruise, and for a depth range from 43 to 45 m depth. The Nasmyth universal spectra is shown as a dashed black line. Turbulent kinetic energy dissipation rate, $\overline{\varepsilon_o}$, is averaged over the depth range value. Dotted thin lines are the confidence interval of 0.95 % for the power spectral density calculation. At the bottom, k represent the wavenumber in cycles per minute. 28

3.2 Snapshots of satellite products covering the area of the PROMECA cruise. Upper panel shows maps of SST from MODIS-A and MODIS-T, and their respective Chl-a maps for the same time-period are shown in the lower panel. Note the increase in the magnitude of the upwelling filament off Cape Ghir in the rightmost column for both the SST and Chl-a maps. 29

3.3 Snapshots of sea level anomaly maps (cm), derived from AVISO altimeter products for the first day of the month and year shown at the top of each panel. The area covered is the region of the Canary Eddy Corridor (Sangrà et al., 2009) in which the anticyclonic eddy examined in Chapter 5 is developed. The signature of the mesoscale structure is highlighted by the black boxes. 30

4.1 Bathymetry of the region at 500 m contour intervals with the hydrographic stations measured around the upwelling filament off Cape Ghir during October 2010. Dashed box delimits the hydrographic stations used in this study as is better shown on the superimposed figure at the bottom right corner. CTD stations along with ADCP survey sites are marked as black squares; microstructure stations as red dots; XBT profiles as small black dots. Transects A, B and C are also indicated. 36

4.2 Snapshots of (a) Sea surface temperature from MODIS-Terra in °C for October 21, 2010 at 14:25 pm and (b) Chlorophyll-a from MODIS-Aqua for October 20, 2010 at 13:45 pm. Superimposed vectors denote the magnitude and direction of the geostrophic velocity fields for the same days, derived through AVISO sea level anomaly data at 1/4° horizontal resolution. Black dots are CTD+ADCP stations while white dots are microstructure profiles. 40

4.3 Hydrographic vertical sections derived from CTD profiles of (a) salinity, S, and (b) potential density anomaly, σ_θ (kg m^{-3}) for the northeastern transect A, and (c) S, and (d) σ_θ for the western transect B. Contours of S are plotted every 0.5 intervals, while σ_θ contours are plotted every 0.1 kg m^{-3}. The accumulative distance between stations in km is shown at the bottom. At the top, the corresponding hydrographic station number is displayed. Inverted triangles show the stations influenced by the upwelling filament. 42

4.4 Vertical sections derived from CTD-temperature profiles combined with XBT temperature profiles where (a), (b) and (c) correspond to transects A, B and an extra transect C, respectively. Isotherms are spaced every 0.5 °C and an offset of approximately 10 m was applied to XBT profiles to guarantee consistency with CTD data depth. At the top, bold numbers in italics denote CTD stations while normal numbers are for XBT stations. Note that not all the station numbers are displayed at the top in order to facilitate viewing; all CTD and XBT stations are taken into account for the vertical section. At the bottom, the cumulative distance in km is shown. 43

4.5 Half-hourly averaged meteorological data: (a) net surface heat flux J_q^o (defined positive upward) and related components: shortwave radiation flux J_q^{Sw}, net longwave heat flux J_q^{Lw}, latent heat flux J_q^{La}, and sensible heat flux J_q^{Se}; (b) net surface buoyancy flux J_b^o, defined as the sum of thermal surface buoyancy flux J_b^T, and haline surface buoyancy flux J_b^S; (c) sea water temperature T_{sw}, and temperature of air T_{air}; (d) wind stress $\boldsymbol{\tau}_o$; (e) Monin-Obukhov length scale L_{mo}, and mixed layer depth h_ρ. Symbols over time series denoted with a superscript s represent the exact value of each meteorological quantity computed using CTD data profiles from each hydrographic station. Thin vertical dashed lines show the hydrographic stations at top, while thick dashed lines indicate the end of each day at bottom. 45

4.6 Vertical section of squared buoyancy frequency, N^2 (rad^2 s^{-2}), in logarithmic scale for all hydrographic stations. Left panel corresponds to transect A and right panel to transect B. Superimposed lines are h_ρ computed by the different methods. To improve the visualization only σ_θ-based algorithms are shown, where gray crosses show h_ρ following Kara et al. (2000), open white circles are h_ρ from the Holte and Talley (2009) algorithm, except for station 50 where a T_θ-based algorithm from Holte and Talley (2009) was more appropriate. Black squares show the σ_θ threshold criteria of de Boyer Montégut et al. (2004), and black triangles show h_ρ computed following the gradient method of Dong et al. (2008). 47

4.7 Vertical profiles of hydrographic and turbulent quantities. Left panels show T_θ (gray), σ_θ (dashed red) and S (violet) superimposed on dissipation profiles of ε_o (black bars), for: (a) station 42, affected by the upwelling filament and (c) station 48, unaffected by the filament. Both stations were measured during stable daytime conditions. Right panels show Ozmidov scales L_o (black bars) and vertical profiles of N^3 (gray) for: (b) station 42 and (d) station 48. Horizontal green and blue lines denote mixed layer depth (h_ρ) and mixing layer depth (h_ε), respectively. 49

4.8 Vertical profiles of Ozmidov scales, L_o (m), for each microstructure station. At the bottom, color columns are profiles of TKE dissipation rates, ε_o. The maximum L_o value corresponds to 5.18 m at station number 34 at 42 m depth, and minimum L_o of 0.0045 m is found at station number 38 at 66 m depth. Thick black profiles show L_o for stations potentially affected by filament waters, while thin profiles are for the rest of L_o. Horizontal lines indicate mixed h_ρ (green) and mixing h_ε (blue) layer depths, respectively. 50

4.9 Vertical sections of total squared vertical shear, Sh^2 (s^{-1}), rotated to the same reference system than geostrophic velocities for (a) transect A and (b) transect B. Geostrophic vertical shear Sh_g^2, where the level of no motion is set at 650 m for transect (c) A and (d) B. Note the logarithmic scale. The accumulative distance in km between stations is shown at the bottom. 51

4.10 Vertical profiles of dissipation rates (ε_o, gray bars), squared vertical shear (Sh^2, violet), squared buoyancy frequency (N^2, red) and gradient Richardson numbers (Ri_g, black) spatially averaged for stations of (a) group-F where $\Delta h > 0$ (a), and (b) stations of group-nF where $\Delta h < 0$. Both ε_o and N^2 are averaged in depth cells of 10 m to match with the vertical resolution of Sh^2. Horizontal solid and dashed lines show h_ρ and h_ε, respectively. 53

4.11 Entrainment rates from three parameterizations. Black rectangles show w_e^G in which the effect of vertical shear Sh^2 at the base of the mixed layer is neglected. White dots show w_e^{GS2} where the vertical shear effect is included. A Ri-dependent entrainment parameterization, w_e^{SF}, shown by dashed crosses which mainly depends on δV as a governing parameter. Shaded areas indicate stations of group-F potentially affected by the upwelling filament. 55

4.12 Comparison between w_e velocities given by the parameterizations of w_e^{SF} (dashed crosses), w_e^{GS2} (gray rectangles), and $w_e^{\Delta h}$ (black dots). Dashed box denotes microstructure profiles of stations in group-F affected by the filament. 57

4.13 Cross-sections of vertical velocities, w (m s^{-1}), at the base of the mixed layer for pair stations of (a) transect A and (b) transect B. Transects of w are integrated from their respective divergences of the flow (c and d) by setting $w = 0$ as boundary conditions at the surface. 58

4.14 Wind speed, $\boldsymbol{u}_r$ (m s^{-1}) for (a) transect A and (b) transect B, with their respective wind direction (clockwise from North). Cross-stream sections of potential vorticity q (s^{-3}) for: (a) transect A, q_A, and (b) transect B, q_B, where dashed lines corresponds to h_ρ and solid lines denote h_ε, both spatially averaged. 59

5.1 Vertical component of the geostrophic relative vorticity, ζ_g, normalized by the planetary vorticity, f, which is an estimate of the Rossby number, Ro. Small box in the left panel delimits the region where the anticyclonic eddy is found. Right panel shows a zoom of the delimited box in which altimeter-derived geostrophic currents are shown. Hydrographic and ADCP (black dots) and microstructure (white dots) stations are superimposed. We define stations 39 to 47 as the northernmost stations, 48 to 51 as the eddy-core stations and 52 to 63 as the southernmost stations. 69

5.2 Vertical sections of the meridional transect in Figure 5.1. (a) Potential density anomaly, σ_θ (kg m^{-3}), and (b) squared buoyancy frequency, N^2 (s^{-2}), in logarithmic scale. The black dashed lines represent the depth of the mixed layer, h_ρ. The white contours denote isopycnals where those corresponding to 25.3 and 26.7 (kg m^{-3}) are highlighted. 70

5.3 Meteorological half-hourly data averages. (a) Net surface heat flux, J_q^o (defined positive upward) and related components: shortwave radiation flux, J_q^{Sw}; net longwave heat flux, J_q^{Lw}; latent heat flux, J_q^{La}; and sensible heat flux, J_q^{Se}. (b) Net surface buoyancy flux, J_b^o, defined as the sum of the thermal surface buoyancy flux, J_b^T, and haline surface buoyancy flux, J_b^S. (c) Wind stress, $\boldsymbol{\tau}_o$. (d) Monin-Obukhov length scale, L_{mo}, where positive and negative values are marked as black and white dots, respectively. Black crosses indicate values of L_{mo} concomitant with CTD time profiles. Thin vertical dashed lines at the top show the hydrographic stations, while thick dashed lines at the bottom indicate the end of each day. 71

5.4 (a) Velocity scales of the three TKE-sources promoting the entrainment process, where u_* is the friction velocity, w_* is free convection and δV is the velocity jump across the mixed layer. (b) Vertical profiles of observed TKE-dissipation rates, ε_o, in logarithmic scale. Superimposed squares are mixed layer depths, h_ρ, and black crosses indicate the value of the mixing layer depths, h_ε. Odd-numbered stations are shown at the top. . 73

5.5 Turbulent diapycnal entrainment rates, w_e, computed from the classic parameterization of Gaspar (1988) through eq. (4.1), w_e^G, and from the new approach proposed by Estrada-Allis et al. (under review) through eq. (4.7), $w_e^{\Delta h}$. Dashed box highlights those stations located near the eddy center. Dashed lines show the trend of absolute w_e values, while only $w_e > 0$ are denoted by symbols. 76

5.6 Subsurface vertical meridional section of squared vertical current shear, Sh^2, in logarithmic scale computed from LADCP profiles. Superimposed color circles are values of ε_o for each microstructure station also in logarithmic scale. Note the absence of station 49. 79

5.7 Depth averaged K_ε (m^2 s^{-1}) in logarithmic scale, where dashed dark gray lines are K_ε averaged from surface to h_ρ; light gray from h_ρ to h_ε, i.e., Δh, and black from h_ε to 500 m. Dashed box indicates stations located within the eddy core. 80

5.8 Diapycnal diffusivities K_v (m^2 s^{-1}), derived from Osborn (1980), K_ε (black profiles) and from Large et al. (1994) KPP parameterization, K_{kpp} (gray profiles). Note that K_{kpp} is computed only for the interior ocean, therefore constant values of $K_{kpp} = 10^{-5}$ m^2 s^{-1} in the upper ocean layer should be considered insignificant. K_v from both parameterizations was averaged over three groups of stations: (a) northernmost stations, (b) eddy-center stations and (c) southernmost stations. 82

5.9 Spatial gradient Richardson number, Ri_g, for each hydrographic station, where large yellow-red circles denote near-critical Ri_c. Smaller circles show, in decreasing order, values of Ri_g from 0.5 to 3. Values above 3 are not shown. Gray rectangle highlights stations sampled at the eddy core. 83

6.1 Horizontal fields of the simulated day 29 of month 08, of (a) vertical component of relative vorticity normalized by the Coriolis parameter, $Ro = \zeta_r/f$, at 1 m depth, and (b) surface vertical velocity, w (m d^{-1}), at 10 m depth. The arrows marked the two vortex analyzed in this study, $A1$ and $A2$. Black horizontal line indicates zonal sections. 89

6.2 Zonal vertical section of potential density, ρ_θ (kg m^{-3}), from -15.4 to -17 °W, at a fixed latitude of 26.55 °N, denoted in Figure 6.1a as a black line, for $A2$ vortex (day 29 of month 8). White contours are isopycnals plotted every 0.15 kg m^{-3}. Continuous black line is h_{ubl}. Dashed line is the surface maximum gradient of N^2. 90

6.3 Horizontal fields, at 20 m depth, corresponding to each forcing term of the overall vertical velocity, w_{ROMS}. (a) w_{ROMS}, (b) Ageostrophic term, ***Ageo***, (c) Stretching term, ***Str***, (c) Tilting term, ***Tilt***, (d) Wind stress term, ***Wstr***, (e) Horizontal mixing term, ***Hmix***, and (f) Vertical mixing term, ***Vmix***. Note changes in the scale of color-bar. The simulated date corresponds to the day 29 of month 08. 93

6.4 Same than Figure 6.3 but at 300 m depth. 94

6.5 Same than Figure 6.3 but at 1000 m depth. 96

6.6 Fields derived from eq. (6.2) for three different vortices. For a synthetic Gaussian vortex: (a) Uniform wind stress field, $\boldsymbol{\tau}_r$, (b) η_r with superimposed geostrophic currents vectors u_g and v_g and (c) total Ekman pumping w_{EkT}. For an asymmetric vortex $A1$: (d) climatological $\boldsymbol{\tau}_r$, (e) η_r and vectors of u_g and v_g, and (f) w_{EkT}. The lowest panels: (g), (h) and (i) are analogous to (d), (e) and (f), but for an elliptical vortex $A2$. Both $A1$ and $A2$ are highlighted in Figure 6.1a. 98

6.7 Latitudinal averages of total w_{EkT}, lineal w_{EkL}, nonlinear w_{EkNL} and classic w_{Ek} Ekman suction/pumping for the case of: (a) vortex $A1$, and (d) vortex $A2$. Shaded areas denote the standard deviation error. Vertical dashed lines show vortices centers. The distance from the eddy center in km is shown at the bottom. Instantaneous snapshots of (b) w_{EkL} and (c) w_{EkNL} are depicted for vortex $A1$, whereas (e) and (f) are analogous to (b) and (c), for vortex $A2$. 100

6.8 (a) An example of horizontal snapshot (day 27 of month 06) of ζ_r/f. Negative relative vorticity fields are isolated in order to only considers anticyclonic eddies. The frequency spectra of vertical velocity is computed at three different depths: (b) 20 m; (c) 300 m and (d) 1000 m. Thin red lines are smoothed signals by using a Hanning filter. The inertial frequency (f) is indicated by vertical lines, while shaded areas denote the frequency range for vortex Rossby waves from 0.0083 to 0.0278 cph (1.5 to 5 days). 102

6.9 Snapshots of diapycnal coefficients, K_v (m^2 s^{-2}) in logarithmic scale, for two depths: (a) 10 m and (b) 50 m, covering the whole model domain. Note the differences in color-bar scales. Zonal (red) and meridional (blue) horizontal K_v profiles tied to the eddy center, shown for (c) vortex $A2$, and (d) vortex $A1$. Vertical continuous and dashed lines denote the eddy center for zonal and meridional sections, respectively. 104

6.10 (a) Root mean square of each forcing term for $A2$ vortex, in logarithmic scale. Surface zonal vertical sections of the $A2$ vortex with (b) overall vertical velocity w_{ROMS}, and (c) vertical mixing forcing term, $\boldsymbol{Vmix}$. Horizontal continuous and dashed lines denote h_{ubl} and the surface maximum gradient of N^2, respectively. Superimposed gray contours are isopycnals plotted every 0.15 (kg m^{-3}). 105

6.11 Horizontal w_{ROMS} at 300 m depth for vortex $A2$ in m d^{-1}. Contours of η_r are superimposed in gray. Lower panels are sub-surface vertical sections of w_{ROMS} with (b) a zonal section and (c) a meridional section. Isolines of ζ_r are superimposed in gray for negative and black for positive values. Dashed black lines in (a) denote coordinates for both meridional and zonal sections. 106

6.12 Temporal evolution of the w-dipoles for various vortices south of the Canary Islands. Snapshots correspond to horizontal maps of w_{ROMS} at 300 m depth in m d^{-1}, plotted every 5 days from day 01 of month 09. The date is shown at the top. Contours of η_r are superimposed in white in order to highlight the shape of each vortex. 107

6.13 Horizontal maps of w_{ROMS} (in m d^{-1}) for vortex $A2$ at four different depths: 100, 200, 300 and 1000 m. To show variations of the w-dipole magnitude, three dates are taken into account: (a) day 23 of month 08, (b) day 09 of month 09, and (c) day 23 of month 09. Contours of ζ_r are also represented in red for $\zeta_r > 0$ and blue for $\zeta_r < 0$. 108

6.14 Time sequence from a Lagrangian particle experiment, where (a) shows the release area of the Lagrangian experiment corresponding to the $A2$ vortex core. Color scale for negative OW denotes vorticity-dominated regions. Month, day and time-step (dt) of each snapshot is shown in the lower left corner. 110

6.15 Zonal vertical sections of vortex $A2$ with (a) w_{ROMS} and (b) w_{OMEGA} (in m d^{-1}). White contours are isopycnals plotted every 0.25 kg m^{-3}. Both vertical velocities have an horizontal resolution of 5 km. The rms of the forcing terms computed from eq. (6.7) are shown in (c), including the diagnosed w_{OMEGA}. 113

8.1 Mapa de energía cinética de remolinos, EKE (m^2 s^{-2}), derivado de los productos de altimetría de AVISO. La instantánea corresponde a la fecha 01 de enero de 2014. Los recuadros blancos delimitan las áreas de estudio comprendidas en esta tesis. El recuadro superior muestra la región del filamento de Cabo Ghir estudiada en el proyecto PROMECA del Capítulo 4. El recuadro inferior delimita el inicio del corredor de remolinos canario (Sangrà et al., 2009), como parte del proyecto PUMP examinado en los Capítulos 5 y 6. 129

8.2 Batimetría de la región de estudio en intervalos de 500 m. Se muestran las estaciones hidrográficas medidas en las vecindades del filamento de afloramiento de Cabo Ghir al noroeste de África en octubre de 2010. La región englobada dentro del recuadro de líneas discontinuas delimita las estaciones hidrográficas utilizadas en esta tesis. La región de estudio se amplifica para su mejor visualización en la figura superpuesta de la esquina izquierda inferior. Los cuadrados negros muestran las estaciones CTD, junto con las medidas de ADCP; los puntos en rojo denotan estaciones de microestructura; mientras que los pequeños puntos en negro son perfiles de XBT no utilizados en este resumen pero sí en el Capítulo 4 de esta tesis en inglés. Los transectos A, y B son también indicados. . 135

8.3 Mapas instantáneos de (a) temperatura superficial del mar de MODIS-Terra en °C para el 21 de octubre de 2010 a las 14:25 pm y (b) Clorofila de MODIS-Aqua para el 21 de octubre de 2010 a las 13:45 pm. Los vectores superpuestos denotan la magnitud y dirección del campo de velocidades geostróficas derivados de datos de altimetría de AVISO, a una resolución horizontal de 1/4°. Las estaciones CTD+ADCP son mostradas como puntos en negro. Las estaciones de microestructura son representadas mediante puntos en blanco. 137

8.4 Secciones vertical hidrográficas derivadas de los perfiles de CTD de salinidad, S, y (b) anomalía de la densidad potencial, σ_θ (kg m^{-3}), para el transecto A. De forma análoga, (c) S, y (d) σ_θ lo son para el transecto B. Contornos de S son trazados en intervalos de 0.5, mientras que los contornos de σ_θ son representados cada 0.1 kg m^{-3}. La distancia acumulativa entre las estaciones en km se muestra en la parte inferior. En la parte superior de la figura se muestran los correspondientes números de las estaciones hidrográficas. Los triángulos invertidos muestran las estaciones influenciadas por las aguas de filamento. 138

8.5 Datos meteorológicos promediados en intervalos de media hora. (a) flujo neto superficial de calor, J_q^o (positivo desde océano hacia atmósfera), y sus componentes relacionados: radiación de onda corta, J_q^{Sw}, flujo de calor de onda larga J_q^{Lw}, flujo de calor latente, J_q^{La}, y flujo de calor sensible, J_q^{Se}; (b) flujo neto superficial de flotabilidad, J_b^o, definido como la suma de sus contribuciones termales, J_b^T, y salinas J_b^S; (c) tensión del viento $\boldsymbol{\tau}_o$; (d) escala de Monin-Obukhov, L_{mo}, y profundidad de la capa de mezcla, h_ρ. Los símbolos sobre las series temporales denotados con el superíndice s representan el valor exacto de cada cantidad meteorológica, calculada a partir de los datos de cada perfil de CTD. Las líneas finas verticales muestran cada estación hidrográfica. Las líneas verticales gruesas indican el final de cada día muestreado. 140

8.6 Perfiles verticales hidrográficos y de microestructura. Las figuras de la izquierda muestran T_θ (gris), σ_θ (rojo) y S (violeta), superpuestas a perfiles de ε_o (barras negras) correspondientes a: (a) estación 42 del grupo-F; y (c) la estación 48, del grupo-nF. Ambas estaciones fueron medidas durante estables condiciones diurnas. Las figuras de la derecha muestran las escalas de Ozmidov, L_o (barras negras), y los perfiles de N^{-3} (gris) para (b) la estación 42 y (d) la estación 48. Las líneas horizontales amarillas y azules denotan h_ρ y h_ε, respectivamente. 142

8.7 Perfiles verticales de las escalas de Ozmidov L_o para cada estación de microestructura. En el fondo se muestran perfiles de ε_o. El máximo valor de L_o corresponde a 5.18 m para la estación 34 a 42 m de profundidad, y el mínimo valor de L_o de 0.0045 m fue registrado en la estación 38 a 66 m de profundidad. Las estaciones del grupo-F se destacan de las del grupo-nF a través de perfiles verticales gruesos. Las líneas horizontales verdes y azules indican la profundidad de h_ρ y h_ε, respectivamente. . . . 143

8.8 (a) Velocidades diapicnas w_e obtenidas mediante tres parametrizaciones: w_e^G, en la cual el efecto de la cizalla vertical no es tenido en cuenta en su parametrización. w_e^{GS2}, en cuya formulación viene incluido el término DIT de cizalla vertical. w_e^{SF}, basada en un enfoque dependiente de Ri_v. Las áreas sombreadas indican aquellas estaciones pertenecientes al grupo-F. (b) Comparación entre velocidades diapicnas w_e dadas por las parametrizaciones de w_e^{SF}, w_e^{GS2}, y $w_e^{\Delta h}$. Las estaciones de microestructura potencialmente influenciadas por el filamento son destacadas en el rectángulo de líneas discontinuas. 144

8.9 (a) Componente vertical de la vorticidad relativa geostrófica normalizada por la vorticidad planetaria, $Ro = \zeta_g/f$. A la izquierda, se amplifica la zona muestreada del remolino donde se denotan las estaciones hidrográficas y de ADCP con puntos en negro. Los puntos blancos muestran las estaciones de microestructura. Las estaciones 39 a la 47 se denominan estaciones norte; desde la 48 a la 51 estaciones del centro del remolino y las estaciones sur comprenderán desde la estación 52 a la 63. Los vectores representan la corriente geostrófica calculada a través de datos de altimetría. Las figuras inferiores representan las secciones verticales meridionales del remolino donde (b) anomalía de la densidad potencial, σ_θ (km m^{-3}), y (b) frecuencia de flotabilidad al cuadrado, N^2 (s^{-2}). Las líneas negras punteadas representan la profundidad de la capa de mezcla, h_ρ, y los contornos blancos denotan las isopicnas. 151

8.10 (a) Escalas de velocidad de las tres fuentes de ECT implicadas en el proceso de *entrainment* diapicno, donde u_* es la velocidad de fricción, w_* es la convección libre, y δV es el salto de velocidad a través de h_ρ. (b) Perfiles verticales de ε_o observados. Los símbolos cuadrados muestran valores de h_ρ y las cruces negras indican h_ε. Para una mejor visualización solo se muestra el número de las estaciones impares en la parte superior del gráfico. 152

8.11 (a) Tasas de *entrainment* diapicno turbulento w_e calculadas a partir de la clásica parametrización de Gaspar (1988) w_e^G (ec. 8.5), y a partir del nuevo enfoque propuesto por Estrada-Allis et al. (under review) $w_e^{\Delta h}$ (ec. 8.9). Las líneas punteadas muestran la tendencia de los valores absolutos de w_e, mientras que solamente valores positivos de w_e son denotados con símbolos. (b) Promedio vertical de los coeficientes de difusividad diapicna, K_ε (m^2 s^{-1}), para las tres profundidades en las que se divide el análisis de mezcla del remolino. Los recuadros punteados dentro de ambas figuras remarcan aquellas estaciones localizadas en el centro del remolino. 153

8.12 Sección vertical subsuperficial meridional de la cizalla vertical inducida por corrientes horizontales, Sh^2, en escala logarítmica, calculada a partir de los perfiles de LADCP. Los símbolos de colores superpuestos indican valores de ε_o para cada estación de microestructura y cada profundidad en la que fue promediada. Note que la ausencia de la estación 49 de LADCP impide la representación del perfil de ε_o para dicha estación. . . 155

8.13 (a) Campo horizontal simulado del día 29, mes 8 de la vorticidad relativa normalizada por la vorticidad planetaria, $Ro = \zeta_r/f$, a 1 m de profundidad. Las flechas delimitan los dos vórtices analizados en este estudio $A1$ y $A2$. La barra horizontal negra indica el corte para las secciones zonales verticales posteriores. (b) Sección zonal vertical de la densidad potencial, ρ_θ (kg m^{-3}), de $A2$ para la misma fecha que (a). Los contornos blancos son isopicnas trazadas cada 0.15 kg m^{-3}. La línea continua negra denota la capa de frontera superior, h_{ubl}, mientras que la línea discontinua muestra el máximo gradiente superficial del cuadrado de la frecuencia de flotabilidad, N^2. 158

8.14 Campo horizontal a 20 m de profundidad, para cada uno de los términos en los que se descompone w_{ROMS} a través de la ec. (8.10). (a) w_{ROMS} total, (b) término ageostrófico ***Ageo***, (c) término de estiramiento ***Str***, (c) término de inclinación ***Tilt***, (d) término de tensión del viento ***Wstr***, (e) mezcla horizontal ***Hmix*** y (f) mezcla vertical ***Vmix***. Note las variaciones en la escala de colores. El campo simulado corresponde al día 29 del mes 08. 161

8.15 Igual que en la Figura 8.14, pero a -300 m. 162

8.16 Promedio latitudinal de succión de Ekman total, w_{EkT}, lineal, w_{EkL}, no lineal, w_{EkL} y succión de Ekman clásico, w_{Ek}, para el caso de (a) vórtice $A1$ y (d) vórtice $A2$ donde las áreas sombreadas denotan la desviación estándar y las líneas verticales muestran el centro de los vórtices. La distancia desde el centro del remolino en km se muestra en la parte inferior de las figuras. Mapas instantáneos de (b) w_{EkL} y (c) w_{EkNL} para el vórtice $A1$, mientras que de forma análoga (e) y (f) lo son para el vórtice $A2$. 164

8.17 (a) Ejemplo de una instantánea horizontal $\zeta_r < 0$ normalizada con f del día 27 y mes 06, cribando así solamente aquellos remolinos anticiclónicos en los que se realiza el promedio para el análisis espectral. La frecuencia espectral de la velocidad vertical se calcula para tres profundidades: (b) 20 m; (c) 300 m y (d) 1000 m. Las líneas rojas finas denotan el filtrado de las señales mediante un filtro de Hanning. La frecuencia inercial f es también indicada por la línea vertical negra, mientras que las áreas sombreadas muestran el rango de frecuencias desde 0.0083 a 0.0278 cph (1.5 a 5 días). 165

8.18 Campo instantáneo de K_v (m^2 s^{-2}) a 10 m de profundidad cubriendo todo el dominio numérico, generado por la parametrización de KPP incluida en ROMS. Las figuras inferiores son perfiles zonales (rojo) y meridionales (azul) de K_v centrados en el núcleo de ambos remolinos (b) $A2$ y (c) $A1$. Las líneas verticales continuas y discontinuas denotan el centro del remolino para las secciones zonales y meridionales respectivamente. . 166

8.19 (a) Error cuadrático medio (rms por sus siglas en inglés) de cada término en los que se descompone w_{ROMS} para el remolino $A2$. Note la escala logarítmica. Secciones zonales verticales donde (b) w_{ROMS}, y (c) término $\boldsymbol{Vmix}$. Las líneas horizontales continuas y discontinuas denotan h_{ubl} y el máximo gradiente de N^2, respectivamente. Los contornos en gris son isopicnas cada 0.15 (kg m^{-3}). 167
8.20 Evolución temporal de los dipolos de w para varios vórtices al sur de las Islas Canarias. Las instantáneas corresponden a los mapas horizontales del campo de w_{ROMS} a 300 m de profundidad trazadas cada 5 días desde el día 01 del mes 09. En la parte superior de los mapas se muestra la fecha correspondiente a cada instantánea. Los contornos blancos denotan valores de superficie libre, η_r, a modo de resaltar la forma de cada vórtice. 168
8.21 Secuencia temporal del experimento de liberación de partículas lagrangianas. (a) Área de vertido de las partículas correspondiente al centro del vórtice $A2$. La escala de colores denota OW negativos indicando solamente regiones dominadas por la vorticidad. El mes, día y tiempo de paso (dt) de cada instantánea se muestra en la esquina inferior izquierda. 170
8.22 Secciones verticales zonales del vórtice $A2$ para el día 29 del mes 08 de (a) w_{ROMS} y (b) w_{OMEGA} (m d^{-1}). Las isopicnas trazadas cada 0.25 kg m^{-3} son trazadas mediante contornos blancos. Ambas w tienen una resolución horizontal de 5 km. El error cuadrático medio (rms por sus siglas en inglés) de cada componente de w_{OMEGA} se muestra en la figura (c). 172

List of Tables

3.1 Configuration characteristics of the L2-ROMS model used in this thesis and initial forcings and boundary conditions interpolated to the model grid. 32

4.1 List of symbols and parameters 38
4.2 Spatially averaged dissipation term of a 1D TKE balance ($\mathrm{m}^3\ \mathrm{s}^{-3}$) for both transect A and B. TKE dissipation rates are also averaged in depth up to h_ρ for the parameterized ε_p and up to h_ε for ε_o and ε_{LG} 61

8.1 Características de la configuración del modelo ROMS de (Mason, 2009) usado en esta tesis, así como los forzamientos iniciales y condiciones de frontera interpoladas en el grillado del modelo. 132
8.2 Términos de disipación de un balance de ECT ($\mathrm{m}^3\ \mathrm{s}^{-3}$), promediados espacialmente para ambos transectos A y B. Las tasas de disipación de ECT son también promediadas verticalmente hasta profundidades de h_ρ para el caso de ε_p y hasta h_ε para ε_o y ε_{LG}. 146

1

Introduction

1.1 The scales of the ocean

Approximately 71% of the Earths surface is covered by the ocean which in turn contains about 97% of the planet's water. Water is essential for the life on Earth that makes this blue planet unique in our solar system. The ocean plays an essential role in the climate and weather systems of the Earth and, hence, an understanding of the processes that control the seas is a key scientific challenge. The wide range of interacting processes at different spatial and temporal scales makes it an extremely complex study. An example of the principal scales and processes that take place in the ocean can be seen in Figure 1.1. The large scales have received much more attention than the small scales, due to the fact that climate change, such as global warming, is included within this scale. However, in the last few decades a large proportion of research studies have been focused towards the mesoscale and its associated submesoscale processes as their role in climate modulation has been recognized (e.g., Smith et al., 2000; Capet et al., 2008c; Lévy et al., 2010; Sasaki et al., 2014; Sheen et al., 2014; Callies et al., 2015). Although techniques to measure and examine submesoscale and small-scale process have been improved in recent years (Chelton et al., 2007; Xu and Fu, 2012; Ponte et al., 2013), the main research effort has been oriented towards theoretical approaches and numerical modeling (e.g., Siegel et al., 2001; Mahadevan and Tandon, 2006; Capet et al., 2008b; Klein et al., 2008; Thomas et al., 2008; Ponte et al., 2013).

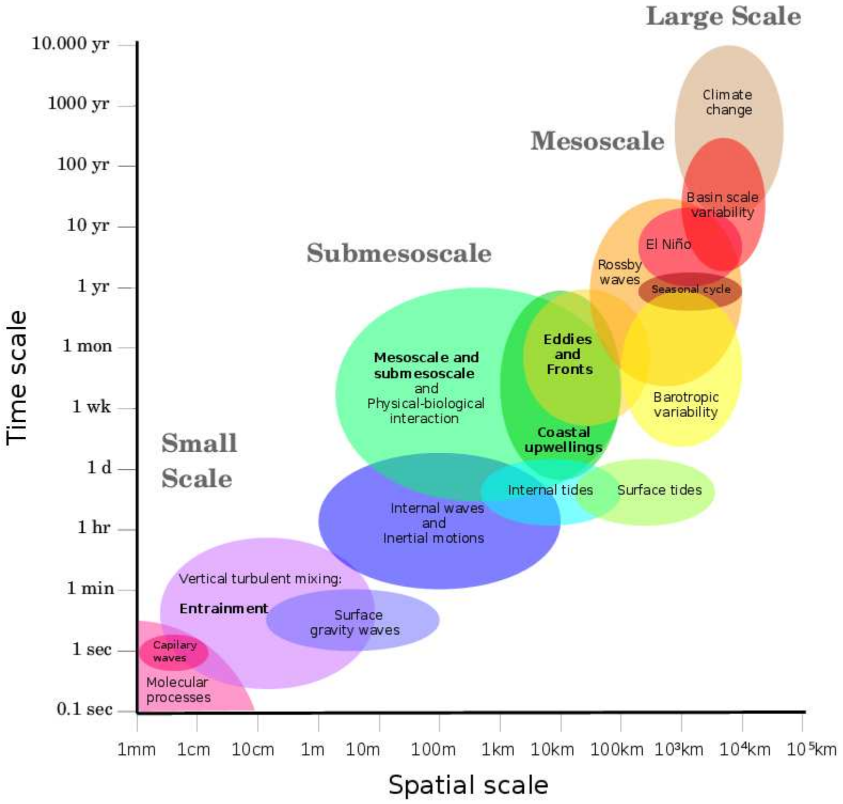
Large Scale
Mesoscale
Submesoscale
Small Scale
Climate change
Basin scale variability
El Niño
Rossby waves
Seasonal cycle
Eddies and Fronts
Mesoscale and submesoscale and Physical-biological interaction
Barotropic variability
Coastal upwellings
Internal tides
Surface tides
Internal waves and Inertial motions
Vertical turbulent mixing:
Entrainment
Surface gravity waves
Capilary waves
Molecular processes
Time scale
10.000 yr
1000 yr
100 yr
10 yr
1 yr
1 mon
1 wk
1 d
1 hr
1 min
1 sec
0.1 sec
Spatial scale
1mm
1cm
10cm
1m
10m
100m
1km
10km
100km
10³km
10⁴km
10⁵km

Figure 1.1: Scheme illustrating the relevant time and space scales in which occur several physical and biological processes crucial for the oceanic and climate systems. From large-scale movements that comprises the climate global change $\mathcal{O}(10.000 \text{ km})$ over tens of years to micro-scales acting at $\mathcal{O}(0.1 \text{ m})$ in only few minutes but with important implications in the meridional overturning circulation. Scheme adapted from Chelton (2001).

A topic that is gaining increasing attention within the research community is the concept of the energy cascade (Kolmogorov, 1941), which helps us to explain how the scales in the ocean are interconnected through pathways of kinetic energy that lead to the global energy balance. Accordingly, energy is transferred from large scales to small scales and finally dissipated by viscosity. As an example, a feedback is produced when unstable submesoscale structures, such as fronts, generate small scale eddies

(McWilliams, 1984; Klein et al., 2008). This concept inspired *L. F. Richardson* who in 1922 postulates:

> "*Big whorls have little whorls,*
> *Which feed in their velocity,*
> *And little whorls have lesser whorls,*
> *And so on to viscosity*"
> *L. F. Richardson (1922)*

On the contrary, the energy can be also transferred from small to large scales when smaller eddies are engulfed and merge with large eddies, or through instabilities generated at the submesoscale (Capet et al., 2008c; Ferrari and Wunsch, 2009; Lévy et al., 2010; Sasaki and Klein, 2012; Sasaki et al., 2014); in other words an inverse cascade of energy.

An understanding of how energy is transferred from the mesoscale to small scale turbulence and finally viscous dissipation, or vice-versa, in order to close the kinetic energy budget for the ocean circulation, still remains as an open issue.

1.2 Mixing processes at small-scales

From small to large scales, mixing in the ocean is ubiquitous (Figure 1.2). An important component of mixing is turbulence. Since the pioneering works of Boussinesq (1877) and Reynolds (1895) which encourage the theoretical prediction of Kolmogorov (1941) for the energy spectrum, turbulence has become one of the main open problems in fluid dynamics.

The implications of turbulence as a mechanism for transport of heat, salt, momentum and biogeochemical properties between different ocean layers have been recognized for many years (see reviews by Jiménez, 1997; Burchard et al., 2008). Because of the complex nature of small scale and microscale turbulent mixing processes, measurement and quantification are not straightforward, often being represented by theoretical parameterizations that need to be continuously validated for a wide range of mechanisms such as those outlined in Figure 1.2. Despite the intermittent nature of turbulent mixing, it is observed throughout the water column. In the interior ocean, processes such as bottom boundary mixing, double diffusive mixing, breaking internal waves, and shear instabilities (e.g., Ferron et al., 1998; Munk and Wunsch, 1998; St. Laurent and Garrett, 2002; Naveira Garabato et al., 2004; Kunze et al., 2006) (Figure 1.2) might be implicated in the global climate system (e.g., Munk, 1966; Ledwell et al., 2000; Ferrari and Wunsch, 2009).

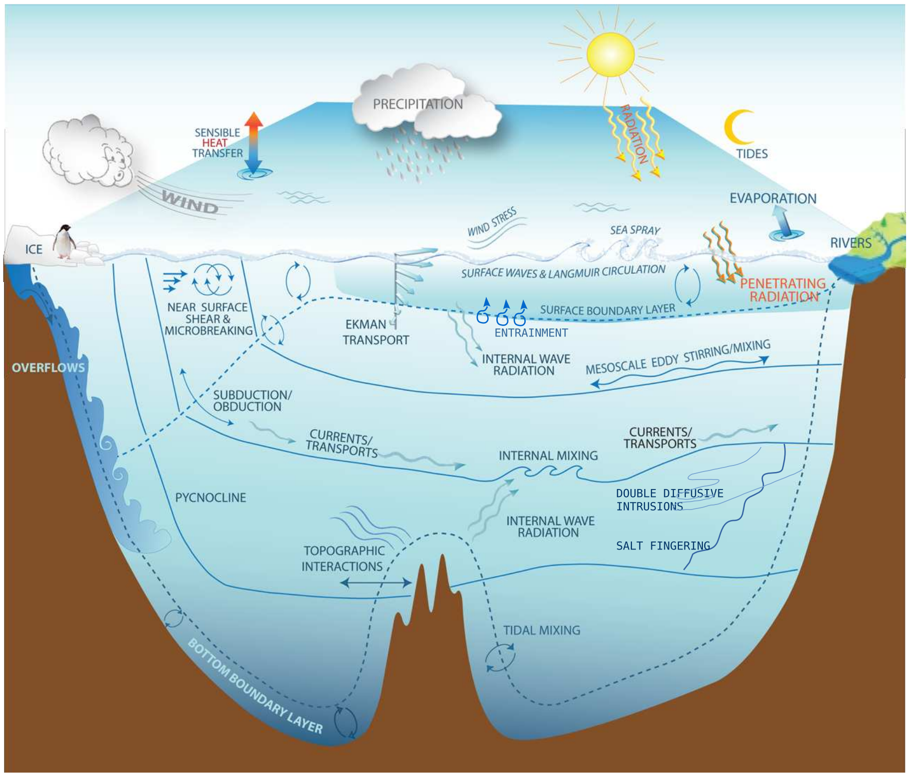
PRECIPITATION
RADIATION
TIDES
SENSIBLE HEAT TRANSFER
WIND
EVAPORATION
WIND STRESS
SEA SPRAY
RIVERS
ICE
SURFACE WAVES & LANGMUIR CIRCULATION
PENETRATING RADIATION
NEAR SURFACE SHEAR & MICROBREAKING
EKMAN TRANSPORT
SURFACE BOUNDARY LAYER
ENTRAINMENT
INTERNAL WAVE RADIATION
MESOSCALE EDDY STIRRING/MIXING
OVERFLOWS
SUBDUCTION/ OBDUCTION
CURRENTS/ TRANSPORTS
INTERNAL MIXING
CURRENTS/ TRANSPORTS
DOUBLE DIFFUSIVE INTRUSIONS
PYCNOCLINE
INTERNAL WAVE RADIATION
SALT FINGERING
TOPOGRAPHIC INTERACTIONS
TIDAL MIXING
BOTTOM BOUNDARY LAYER

Figure 1.2: Scheme of the main mixing processes acting into the ocean at many time and spatial scales. Some of them remain poorly understood. Adapted from Moum et al. (2003).

At the surface, upper ocean mixing is mainly forced by cycles of heating and cooling, wind stirring, and changes in temperature, humidity and freshwater fluxes. As a result a hierarchy of mixing processes arise as depicted in Figure 1.2, such as wind-shear induced turbulence, Langmuir circulation, breaking internal waves at the pycnocline, free and forced convection[*] and vertical current shear at the pycnocline (Turner, 1979; Thorpe, 2005), amongst others. These processes have an important impact on upper boundary layer dynamics and interact with biogeochemical systems, although some of these are not at all well understood (Moum and Smyth, 2001). A relevant, though poorly known turbulent process, occurring at small scales but impacting on the upper ocean dynamics, is the diapycnal entrainment phenomenon. This mixing process evolves forcing sources different from those mentioned above; its examination and clarification is therefore one of the main aims of this thesis.

1.3 The turbulent entrainment process

Between the pycnocline and the upper mixed layer there is an interfacial layer, defined also as the entrainment zone, where vertical velocities can transport material upwards across isopycnals. This is a mixing process named turbulent diapycnal entrainment which is characterized by a diapycnal entrainment rate (w_e).

One of the first studies to focus on interfacial mixing involves the stirring grid experiments of Rouse and Dodu (1955). In their laboratory experiment, they expected that stirring would smear out interfacial gradients but to their surprise they discovered that the interface became sharper with continual transfer of material from non-turbulent to turbulent regions of the fluid where it quickly became well mixed (Turner, 1979). This allows us to make a general definition of the upper ocean turbulent diapycnal entrainment: a process by which turbulent fluid within a well stirred boundary layer (weakly stratified) incorporates adjacent fluid from below the pycnocline (highly stratified) that is not turbulent, or at least much less turbulent. The main effects of this process are an increase in the mixed layer depth (h_ρ) and the transport of physical properties such as heat, salinity and biogeochemical properties between the upper and lower ocean layers (e.g., Deardorff, 1983; Kolodziejczyk et al., 2015). The entrainment mechanism can also modulate the sea surface temperature (e.g., Price et al., 1986; Alexander et al., 2000; Jacob and Shay, 2003; Wada et al., 2009) and impact on the heat fluxes in the upper ocean layer (Alexander et al., 2000; Inoue et al., 2010). Moreover, some studies have pointed out that differential entrainment could be implicated in reinforcing secondary circulation induced by frontogenesis at frontal systems (Dewey and Moum, 1990; Capet et al., 2008b).

---

[*] Free convection occurs where the contributions to the vertical transfer of momentum and heat by mechanical turbulence can be neglected compared to those carried by convection. Forced convection occurs when the generation of turbulence by the wind shear dominates over generation by buoyancy.

However, determination of the entrainment process can be challenging because the overwhelming of entrainment quantities by large-scale motions and high sensitivity of w_e to the available turbulent kinetic energy (hereafter, TKE) sources, as we will see in this thesis.

1.3.1 The Role of w_e in the TKE balance

In a bulk mixed layer model a parameterization of the entrainment process is required to solve the momentum, salinity, and heat fluxes in one-dimensional (1D) equations; therefore, it is necessary to use an explicit expression for the turbulent fluxes (Niiler and Kraus, 1977; Turner, 1979) and also for closure of the TKE budget within the mixed layer. The main assumption is that most of the kinetic energy produced is lost through the dissipation term, whereas the remaining TKE is used to work against buoyancy forces through the increase in potential energy due to mixing.

The turbulent kinetic energy budget in a one-dimensional approach can be formulated (Kraus and Turner, 1967) as:

$$\underbrace{\frac{1}{2}\partial_t(q^2)}_{A} = \underbrace{-\overline{w'\boldsymbol{u}'_h}\partial_z(\overline{\boldsymbol{u}_h})}_{B} + \underbrace{\overline{w'b'}}_{C} - \underbrace{\frac{1}{2}\partial_z[\overline{w'(w'^2+\boldsymbol{u}'^2_h)} + \rho^{-1}\overline{w'\rho'}]}_{D} - \underbrace{\varepsilon}_{E} \tag{1.1}$$

where $q^2 = \overline{w'^2} + \overline{\boldsymbol{u}'^2_h}$ is the mean specific TKE, primes denote turbulent deviations from bulk velocities $\overline{w}$ and $\overline{\boldsymbol{u}_h} = (u, v)$, and the vertical flux of horizontal momentum from the Reynolds stress $(\overline{w'\boldsymbol{u}'_h})$ being their averaged products.

The terms of eq. (1.1) represent: (A) the TKE tendency, (B) the momentum fluxes, where $\overline{w'\boldsymbol{u}'_h}$ works upon the mean vertical shearing of the flow, i.e., shear production, (C) accounts for the rate of buoyancy force work or buoyancy production where $b = g(\rho_o - \rho)/\rho_o$ is the buoyancy, $g \approx 9.81$ m s^{-2} is the constant gravitational acceleration, ρ is the sea water density in kg m^{-3}, and ρ_o the reference density, (D) indicates the convergence of the turbulent vertical transport and the last term (E) accounts for the TKE dissipation rate ε.

Most bulk or slab mixed layer models include eq. (1.1) to resolve, in a simplified 1D approach, the fluxes of momentum, salinity and heat. Niiler and Kraus (1977) listed the main assumptions for bulk-mixed layer models:

(i).- The mean temperature, salinity and horizontal velocity are assumed to be quasi-uniform over the upper ocean boundary layer.

(ii).- On the depth and time scales of the model, a quasi-discontinuous distribution can be envisaged for the above variables across both the upper and lower mixed boundary layer.

(iii).- Temporal changes of the TKE is assumed small when compared to turbulence generation and dissipation effects.

(iv).- Temperature changes associated with frictional dissipation and with changes in salinity are neglected.

In particular, assumption (i) allow us to integrate eq. (1.1) from the base of the mixed layer, $z = -h_\rho$, to the surface $z = 0$, resulting in the expression of Niiler and Kraus (1977):

$$\frac{1}{2} w_e (q^2 + \delta b h_\rho - \overline{\boldsymbol{u}_h^2}) = m u_*^3 + \frac{1}{2} h_\rho J_b^o + J_o \left(\frac{h_\rho}{2} - \frac{1}{\gamma}\right) + \frac{1}{3} C |\overline{\boldsymbol{u}_h^3}| - \int_{-h_\rho}^{0} \varepsilon(dz) \tag{1.2}$$

where $\delta b = b_1 - b_2$ is the buoyancy jump from layer 1 (at base of the mixed layer) to layer 2 (just below the base of the mixed layer) (Figure 1.3), and γ being the attenuation coefficient. Surface buoyancy flux (J_b^o) will be described in Chapter 3 and $J_o \equiv (g\alpha/\rho C) I_o$ is the buoyancy radiation flux with I_o as the surface flux of penetrating solar radiation ($\sim$ 45% of total solar radiation), α (^{o}C^{-1}) is the thermal expansion coefficient and C a generalized drag coefficient that is a function of the particular density stratification (Niiler and Kraus, 1977).

The above system is not closed because a new time dependent variable has been added representing the temporal change of the depth of the mixed layer. This variable usually denotes the deepening of the mixed layer that must be equal to the entrainment rate w_e. Mathematically, this can be written as:

$$\begin{aligned} w_e &= \partial h/\partial t, & \partial h/\partial t > 0 \\ w_e &= 0, & \partial h/\partial t \leq 0 \end{aligned} \tag{1.3}$$

Physically, the relation in eq. (1.3) means that negative or zero w_e will cause a retreat or no further growth of the mixed layer with time since w_e can only be positive. In brief, the entrainment phenomenon can be seen as the sum of sources and sinks of TKE that, combined, control the upper ocean boundary layer dynamics. If one avoids some TKE sources (e.g., significant absorption of solar radiation at depth), there are three mechanisms with their respective velocity scales that dominate entrainment, first mechanical stirring induced by the wind-stress whose velocity scale is the friction velocity (u_*):

$$u_* = \frac{\boldsymbol{\tau}_o}{(\rho_o)^{1/2}} \tag{1.4}$$

where wind-stress $\boldsymbol{\tau}_o = (\tau^x, \tau^y)$ is computed through the Large and Pond (1981) parameterization (see eq. 3.3, Chapter 3).
Second the surface buoyancy flux (destabilizing when positive), is scaled by the free convection velocity (w_*) from Deardorff (1970):

$$w_* = (J_b^o h_\rho)^{1/3} \tag{1.5}$$

The third mechanism is vertical current shear at the base of the mixed layer h_ρ , where the velocity scale is a velocity jump (δV) from layer 2 to layer 1.

$$\delta V = \boldsymbol{u}_h^2 - \boldsymbol{u}_h^1 \tag{1.6}$$

Figure 1.3 shows a simplified schematic of the one dimensional diapycnal turbulent entrainment process. Here, the surface layer and the layer below the pycnocline are interconnected through an interface, already named as the entrainment zone (Δh), in which the deepening of the mixed layer and the transport of properties from stratified to upper layers takes place. The velocity jump is accompanied by sharp changes in density $\delta\rho = \rho_2 - \rho_1$ and buoyancy (δb) across the entrainment zone, i.e., crossing the pycnocline from layer 2 to the surface layer 1. In essence, the three sources of TKE mentioned above act to mix the potential density profile (ρ_θ) through the effect of: (1) wind stirring; (2) free surface convection; and (3) through differences in horizontal currents at the entrainment zone (3) which lead to an extra source of turbulence by current shear.

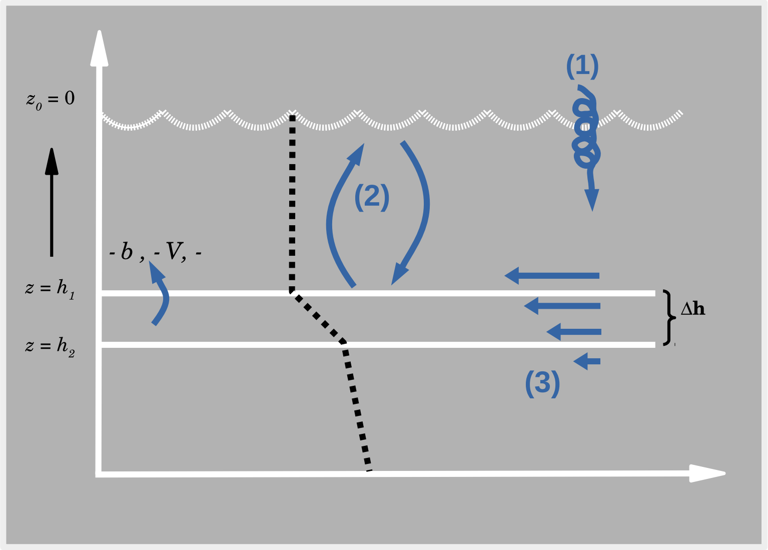

Figure 1.3: Simplified scheme of the turbulent diapycnal entrainment phenomenon for a potential density profile (ρ_θ). Three layers are considered: a well mixed surface layer (h_1), an interfacial layer (Δh) and a more stratified layer below pycnocline (h_2). Upward arrows indicate the jump from pycnocline to surface layers of buoyancy (δb), density ($\delta \rho$) and velocity (δV). Sources of TKE driving entrainment are depicted as: (1) mechanical stirring by wind driving by friction velocity (u_*), (2) convective mixing by free convection velocity scale (w_*) and (3) velocity jump (δV) across the interface as a result of vertical shear by horizontal current.

Based on the closure of Niiler and Kraus (1977) entrainment parameterizations can be divided depending on the sources of TKE (u_*, w_*, δV). Therefore, depending on the sources, the entrainment parameterizations can serve as an indicator of which mixing process is playing a major role in the upper mixed layer. Most existing models only take account of the sources u_* and w_*, neglecting the effect of vertical current shear in the entrainment zone. During this thesis we will see that inappropriate parameterizations of dissipation rates, the omission of δV as a TKE source, and the impact of not considering Δh can result in underestimates of the entrainment rates, especially in highly dynamic areas.

1.3.2 Determination of w_e using a Richardson number dependent argument

An elegant way to determine entrainment rates is based on a Richardson number dependent argument. This alternative way to obtain w_e at the stratified interface is based on entrainment law (e.g., Ellison and Turner, 1959; Kato and Phillips, 1969; Khanta et al., 1977; Strang and Fernando, 2001) which can be seen as the relationship between the entrainment coefficient (E) and the governing parameters implicated in the mixing at the base of h_ρ, such as the bulk Richardson number (Ri_b):

$$Ri_b = \frac{h_\rho \delta b}{{v_{TKE}}^2} \tag{1.7}$$

being v_{TKE} any velocity scale implicated in the entrainment mechanism as responsible for the TKE production (i.e., u_*, w_* or δV). Consequently, the entrainment law can take the following form:

$$E = \frac{w_e}{v_{TKE}} = \gamma_e Ri_b^{-k} \tag{1.8}$$

where γ_e and the power law $-k$ are constants. Laboratory experiments of Ellison and Turner (1959) have shown that the ratio between w_e and the TKE velocity scale is a decreasing function of Ri_b.

Because there exist different mechanisms that can activate the entrainment process, several power laws have been published (Fernando, 1991) in which the values for k range from 0 to 2.5. As pointed out by Fernando (1991) and Pelegrí and Richman (1993), there is no unified law or parameterization for describing the entrainment process due, in part, to the extensive list of power laws proposed in the literature that can be fitted for a wide range of experimental, modeling and observational data (Khanta et al., 1977; Deardorff, 1983; Price et al., 1986; Gaspar, 1988; Fernando, 1991; Pelegrí and Richman, 1993; Strang and Fernando, 2001; Nagai et al., 2005; Wada et al., 2009). This characteristic makes applying the entrainment law unclear (Pelegrí and Richman, 1993; Nagai et al., 2005; Jonker et al., 2013).

1.4 Vertical velocity at the mesoscale

Whereas entrainment rates are based on diapycnal velocities occurring at the microscale, the net vertical transport is also epypicnal, that is, along isopycnals. Both velocities[*] comprise the total vertical velocity (w) field.

In recent decades, several studies have pointed out that the bulk of the w-field occurs within the mesoscale and submesoscale ranges (e.g., Vélez-Belchí and Tintoré, 2001; Capet et al., 2008b; Le Traon et al., 2008; Klein et al., 2009; Pallàs-Sanz et al., 2010). Inferred velocities at the mesoscale are of $\mathcal{O}(1 \text{ m d}^{-1})$, whereas there are much higher $\mathcal{O}(100 \text{ m d}^{-1})$ values at the submesoscale. In the mesoscale, available potential energy (APE) is converted to eddy kinetic energy (hereafter, EKE) through baroclinic instability, where final stage is dissipation. Baroclinic instability can be found in any mesoscale feature contained within the internal Rossby deformation radius (Ld), such as cyclonic/anticyclonic eddies or thermohaline fronts which in turn are largely linked through frontogenesis and baroclinic/barotropic instability generation.

Vertical velocities are mainly generated through two physical processes in the ocean: the Ekman pumping mechanism (e.g., Martin and Richards, 2001; Gaube et al., 2015) or by frontogenetic processes (e.g., Pollard and Regier, 1992; Nagai et al., 2006; Capet et al., 2008b). The vertical velocity field can be also influenced by wave-like patterns, these are likely induced by quasi-inertial waves which result from vortex-mean flow interactions (e.g., Koszalka et al., 2009; 2010; Cardona and Bracco, 2012; Nardelli, 2013). As we will see in Chapter 6, these waves are analogous to planetary Rossby waves in large scale flows but with the radial gradient of vertical vorticity serving as the restoring mechanism (Montgomery and Kallenbach, 1997), so they are usually called vortex Rossby waves (VRWs).

Although vertical velocities in the ocean are small when compared to the horizontal velocity field, they strongly impact both the biogeochemical and climate systems by supplying nutrients to the photic layers, transporting heat, salt and momentum fluxes, and exchanging gases with the atmosphere. Similarly to the case of diapycnal entrainment velocities, vertical velocities are difficult to measure and determine due to the lack of reliable observational techniques for the small values involved (Vélez-Belchí and

---

[*] The study of both diapycnal and epypicnal velocities can be carried out by considering an isopycnal reference system.

Tintoré, 2001). Therefore, estimates of w can be carried out mainly by indirect methods. One of the most successful methods is the omega equation (ω-equation) which diagnostically lead to w by assuming quasi-geostrophic (QG) balance and requiring only the density field at synoptic time-scales (e.g., Hoskins et al., 1978; Tintore et al., 1991; Pinot et al., 1996).

However, systematic errors in omega w accuracy arise due to the required synopticity of a suitable sampled grid. In addition, the QG-approximation can fail when reproducing local ageostrophic effects, especially at the oceanic mesoscale (Giordani et al., 2006; Koszalka et al., 2009). To deal with this, a semi-geostrophic (SG) ω-equation (e.g., Pinot et al., 1996; Viúdez and Dritschel, 2004) can be considered where the ageostrophic advection of horizontal geostrophic velocity is included in the formulation. Lastly, when density and velocity fields are available that incorporate ageostrophic flows, a generalized form of the ω-equation developed by Viúdez et al. (1996) can be invoked and is implemented in Chapter 6.

Consideration of mixing process within ω-equations can also be cumbersome owing to the need for higher order derivatives and Richardson number dependent parameterizations. A small number of related studies of the diabatic ω-equation have found that the impact of mixing process, buoyancy and momentum fluxes on the vertical velocity field is restricted to the upper ocean layers (Giordani et al., 2006; Nagai et al., 2006; Pallàs-Sanz et al., 2010). Consequently, there is still room to explore the consequences of mixing and vertical transport within mesoscale and submesoscale features. There are also discrepancies when w from ω-equation is compared with w diagnosed from primitive equation (PE) simulations (Koszalka et al., 2009). In high resolution PE models, vertical velocities can be diagnosed from the instantaneous divergence of the flow by the continuity equation (Vallis, 2006). Owing to the availability of three-dimensional (3D) model fields of density, velocity and atmospheric fluxes, in this thesis (Chapter 6) the latter approach is also considered by following the study of Koszalka et al. (2009), which allows the inclusion of other sources of w not taken into consideration for the ω-equation.

1.5 Mesoscale structures: Filaments and eddies in the Canary Basin

In this thesis, vertical processes such as diapycnal turbulent entrainment, and the components of the forces acting on the vertical velocity field will be studied within two mesoscale structures: a filament generated by the eastern boundary upwelling of the Northeast African coast near Cape Ghir, and an anticyclonic eddy formed in the lee of the Canary Island archipelago. In the framework of two projects, namely: "Mixing Processes in the Canary Basin: Canary Current and Upwelling System off Northwest Africa" (PROMECA) and "Study of the vertical oceanic pump in mesoscale eddies" (PUMP), these areas of study can separated into two main regions as shown in the EKE map of Figure 1.4.

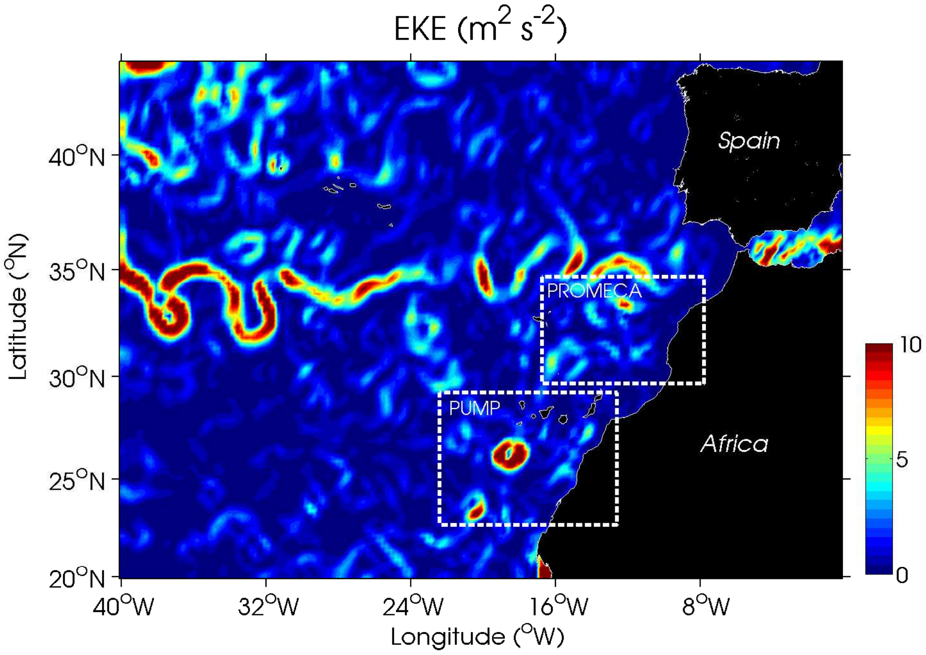

Figure 1.4: EKE map (m^2 s^{-2}) derived from AVISO altimeter products. The snapshot correspond to the date of January 01 for 2014. White dashed boxes denote the oceanic study areas comprised in this thesis, where the uppermost box shows the Cape Ghir filament region studied in PROMECA project of Chapter 4, and lowermost box delimits the onset of the Canary Eddy Corridor (Sangrà et al., 2009) as part of the PUMP project, examined in both Chapters 5 and 6.

.

Further information about measurements during the oceanographic cruises of both projects is provided in Chapter 3.

1.5.1 Mesoscale upwelling filaments

The Eastern Boundary Upwelling Systems or EBUS are some of the most productive oceanic regions in the world. They are driven by large-scale wind patterns that induce Ekman transport to the right of the prevailing wind direction in the Northern Hemisphere. The result of this process is an upwelling of cool and nutrient rich waters that are injected into the euphotic layer.

The coastal upwelling area off Northwest Africa is one of the four large EBUS systems (e.g., Barton et al., 1998; Hagen, 2001; Pelegrí et al., 2005a). It is a highly dynamic system in which a wide variety of physical-biological processes coexist with different spatial and temporal scales. The equatorward component of the Trade winds blowing along the Northwest African coast is responsible for an offshore Ekman transport which sets up the coastal upwelling. Despite the simplicity of this mechanism the reality is that there are many more mechanisms in play during upwelling. The complexity of the EBUS, in particular the Northwest African Upwelling System, is schematized by Hagen (2001). In their figure 3, which includes zones of near-shore countercurrents and the Canary Current, downwelling at the front, intense mixing, and a poleward flowing undercurrent, amongst other process. In this regard, observations by Pelegrí et al. (2005b) support the existence of two recirculation cells, the first related to a wind-induced filament and other associated filaments, and the second being a horizontal cell which connects the interior eastern boundary currents with the coast.

Upwelling filaments are typical mesoscale structure of the four EBUS. Filaments are narrow $\mathcal{O}(10$ km), elongated $\mathcal{O}(100$ km) structures of cold water extending offshore in the upper surface layer $\mathcal{O}(100$ m), often located near irregularities of the coastline (Hagen et al., 1996; Sangrà et al., 2015). They are recurrent structures identifiable by low surface temperature and high chlorophyll-a concentration signals (Sangrà et al., 2015). The pycnocline usually rises in these regions (Dewey and Moum, 1990; Pelegrí et al., 2005b; Arcos-Pulido et al., 2014), producing sharp gradients in the relatively well-mixed upper ocean layer with respect to the surrounding waters. This thermohaline front affects the vertical turbulent mixing and hence involves two processes of exchange: nutrient diapycnal transport from pycnocline to surface waters and the exchanges of surface heat and buoyancy fluxes between the near-surface atmospheric layer and the upper oceanic layer.

In this thesis, we focus on the filament at Cape Ghir off the Northwest African coast (e.g., Sangrà et al., 2015). This is a quasi-permanent filament, and is one of the largest of the NW Africa EBUS. Its extension varies with its intensity and the direction of the wind field, and is clearly visible in sea surface temperature and chlorophyll satellite imagery (e.g., Van Camp et al., 1991; García-Weil et al., 1994; Hernández-Guerra and Nykjaer, 1997). Many filaments are rooted to capes, and their generation mechanisms have been linked with topographic irregularities (e.g., Hagen et al., 1996; Pelegrí et al., 2005b). Other proposed mechanisms are the effect of baroclinic instabilities along the filament jet (Ikeda and Emery, 1984), wind intensification near capes, and interaction with mesoscale eddies (Mooers and Robinson, 1984; Strub et al., 1991; Peliz et al., 2004). More recently Troupin et al. (2012) in their high resolution model show that the filament of Cape Ghir may be the result of an injection of wind-induced positive relative vorticity near the cape that prevents the flow from continuing southward along the upwelling related band of negative potential vorticity.

Points of relevance about the Cape Ghir upwelling filament are:

- Its offshore deflection may help to maintain the horizontal recirculation upwelling cell (Pelegrí et al., 2005a).
- Filaments can interact with mesoscale eddies, either being trapped or wrapping around them, hence exporting high-nutrient upwelling water to oligotrophic regions offshore (Pacheco and Hernández-Guerra, 1999; Pelegrí et al., 2005a).
- Filaments enhance diapycnal fluxes of nutrients when various mixing process can coexist (Arcos-Pulido et al., 2014).

Furthermore, as we will see in Chapter 4, upwelling filaments can also be regions of relatively intense mixing where diapycnal velocities are enhanced, favoring the exchange between the mixed photic layer and water below this layer (Arcos-Pulido et al., 2014) through the entrainment process (Estrada-Allis et al., under review).

1.5.2 Mesoscale anticyclonic eddies

Mesoscale oceanic eddies populate the entire ocean, and can be viewed as "oases" of nutrients and turbulent mixing that act as pathways connecting the surface layers to the deep ocean. In recent decades considerable effort has been made in order to study their dynamics through observational methods (e.g., Martin and Richards, 2001; Ledwell et al., 2008; Sangrà et al., 2009) and by using numerical models (e.g., Viúdez and Dritschel, 2003; McGillicuddy et al., 2007; Koszalka et al., 2009; Cardona and Bracco, 2012)

The role of mesoscale eddies, and their associated sub-mesoscale structures is to:

- Impact the global climate system as pathways of turbulence and deep mixing (e.g., Cuypers et al., 2012; Sheen et al., 2014; Stanley and Saenko, 2014)
- Contribute to the transfer of kinetic energy dissipation by wind-stress surface inputs (e.g., Munk and Wunsch, 1998; Wunsch and Ferrari, 2004)
- They are implicated in the carbon cycle pump through nutrient redistribution (e.g., Arístegui et al., 1994; Martin and Richards, 2001; Ledwell et al., 2008; McGillicuddy et al., 2007; Mahadevan, 2014).

In the Northern Hemisphere, counter-clockwise rotating mesoscale structures are called cyclones while clockwise rotating structures are called anticyclones. Cyclones and anticyclones shoal and deepen the main thermocline, respectively. A particular type of anticyclonic eddy is the intrathermocline eddy, often called mode-water eddies. They are recognizable in a density field by a doming of the isopycnals in the upper levels and a deepening in the lower levels. They have the same signature as anticyclones in altimetry. Although many mechanisms have been proposed for their signature in the density field (Thomas, 2008; McGillicuddy, 2015) the underlying processes are still unknown.

The Canary archipelago (PUMP box in figure 1.4) represents a natural laboratory for the study of mesoscale eddies. They modulate the local biology (Arístegui et al., 1994; Pelegrí et al., 2005a) and interacts with upwelling filaments stretching from the African coast (e.g., Arístegui et al., 1994; Pacheco and Hernández-Guerra, 1999; Pelegrí et al., 2005b; Brochier et al., 2011). These eddies are generated by the perturbation of the southwestward flowing Canary Current and Trade winds by the islands topography (Sangrà et al., 2005; Jiménez et al., 2008; Piedeleu et al., 2009). Topographic forcing (Canary Current) is the main process responsible for eddy shedding, although atmospheric forcing (Trade winds) has a secondary role, triggering the shedding process for low intensities of the Canary Current (Jiménez et al., 2008; Piedeleu et al., 2009). The eddies evolve first as nearly coherent structures in near solid-body rotation (Rankine like), and then they lose their solid body rotation as they approach maturity and their vorticity is progressively reduced with changes in their orbital radii in the form of pulsations (Sangrà et al., 2005; 2007). Their initial radii are close to the internal Rossby deformation radius ∼25 km, and their signal extends to 300-700 depth.

Sangrà et al. (2009) first described the so-called Canary Eddy Corridor (hereafter, CEC), which is considered to be the main pathway for long lived eddies in the northeast subtropical Atlantic. The corridor is composed of long lived eddies that mainly propagate westward from between 22°N to 29°N. It represents an important source of EKE in this oceanic region, as occurs in areas of strong eddying flows (Calil and Richards, 2010; Sheen et al., 2014). Sangrà et al. (2009) observed a clear dominance of long lived anticyclones over cyclones; such dominance in the long lived ocean eddy field has also been reported in several theoretical and modeling studies (e.g., Graves et al., 2006; Koszalka et al., 2009; 2010; Mason et al., 2014). Sangrà et al. (2007) proposed that the stability of anticyclones is related to the initial cyclonic shear at their periphery, as their Rankine like vortex characteristics render them more stable to inertial perturbations than cyclones, and thus they may have a larger live expectancy. Additionally, the observed asymmetry between anticyclonic/cyclonic eddies may be due to an external strain-induced perturbation of the vortex. When this occurs, the vortex tends to a more stable axisymmetric state on an advective time scale[*]. During this relaxation process towards a more circular shape, shielding rings of positive vorticity are developed and propagate outward whilst being sheared by the angular velocity of the vortex (Montgomery and Kallenbach, 1997; McWilliams et al., 2003). These waves are also called vortex Rossby waves (hereafter, VRWs) and can transfer their energy back into the vortex, strengthening anticyclones while weakening cyclones (Graves et al., 2006). Chavanne et al. (2010) documented the existence of VRWs within a cyclone observed west of Oahu, Hawaii, using high-frequency radio Doppler current meters and moored acoustic Doppler current profilers (ADCPs). Koszalka et al. (2009) investigated, for the first time, their formation and structure in a fully nonlinear regime using a regional ocean model in an idealized configuration. A few studies have related the presence of VRWs with wave-like patterns in the vertical velocity field within mesoscale eddies (Koszalka et al., 2009; 2010; Cardona and Bracco, 2012; Nardelli, 2013). Therefore, further research is needed to better understand the role of the VRWs and other forcing terms, in the vertical velocity field within mesoscale structures.

---

[*] Since axisymmetry guarantees a linear stable solution of gradient wind and hydrostatic balance

2

Objectives and Organization

2.1 Motivation

As already mentioned in Chapter 1, the aim of this thesis is to investigate small scale turbulent processes and submesoscale vertical velocities within two mesoscale structures in the North Atlantic: (*i*).- The Cape Ghir filament and (*ii*).- Anticyclonic eddies in the Canary Eddy Corridor. The main issues to be addressed in this work are:

1. Elucidate the main sources of turbulent kinetic energy that control the upper ocean layer within highly dynamic mesoscale structures such as the Cape Ghir upwelling filament. Based on a one-dimensional turbulent kinetic energy balance, what is the state-of-the-art of different entrainment parameterizations? How is the entrainment process affected by considering vertical current shear acting at the pycnocline? and by considering an entrainment zone defined by the difference between mixed and active mixing layer depths?
2. To inspect both the entrainment process and diapycnal mixing inside anticyclonic eddies, paying particular attention to the sources that lead to enhancement of turbulent mixing. We focus our research on the mechanisms of diapycnal mixing, not

only at the near surface layers but also at intermediate and deeper layers, aiming thus to provide the full picture of diapycnal mixing inside anticyclonic eddies. The approach is mainly observational and uses high resolution data collected with a microstructure turbulence profiler.

3. To investigate numerically the mechanisms responsible for the vertical velocity field inside mesoscale anticyclonic eddies. We use a diagnostic approach using both an instantaneous divergence of the flow equation and a generalized omega equation. The main issues to be addressed are: (i) what is the 3D structure of the vertical velocity field and what are the main forcing mechanisms? (ii) what is the contribution, if any, of vertical mixing on modulatiion of the vertical velocity field? (iii) what is the importance of eddy wind interaction through Ekman pumping? (iv) do Rossby vortex waves occurs and if so what is their role in the forcing of the vertical velocity field?

2.2 Thesis organization

Chapter 1 provided a background of past studies on the topics covered by this thesis. In Chapter 3 we describe the datasets that have been analyzed and the main methodological tools applied. The next three chapters are organized as three independent research articles.

With respect to the first set of objectives outlined above we explore in Chapter 4 the effects of the entrainment process inside the Cape Ghir upwelling filament. Sampling with a microstructure turbulence profiler was carried out for the first time in this region. Due the lack of consistency between different entrainment formulations described in the literature, a new approach for the entrainment parameterization is proposed. The role of vertical current shear as a relevant source of turbulent kinetic energy in the upper ocean layer of Cape Ghir filament is highlighted.

To achieve the objectives of the second point outlined above we examine in Chapter 5 the diapycnal mixing within an intrathermocline anticyclonic eddy, where the new parameterization proposed in Chapter 4 is implemented. Turbulent mixing is also explored over the vertical extent of the eddy, and is described using near synoptic micro-scale turbulent profiles that were obtained with considerable effort and at a resolution not attained previously in similar studies of anticyclonic eddies.

In Chapter 6 we address the objectives of the last point outlined above. For this task we use data from a high resolution numerical model (ROMS), previously validated by Mason (2009). The vertical velocity field inside numerical anticyclonic eddies is investigated and compared with that diagnosed using a divergence approach and also using a generalized omega equation.

The main conclusions of this thesis and planned future research are presented in Chapter 7. A summary of these written in Spanish follows this chapter and, finally, a reference list and appendices complementing this research thesis are included at the end of the manuscript.

3

Material and Methods

3.1 Data collection

The data used in this thesis were acquired during two cruises in the framework of projects PROMECA and PUMP. The PROMECA cruise was conducted in the Cape Ghir region located off the northwest African coast in order to sample the upwelling filament of Cape Ghir, for which a detailed study is included in Chapter 4. The PUMP cruise was carried out southwest of the Canary Islands where the objective was to perform an interdisciplinary sampling of an anticyclonic eddy. Its mixing dynamics will be addressed in Chapter 5. In addition, a numerical study of anticyclonic eddies shed at the Canary Islands is also undertaken in Chapter 6. Figure 1.4 depicts the observational domains of both cruises, namely, the region of the Cape Ghir filament and the region of the anticyclonic eddy.

3.1.1 CTD, XBT, ADCP data

A conductivity-temperature-depth (CTD) SBE911+ probe was used to acquire vertical profiles of temperature, salinity and hence density during both cruises. The CTD data were recorded on board at a sampling rate of 24 Hz. After processing and calibration the data were averaged to 1 dbar. Additional physical parameters were derived from the CTD data. Once salinity was calibrated, potential density anomaly, σ_θ (kg m^{-3}), salinity, S, and potential temperature, T_θ (°C), were calculated according to the Thermodynamic Equation Of Seawater - 2010 (TEOS-10 `http://www.teos-10.org/`), which is the new algorithm for the equation of state for sea water replacing the previous EOS-80.

Between each CTD station of the PROMECA cruise (Chapter 4), vertical profiles of temperature were also obtained from expendable bathythermograph (XBT) Sippican T5 probes that transmitted data from as deep as 2000 m. The temperature profiles measured with the XBT probes were smoothed by using a low-pass Butterworth filter to remove spikes. A comparison with temperature profiles from the CTD revealed an offset of approximately 10 m in the XBT data. Although uncommon, an offset has been observed in other similar studies near the Cape Ghir filament (Pelegrí et al., 2005b).

During both cruises, current velocities were also collected nearly continuously by using the vessel-mounted 75 KHz Ocean Surveyor Acoustic Doppler Current Profiler (SADCP). They were processed with Common Ocean Data Access System (CODAS) software (Firing et al., 1995). The SADCP were processed to obtain vertical bin sizes of 10 m for the PROMECA cruise (Chapter 4) and 8 m for PUMP cruise (Chapter 5), averaged into 2-h periods.

For the PUMP cruise, a Lowered Ocean Surveyor Acoustic Doppler Current Profiler (LADCP) was also mounted on the CTD rosette. The LADCP system consisted of two synchronized self-contained 300 kHz RDI Workhorse broadband ADCPs, which were run in master/slave mode, one upward looking (slave) and one downward looking (master) with a shared battery pack. A vertical bin size of 8 m was applied in order to be consistent with the SADCP data. The LADCP data were processed by means of a gridded profile of velocity shear described in Firing and Gordon (1990) and Fischer and Visbeck (1993), in which the shear is vertically integrated and referenced using a single constraint. A set of Matlab routines from IFM-GEOMAR/LDEO Matlab LADCP-Processing System (v10.0-v10.2 beta) was used for this purpose.

3.1.2 Meteorological-related quantities and surface fluxes

Standard meteorological parameters were continuously recorded by a meteorological station mounted on the *R/V García del Cid* for the PROMECA cruise and on the *BIO Hespérides* for the PUMP cruise, which consists of eight sensors measuring wind speed, instantaneous wind speed, wind direction, air temperature, water temperature, relative humidity, air pressure, and incoming solar radiation at $\sim$ 2 min intervals. In order to maintain the temporal consistency with the measurements of each hydrographic station, meteorological parameters were averaged over time intervals of 2 h, which is the time-resolution of each CTD profile.

Net surface fluxes

To assess the relationship between atmospheric forcing and upper ocean turbulence, meteorological data were used to compute the net surface heat flux (J_q^o) as the sum of four individual components $J_q^o = J_q^{Sw} + J_q^{Lw} + J_q^{Se} + J_q^{La}$, where J_q^{Sw} is the net shortwave radiation flux which is directly obtained from the on-board meteorological station. The net longwave radiation (J_q^{Lw}) was estimated following the expression of Berliand and Berliand (1952):

$$J_q^{Lw} = E_{Lw}\sigma T_{air}^4(0.39 - 0.5\sqrt{e}_a)F_c - 4E_{Lw}\sigma T_{air}^3(T_{sw} - T_{air}) \tag{3.1}$$

where $E_{Lw} = 0.985$ is the longwave emissivity from Dickey et al. (1994), $\sigma = 5.67 \times 10^{-8}$ m^{2}K^{-4} is the Stefan-Boltzman constant, T_{air} is the air temperature measured at 10 m height above the sea surface, T_{sw} is the surface water temperature, e_a the vapor pressure and F_c is the cloud correction factor with values from 0.4 to 1 during daytime since the sky was mostly clear throughout both cruises. Surface sensible heat flux (J_q^{Se}) and latent heat flux (J_q^{La}) were determined by using the Tropical Ocean Global Atmosphere Coupled Ocean Atmosphere Response Experiment *TOGA-COARE* code through the Matlab AirSea toolbox (version 3.0; http://sea-mat.whoi.edu) developed by the air-sea fluxes science group of the TOGA COARE project, which is a version of the bulk flux described in Fairall et al. (1996).

Once net surface heat fluxes were obtained, we computed the net surface buoyancy flux (J_b^o) as:

$$J_b^o = \frac{g}{\rho_o}\left(\frac{\alpha J_q^o}{C_p}\right) + g\beta(E-P)So \tag{3.2}$$

where C_p is the specific heat capacity of seawater, and α and β are the respective thermal and haline coefficients of the expansion of seawater. The first of eq. (3.2) term corresponds to the thermal surface buoyancy flux (J_b^T), while the second term is related to the contribution of the haline surface buoyancy flux (J_b^S) as suggested by Dorrestein (1979), where So is the surface salinity and $(E-P)$ the difference between the evaporation rate and the precipitation rate.

These meteorological-related quantities were averaged over windows of approximately 30 min. However, because α and C_p were not measured for the entire spatio-temporal series of the meteorological station due their dependence on the CTD measurements, only the meteorological-related quantities averaged over a window of 2 h coincident with the CTD time profiles were used in this study. The window size was determined to be between one hour before and one hour after the release of the CTD, which is the usual time required for the CTD to complete a cast.

Wind stress

Surface wind stress ($\boldsymbol{\tau}_o$) is computed from $\boldsymbol{\tau}_o = \rho_a C_d |\boldsymbol{u}_r| \boldsymbol{u}_r$, where $\rho_a = 1.2$ kg m^{-3} is the reference density of air at 10 m height above the sea surface, $\boldsymbol{u}_r(u_r, v_r)$ is the wind speed, and C_d is the drag coefficient derived from the Large and Pond (1981) formula:

$$\begin{aligned} C_d &= 1.14 \times 10^{-3} for \quad \boldsymbol{u}_r \leq 10(m \quad s^{-1}) \\ C_d &= (0.49 + 0.065\boldsymbol{u}_r) \times 10^{-3} for \quad \boldsymbol{u}_r > 10(m \quad s^{-1}) \end{aligned} \tag{3.3}$$

3.1.3 Microstructure data processing

A TurboMAP-L microstructure profiler (Wolk et al., 2002) was used to acquire profiles of turbulent kinetic energy dissipation rates (ε_o). This is a vertical free-fall profiler that carries micro-structure sensors including two shear probes and an FP07 thermistor, CTD sensors, and internally mounted accelerometers. The instrument falls freely at a speed of ~ 0.7 m s^{-1} while sampling at a rate of 512 Hz. All data were integrated at intervals of 2 m down to $\sim$ 500 m depth and were processed using TMTools version 3.04 A.

After removing spikes from the profiles, turbulent kinetic energy dissipation rates are computed by multiplying the frequency power spectrum by the vertical velocity profile, thereby obtaining the vertical wavenumber power spectrum $\psi(k)$, where k is the wavenumber. Under the assumption of isotropic turbulence (Hinze, 1979) the observed ε_o was estimated by integrating the wavenumber power spectrum within an appropriate wavenumber range following Oakey (1982) as:

$$\varepsilon_o = \frac{15}{2}\nu \int_{k_1}^{k_2} \psi(k)dk \tag{3.4}$$

where ν is the molecular viscosity coefficient with a value of 1×10^{-6} m^2 s^{-1}, the lowest cutoff wavenumber is k_1 and was set to 1 cpm, whereas the upper limit integration k_2 is the highest vertical wavenumber which is free of noise, and is usually taken to be the Kolmogorov wavenumber $k_c = (2\pi)^{-1}(\varepsilon_o \nu^{-3})^{1/4}$.

After segmenting each microstructure profile within vertical bin sizes of 2 m, the observed shear spectrum is fitted to the Nasmyth empirical universal spectra for turbulence (Oakey, 1982; Wolk et al., 2002). This spectrum is considered to be representative of the spectral form for oceanic turbulence and is commonly used to verify a shear spectrum measurements. An example of microshear power spectral density $\psi(k)$ and the Nasmyth spectra can be seen in Figure 3.1 for a depth range from 43 to 45 m at station number 24 from the PROMECA cruise.

Because records of micro-scale velocity shear can be contaminated by noise (such as from the mechanical vibration of the instrument and, particularly at the surface, the influence of the rope) until it reaches a quasi-constant free-falling velocity, data within the first 16 meters of the water column were removed. In addition, the vertical profiles of ε_o can have large variability over short time periods; therefore, the casts were repeated at least twice at each station.

3.2 Satellite data: SST, chlorophyll and altimetric products

Given the large temporal and spatial variability of meso- and submesoscale structures, prior examination of satellite data is pertinent. To obtain a synoptic picture of the Cape

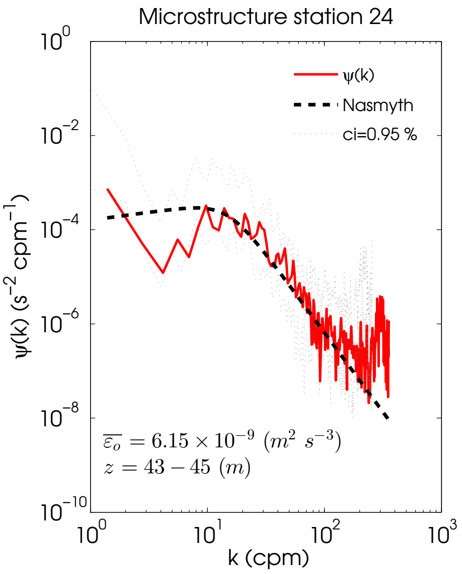

Figure 3.1: Shear power spectral density, $\psi(k)$ (red solid line), for first profile of station 24 from PROMECA-cruise, and for a depth range from 43 to 45 m depth. The Nasmyth universal spectra is shown as a dashed black line. Turbulent kinetic energy dissipation rate, $\overline{\varepsilon_o}$, is averaged over the depth range value. Dotted thin lines are the confidence interval of 0.95 % for the power spectral density calculation. At the bottom, k represent the wavenumber in cycles per minute.

.

Ghir upwelling filament both before and during the PROMECA cruise, sea surface temperature (SST) and chlorophyll (Chl-a) satellite images were obtained from the Moderate Resolution Imaging Spectroradiometer (MODIS) sensor on-board AQUA and TERRA satellites. In addition, images were downloaded from the Ocean Color Web (`http://oceancolor.gsfc.nasa.gov`) for analysis. An example of the spatio-temporal coverage can be seen in the satellite imagery sequence of Figures 3.2, where the evolution of the Cape Ghir upwelling filament is shown. Note the variability of the filament at short time periods, which is most intense on the last upper-right snapshot of Figure 3.2 (2010/11/03), in agreement with a large increase of the wind speed (see Chapter 4), thus ending the measurements due to inclement weather conditions.

Owing to the geostrophic balance of mesoscale rotating features, their signature is clearly visible in maps of sea level anomalies (SLA). The SLA data used here were provided by AVISO altimeter products at a spatial resolution of 1/4° × 1/4° downloaded via OpenDAP from the AVISO Website (`http://www.aviso.altimetry.fr/en/home.`

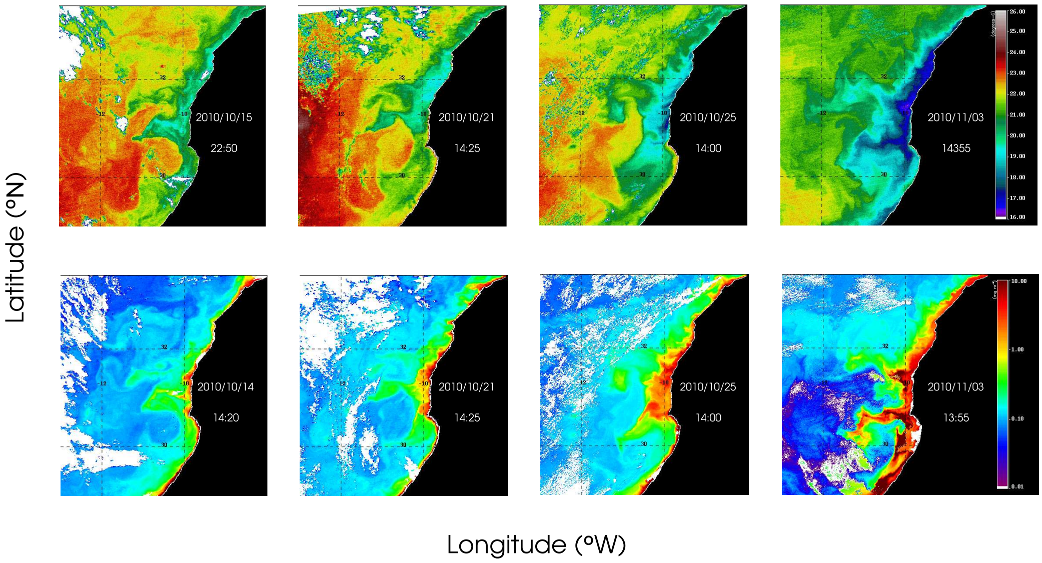
Latitude (°N)
Longitude (°W)
2010/10/15
22:50
2010/10/21
14:25
2010/10/25
14:00
2010/11/03
14355
26.00
25.00
24.00
23.00
22.00
21.00
20.00
19.00
18.00
17.00
16.00
2010/10/14
14:20
2010/10/21
14:25
2010/10/25
14:00
2010/11/03
13:55
10.00
1.00
0.10
0.01

Figure 3.2: Snapshots of satellite products covering the area of the PROMECA cruise. Upper panel shows maps of SST from MODIS-A and MODIS-T, and their respective Chl-a maps for the same time-period are shown in the lower panel. Note the increase in the magnitude of the upwelling filament off Cape Ghir in the rightmost column for both the SST and Chl-a maps.

.

`html`) at daily resolution (Capet et al., 2014). The evolution in terms of SLA of the anticyclonic eddy, examined in Chapter 5 for the PUMP-project, is shown in Figure 3.3.

Through SLA (η^A) altimeter data, geostrophic currents can also be obtained by assuming geostrophic balance through the thermal wind relation:

$$\begin{aligned} u_g &= -\frac{g}{f}\frac{\Delta\eta^A}{\Delta y} \\ v_g &= \frac{g}{f}\frac{\Delta\eta^A}{\Delta x} \end{aligned} \tag{3.5}$$

as well as their derived products such as maps of the vertical component of the geostrophic relative vorticity $\zeta_g = \partial_z v_g - \partial_z u_g$, and maps of eddy kinetic energy $EKE = 0.5(u_g^2 + v_g)^2$ (Figure 1.4) (e.g., Jia et al., 2011).

Many advances have been made in recent years in the scope of altimetry products for

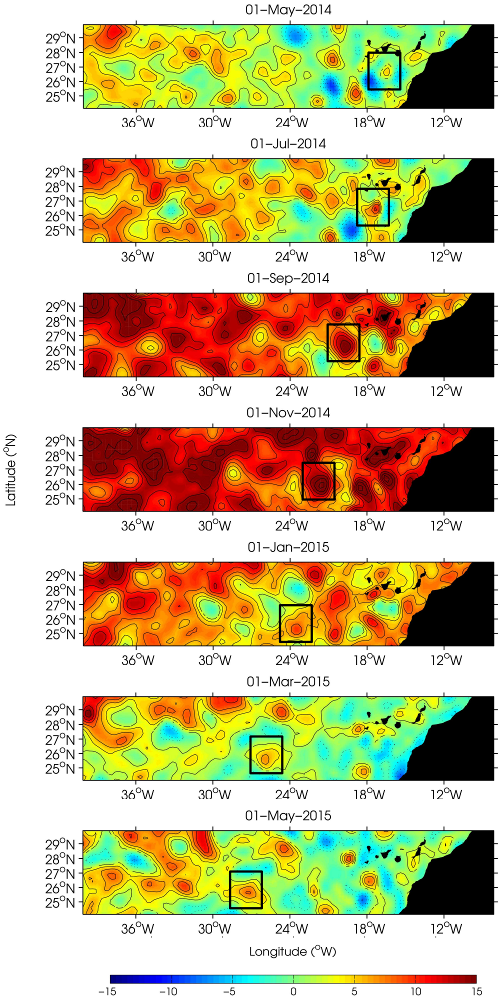
01–May–2014
01–Jul–2014
01–Sep–2014
01–Nov–2014
01–Jan–2015
01–Mar–2015
01–May–2015
29°N
28°N
27°N
26°N
25°N
Latitude (°N)
36°W
30°W
24°W
18°W
12°W
Longitude (°W)
−15
−10
−5
0
5
10
15

Figure 3.3: Snapshots of sea level anomaly maps (cm), derived from AVISO altimeter products for the first day of the month and year shown at the top of each panel. The area covered is the region of the Canary Eddy Corridor (Sangrà et al., 2009) in which the anticyclonic eddy examined in Chapter 5 is developed. The signature of the mesoscale structure is highlighted by the black boxes.

oceanographic research (e.g., Klein et al., 2009; Chavanne and Klein, 2010; Nardelli, 2013; Sasaki et al., 2014), representing an extraordinary tool to set a synoptic vision of mesoscale features. However, it is important to consider observational biases and nominal errors inherent in the collection and processing of satellite data (Lea et al., 2008).

3.3 The numerical model solution: ROMS

The results and analysis in Chapter 6 of this thesis are based on a high resolution regional oceanic model (ROMS) in the framework of the PUMP-project. ROMS is a primitive equation, free-surface model with Boussinesq approximation and hydrostatic vertical momentum balance, which uses an orthogonal curvilinear coordinate system in the horizontal direction and a generalized terrain-following or *sigma* coordinate in the vertical (Haidvogel and Beckmann, 1999). The barotropic and baroclinic momentum equations are resolved separately in ROMS. The density is calculated diagnostically by the equation of state of seawater, and the vertical velocity is calculated diagnostically from the flow divergence:

$$\boldsymbol{\nabla} \cdot \boldsymbol{u}_h + \partial_z w = 0 \tag{3.6}$$

Subgrid-scale vertical mixing processes are parameterized using the non-local K-profile planetary (KPP) boundary layer formulation from Large et al. (1994).

The ROMS outputs prepared by Evan Mason as part of his PhD Thesis (Mason, 2009), by using the UCLA variant of the ROMS-kernel (Shchepetkin and McWilliams, 2005; 2009). The high resolution outputs at 1 km grid resolution, hereinafter called L2, come from a parent model grid of initially $\sim$ 7.5 km (referred to as L0). Mason (2009) adopts a 2-stage nesting by the inclusion of an intermediate 3-km grid (L1) in order to achieve 1-km resolution in the Canary Islands region (L2), which is used in Chapter 6. Details of the validation and characteristics of these solutions can be found in Mason (2009) and related research articles (Mason et al., 2010; 2011; 2012). Table 3.1 provides a summary of the main characteristics and parameterizations relating to the L2 configuration.

3.3.1 Lagrangian Passive Tracers: Roff

A Lagrangian drifter-tracking code is used to simulate particle trajectories within a mesoscale eddy in Chapter 6, by using the stored ROMS three-dimensional velocity fields $\boldsymbol{u} = (u, v, w)$ from the L2 configuration. The tracking code is ROMS Ofline Floats (Roff, version 2.0.1) (Carr et al., 2008). Roff is the lagrangian module of ROMS subsequently modified to be compatible with offline computation by using existing netcdf output files from ROMS to advect numerical floats.

Table 3.1: Configuration characteristics of the L2-ROMS model used in this thesis and initial forcings and boundary conditions interpolated to the model grid.

Model configuration	
Horizontal resolution	1 km
Length	3 years
Grid dimensions	592 × 612
Sigma layers	60
Minimal depth	0.08 m
Model forcing files	
Lateral boundary and initial conditions	NEAClim 0.1° climatology[a]
Surface atmospheric fluxes (E-P)	COADS 1° climatology[b]
Surface wind stress	SCOW 0.25° climatology[c]
Sea Surface Temperature (SST)	Monthly 4-km Global product from NOAA/NASA AVHRR[d]
Sea Surface Height (SSH)	15-year climatology from absolute SLA AVISO data
Topography	GEBCO[e]

[a] DIVA climatology from Troupin et al. (2010)

[b] Comprehensive Ocean-Atmosphere Dataset (da Silva et al., 1994; Worley et al., 2005)

[c] 8-year Scatterometer Climatology of Ocean Winds, based on QuickSCAT (Risien and Chelton, 2008)

[d] from Kilpatrick et al. (2001)

[e] General Bathymetric Chart of the Ocean dataset (Hunter and Macnab, 2003)

The Roff code has been proven to be a useful tool for example for the study of vertical water parcel transport in coastal upwelling (e.g., Capet et al., 2008a; Mason et al., 2012). The code uses a fourth-order accurate Adams-Bashford-Moulton predictor-corrector scheme to integrate over time $d\boldsymbol{u}/dt = \boldsymbol{u}(\boldsymbol{x}, t)$ by setting $\boldsymbol{x}(t_o) = \boldsymbol{x_o}$ as initial conditions. The temporal integration is simulated through linear interpolation in time and space of the discrete 3D velocity ROMS fields, where $\boldsymbol{u}$ are daily averages. The Fortran code can be downloaded through `http://people.atmos.ucla.edu/capet/Myresearch/my_research_floats.html`.

4

Diapycnal Entrainment in an Eastern-Boundary Upwelling Filament[*]

4.1 Introduction

Vertical entrainment is one of the main mechanisms by which the upper ocean layer is altered (see Chapter 1). Entrainment is implicated in the temporal increase of the mixed layer and in the transport of tracers such as heat, salinity and biological properties. In recent decades, considerable efforts have been made to clarify this process through laboratory experiments (e.g., Deardorff, 1983; Fernando, 1991; Pelegrí and Richman, 1993; Jackson and Rehmann, 2014), modeling approaches (e.g., Jacob and Shay, 2003; Sun and Wang, 2008) and observational studies (e.g., Dewey and Moum, 1990; Anis and Moum, 1994; Nagai et al., 2005). Only a few observational studies have attempted to compare different entrainment parameterizations. For example Anis and Moum (1994), using microstructure profiles in convective conditions, observe that results from different entrainment parameterizations differ by a factor of two. Nagai et al. (2005) determined that the entrainment law cannot be represented as a simple sum of wind and buoyancy contributions.

---

[*] Estrada-Allis, S., Rodríguez-Santana, Á., Naveira-Garabato, A., García-Weil, L., Arcos-Pulido, M., and Emelianov, M. Diapycnal Entrainment in an Eastern-Boundary Upwelling Filament. *Second round of revision in Journal of Geophysical Research.*

Entrainment rates are needed for closure in one-dimensional turbulent kinetic energy (TKE), bulk models, hence they can also help to elucidate the roles of different energy sources that drive mixing in the upper ocean layer. Examination of TKE-sources through entrainment rates may be particularly useful in energetic ocean areas where several sources and spatio-temporal scales can coexist. An example of high dynamic variability can be found in coastal upwelling areas and within their associated upwelling filaments (Chapter 1).

In this regard, only a few analyses have focused on characterization of vertical turbulent entrainment in upwelling areas. Dewey and Moum (1990) show that wind-induced turbulent entrainment is more efficient on the cold side of fronts, where the pycnocline outcrops near the surface. Dewey et al. (1993) also suggest that entrainment could be a process by which the cool surface signature in an upwelling filament is maintained. More recently, Grodsky et al. (2008) used satellite datasets to determine that thermocline shoaling increases the entrainment of cold nutrient-rich water into the mixed layer, leading to a bloom of phytoplankton.

In this study we focus on the vertical current shear as a source of TKE, which may play an important role in frontal areas such as upwelling filaments. Within the filament, baroclinicity can increase vertical shear levels at the base of the mixed layer, which may be associated with an enhancement of turbulent mixing within the seasonal thermocline and with regions of high vertical diffusion (Barton et al., 2001; Schafstall et al., 2010). The results of Small et al. (2012) suggest that entrainment by shear instability at the base of the mixed layer is a dominant process for surface cooling in the North East Atlantic. However, the effect of vertical shear is not integrated into most of the existing entrainment parameterizations.

Using novel observations of TKE dissipation rates for this area, the degree of turbulent mixing that affects the filament and its relation with the entrainment process can be determined. In the literature, some studies can be found that link intense mixing levels with upwelling filaments or thermohaline frontal systems. Dewey et al. (1993), for example, observed an increase of ε_o in dynamic structures known as mini-filaments. In addition, Nagai et al. (2009) showed an enhancement of dissipation rates below the mixed layer in the Kuroshio front. Recently Johnson et al. (2012) reported high ε_o on the cyclonic side of a California Current System front. Other microstructure observations indicate that the rate of mixing induced at the surface may be enhanced with proximity to the filament front, setting strong horizontal density gradients that can help to maintain the frontal system (Dewey and Moum, 1990; Dewey et al., 1993; Nagai et al., 2012).

The primary objective of this study is to investigate the governing upper ocean TKE sources, within and outside of the Cape Ghir upwelling filament by using a one-dimensional bulk TKE balance. We analyze where the turbulent mixing takes place and how it relates to the entrainment process, focusing on the vertical shear as a relevant source of TKE. This is carried out by using meteorological, hydrographic and satellite data, in conjunction with the first microstructure turbulent profiles taken in this area. The entrainment parameterizations used in this study are introduced in Chapter 1 and described in section 4.2. Topics such as the hydrography of the filament, comparison with different entrainment parameterizations, and the relevance of considering an active region of mixing are addressed in section 4.3. We discuss these results in section 4.4, including a proposal for a new approach to analysis of the entrainment process. Finally, section 4.5 addresses the main conclusions of this study.

4.2 Case study: Cape Ghir upwelling filament

The hydrographic data used here correspond to a field survey in the scope of the Mixing Processes in the Canary Basin (PROMECA) project conducted in the Cape Ghir region located off northwest Africa (Figure 4.1) onboard the *R/V García del Cid*. The data are based on CTD, XBT, and microstructure profiles collected at approximately 10 km intervals during October 18–29, 2010. These measurements were taken in early fall, the time at which the Trade winds typically weaken. During the cruise, current velocities were also collected quasi-continuously by using the vessel-mounted 75 Hz SADCP (for more information see Chapter 3).

4.2.1 Entrainment parameterizations

The main assumption of a bulk mixed layer model is that most of the kinetic energy produced is lost by the dissipation term, whereas the remaining TKE is used to work

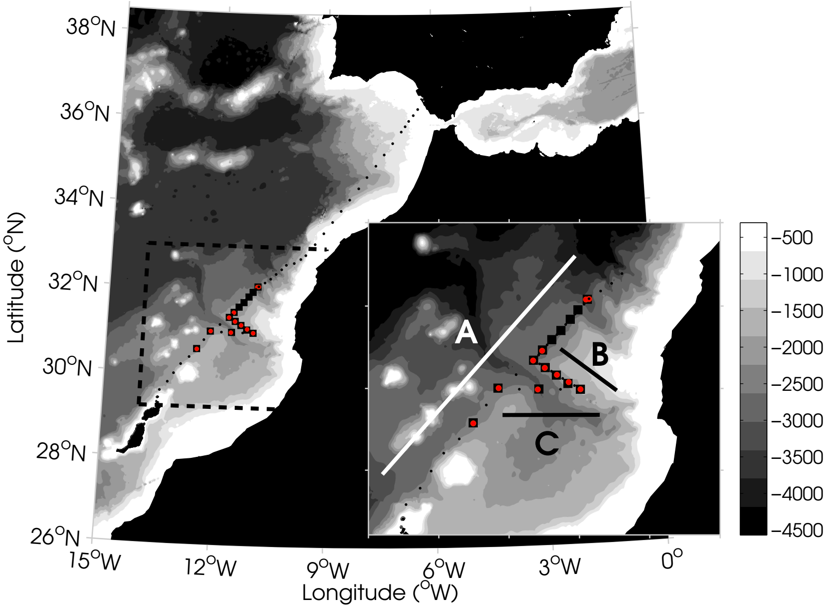

Figure 4.1: Bathymetry of the region at 500 m contour intervals with the hydrographic stations measured around the upwelling filament off Cape Ghir during October 2010. Dashed box delimits the hydrographic stations used in this study as is better shown on the superimposed figure at the bottom right corner. CTD stations along with ADCP survey sites are marked as black squares; microstructure stations as red dots; XBT profiles as small black dots. Transects A, B and C are also indicated.

against buoyancy forces through the increase in potential energy due to mixing. High-order closure schemes, such as K-profile parameterization (KPP) from Large et al. (1994), are commonly implemented in numerical oceanic models instead of simple bulk (slab) mixed layer models. With the advent of fast computers, the choice of the latter parameterization is often the better option. In fact, bulk mixed layer models are widely incorporated into high-resolution ocean models in climatological studies to assess the factors influencing the mixed layer (e.g., Wallcraft et al., 2003; Nagai et al., 2005; Endoh et al., 2009; Kang et al., 2010; Liu et al., 2012). This is largely due to the explicit representation of the flux terms and the turbulent mixing at the base of the mixed layer. The choice of an appropriate entrainment parameterization in such cases depends on the application (Burchard et al., 2008). This decision can be addressed through sensitivity test by using numerical ocean models with hybrid coordinates that are able to compare numerical solutions using different mixing schemes (e.g., Jacob and Shay, 2003; Jacob and Koblinsky, 2007).

In this study we focus on a bulk 1D mixed layer approach, which depends on three controlling parametersa s sources of TKE, namely: friction velocity u_*, free-convection w_*, and the velocity jump across the mixed layer δV, (Chapter 1, eq. 1.4, 1.5 and 1.6, respectively). Therefore, depending on the source of TKE, entrainment parameterizations can serve as indicators of which mixing forcing is playing a major role in the upper mixed layer. It should be noted that other sources can be included as entrainment mechanisms such as the breaking of internal waves at the interface (Strang and Fernando, 2001) or Langmuir vortices within the mixed layer (Flór et al., 2010); further research is required to determine the roles of these sources in the entrainment phenomena.

Several formulations have been proposed to compute the entrainment rate or w_e as the effective vertical velocity transporting buoyancy across the base of the mixed layer. This study focuses on two different approaches. In the first, w_e is computed from a TKE balance following the mixed layer bulk model of Niiler and Kraus (1977) (eq. 1.2). In the second approach, w_e can be obtained through the relationship between the bulk Richardson number based on eq. (1.8). All variables and parameters used in this study are summarized in Table 4.1.

For the first approach, the w_e parameterization used in this study comes from the bulk mixed layer model of Gaspar (1988), (hereafter, w_e^G), where the evolution of h_ρ can be computed by using the following expression:

$$w_e^G = \frac{(m_1 + m_2)u_*^3 + 0.5 h_\rho J_b^o - \overline{\varepsilon_p} h_\rho}{0.5(\delta b h_\rho)} \tag{4.1}$$

where $m_1 = 2.6$ and $m_2 = 1.9$ are empirical constants and ε_p is the parameterized TKE dissipation rate. This formulation is similar to that of Niiler and Kraus (1977). The main difference lies in how ε_p is parameterized (Appendix A), which is analyzed further in section 4.4. Adding the Niiler and Kraus (1977) dynamic instability term $DIT = 0.5 w_e(\delta u^2 + \delta v^2)$ to w_e^G (eq. 4.1), it is possible to include a proxy for the vertical current shear, defined as $Sh^2 = (\partial_z u)^2 + (\partial_z v)^2$, as a source of TKE in the

4. DIAPYCNAL ENTRAINMENT IN AN EASTERN-BOUNDARY UPWELLING FILAMENT

Table 4.1: List of symbols and parameters

Symbol	**Unit**	**Definition**
h_ρ	m	mixed layer depth
h_ε	m	mixing layer depth
Δh	m	entrainment zone $\Delta h = h_\varepsilon - h_\rho$
ε_o	$m^2\ s^{-3}$	observed TKE dissipation rate
ε_p	$m^2\ s^{-3}$	parameterized TKE dissipation rate
L_o	m	Ozmidov length scale
u_*	$m\ s^{-1}$	friction velocity
w_*	$m\ s^{-1}$	free-convection velocity
δV	$m\ s^{-1}$	velocity jump at the base of the mixed layer
b	$m\ s^{-2}$	buoyancy $b = g(\rho_o - \rho)\rho_o^{-1}$
δb	$m\ s^{-2}$	buoyancy jump at the base of the mixed layer
DIT	$m\ s^{-1}$	Dynamic Instability Term, $DIT = 0.5(\delta u^2 + \delta v^2)$
w_e^G	$m\ s^{-1}$	TKE bulk-based entrainment rate from Gaspar (1988)
w_e^{GS2}	$m\ s^{-1}$	w_e^G addition of current vertical shear
$w_e^{\Delta h}$	$m\ s^{-1}$	new approach for a TKE bulk-based entrainment rate
w_e^{SF}	$m\ s^{-1}$	Richardson-based entrainment rate from Strang and Fernando (2001)
v_{TKE}	$m\ s^{-1}$	any TKE velocity scale (u_*, w_* or δV)
E	dimensionless	entrainment coefficient, $E = w_e(v_{TKE})^{-1}$
N^2	s^{-2}	square buoyancy frequency
Sh^2	s^{-2}	square vertical current shear
Ri_g	dimensionless	gradient Richardson number, $Ri_g = N^2 Sh^{-2}$
Ri_b	dimensionless	bulk Richardson number, $Ri_b = h_\rho \delta b (v_{TKE})^{-2}$
Ri_τ	dimensionless	mechanical Ri_b, $Ri_\tau = h_\rho \delta b (u_*)^{-2}$
Ri_*	dimensionless	convective Ri_b, $Ri_* = h_\rho \delta b (w_*)^{-2}$
Ri_v	dimensionless	sheared Ri_b, $Ri_v = h_\rho \delta b (\delta V)^{-2}$
τ_o	$N\ m^{-2}$	wind stress
L_{mo}	m	Monin-Obukhov length scale
J_q^o	$W\ m^{-2}$	surface net heat flux
J_q^{Lw}	$W\ m^{-2}$	surface longwave heat flux
J_q^{Sw}	$W\ m^{-2}$	surface shortwave heat flux
J_q^{Se}	$W\ m^{-2}$	surface sensible heat flux
J_q^{La}	$W\ m^{-2}$	surface latent heat flux
J_b^o	$W\ kg^{-1}$	surface net buoyancy flux
J_b^T	$W\ kg^{-1}$	surface thermal buoyancy flux
J_b^S	$W\ kg^{-1}$	surface haline buoyancy flux
$(J_b^{\Delta h})_I$	$m^3\ s^{-3}$	integrated turbulent diapycnal buoyancy flux, $\int_{-h_\varepsilon}^{-h_\rho} \overline{(w'b')}(dz)$
T_{res}	minutes	turbulent residence time
T_{air}	°C	air temperature at 10 m height
T_{sw}	°C	sea water temperature

energy budget. Then, we obtain:

$$w_e^{GS2} = \frac{(m_2 + m_3)u_*^3 + 0.5h_\rho J_b^o - \overline{\varepsilon_p} h_\rho}{0.5[(\delta b h_\rho) - (\delta u^2 + \delta v^2)]} \tag{4.2}$$

Equation (4.2) (hereafter, w_e^{GS2}) has been used in the model of Samson et al. (2009) to examine the response of the oceanic mixed layer during the passage of a hurricane. For the second approach, we compute an alternative w_e based on the entrainment law (e.g., Ellison and Turner, 1959; Kato and Phillips, 1969; Khanta et al., 1977; Strang and Fernando, 2001) described in Chapter 1 (eq. 1.7).

A comparison between the two parameterization schemes may help to discern if the vertical shear could play a relevant role in the dynamics of upper ocean layer filament waters, which is a key objective of this study. The Richardson-based entrainment parameterization used in this work is the law suggested by Strang and Fernando (2001) (hereafter, w_e^{SF}). In their laboratory tank experiments, they compared three entrainment regimes based on a shear Richardson number $Ri_v = h_\rho \delta b (\delta V)^{-2}$:

$$\begin{aligned} E_v &= 0.024 && if && Ri_v < 1.5 \\ E_v &= 0.22 Ri_v^{-2.6} && if && 1.5 < Ri_v < 5 \\ E_v &= 0.02 Ri_v^{-1.3} && if && Ri_v > 5 \end{aligned} \tag{4.3}$$

Hence, the entrainment rate according to eq. (4.3) would take the simple form of $w_e^{SF} = E_v \delta V$. It should be noted that this Richardson-based law is empirically found for a specific range of Ri_v in which the entrainment is effective; such a range is in agreement with the Ri_v found in this study.

4.3 Results

4.3.1 Hydrographic background of the filament

The study of turbulent processes in the ocean is challenging. Upwelling areas are highly dynamic systems (e.g., Barton et al., 1998; Hagen, 2001; Pelegrí et al., 2005b) in which the interaction between many temporal and spatial scales makes isolation of a single process difficult to analyze, unlike laboratory or modeling experiments. Therefore, a general description of the area is required.

Sea surface temperature and Chlorophyll satellite images in Figure 4.2 show the extension and location of the Cape Ghir upwelling filament over a two-day period (October 20-21 2010). The meander-like structure is identifiable as a cool feature with high Chl-a concentration that crosses stations in both transect A and B (Figure 4.2). The filament waters have a difference of ∼ 2 °C from the surrounding waters and are highly conditioned by the mesoscale dynamics of the area, as shown in the superimposed geostrophic currents from the AVISO product in Figure 4.2.

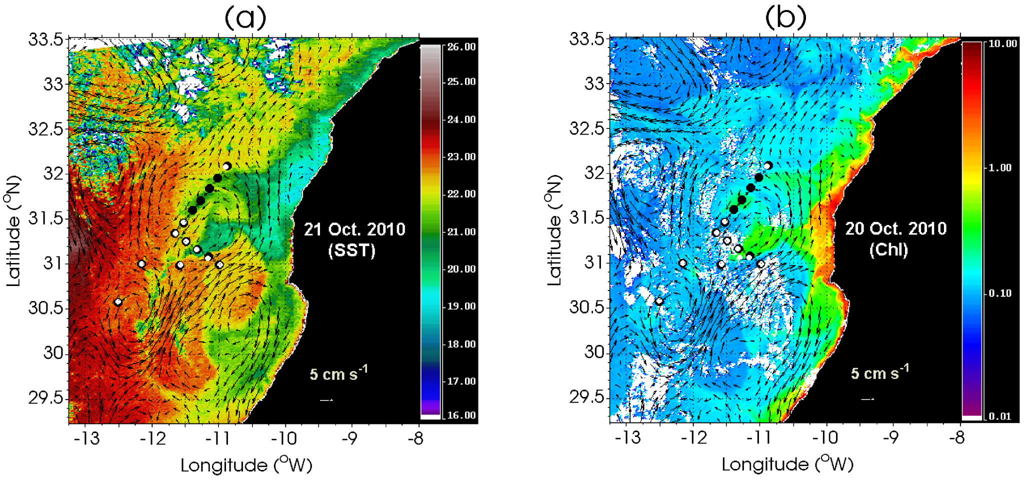

Figure 4.2: Snapshots of (a) Sea surface temperature from MODIS-Terra in °C for October 21, 2010 at 14:25 pm and (b) Chlorophyll-a from MODIS-Aqua for October 20, 2010 at 13:45 pm. Superimposed vectors denote the magnitude and direction of the geostrophic velocity fields for the same days, derived through AVISO sea level anomaly data at 1/4° horizontal resolution. Black dots are CTD+ADCP stations while white dots are microstructure profiles.

.

Although representative images with low cloud coverage were chosen here, subsequent images show that the filament was present during almost all the sampling period (see Figures 3.2). The filament signal intensified after the last CTD station number 50, when stronger wind speeds were recorded. The general description of this filament agrees with previous observational studies of African upwelling filaments (e.g., Barton et al., 2001; Hagen, 2001), especially so for the study of Pelegrí et al. (2005b) for the

same filament and season examined in 1995 and 1997.
Vertical sections of salinity and potential density anomaly in Figure 4.3 show a doming of isohalines and isopycnals in the northeastern stations of transect A (Figures 4.3a and b). In addition, combined vertical sections of CTD-XBT also show the lifting of isotherms at the same locations (Figure 4.4a). This dome-like structure seems to be well correlated with stations that cross the filament front according to satellite imagery (Figure 4.2).

Although it is not the aim of this work, it is interesting to note that our $T_\theta - S$ relationship (not shown) indicates a subsurface maximum in salinity below the mixed layer ($\sim$ 50 m), with mean values of S=36.55, T_θ=19 °C and σ_θ=[26-26.5] kg m^{-3} in stations number 38 and 40 of transect B (Figures 4.3c, d and 4.4b). This subsurface salinity maximum agrees rather well with the salinity maximum found by Pelegrí et al. (2005b). In their study, they suggest that this may indicate an interconnection of a horizontal recirculation cell along the African upwelling. A $T_\theta - S$ diagram can be found in Arcos-Pulido et al. (2014) (their figure 1), wich use the same dataset and where the subsurface salinity maximum is also shown.
Transect B, mostly onshore, shows an abrupt upwelling of isohalines and isopycnals (Figures 4.3c and d) and isotherms (Figure 4.4b) from station 44 to 48. The combined CTD-XBT vertical section allows for an additional transect C (Figure 4.4c), where the outcropping of the isotherms is smoother than in transect B. This result may be due to the proximity of the filament to transect B.

In general, it appears that the rising of the isotherms and isopycnals is concentrated in the first 200 m of the water column, particularly in stations located in the upwelling filament waters. This finding agrees well with the study of Pelegrí et al. (2005b), who suggested the filament originates at shallow depths in the water column. On the other hand, the area of interest is strongly influenced by strong mesoscale dynamics. In order to more effectively show these structures, geostrophic velocities derived from AVISO altimeter products were superimposed on the satellite images (Figure 4.2). In this figure, a counter-clockwise mesoscale structure appears to induce a northward along-front flow in transect A. A poleward geostrophic current crosses the section B as induced by an anticyclonic structure in opposite direction to the filament flow.
Based on the SST and Chl-a satellite imagery and its agreement with the lifting of the isopycnals, we conclude that the hydrographic stations can be separated into two

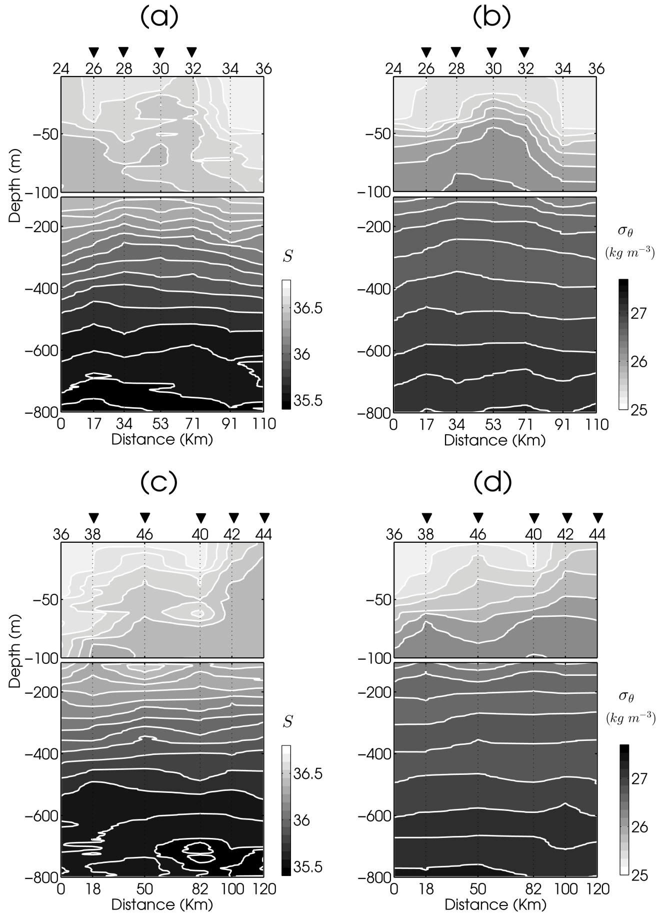

Figure 4.3: Hydrographic vertical sections derived from CTD profiles of (a) salinity, S, and (b) potential density anomaly, σ_θ (kg m^{-3}) for the northeastern transect A, and (c) S, and (d) σ_θ for the western transect B. Contours of S are plotted every 0.5 intervals, while σ_θ contours are plotted every 0.1 kg m^{-3}. The accumulative distance between stations in km is shown at the bottom. At the top, the corresponding hydrographic station number is displayed. Inverted triangles show the stations influenced by the upwelling filament.

groups: the first group (group-F, hereinafter) comprises those stations influenced by the upwelling filament, that is from station 26 to 32 of transect A, and from station 38 to 46 of transect B. The alternate group (group-nF, hereinafter) covers the remaining stations which are not directly influenced by the mesoscale structure, i.e., stations 24 and 34 to 36 of transect A, and 48 to 50 of transect B. A related study by Arcos-Pulido

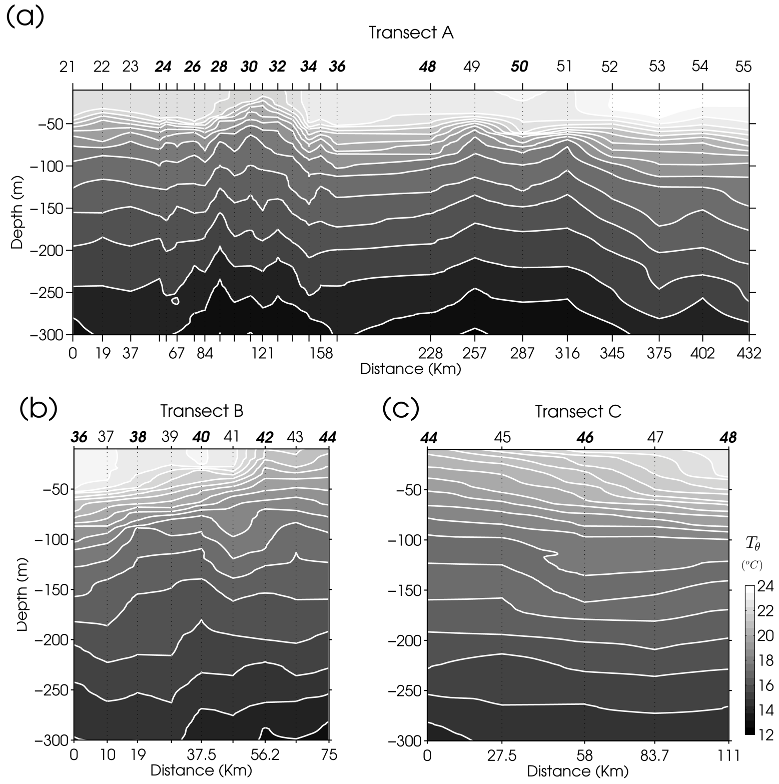

Figure 4.4: Vertical sections derived from CTD-temperature profiles combined with XBT temperature profiles where (a), (b) and (c) correspond to transects A, B and an extra transect C, respectively. Isotherms are spaced every 0.5 °C and an offset of approximately 10 m was applied to XBT profiles to guarantee consistency with CTD data depth. At the top, bold numbers in italics denote CTD stations while normal numbers are for XBT stations. Note that not all the station numbers are displayed at the top in order to facilitate viewing; all CTD and XBT stations are taken into account for the vertical section. At the bottom, the cumulative distance in km is shown.

.

et al. (2014), shows that group-F of hydrographic stations experiences an enhancement of nutrient concentration below the mixed layer.

4.3.2 Meteorological conditions

Surface fluxes showed a regular diurnal cycle in which both J_q^o and J_b^o are positive when upward fluxes occur during the night (Figures 5.3a and 5.3b). The values of J_q^o varied between -3 W m^{-2} and -731 W m^{-2} during daytime and 2 W m^{-2} to 309 W m^{-2} at night (Figure 5.3a), resulting in convective conditions with mean values of 1.18 × 10^{-8} W kg^{-1} during nighttime (Figure 5.3b). In this regard, haline buoyancy fluxes were always lower than thermal buoyancy fluxes, differing by one order of magnitude. On the other hand, the main contributors to the net total heat flux during nighttime were J_q^{La} and J_q^{Lw} (Figure 5.3a).

Air temperature was generally warmer than sea water temperature, except for CTD stations 30-32 and 42-44 which had comparable air temperatures and SSTs (Figure 5.3c). This decrease of the sea water temperature may be related to the fact that these stations are in the cooler upwelling filament waters. It is noteworthy that the mean difference in temperature between waters within and outside the filament is 1.09 °C. Weak northeasterly winds prevailed throughout the cruise, with a mean speed of $\boldsymbol{u}_r$ = 3.78 m s^{-1} and $\boldsymbol{\tau}_o$ varying from 0.0026 N m^{-2} to 0.065 N m^{-2} on the last day of sampling (Figure 5.3d). This wind pattern is characteristic of this season in which Trade winds are less intense. A sudden increase in wind speed was observed on October 24 (Figure 5.3d).

Because both wind-stress and surface heat fluxes can act as forcing mechanisms to enhance mixing at the base of the mixed layer and hence increase w_e, a meteorological-related quantity such as the Monin–Obukhov length scale (L_{mo}) (Figure 5.3e) is useful in determining which forcing dominates the dynamics of the upper ocean layer. To indicate the depth at which both mechanical and convection forces are comparable, this scale can take the following form:

$$L_{mo} = -\frac{u^{*3}}{\kappa J_b^o} \tag{4.4}$$

where $\kappa = 0.4$ is the von Kármán constant (e.g., Huffman and Radshaw, 1972). Values of $L_{mo} > 0$ (Figure 5.3e) indicates that the turbulence generated by wind stirring is suppressed by stable stratification that occurs during daytime, while $L_{mo} < 0$ occurs under unstable conditions at night. Moreover, $|L_{mo}|$ is generally shallower than h_ρ (Figure 5.3e). This suggests that wind-induced mixing might not to be a significant source of control of the depth of the mixed layer.

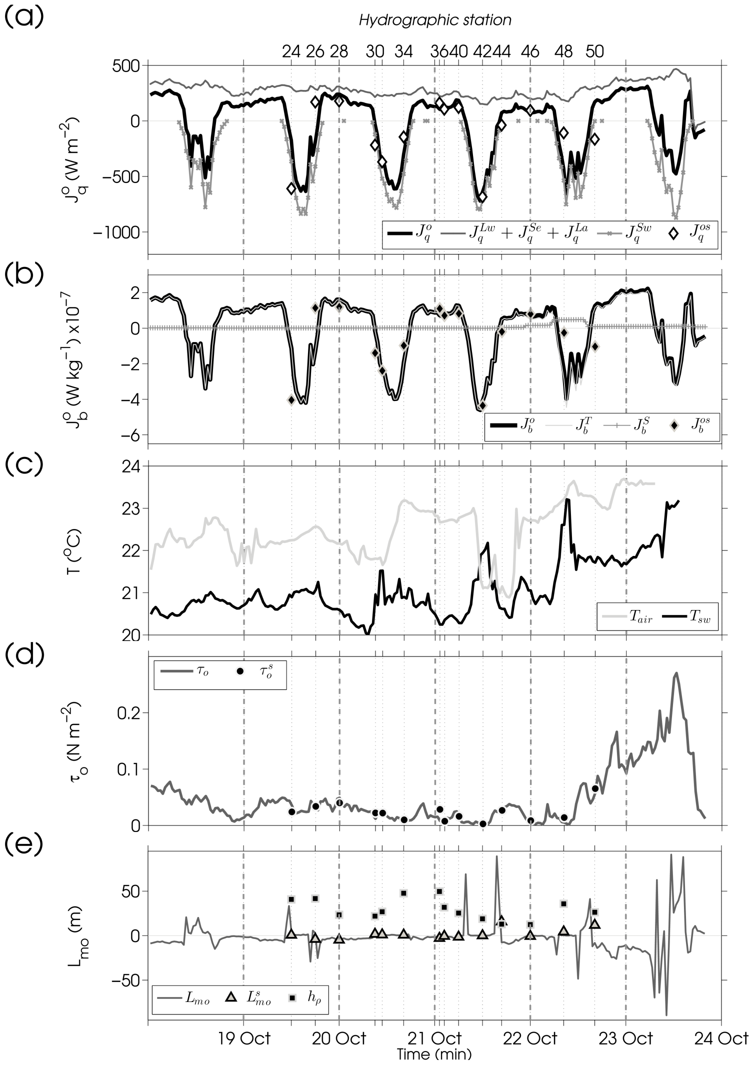

Figure 4.5: Half-hourly averaged meteorological data: (a) net surface heat flux J_q^o (defined positive upward) and related components: shortwave radiation flux J_q^{Sw}, net longwave heat flux J_q^{Lw}, latent heat flux J_q^{La}, and sensible heat flux J_q^{Se}; (b) net surface buoyancy flux J_b^o, defined as the sum of thermal surface buoyancy flux J_b^T, and haline surface buoyancy flux J_b^S; (c) sea water temperature T_{sw}, and temperature of air T_{air}; (d) wind stress $\boldsymbol{\tau}_o$; (e) Monin-Obukhov length scale L_{mo}, and mixed layer depth h_ρ. Symbols over time series denoted with a superscript s represent the exact value of each meteorological quantity computed using CTD data profiles from each hydrographic station. Thin vertical dashed lines show the hydrographic stations at top, while thick dashed lines indicate the end of each day at bottom.

.

4.3.3 Active mixing in filament waters

A description and determination of the mixed and mixing layer is required since bulk mixed layer models, and hence entrainment rates, largely depend on the depth of the mixed layer as a diagnostic quantity. This is attributed to the jumps δV and δb (Ravindran et al., 1999), which vary greatly with the depth of the mixed layer. Therefore, a careful determination of h_ρ was made by comparing different methods (Figure 4.6). Except for station 50, the σ_θ algorithm developed by Holte and Talley (2009) is chosen to find h_ρ. This method can be based on the shape of either potential density or potential temperature profile of each hydrographic station. For station 50, the T_θ method of Holte and Talley (2009) was more appropriate, largely due to the existence of salinity barriers around the area caused by the subsurface salinity maximum (Pelegrí et al., 2005b). This algorithm agrees rather well with the depth of the maximum gradient of the squared Brunt Väisälä frequency, $N^2 = -g/\rho_o(\partial_z \rho)$, (Figure 4.6), as well as with the threshold method of $\Delta\sigma_\theta = 0.03$ kg m^{-3} (de Boyer Montégut et al., 2004). Further, we found that the algorithm given by Kara et al. (2000) tends to overestimate h_ρ, whereas gradient methods given by Dong et al. (2008) tended to underestimate h_ρ when particular profiles were analyzed. These results are in agreement with the findings of Holte and Talley (2009) for large databases of hydrographic profiles.

Several authors have emphasized the need to consider a boundary region of elevated and active mixing in the pycnocline at the base of the mixed layer (e.g., Dewey and Moum, 1990; Brainerd and Gregg, 1995; Nagai et al., 2005; Inoue et al., 2010; Sutherland et al., 2014), usually referred to as the mixing layer depth (h_ε). The difference lies in that h_ε is the depth at which turbulent processes are active and work to maintain the homogeneity of the mixed layer and entrain buoyancy across the pycnocline. However, h_ρ represents the depth at which these surface fluxes have been mixed in a recent past, that is in a daily cycle or longer time scale. In other words, the mixed layer represents the history of mixing layer events. Therefore, depending on the time scale and spatial resolution used, h_ε could be more appropriate for entrainment than h_ρ (Brainerd and Gregg, 1995; Franks, 2014; Sutherland et al., 2014). For example, fine-scale processes forced by transient mixing events, in which flux conditions can change in a given moment of the day, require the measurement of an active mixing layer.

Sometimes, the active mixing layer can extend deeper than the mixed layer, that is

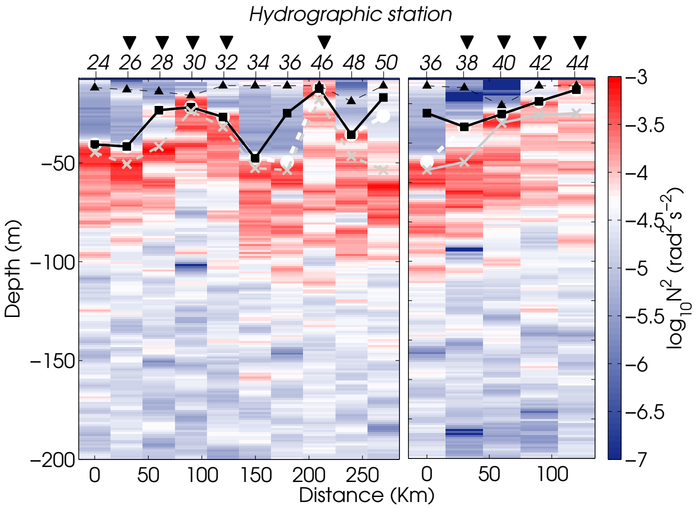

Figure 4.6: Vertical section of squared buoyancy frequency, N^2 (rad^2 s^{-2}), in logarithmic scale for all hydrographic stations. Left panel corresponds to transect A and right panel to transect B. Superimposed lines are h_ρ computed by the different methods. To improve the visualization only σ_θ-based algorithms are shown, where gray crosses show h_ρ following Kara et al. (2000), open white circles are h_ρ from the Holte and Talley (2009) algorithm, except for station 50 where a T_θ-based algorithm from Holte and Talley (2009) was more appropriate. Black squares show the σ_θ threshold criteria of de Boyer Montégut et al. (2004), and black triangles show h_ρ computed following the gradient method of Dong et al. (2008).

$h_\varepsilon > h_\rho$ (Dewey and Moum, 1990; Brainerd and Gregg, 1995; Inoue et al., 2010). The enhancement of the turbulence below h_ρ could be related to shear instabilities produced by internal waves as a result of impinging convective plumes from beneath h_ρ (Moum et al., 1989). An example of observational data was given by MacKinnon and Gregg (2005) who found higher correlations of ε_o and internal wave energy than between ε_o and $\boldsymbol{\tau}_o$ below the mixed layer.

On the other hand, Dewey and Moum (1990), in their examination of microstructure data in upwelling filaments off northern California, noted that the entrainment process can take place only when h_ε exceeds h_ρ; otherwise, when mixing is not strong enough to overcome the effects of the stratification in the pycnocline, entrainment cannot occur. Inoue et al. (2010) also distinguished between h_ε and h_ρ in order to measure entrainment heat fluxes based on dissipation profiles across the Gulf Stream, provided that h_ε is deeper than h_ρ. The same approach is considered here, by defining the entrainment zone or interface as $\Delta h = h_\varepsilon - h_\rho$.

In general, h_ε can be directly obtained by ε_o from microstructure data (Brainerd and Gregg, 1995; Inoue et al., 2010; Franks, 2014; Sutherland et al., 2014), from microstructure temperature gradients (Nagai et al., 2005), or by measurements of largest overturning through turbulent length scales such as Thorpe scales (Brainerd and Gregg, 1995). In this study we determine the base of the mixing layer when the dissipation profile decreases by two orders of magnitude from the surface. However, not all ε_o profiles show a clear transition. Therefore, a turbulent length scale such as the Ozmidov scale L_o (Ozmidov, 1965) could help to clarify the extension of the active mixing or h_ε, where L_o takes the form:

$$L_o = \sqrt{\varepsilon_o / N^3} \tag{4.5}$$

In such a case, L_o is interpreted to be the size of the largest turbulent eddy in a region of stable stratification.

An example can be seen in Figure 4.7, where h_ε is found to be deeper than h_ρ for station 42 in group-F (Figure 4.7a and b). In contrast to station 48 in group-nF (Figure 4.7c and d) where both h_ε and h_ρ have the same depth. Both stations were measured during daytime conditions, i.e. during the restratification of the mixed layer at the moment in which convection is absent.

A complete view of the active turbulent mixing is given in Figure 4.8, which shows vertical profiles of ε_o and superimposed profiles of L_o scales computed for each microstructure station with its respective h_ρ and h_ε depths. An interesting result of this analysis indicates that filament stations (thick profiles in Figure 4.8) have h_ε deeper than h_ρ (i.e., $\Delta h > 0$). The latter suggests that only these stations are susceptible to diapycnal entrainment (Dewey and Moum, 1990; Inoue et al., 2010). A reasonable explanation for this can be related to elevated ε_o at stations 26-32 and 38-46 in group-F together with shallow mixed layers produced by the outcropping of the isopycnals due the influence of the frontal filament system.

Mixing layer depths based on L_o sometimes seem to extend deeper than h_ε (Figure 4.8). This large depth extension of L_o below h_ε may be attributed to other processes that do not contribute to the upper mixing layer (Brainerd and Gregg, 1995). A possible explanation to this maximum might be the contribution of breaking inertial waves.

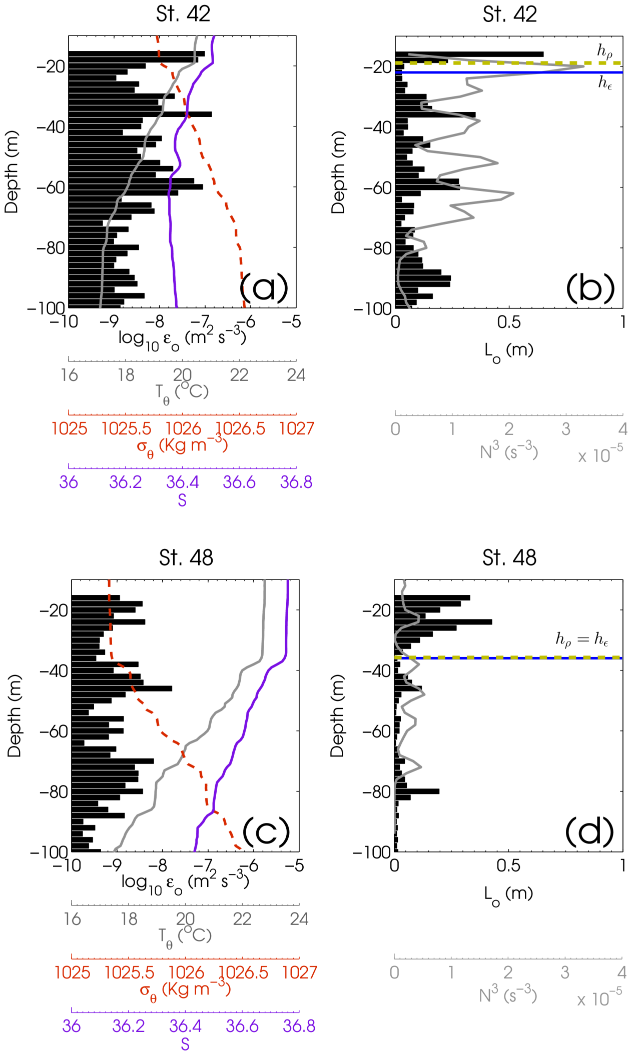

Figure 4.7: Vertical profiles of hydrographic and turbulent quantities. Left panels show T_θ (gray), σ_θ (dashed red) and S (violet) superimposed on dissipation profiles of ε_o (black bars), for: (a) station 42, affected by the upwelling filament and (c) station 48, unaffected by the filament. Both stations were measured during stable daytime conditions. Right panels show Ozmidov scales L_o (black bars) and vertical profiles of N^3 (gray) for: (b) station 42 and (d) station 48. Horizontal green and blue lines denote mixed layer depth (h_ρ) and mixing layer depth (h_ε), respectively.

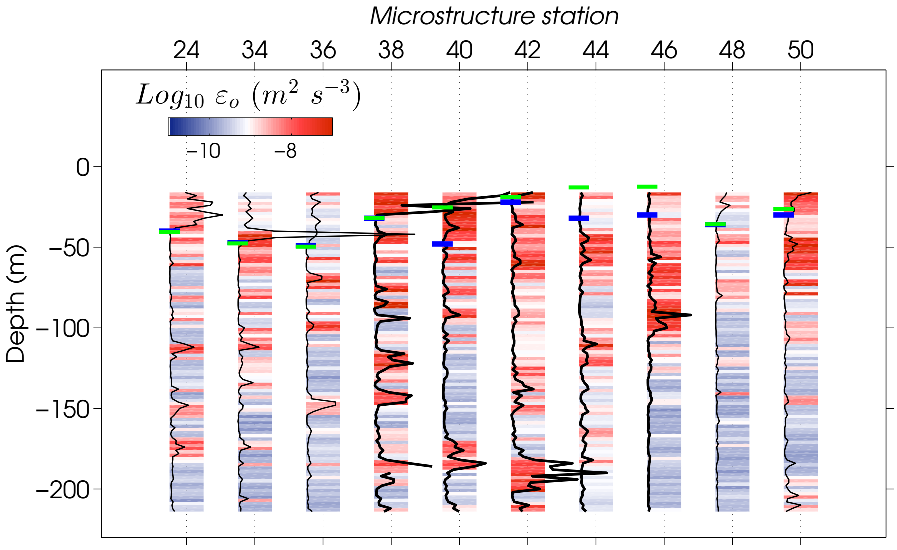

Figure 4.8: Vertical profiles of Ozmidov scales, L_o (m), for each microstructure station. At the bottom, color columns are profiles of TKE dissipation rates, ε_o. The maximum L_o value corresponds to 5.18 m at station number 34 at 42 m depth, and minimum L_o of 0.0045 m is found at station number 38 at 66 m depth. Thick black profiles show L_o for stations potentially affected by filament waters, while thin profiles are for the rest of L_o. Horizontal lines indicate mixed h_ρ (green) and mixing h_ε (blue) layer depths, respectively.

The enhancement of TKE dissipation rates below the mixed layer of filament waters shown in Figure 4.8 is often linked with elevated vertical shear levels (Figure 4.9). Weak wind regime during the days of the measurements, as shown by the L_{mo} scales (Figure 5.3e), indicates that the generation of turbulence within the upwelling filament by wind stress was likely small compared to turbulent diapycnal buoyancy fluxes or vertical shear at the base of the mixed layer. This is probably as a result of the baroclinicity of the front.

As already mentioned, vertical current shear increases in areas associated to the outcropping of the isopycnals, which in turn are related to filament stations of group-F (Figures 4.9).

We therefore examine the nature of those shear values. In order to ensure consistency when comparing ADCP-Sh^2 with geostrophic shear (Sh_g^2), ADCP velocities were previously rotated to a same reference system and interpolated between pair stations. Geostrophic shear is computed through thermal wind relation by setting a reference

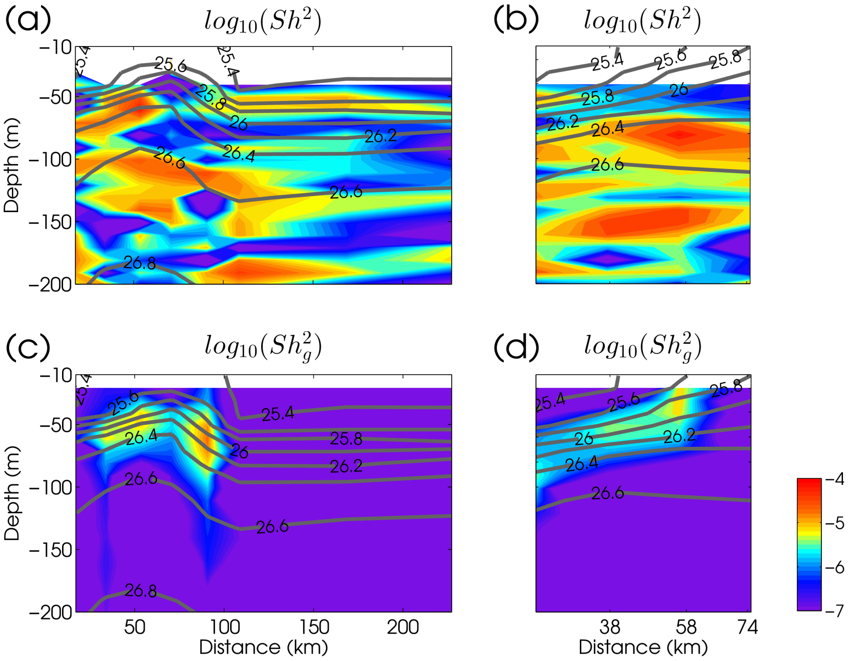

Figure 4.9: Vertical sections of total squared vertical shear, Sh^2 (s^{-1}), rotated to the same reference system than geostrophic velocities for (a) transect A and (b) transect B. Geostrophic vertical shear Sh_g^2, where the level of no motion is set at 650 m for transect (c) A and (d) B. Note the logarithmic scale. The accumulative distance in km between stations is shown at the bottom.

level of no motion in 650 m. Results of Figure 4.9a show that in transect A, the Sh^2 in group-F stations is mainly driven by the resolved component of the geostrophic velocity field (Figures 4.9a and c). In transect B, isopycnals outcropping towards the coast not only because the presence of the filament but because the proximity to the coastal transition zone (Figure 4.9d). Here, the resolved geostrophic component becomes less relevant and ageostrophic effects are likely forcing the total vertical shear in stations of group-F (Figures 4.9b and d). These results are also supported by geostrophic currents of altimetry data (see Figure 4.2). A northward geostrophic current agrees with a predominance of geostrophic shear in transect A. In contrast, a departure from geostrophy seems to take place in the coastal transition zone of transect B, where the filament flows southwards in opposite direction to the geostrophic flow.

Following the linear stability analysis, a useful related quantity is the gradient Richardson number $Ri_g = N^2(Sh)^{-2}$. In steady stratified shear flows, $Ri_g < (Ri_c = 0.25)$ indicates a necessary condition for the flow to become turbulent, where Ri_c is the critical Richardson number (Howard, 1961; Miles, 1961). However, an intensive debate can be found in the literature about the strict dependence of active stratified turbulence and the Ri_c below which turbulent entrainment becomes significant. Although Ri_g has been extensively reported to be in the range of 0.1 to 1 (Price, 1979; Pelegrí and Richman, 1993), other studies (Strang and Fernando, 2001; Zaron and Moum, 2009; Pham et al., 2012) indicate that turbulence can also be generated at $Ri_g > 1$ because of its dependence on the flow conditions. Therefore, special care must be taken when parameterizations are based on Richardson linear theory, particularly if velocity measurements have coarse vertical resolution.

Keeping these considerations in mind, Ri_g is derived in order to support the extension of the mixing at filament stations. Figure 4.10 shows ε_o, N^2 and Sh^2 horizontally averaged over stations 26-32 and 38-46 (group-F) in which $\Delta h > 0$ (Figure 4.10a) and, to the contrary, over the remaining stations (group-nF) with $\Delta h < 0$ (Figure 4.10b). In the first case of group-F stations, the relatively high value of vertical shear in the entrainment zone combined with the low stratification allows Ri_b to be closer to Ri_c, ranging between 1 and 3 just below the mixed layer (Figure 4.10a). However, for stations of group-nF, low levels of vertical shear at the entrainment zone coincides with an increase of Ri_g leading values much greater than Ri_c (Figure 4.10b). Notice how the spatially averaged dissipation of TKE is higher in stations of group-F than in group-nF.

4.4 Discussion

An important result of this study suggests that, apart from wind-stirring and convection, other forcings can affect the upper ocean layer in a filament frontal system. Vertical current shear, dissipation of turbulent kinetic energy, and buoyancy fluxes must often be taken into consideration in a region of active mixing where $\Delta h > 0$. We now analyze in more detail the effect of vertical shear in some widely used entrainment parameterizations, and propose a new approach for a bulk entrainment 1D formulation, where all relevant mixing-controlling factors are considered.

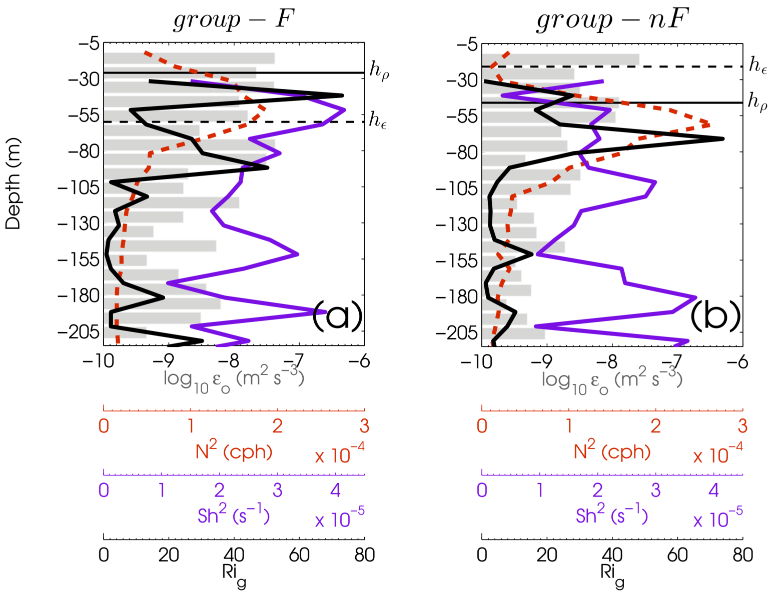

Figure 4.10: Vertical profiles of dissipation rates (ε_o, gray bars), squared vertical shear (Sh^2, violet), squared buoyancy frequency (N^2, red) and gradient Richardson numbers (Ri_g, black) spatially averaged for stations of (a) group-F where $\Delta h > 0$ (a), and (b) stations of group-nF where $\Delta h < 0$. Both ε_o and N^2 are averaged in depth cells of 10 m to match with the vertical resolution of Sh^2. Horizontal solid and dashed lines show h_ρ and h_ε, respectively.

4.4.1 Vertical Current Shear as Mixing Forcing

Price et al. (1978) were one of the first to include the effect of vertical shear as a main forcing mechanism in the upper ocean layer. Numerical and modeling experiments have shown that vertical shear is a relevant source of entrainment after the passage of strong storms as a consequence of strong winds (Jacob and Shay, 2003; Wada et al., 2009). However, the inclusion of the vertical current shear term allows for a singularity, pointed out in many studies (e.g., Deardorff, 1983; Pelegrí and Richman, 1993) as a physically unrealistic w_e when Ri_b approaches Ri_c[*]. For example, Gaspar (1988) neglected the DIT term based on the assumption of Pollard et al. (1973), who showed a time response of less than one inertial period. Their theory indicates that rapid transient forcing can be avoided in a long-term series. Others such as Pelegrí and Richman (1993) formulated a hybrid two-layer model for coastal upwelling that passes from a bulk-based entrainment parameterization to a Ri-dependent regimen when $Ri_b \approx Ri_c$. Deardorff (1983) derived an entrainment formulation that avoids the above singularity while recognizing the Ri_c concept, although its formulation depends on a critical value of 5.

---

[*] The representation of w_e given in Niiler and Kraus (1977) causes a physically unrealistic singularity. When Ri_b approaches its critical value $s \approx Ri_c$, w_e goes to very large positive or negative values, depending whether Ri_b stays above or below s.

It appears reasonable that vertical current shear at the base of the mixed layer should play a role in the entrainment process, particularly in filament structures where baroclinic effects could be important (Pelegrí et al., 2005b; Troupin et al., 2012). Hence, an effort to include vertical shear as a source of TKE for entrainment in frontal areas must be done. In this regard, to investigate the role of shear-driven mixing at the base of the mixed layer, a comparative analysis is carried out on the basis of three parameterizations described in section 4.3, which are two TKE bulk-based schemes: w_e^G without the shear effect (eq. 4.1); and w_e^{GS2} which includes Sh^2 by means of the DIT term (eq. 4.2); and a Ri_b-related entrainment formulation w_e^{SF} that considers the Sh^2 effect through δV as the main TKE source of entrainment (eq. 4.3). As expected, Figure 4.11 indicates that w_e^{GS2} underwent w_e enhancement at all hydrographic stations compared to w_e^G. The effect is more intense at stations 28, 44, and 46 with differences of $\sim 4 \times 10^{-4}$ m s^{-1}; these stations are largely affected by the filament signal. The last station, 50, also shows an elevated w_e, likely due to the influence of a mesoscale cyclonic structure as observed in satellite imagery (Figures 4.2a and b). However, further investigation of the role of TKE sources for entrainment and mixing processes in mesoscale eddies is needed to corroborate this, and which is addressed in Chapter 5.

In stations sampled during stable daytime conditions, w_e^G exhibited $w_e < 0$, resulting in detrainment or retreat of the mixed layer with time (Gaspar, 1988). This indicates that wind forcing alone is inefficient to induce mixing down to the base of the mixed layer. Therefore, it cannot act against the stably stratified layer below, which is consistent with the L_{mo}-length scales (Figure 5.3e). On the other hand, w_e^{SF} always has positive entrainment due its dependence on a Richardson approach and shows an enhancement of w_e in stations of group-F (shaded areas in Figure 4.11), except for station 42, likely due to a combination of high turbulent buoyancy fluxes and relatively low vertical shear at the interface.

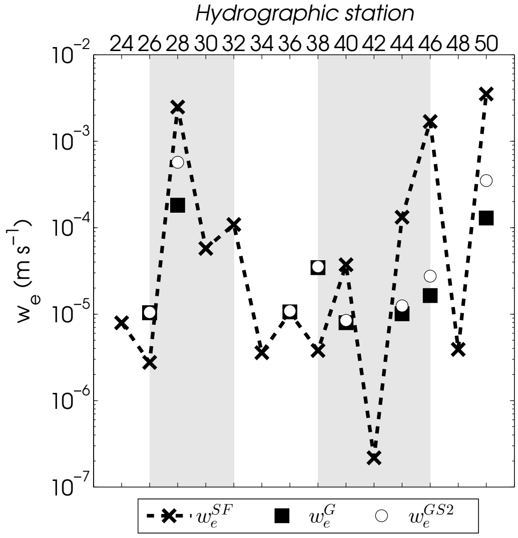

Figure 4.11: Entrainment rates from three parameterizations. Black rectangles show w_e^G in which the effect of vertical shear Sh^2 at the base of the mixed layer is neglected. White dots show w_e^{GS2} where the vertical shear effect is included. A Ri-dependent entrainment parameterization, w_e^{SF}, shown by dashed crosses which mainly depends on δV as a governing parameter. Shaded areas indicate stations of group-F potentially affected by the upwelling filament.

4.4.2 New entrainment approach

In agreement with Dewey and Moum (1990) and Inoue et al. (2010), we assume that turbulent entrainment can occur only when the active mixing in a stratified fluid is strong enough to overcome buoyancy effects and hence to erode the pycnocline. Because we have direct measurements of h_ε, we restricted our analysis to the stations in which both conditions of available ε_o and $\Delta h > 0$ are satisfied.

Most bulk mixed layer models (e.g., Kraus and Turner, 1967; Niiler and Kraus, 1977; Gaspar, 1988) do not account for the variable h_ε (Dewey and Moum, 1990). Thus, such models are inappropriate for frontal areas in which shallow h_ρ values are driven by the rising of the pycnocline favoring $\Delta h > 0$. We integrated the parameterization derived from Osborn (1980) over Δh to consider the diapycnal turbulent buoyancy flux ($\overline{w'b'}$), resulting in

$$\int_{-h_\varepsilon}^{-h_\rho} \overline{w'b'}(dz) = (J_b^{\Delta h})_I = -\int_{-h_\varepsilon}^{-h_\rho} 0.2\varepsilon_o(dz) \tag{4.6}$$

where $(J_b^{\Delta h})_I$ is the buoyancy flux integrated over the entrainment zone. Hence, this term represent a sink of TKE in the entrainment zone only when $\Delta h > 0$, as the energy is consumed in breaking the stratification. Following this reasoning, we should also consider the integration of the dissipation term over the entire active mixing layer $\int_{-h_\varepsilon}^{0} \varepsilon_o(dz) = \overline{\varepsilon_o} h_\varepsilon$, similarly to Dewey and Moum (1990). Adding these modifications to w_e^{GS2}, the entrainment TKE-based parameterization can take the following form:

$$w_e^{\Delta h} = \frac{(m_2 + m_3)u_*^3 + 0.5 h_\rho J_b^o + (J_b^{\Delta h})_I - \overline{\varepsilon_o} h_\varepsilon}{0.5[(\delta b h_\rho) - (\delta u^2 + \delta v^2)]} \tag{4.7}$$

Unlike other parameterizations, eq. (4.7) permits consideration of TKE entrainment sources of: mechanical stirring by means of u_*, vertical shear at the base of h_ρ through the DIT term, buoyancy fluxes at the surface and turbulent buoyancy fluxes at the entrainment zone (i.e., J_b^o and $(J_b^{\Delta h})_I$), as well as the dissipation of TKE across the layer in which the active mixing operates.
An interesting result is shown in Figure 4.12, in which an enhancement of w_e in stations affected by the upwelling filament is possible if the new approach is considered through eq. (4.7). These results are consistent with elevated mixing levels shown in Figure 4.8, suggesting the dependence of the entrainment process on the turbulent dynamics of the filament. Buoyancy Reynolds numbers, $Re_b = \varepsilon_o / \nu N^2$, computed at the entrainment zone, were $Re_b > 20$ in stations of group-F, except in station 42 ($Re_b = 11.07$) which exhibit null entrainment (Figure 4.12). Therefore, the observed ε_o seems to be sufficient to support heat flux below the base of the mixed layer and hence entrainment is expected (Smyth and Moum, 2000).

Our suggested entrainment formulation has a mean of $\overline{w_e^{\Delta h}}$=1.73 $\times 10^{-4}$ m s^{-1} (15 m d^{-1}), in contrast to $\overline{w_e^{GS2}} = 0.19 \times 10^{-4}$ m s^{-1} (1.7 m d^{-1}) and $\overline{w_e^{SF}}$=5.99 $\times 10^{-4}$ m s^{-1} (52 m d^{-1}), differing by approximately one order of magnitude. However, some velocities computed by w_e^{SF} reach values of similar orders with a correlation coefficient of $r^2 = 0.81$ between w_e^{SF} and $w_e^{\Delta h}$. This result is related to the DIT term and reinforces our assumption that for a better understanding of sheared flow Ri_v rather than Ri_τ (Table 4.1) needs to be considered (Pollard et al., 1973; Price, 1979; Jonker et al., 2013). On the other hand, high values of w_e around 10^{-3} m s^{-1} have been obtained by Pelegrí and Richman (1993) and other modelling experiments (Jacob and Shay, 2003). The

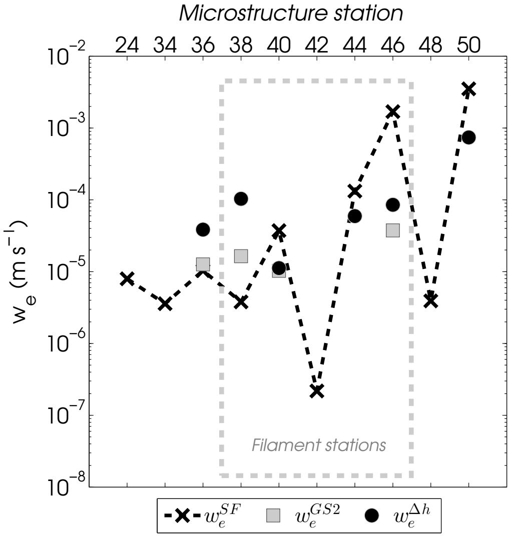

Figure 4.12: Comparison between w_e velocities given by the parameterizations of w_e^{SF} (dashed crosses), w_e^{GS2} (gray rectangles), and $w_e^{\Delta h}$ (black dots). Dashed box denotes microstructure profiles of stations in group-F affected by the filament.

elevated values of $w_e^{\Delta h}$ could be explained through the residence time of turbulence, $t_{res} = (B_1^{2/3}/N)ln(\varepsilon_o/\nu N^2)$ (Zhurbas, 2001), where B_1 is a constant of 3.4. At the depth of h_ε, the turbulent residence time takes on the order of minutes ($t_{res} \sim 30$ min) which means that the remaining kinetic energy available for entrainment is no longer sufficient to overcome stratification effects. The latter suggests that transient mixing events may enhance w_e in localized regions.

Under the assumption of minimal zonal(meridional) divergence for transect A(B), the divergence of the flow is also computed (Figure 4.13). Results show an upwelling cell in the dense(cold) side of both front A and B. In contrast, a downwelling is generated at the light(warm) side of the front. This result agrees with Dewey et al. (1993) for a minifilament structure and can be related with the process of frontogenesis (Hoskins, 1982). Vertical velocities (w) derived from the divergence of the flow for transect A ($\partial_z w = -\partial_y v$) and B ($\partial_z w = -\partial_x u$) are shown in Figure 4.13a and b. The values of w are found to be in the same order of magnitude than values of entrainment given by $w_e^{\Delta h}$. The upwelling of transect A coincides with a positive entrainment velocity $w_e^{\Delta h}$ = 7.40 $\times 10^{-4}$ m s^{-1} (64 m d^{-1}) (Figure 4.13a) in station 50. Similarly for transect B (Figure 4.13b), positive w is consistent with a mean value of $\overline{w_e^{\Delta h}} = 7.09 \times 10^{-4}$ m s^{-1}

(6 m d^{-1}) between station 36 and 38. It is unlikely the signature of the filament be maintained only by w_e velocities (Dewey et al., 1993). However, entrainment velocities might impact in the net balance of the vertical transport, and this effect could be particularly important within mesoscale and energetic structures.

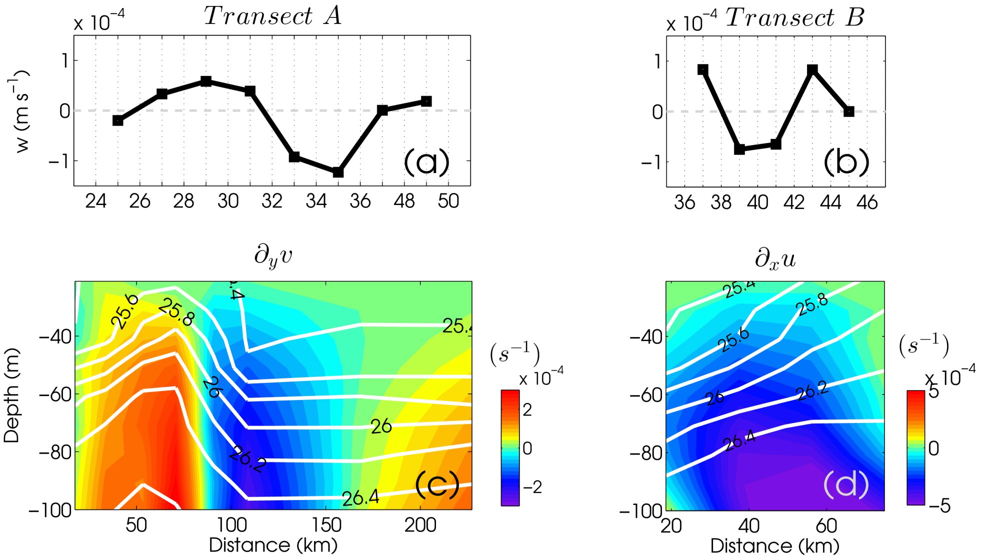

Figure 4.13: Cross-sections of vertical velocities, w (m s^{-1}), at the base of the mixed layer for pair stations of (a) transect A and (b) transect B. Transects of w are integrated from their respective divergences of the flow (c and d) by setting $w = 0$ as boundary conditions at the surface.

4.4.3 2D Submesoscale processes

Turbulence is a three-dimensional (3D) process; hence, to restrict the entrainment analysis to a 1D approach, we need a previous examination of 2D instabilities that could occur at frontal structures.

In an upwelling filament, two-dimensional (2D) submesoscale processes could play important roles in mixing by serving as paths for conducting kinetic energy extracted from the mean flow to the final dissipation range throughout its secondary instabilities (Capet et al., 2008b; D'Asaro et al., 2011; Thomas et al., 2013). To determine whether this type of process can affect this particular front, vertical distributions of potential vorticity and submesoscale energy sources are shown in Figures 4.14.

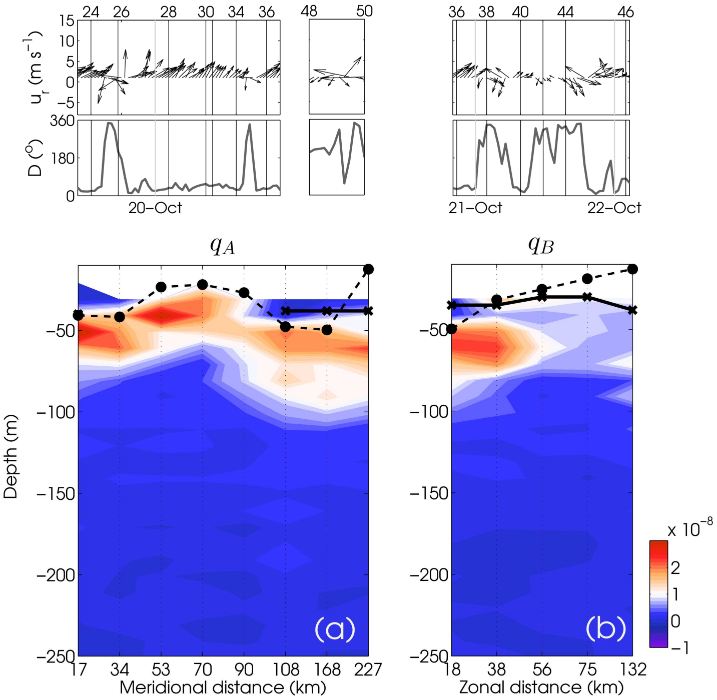

Figure 4.14: Wind speed, $\boldsymbol{u}_r$ (m s^{-1}) for (a) transect A and (b) transect B, with their respective wind direction (clockwise from North). Cross-stream sections of potential vorticity q (s^{-3}) for: (a) transect A, q_A, and (b) transect B, q_B, where dashed lines corresponds to h_ρ and solid lines denote h_ε, both spatially averaged.

Following the analysis of Thomas et al. (2013), the potential vorticity q can be determined as $q_A = (f - \partial_x v)N^2 - (\partial_x b)^2 f^{-1}$ for transect A and similarly $q_B = (f - \partial_y u)N^2 - (\partial_y b)^2 f^{-1}$ for transect B. Despite the lack of synoptic measurements, analysis of q reveals positive values for along-front q_A (Figure 4.14a) indicating stable conditions (e.g, D'Asaro et al., 2011). Transect B (Figure 4.14b) exhibits a similar pattern to transect A in the along-front q_B, with slightly near zero values at locations where isopycnals outcrop to the surface and $\Delta h > 0$, i.e., at the upwelling filament.

In this first approximation to the problem, results show that at the moment of sampling, submesoscale 2D instabilities such as symmetric instabilities appear to have a weak effect on the frontal structure. A cross-front wind in transect A (Figures 4.14a) is likely inefficient to induce an Ekman transport that makes the front unstable to symmetric instabilities (e.g., D'Asaro et al., 2011). Thus, a 1D perspective determined by the TKE balance seems to be appropriate in this case study.

4.4.4 Accuracy of parameterized ε_p

To the best of our knowledge, the microstructure profile data obtained in this study represent the first measurements taken in this area; no previous qualitative/quantitative studies offer direct comparisons of the behavior of parameterized ε_p in entrainment formulations. The TKE budget exhibits a high sensitivity to the parameterization of the dissipation term, which has proved to be a dominant sink in the energy balance (e.g., Deardorff, 1983; Gaspar, 1988; Wada et al., 2009). Therefore, such a comparison could be useful for future research.

Assuming a well-mixed upper ocean layer such as in a bulk mixed layer model, the averaged ε_o from surface levels (sufficiently far from surface breaking wave effects, ~ 16 m) to h_ε, was compared to those ε_p parameterized in both w_e^G and w_e^{GS2} following Gaspar (1988), which is briefly described in Appendix A of this thesis. Results of Table 4.2 indicates that ε_p can be overestimate by one order of magnitude. In the context of a 1D TKE balance, most of the energy transferred to the interface is dissipated by viscosity. The remaining kinetic energy is stored in the form of potential energy, having to work against the buoyancy forces or as energy that will be subsequently converted to kinetic energy by entrainment. Because of this one-dimensional balance, overestimation of the dissipation term lies in lower entrainment velocities than expected, suggesting that the parameterized dissipation term extracts more energy from the system and leaves little energy for the entrainment process. Thus, one can expect that decreasing the dissipation term in the entrainment parameterizations to match the observed dissipation term will lead to an enhancement of w_e. This is shown in Figure 4.12, where averaged w_e increases by an order of magnitude from 10^{-5} to 10^{-4} m s^{-1} when the parameterized dissipation term $\overline{\varepsilon_p} h_\rho$ is replaced by the integration of observed ε_o from surface to h_ε as in eq. (4.7).

Most of the entrainment parameterizations based on the Niiler and Kraus (1977) approach assume that dissipation is simply a constant fraction of the TKE budget that mainly depends on u_* as relevant turbulent length scale. However, others as Gaspar

Table 4.2: Spatially averaged dissipation term of a 1D TKE balance (m^3 s^{-3}) for both transect A and B. TKE dissipation rates are also averaged in depth up to h_ρ for the parameterized ε_p and up to h_ε for ε_o and ε_{LG}

Dissipation term	**Transect A**	**Transect B**
$\overline{\varepsilon_o}\ h_\varepsilon$	0.23×10^{-6}	0.18×10^{-6}
$\overline{\varepsilon_p}\ h_\rho$	2.66×10^{-6}	1.76×10^{-6}
$\overline{\varepsilon_{LG}}\ h_\varepsilon$	3.25×10^{-6}	2.17×10^{-6}

(1988) parameterize the dissipation term as a function of the stability and rotation parameters (Deardorff, 1983) and do not rely solely on u_* (see Appendix A). This dissipation length allows for a more accurate ε_p even in convective conditions, although the dissipation due to vertical current shear is also neglected due the omission of the DIT term in eq. 4.1. Therefore, a possible cause of the disagreement between ε_o and ε_p lies in the role of Sh^2 in the entrainment zone.

Our previous results suggest that buoyancy and current shear effects should not be ignored in the ε_p parameterization of a 1D TKE balance. Therefore, a scaling based on the familiar " law of the wall ", $\varepsilon_w = u_*^3/\kappa z$ (e.g., Oakey and Elliott, 1982), might not be adequate to represent the vertical structure of ε_p from surface to the mixing layer. Comparisons with the dissipation scaling given by Lombardo and Gregg (1989), $\varepsilon_{LG}(z) = 1.76\varepsilon_w(z) + 0.58J_b^o$, though taking into account both u_* and J_b^o sources, overestimates by an order of magnitude the observed ε_o at surface as depicted in Table 4.2.

Although this needs to be analyzed in greater detail with proper temporal series of velocity currents and microstructure turbulent profiles, we suggest for future studies, that the parameterization of the dissipation term proposed by Gaspar (1988) might be modified by validating empirical constants in rotation and stability parameters within highly dynamic areas such as filaments and near coastal mesoscale structures.

4.5 Conclusions

The entrainment process directly influences SST (e.g., Wada et al., 2009) and h_ρ, and is crucial for the diapycnal transport of biogeochemical properties to the surface ocean layers (Nilsen and Falck, 2006). Moreover, in a one-dimensional bulk sense, the entrainment parameterization serves as a proxy to elucidate the dominant sources of TKE that control the upper water column. In this study, we have analyzed the diapycnal turbulent entrainment process in the dynamical area of the Cape Ghir upwelling filament by using satellite imagery and *in-situ* hydrographic measurements including novel ε_o measurements from a microstructure profiler.

Similar to a laboratory experiment, the absence of strong winds enabled us to highlight other sources of TKE involved in the entrainment phenomenon. Therefore, when the effect of vertical current shear is included in a bulk mixed layer entrainment parameterization, an expected increase in w_e is observed. This entrainment enhancement is particularly high in filament waters suggesting that vertical shear-induced mixing at the base of the mixed layer should not be neglected in TKE-bulk mixed layer models of filament regions.

One of the most important results here suggests that active mixing, determined by the extension of h_ε, creates optimal conditions for the occurrence of entrainment when this depth exceeds the depth of h_ρ. This theory is supported by the fact that Δh becomes positive in those areas directly affected by the upwelling filament in which the pycnocline is close to the surface. In such cases, turbulent mixing can act more efficiently within a smaller volume of the upper ocean layer, hence the importance of separating h_ρ and h_ε (Dewey and Moum, 1990). The latter analysis also shows an increase in ε_o levels in the upwelling filament front, which agrees rather well with the enhancement of w_e and vertical current shear. This result highlights the relationship of the dynamics of mesoscale structure and the enhancement of turbulent mixing.

The parameterization of dissipation terms in the entrainment formulation differs from the observed dissipation rates, resulting in an underestimation of w_e in all hydrographic stations. The impact of these anomalous vertical velocities could lead to an overheating of the SST in numerical models that include such mixing schemes. This might be addressed by fitting empirical constants and functions from Gaspar (1988) ε_p parameterization.

In view of the latter results, a new approach for estimation of entrainment velocities is proposed in which integrated ε_o from the surface to h_ε, mechanical stirring, vertical shear, surface buoyancy fluxes, and turbulent buoyancy fluxes at the entrainment zone Δh, are included in a single formulation. These w_e values are in slight agreement with the Ri-dependent entrainment law from the experimental study of Strang and Fernando (2001), which depends on Ri_v as a governing parameter and includes the effects of internal waves breaking at the entrainment zone.

Finally, this study has aimed to establish a basis for future work involving *in situ* data with proper temporal and spatial resolutions as well as numerical simulations. The inclusion of additional sources of TKE in the entrainment process, such as radiating energy from breaking interfacial waves impinging on Δh, and Langmuir turbulent circulation, may improve the knowledge of this turbulent process in the upper mixed layers of ocean fronts.

5

Turbulent Diapycnal Mixing within an Intrathermocline Anticyclonic Eddy*

5.1 Introduction

An understanding of surface turbulent diapycnal mixing is crucial for a quantification of vertical transports of salinity, heat, momentum and biogeochemical properties (e.g., Sverdrup, 1953; Lewis et al., 1986; Klein and Lapeyre, 2009; Stramma et al., 2013), especially in highly oligotrophic regions (Cuypers et al., 2012) such as the subtropical Northeast Atlantic basin. Surface mixing processes are also responsible for the interchanges between the ocean-atmosphere system (e.g., Blanke et al., 2002; Belcher et al., 2012) and transfer wind energy and momentum to the ocean via wave breaking (Burchard et al., 2008).

The upper ocean layer is strongly dependent on air-sea interaction and the resulting convection and wind-stirring processes at the sea surface (e.g., Gaspar, 1988; Nagai

---

[*] Estrada-Allis, S., Rodríguez-Santana, Á., Aguiar-Gonzàlez, B., Sangrà, P., Martínez-Marrero, A., and Gordo, C. Surface Diapycnal Mixing in a Mode Water Anticyclonic Eddy South of the Canary Islands. *Submitted to the Journal Geophysical Letters.*

et al., 2005). Additionally, it can be sensitive to other processes occurring at the interface between the seasonal pycnocline and the stably stratified ocean layer below it, such as local increases of vertical current shear at the base of the mixed layer (Strang and Fernando, 2001; Samson et al., 2009; Estrada-Allis et al., under review). The effects of this vertical shear as a source of turbulent kinetic energy may enhance turbulent mixing at the interface between the mixed layer and the underlying pycnocline. This results in increases of vertical entrainment. Diapycnal entrainment rates w_e, promote the redistribution of physical properties from the deep stably stratified layer towards the ocean upper boundary layer (Kolodziejczyk et al., 2015), amongst other effects. Nevertheless, controlling factors remain unknown since w_e is a small-scale related quantity that acts as transient turbulent process. As examined in Chapter 4, entrainment-driven sources depend on the interface or entrainment zone, (i.e., Δh). This layer is often determined by the difference between the mixed and mixing layer, where h_ε represents the layer where active mixing occurs (Brainerd and Gregg, 1995; Sutherland et al., 2014). $\Delta h > 0$ is an indicator for the occurrence of entrainment according to eq. (4.7) derived in Chapter 4. This is because w_e can only be induced in regions of active mixing, where the turbulence within the pycnocline (below h_ε) is strong enough to overcome the effects of stratification (Dewey and Moum, 1990; Inoue et al., 2010).

Below the mixed layer, the deep ocean is mainly mixed by the downward propagating energy of wind stress and tides (Wunsch and Ferrari, 2004). Deep mixing is critical for providing the potential energy to sustain the global ocean circulation (Wunsch and Ferrari, 2004). In addition to tides and winds, theoretical and numerical studies predict that anticyclonic eddies may also play an important role in enhancing deep diapycnal mixing by trapping of near-inertial waves (e.g., Kunze, 1985; Zhai et al., 2005; Ferrari and Wunsch, 2009; Stanley and Saenko, 2014; Zhang et al., 2015). This occurs as the local inertial frequency of the inertial waves is reduced inside an anticyclonic eddy as detailed by Lueck and Osborn (1986). The inertial waves then become subinertial as they travel towards the edge of the eddy. At a critical point, where the frequency of the wave equals the local inertial frequency, the wave number vector becomes vertical and waves reflect back into the eddy, hence they are trapped. Moreover, the eddy's vorticity decreases with depth because of vertical shear, and so a downward propagating wave tends to become subinertial with increasing depth. Because the wave cannot reflect upward, the amplitude of the wave must grow to conserve its downward momentum flux leading to nonlinear effects that eventually act to extract and dissipate the energy of the waves. Therefore, diapycnal mixing linked to the strong shear introduced by trapped inertial waves may occur at the base of the eddy. Although there is increasing evidence of near inertial wave trapping by anticyclonic eddies (e.g., Danioux et al., 2008; Cuypers et al., 2012; Forryan et al., 2012; Joyce et al., 2013; Sheen et al., 2014) there is a lack of observations in the literature about the associated enhancement of diapycnal mixing. This is related to the difficulty of performing a synoptic high resolution sampling of the phenomenon with microstructure profilers.

As is the case for near-inertial wave trapping in deep mixing, the upper mixing processes sketched above may be particularly active in mesoscale eddies and their associated submesoscale structures. These can induce frontogenesis and instability cascades from mesoscale kinetic energy scales to mixing and dissipation (Capet et al., 2008b; Klein and Lapeyre, 2009). In this context our study region, the Canary Eddy Corridor, is a major pathway of westward propagating eddies in the Northeast Atlantic with a high eddy population (Sangrà et al., 2009; Mason et al., 2014). It has been hypothesized that the CEC may represent a quasi-constant source of turbulent mixing in the subtropical Northeast Atlantic basin for both surface and deep levels of the water column (Sangrà et al., 2009). However, high resolution observations of the mixing processes inside the CEC eddies are missing in order to confirm this hypothesis, in particular those related to anticyclonic eddies as they clearly dominate inside the CEC (Sangrà et al., 2009) .

Despite the importance of mixing processes acting within mesoscale structures, two major questions remain unresolved. The first is related to identifying the sources of TKE that control the upper mixed layer within mesoscale eddies. The second question concerns quantifying the proportion of this energy that is dissipated or used to enhance deep ocean mixing.

The goal of this study is to characterize diapycnal mixing within a typical intrathermocline anticyclonic eddy of the CEC in the subtropical Northeast Atlantic. The mesoscale structure was surveyed during the PUMP cruise in September 2014 (section 5.2). The reader is referred to Chapter 3 for details of the sampling strategy, data collection and methodology. We first show our main results evaluating the correlation between the principal mixing-forcing mechanisms and the resulting diapycnal mixing at the surface (section 5.3), interface (section 5.5), and eddy bottom (section 5.6) levels. In addition, we provide evidence for enhancement of deep diapycnal mixing at the base of the intrathermocline eddy. An examination of micro-scale diffusivity coefficients and comparison with fine-structure parameterized diffusivities is addressed in section 5.7. Conclusions are presented in section 5.8.

5.2 Case study: the PUMP intrathermocline eddy

Within the framework of the PUMP project, an anticyclonic eddy was surveyed southwest of the Canary Islands inside the CEC (Figure 5.1). The survey was carried out aboard the *BIO Hespérides* from August 31 to September 23 2014. The eddy was generated by the island of Tenerife and at the time of the survey it was four months old. For this study we selected a meridional transect crossing the eddy center, in which CTD, LADCP, SADCP, meteorological and turbulent microstructure profiler data were collected (Figure 5.1). Turbulent mixing was measured through a microstructure profiler TurboMAP. CTD and LADCP stations (25 and 24 respectively) were 5 nautical miles apart, whereas TurboMAP stations (13) were 10 nautical miles apart. SADCP data were averaged along CTD stations. The transect was sampled over about 3.5 days.

Figure 5.1 shows the normalized vorticity (Rossby number) and velocity fields of the studied eddy as obtained from merged altimeter data. The eddy is noticeable by a local minimum of the normalized vorticity and a corresponding anticyclonic closed circulation located 540 km southwest of Tenerife. The corresponding vertical density section along the transect indicates that the eddy is $\sim$ 600 m depth and 110 km diameter (Figure 5.2). Notice that in the upper layers the isopycnals have a dome shape, whereas in the deeper layers they have a bowl shape. This is a typical signature of an intrathermocline eddy, also often referred to as a mode water eddy. The origin of this type of eddies is still under discussion. Recently it has been proposed that its characteristic dome-shape at uppers levels may be the result of disturbances of the upper thermocline due to eddy-wind interactions (McGillicuddy, 2015).

The layer of maximum stratification, given by N^2, was located near the surface on 120 m at the eddy periphery, and shallowing up to 80 m depth at the eddy core (Figure 5.2b). Between 200 m and 400 m depth, a clear minimum in N^2 is observed at the eddy core, suggesting favorable conditions for the development of diapycnal mixing by turbulent processes, as shown later.

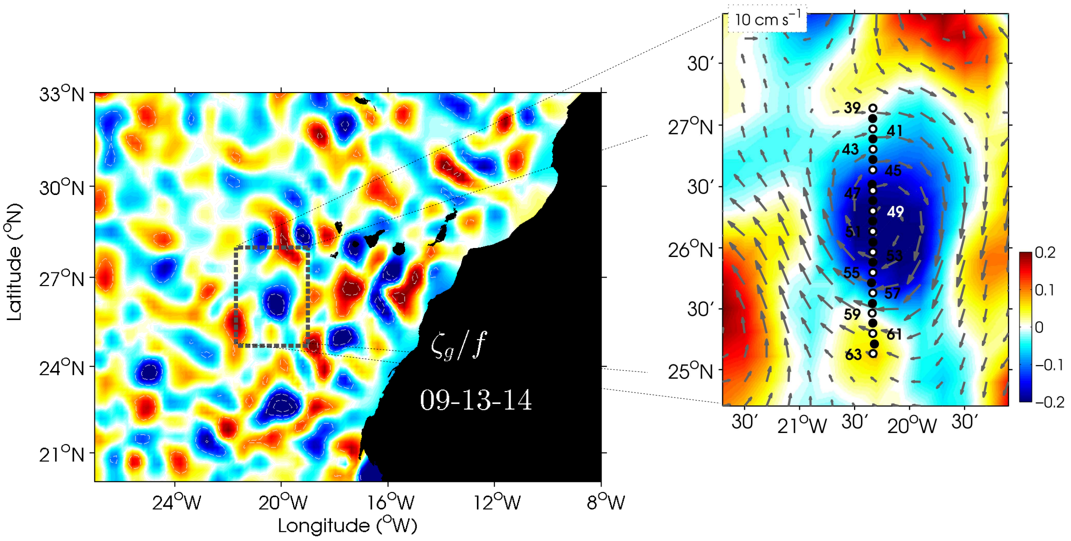

Figure 5.1: Vertical component of the geostrophic relative vorticity, ζ_g, normalized by the planetary vorticity, f, which is an estimate of the Rossby number, Ro. Small box in the left panel delimits the region where the anticyclonic eddy is found. Right panel shows a zoom of the delimited box in which altimeter-derived geostrophic currents are shown. Hydrographic and ADCP (black dots) and microstructure (white dots) stations are superimposed. We define stations 39 to 47 as the northernmost stations, 48 to 51 as the eddy-core stations and 52 to 63 as the southernmost stations.

5.3 Air-sea fluxes and diapycnal mixing

In order to compute the sources of heat and momentum at the surface that affect the mixed layer depth, an initial examination of the air-sea fluxes is needed (Figure 5.3). Figure 5.3a shows the surface fluxes of heat acting over the ocean surface along the meridional transect as computed in Chapter 3. The components contributing to J_q^o are also shown[*]. The net surface buoyancy flux (Figure 5.3b) was calculated according to eq. (3.2) considering both haline and thermal contributions (Dorrestein, 1979). The meteorological quantities shown in Figure 5.3 were averaged over windows of approximately 30 minutes centered in time with the time of the CTD casts. As shown in Figure 5.3a, the surface daily heat cycle is well defined. The main contributor to the

---

[*] See Chapter 3 and Table 4.1 for formulation and nomenclature, respectively.

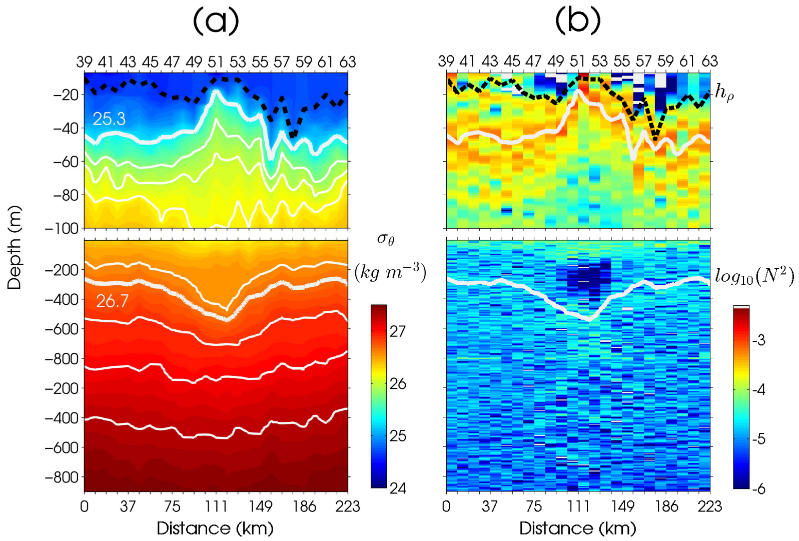

Figure 5.2: Vertical sections of the meridional transect in Figure 5.1. (a) Potential density anomaly, σ_θ (kg m^{-3}), and (b) squared buoyancy frequency, N^2 (s^{-2}), in logarithmic scale. The black dashed lines represent the depth of the mixed layer, h_ρ. The white contours denote isopycnals where those corresponding to 25.3 and 26.7 (kg m^{-3}) are highlighted.

net surface heat flux is the short wave radiation during daytime and the latent surface heat flux during nighttime, ranging from -896 to 227 W m^{-2} (Figure 5.3a).

The net buoyancy flux clearly matches the trend of the surface heat cycle (Figures 5.3a and b). Mean values of the surface buoyancy flux were 1.15×10^{-7} W kg^{-1} at night and -3.37×10^{-7} W kg^{-1} during the daytime (Figure 5.3b). As in the case of the upwelling filament in Chapter 4, thermal contributions from thermal buoyancy flux to the net buoyancy flux were more important than haline buoyancy fluxes (Figure 5.3b), suggesting that, as expected, freshwater fluxes have little effect in this region due to low precipitation rates and the absence of river discharges (e.g., Kara et al., 2010). It is worth noting that during nighttime the total heat flux is positive (towards the atmosphere), which leads to an increase of the surface buoyancy flux ($J_b^o > 0$) setting up convection-favorable conditions for the turbulent surface mixing.

Wind stress also modulates the depth of the upper mixed layer through the flux of momentum. Figure 5.3c shows the computed surface wind stresses along the transect of study. A weak northeasterly wind field prevailed throughout the transect, with low mean velocity values of $\overline{u_r} = 7.87$ m s^{-1} and $\overline{\tau_o} = 0.08$ N m^{-2}. However, on the last day of the sampling, wind speed increased with peaks of 13.21 m s^{-1}, sustaining rather

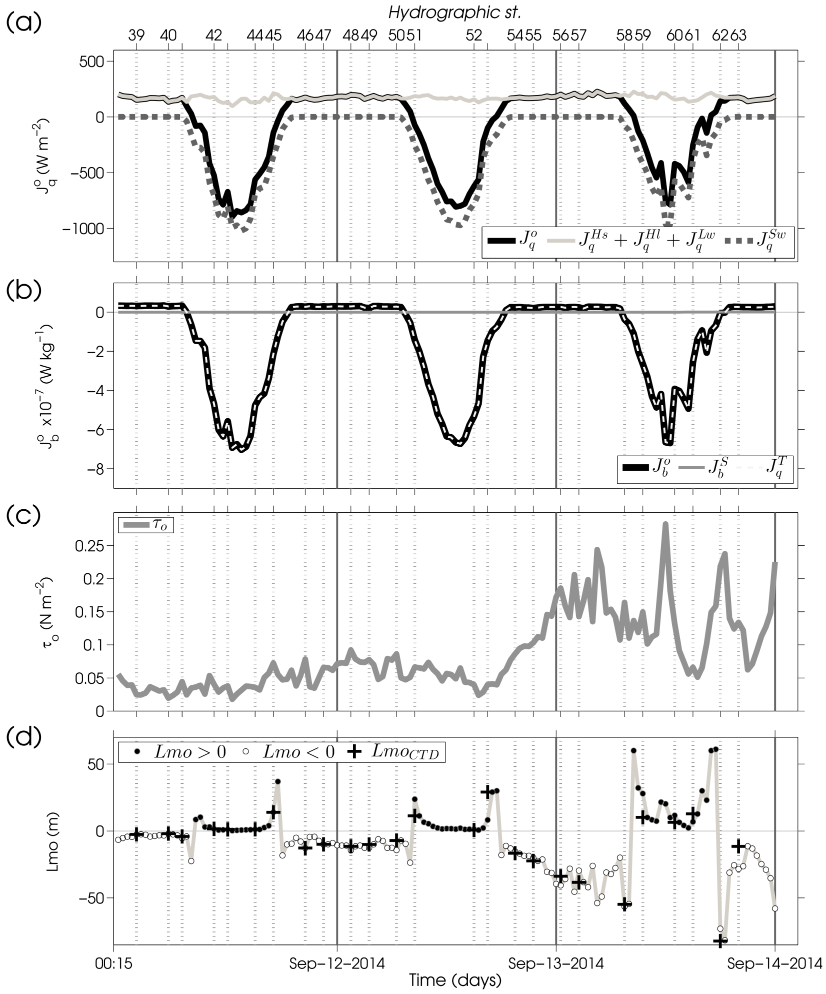

Figure 5.3: Meteorological half-hourly data averages. (a) Net surface heat flux, J_q^o (defined positive upward) and related components: shortwave radiation flux, J_q^{Sw}; net longwave heat flux, J_q^{Lw}; latent heat flux, J_q^{La}; and sensible heat flux, J_q^{Se}. (b) Net surface buoyancy flux, J_b^o, defined as the sum of the thermal surface buoyancy flux, J_b^T, and haline surface buoyancy flux, J_b^S. (c) Wind stress, $\boldsymbol{\tau_o}$. (d) Monin-Obukhov length scale, L_{mo}, where positive and negative values are marked as black and white dots, respectively. Black crosses indicate values of L_{mo} concomitant with CTD time profiles. Thin vertical dashed lines at the top show the hydrographic stations, while thick dashed lines at the bottom indicate the end of each day.

high values of $\boldsymbol{\tau_o}$ of 0.3 N m^{-2} at stations 57, 60 and 62 (Figure 5.3c). The resulting observed mixed layer depth is a consequence of the wind stress momentum flux through mechanical forces, and the above air-sea fluxes through convective forces. Under similarity theory, the Monin-Obukhov lengthscale (eq. 4.4 from Chapter 4) gives us the depth at which both mechanical and convective forces are comparable. Values of $L_{mo} > 0$ indicate that the turbulence generated by wind stirring is suppressed by a stable stratification. The opposite occurs when $L_{mo} < 0$.

As depicted in Figure 5.3d, along the entire transect, the competition between wind-mixing and convection-mixing seems to alternate in time, indicating that both forcings are important sources of TKE for the upper layer of the eddy. However, the mixed layer deepens at the southernmost stations, where absolute values of L_{mo} increase, suggesting that at the southern edge of the eddy, turbulence is mainly affected by mechanical wind stirring.

The observed increase of the wind stress at the last stations coincides with an enhancement of TKE dissipation rates (Figure 5.4a). Spatial and surface-depth averages of ε_o (from $z = 0$ to $z = -h_\rho$) present values of 1.2×10^{-7} m^2 s^{-3} at the eddy core (stations 47 to 53) and 0.7×10^{-7} m^2 s^{-3} and 2.7×10^{-7} m^2 s^{-3} at the northern (stations 39 to 45) and southern (stations 55 o 63) edges, respectively. This sudden enhancement of the dissipation of TKE at southern stations suggests that the surface mixing response to the atmospheric forcing is almost instantaneous.

5.4 Mixed and mixing layer depths

The depth of the mixed layer is an important quantity in oceanographic studies and is a crucial depth when fine- and micro-structures are analyzed due the sensitivity of the turbulence parameterizations at this depth. Its definition can be cumbersome if potential density gradients are smoothed, hence the wide variety of algorithms to determine it.

A comparison between different methods proposed in the literature was made (not shown). We found an underestimation of h_ρ when this is inferred from gradient algorithms, whereas an overestimation of h_ρ is observed by applying the method described by Kara et al. (2000), in agreement with previous studies (Holte and Talley, 2009; Estrada-Allis et al., under review). To ensure the correct definition of h_ρ, we also validate it by observing the apparent h_ρ at each particular profile. After this analysis, the

σ_θ-based algorithm developed by Holte and Talley (2009) was finally chosen. In agreement with Chapter 4, this algorithm shows the best fit with the maximum gradient of the stratified layer given by N^2 (Figure 5.2b), and is also consistent with a threshold value of $\Delta\sigma_\theta = 0.03$ kg m^{-3} (de Boyer Montégut et al., 2004).

Besides the above definition of the mixed layer, the determination of the mixing layer depth is also relevant (Brainerd and Gregg, 1995). Sometimes, active mixing events extend h_ε deeper than h_ρ as shown in Figure 5.4b. When this occurs, the region between h_ρ and h_ε, i.e., the entrainment zone Δh, becomes positive and turbulent mixing may be large enough to overcome the restoring effects of the stratification in the pycnocline (Dewey and Moum, 1990; Inoue et al., 2010). Thus, nonzero Δh means that turbulent mixing processes, including diapycnal entrainment, can take place. It is hypothesized that this mixing layer could be the result of shear instabilities produced by internal waves that impinge on the interfacial layer (Moum et al., 1989; MacKinnon and Gregg, 2005) producing Kelvin-Helmholtz type instabilities (Strang and Fernando, 2001).

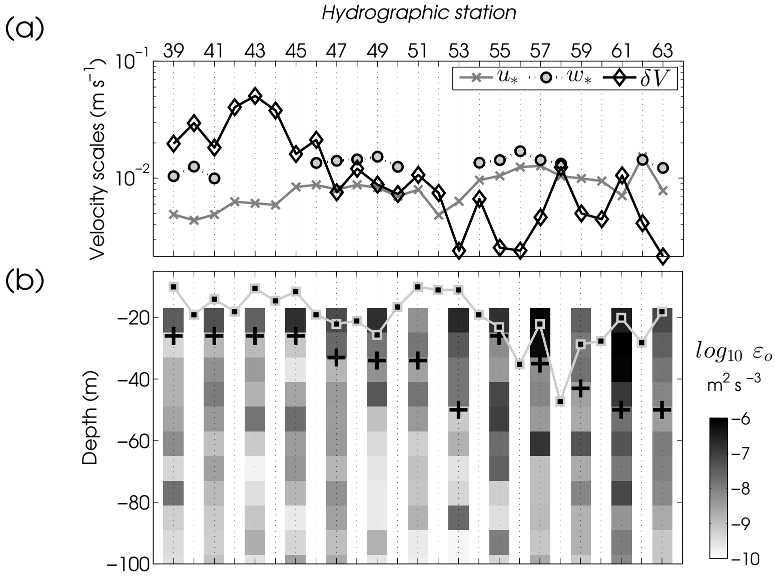

Figure 5.4: (a) Velocity scales of the three TKE-sources promoting the entrainment process, where u_* is the friction velocity, w_* is free convection and δV is the velocity jump across the mixed layer. (b) Vertical profiles of observed TKE-dissipation rates, ε_o, in logarithmic scale. Superimposed squares are mixed layer depths, h_ρ, and black crosses indicate the value of the mixing layer depths, h_ε. Odd-numbered stations are shown at the top.

As seen in Figure 5.4b, Δh is higher than zero at each microstructure station, even under weak wind conditions. It appears also to be independent of day/night-time conditions (Figures 5.3a, 5.3b and 5.3c). This is a striking result since it is seldom observed in nature. A plausible explanation may be related to the shallow depth of the mixed layer as a result of a low momentum transfer by relatively low Trade winds and also weak buoyancy flux. Thus, intermittent surface mixing events such as, for example, an instantaneous increase in the wind speed, can easily be extended below the shallow mixed layer leading to positive Δh.

5.5 Mixing at the entrainment zone

The entrainment zone can act as a pathway to lift turbulent water from the seasonal pycnocline to the less stratified surface layer connecting upper and interior ocean layers. The diapycnal velocity responsible for this upward transport is the entrainment rate and its parameterization is strictly necessary to close the one-dimensional turbulent kinetic energy budget system equations (Niiler and Kraus, 1977). Hence, the entrainment process can be analyzed through 1D bulk mixed layer models which mainly depend on three sources of TKE, as in the case of the upwelling filament of Chapter 4.

5.5.1 Sources of TKE for entrainment

To assess the contribution of the main sources of TKE, we compare velocity scales from the three main mixing forcings described in Chapter 1, namely: friction velocity, free-convection velocity of Deardorff and the generation of TKE by the squared vertical shear induced by horizontal currents, whose velocity scale is the velocity jump across the mixed layer. Note that the velocity jump is computed here through SADCP data[*]. Figure 5.4a shows that one of the main contributors to the TKE budget is the velocity jump, induced by the effect of vertical current shear at the entrainment zone. The contribution of the vertical shear is particularly enhanced at the northernmost stations. This result highlights the important role of δV to the total energy balance, which is often neglected in many bulk mixed layer models (Gaspar, 1988). However, the enhancement of the velocity jump at the northern eddy edge seems to be uncorrelated with wind-stress peaks. These high values of δV may be a consequence of active mixing acting over the shallow mixed layers of the hydrographic stations.

---

[*] Although numerous methods (from simple to optimal interpolation and empirical orthogonal functions) were implemented in order to solve the inconsistencies in some surface depths of LADCP profiles, the availability of well-resolved surface SADCP data were used at surface depths.

Figure 5.4a illustrates the interaction between these three sources of TKE in terms of their velocity scales. The increase of friction velocity during the last day of sampling (Figure 5.4a) is the result of wind-speed peaks. This u_* leads to a slight deepening of both h_ρ and h_ε, which is also consistent with an enhancement of TKE dissipation. As expected, w_* shows a similar pattern to the surface net heat and buoyancy fluxes, being positive only during unstable night conditions. It is worth noting how the magnitude of w_* was lower than δV, but higher than u_*. As will be shown, this will have an important effect on w_e values.

By contrast, at the southernmost stations, all TKE sources are comparable in magnitude suggesting that mechanical wind stirring, surface convective processes, and vertical current shear at the entrainment zone are essential for the modulation of h_ρ and h_ε within the eddy.

5.5.2 Entrainment rates, $w_e^{\Delta h}$

Previous studies have indicated a lack of consistency between different entrainment rate parameterizations (Anis and Moum, 1994; Nagai et al., 2005; Burchard et al., 2008; Estrada-Allis et al., under review). Underestimation of entrainment rates may affect the modulation of mixed layer deepening and the representation of sea surface temperatures in bulk mixed layer models. This is partly due to overestimation of parameterized TKE dissipation rates and also due the neglected influence of vertical shear at the entrainment zone (Estrada-Allis et al., under review).

In the study of Chapter 4, both observed ε_o and parameterized ε_p were compared. Results show an overestimation of the depth-integrated ε_p values, which leads to an underestimation of about one order of magnitude of the entrainment rates. Here, we analyze the entrainment phenomenon using the same w_e-parameterization derived from eq. (4.7), $w_e^{\Delta h}$. Based on this formulation, observed dissipation rates, current shear at the mixed layer, and diapycnal buoyancy fluxes at the interface are considered within a TKE 1D balance.

Notice that in eq. (4.7) a positive Δh is a necessary condition for entrainment. As depicted in Figure 5.5, $w_e^{\Delta h}$ tends to increase at the eddy boundaries located at stations 43 and 57, while it is reduced at the eddy core. On average, velocities of 3.3×10^{-6} m s^{-1}(0.28 m d^{-1}) were found at the eddy periphery, while a slight decrease in $w_e^{\Delta h}$ are found at the eddy center with 2.8×10^{-6} m s^{-1}(0.24 m d^{-1}). Additionally, ε_o averaged over the entrainment zone gives values about 0.4×10^{-7} m^2 s^{-3} at the eddy center, whereas 0.3×10^{-7} m^2 s^{-3} and 2.2×10^{-7} m^2 s^{-3} are found at the northern and southern eddy edges, respectively. As in the case of surface averaged ε_o, southern stations also exhibit high dissipation levels even at the base of the mixed layer.

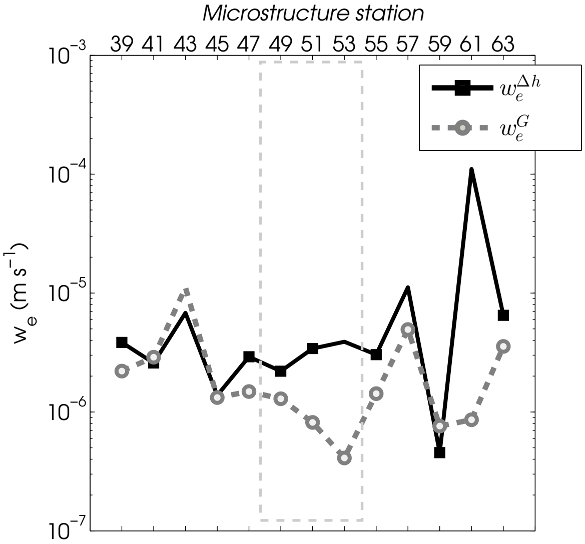

Figure 5.5: Turbulent diapycnal entrainment rates, w_e, computed from the classic parameterization of Gaspar (1988) through eq. (4.1), w_e^G, and from the new approach proposed by Estrada-Allis et al. (under review) through eq. (4.7), $w_e^{\Delta h}$. Dashed box highlights those stations located near the eddy center. Dashed lines show the trend of absolute w_e values, while only $w_e > 0$ are denoted by symbols.

Increased diapycnal velocities at the eddy periphery suggest that concentrations of nutrients may be enhanced at these locations, by permitting their exchange between the pycnocline and the euphotic layer. In fact, an increase in fluorescence was observed at the eddy rims (not shown).

Figure 5.5 shows that almost all hydrographic stations have positive $w_e^{\Delta h}$. This is indicative of vertical shear forcing at the base of the mixed layer and wind-stirring at the surface that can drive positive Δh even with non-favorable convection conditions during daytime. Because the primary effect of nonzero Δh is to overcome stratification effects, these atmospheric/shear conditions are maintained near stationary, and may lead to the deepening of the mixed layer over time.

Figure 5.5 also illustrates the comparison between the $w_e^{\Delta h}$ and w_e^G parameterizations. In Chapter 4 we discussed how w_e^G from Gaspar (1988) (eq. 4.1) differs from $w_e^{\Delta h}$ (eq. 4.7) in that the former does not take into account δV as a TKE source and includes parameterized rather than observed dissipation rates. In spite of these differences, the bias between both $w_e^{\Delta h}$ and w_e^G was lower than expected. This contrasts with the large bias found for the case of the Cape Ghir filament in Chapter 4. Nevertheless, underestimation of entrainment velocities from w_e^G with respect to $w_e^{\Delta h}$ is observed at the southernmost and center eddy stations. These biases are likely related to an overestimation of ε_p with respect to ε_o, which may be amplified at these locations as explained.

Our results point out that entrainment velocities can be due to a combined effect of wind-stirring, free convection and vertical shear at the entrainment zone. Simultaneously, since spatial variations of the pycnocline can result in enhancement of entrainment velocities (Dewey and Moum, 1990), the shape of isopycnals of an intrathermocline eddy would be implicated in the magnitude of w_e. The doming of the isopycnals induces a shallow mixed layer, reducing the depth of the stratified layer so that TKE sources can penetrate up to the pycnocline and erode it more effectively. As a result, a local enhancement of entrainment velocities is expected (Estrada-Allis et al., under review). This effect has been analyzed in Chapter 4 for the shoaling of the mixed layer due the influence of mesoscale upwelling filaments. However, in this study, w_e velocities show the tendency to decrease at the eddy core (Figure 5.5), where h_ρ shallows. The reason for this discrepancy may be related to the shape of the isopycnals of the intrathermocline eddy. Our results show that the mixed layer deepens at the eddy periphery while it shallows at the eddy center. In contrast, the mixing layer shows a tendency to deepen (shoal) at the eddy core (periphery). Entrainment velocities follow the tendency of the mixing layer depth rather than those corresponding to the mixed layer depth. Notice that in the filament case discussed in Chapter 4, both h_ρ and h_ε are shallow at the front, and the Δh zone was on average smaller than the Δh for this intrathermocline eddy. Furthermore, the decrease of entrainment rates at the eddy core may also be accomplished by the absence of favorable convective-conditions, thus preventing the growth of TKE sources.

5.6 Deep enhanced diapycnal mixing

As already mentioned, theoretical studies have indicated that anticyclonic eddies may trap near inertial waves at their base (e.g., Kunze, 1985; Cuypers et al., 2012; Stanley and Saenko, 2014). It has been suggested that this trapping may represent an extra source of diapycnal mixing at deeper levels of the water column where the base of the eddy is located. However to our knowledge there are still a lack of field observations of such a process. Here, thanks to our TurboMAP section crossing the eddy, we have been able to provide the first evidence for such deep diapycnal mixing.
Figure 5.6 shows the distribution of the kinetic energy dissipation rate, along the transect crossing the eddy as obtained with the microstructure turbulence profiler. There is a noticeable enhancement of ε_o in the deepest layers of microstructure sampling at stations 51 and 53, located within the eddy core. The values are the highest of our sampled section and comparable to those observed in the surface mixing layer.

This deep local maximum in the kinetic energy dissipation rate coincides with a region of large vertical shear extending to just below the base of the eddy core until the deepest LADCP sampled level at 900 m. Martínez-Marrero et al. (in prep.) has attributed this strong shear layer to the trapping of inertial waves at the eddy base. This trapping was observed in all transects sampled during the 20 day cruise, thus being a recurrent phenomenon. Consequently, these results suggest that the enhancement of subsurface turbulent mixing might be due to breaking near-inertial internal waves, previously trapped by the anticyclonic eddy (Martínez-Marrero et al., in prep.). It should be noted that since the LADCP-derived vertical shears were more intense than those from the SADCP, the first is included in the analysis of Figure 5.6. Low Sh^2 intensity from the SADCP might be due to the spatial averaging that acts as a filter of high frequency internal waves. Instead, the LADCP gives a more instantaneous current profile which in turn can reach deeper levels of the water column ($\approx$ 900 m). On the contrary, the SADCP values were more consistent than the LADCP profiles at the surface layers.

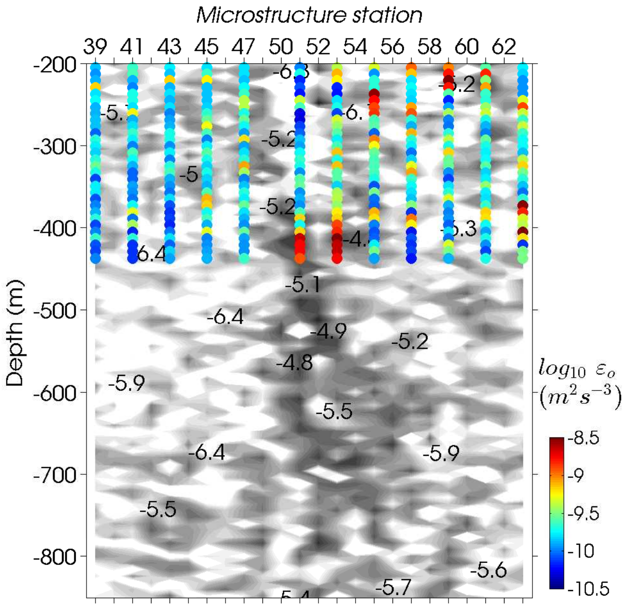

Figure 5.6: Subsurface vertical meridional section of squared vertical current shear, Sh^2, in logarithmic scale computed from LADCP profiles. Superimposed color circles are values of ε_o for each microstructure station also in logarithmic scale. Note the absence of station 49.

5.7 Diapycnal diffusivity coefficients

Diapycnal mixing in stratified flows are modulated by the vertical diffusivity coefficient (K_v). Therefore this is an indicator of turbulent mixing. The observed K_v (K_ε, hereafter) given by the classic expression of Osborn (1980):

$$K_\varepsilon = \Gamma \frac{\varepsilon_o}{N^2} \tag{5.1}$$

where it has been assumed that diffusivities of buoyancy and heat are of the same order. The mixing efficiency Γ is the ratio between the vertical buoyancy flux and ε_o, here taken to be a constant of 0.2.

5.7.1 Surface K_ε

As depicted in Figure 5.7, at surface eddy layers, diapycnal diffusivity decreases at the eddy core (station 51), with a value of $K_\varepsilon = 0.17{\times}10^{-5}$ m^{2}s^{-1}, while it is enhanced at the northern and southern flanks of the eddy. Below this first layer, within the entrainment zone, K_ε exhibits a similar behavior as at the surface layers (Figure 5.7), increasing with respect to surface layers of the eddy core station 51, $K_\varepsilon = 0.96 \times 10^{-5}$ $\mathrm{m^2s^{-1}}$.

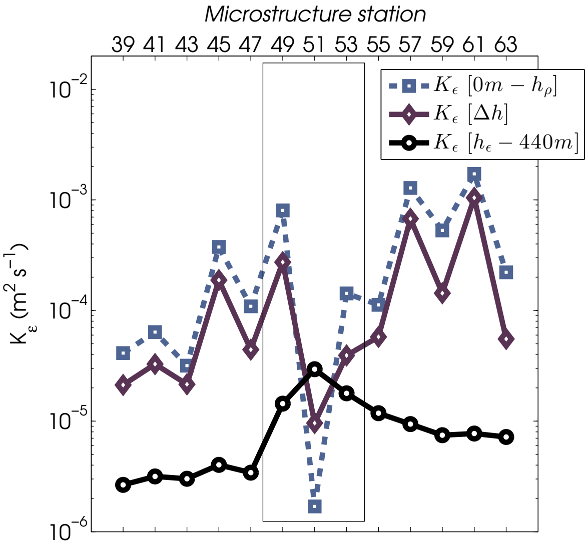

Figure 5.7: Depth averaged K_ε ($\mathrm{m^2\ s^{-1}}$) in logarithmic scale, where dashed dark gray lines are K_ε averaged from surface to h_ρ; light gray from h_ρ to h_ε, i.e., Δh, and black from h_ε to 500 m. Dashed box indicates stations located within the eddy core.

Thus, diapycnal diffusivity is largely depth dependent and should not be constant in numerical models even in the surface layers, especially in strongly eddying flows like the CEC.

5.7.2 Deep K_ε

As already mentioned, a clear enhancement of the dissipation rate of turbulent kinetic energy was observed at the base (400 m) of the eddy core indicating diapycnal mixing in this region. This is also reflected in the deep average diffusivity coefficient values (Figure 5.7), where $K_\varepsilon = 2.94 \times 10^{-5}$ $\mathrm{m^2s^{-1}}$ at station 51, and even lower values at the northern and southern eddy periphery. These enhancements at the eddy core are in accordance with an increase of the vertical shear.

In addition, diapycnal diffusivity coefficients obtained in this study can serve as indicators of vertical nutrient transport following the *Fick's Law* (Csanady, 1973) for future physical-biological study purposes.

5.7.3 K_ε versus K_{kpp}

In order to preserve numerical consistency for many numerical and theoretical models, K_v is set artificially to a uniform value. These K_v often take relatively low values in most ocean general circulation models with $K_v[\mathcal{O}(10^{-5})\ \mathrm{m}^2\ \mathrm{s}^{-1}]$, and hence independent of the physical flow conditions (Stanley and Saenko, 2014). However, there is field evidence that suggest that diapycnal diffusivity is far from being constant, particularly in the abyssal ocean associated with rough topography and strongly eddying regions (e.g., Naveira Garabato et al., 2004; Sheen et al., 2014; Stanley and Saenko, 2014). If mesoscale fields are energetic pathways to deep diapycnal mixing, many climatological ocean models used for predictions of climate change scenarios may be giving inaccurate results when uniform abyssal diapycnal mixing coefficients are considered in numerical setups. To deal with this, many ocean models implement high-order closure schemes to parameterize diapycnal mixing, such as KPP (Large et al., 1994), as we will see in the next Chapter 6. According to KPP, interior diapycnal coefficients (hereinafter K_{kpp}), can be understood as the sum of three main contributions: shear instability mixing, internal wave mixing and double diffusive processes which, in turn, includes salt-fingering and diffusive convection.

Next we derive and compare K_{kpp} and K_ε values along the transect crossing the eddy in order to quantify the distribution of diffusivity through those coefficients. It must be noted however that discrepancy is found when K_{kpp} are compared against the parameterized forms of K_v. For instance, Zaron and Moum (2009) found that KPP overestimates the diffusivity by a factor of 4 between the surface mixed layer and the Equatorial Undercurrent. Figure 5.8 indicate that K_{kpp} is overestimated respect to K_ε by one to two orders of magnitude in the interior ocean. Mean values at the base of the eddy core were about 4.5×10^{-3} m^2 s^{-1} for K_{kpp}. This contrast to the 2.05×10^{-5} m^2 s^{-1} derived from K_ε (Figure 5.8b). The differences at the eddy periphery were also noticeable, with bias of the order 10^{-4} m^2 s^{-1} and 10^{-3} m^2 s^{-1} for the northern and southern eddy edges, respectively (Figures 5.8a and 5.8c). Despite these differences, both diffusivity profiles show an enhancement of diapycnal diffusivity at the base of the eddy core as was also the case for ε_o.

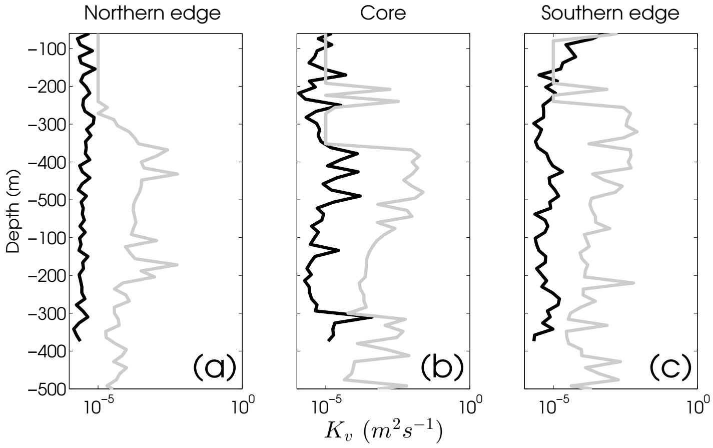

Figure 5.8: Diapycnal diffusivities K_v (m^2 s^{-1}), derived from Osborn (1980), K_ε (black profiles) and from Large et al. (1994) KPP parameterization, K_{kpp} (gray profiles). Note that K_{kpp} is computed only for the interior ocean, therefore constant values of $K_{kpp} = 10^{-5}$ m^2 s^{-1} in the upper ocean layer should be considered insignificant. K_v from both parameterizations was averaged over three groups of stations: (a) northernmost stations, (b) eddy-center stations and (c) southernmost stations.

However, it should be noted that as K_{kpp} is a fine-scale based diffusivity and K_ε is based on micro-scales, a direct comparison should not be so simple (Zaron and Moum, 2009). Because of the strong dependence of K_{kpp} with Ri_g (Table 4.1), Zaron and Moum (2009) compared both K_ε and K_{kpp} during a long period of time (20 days), for which previous studies have ensured the occurrence of low Ri_g. In our case, long time series are not possible. However, we can examine if low Ri_g values are feasible from our measurements. Linear stability theory for stratified sheared flows (e.g., Miles, 1961) predicts that a necessary (but not sufficient) condition for shear instability is when Ri_g drops below a critical threshold of $Ri_c = 0.25$ (e.g., Kunze et al., 1990). When Ri_g approaches Ri_c, the shear becomes unstable and mixing instabilities such as Kelvin-Helmholtz (K-H) instabilities at the interface (e.g., Strang and Fernando, 2001; Muench et al., 2002) can occur. Consequently, at sub-critical Ri_g the released energy will be used to generate local patches of turbulent mixing. Indeed, sub-critical Ri_g are rarely observed in the ocean due the lack of vertical resolution of velocity measurements and because of the inherent intermittent nature of turbulence. In Figure 5.9 we show the

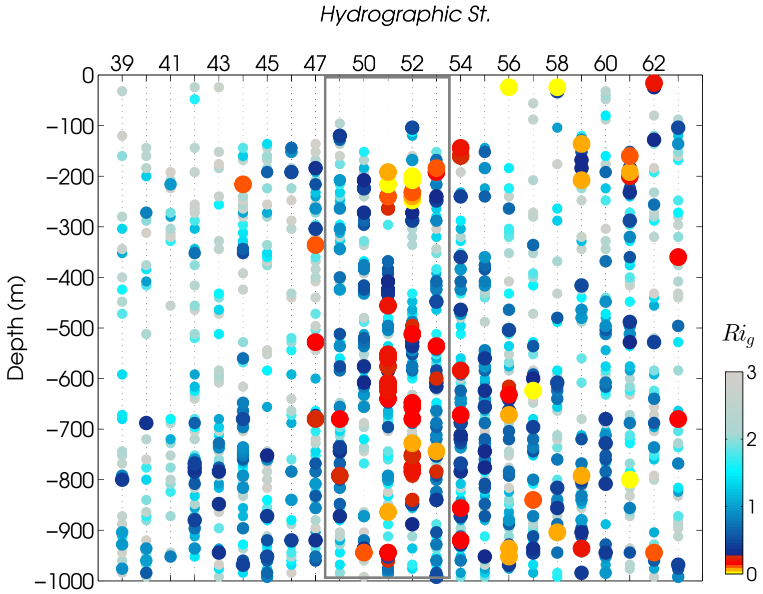

Figure 5.9: Spatial gradient Richardson number, Ri_g, for each hydrographic station, where large yellow-red circles denote near-critical Ri_c. Smaller circles show, in decreasing order, values of Ri_g from 0.5 to 3. Values above 3 are not shown. Gray rectangle highlights stations sampled at the eddy core.

distribution of Ri_g along the transect crossing the eddy. Note that minimum values of Ri_g ranging from 0 to 1 are reached just below the base of the eddy core located between stations 47 and 54, from 400 m to the maximum sampled depth. Notice also that inside this portion of the water column there is a high density of patching regions where $Ri_c < 0.25$, and hence a high density of patching regions where turbulent mixing may develop. These low Ri_g values are consistent with our previous observations on the enhancement of diapycnal shear and the dissipation rate of turbulent kinetic energy below the base of the eddy. Therefore, all of the mixing related parameters indicate that there is an enhancement of diapycnal mixing at the base of the eddy which is related to the strong vertical shear due the trapping of near inertial waves, as observed by Martínez-Marrero et al. (in prep.).

N^2 from CTD data were averaged at the same 8 m depth cells used for vertical shear from the LADCP and SADCP profiles. Although u and v absolute velocity components are measured at the same time as the CTD hydrographic profiles, we have filtered Ri_g in order to reduce possible nominal errors from u and v. As a consequence, we follow

Muench et al. (2002) by considering that $(\overline{N^2})^{1/2} < 0.7$ cph must be removed to avoid possible inversions.

5.8 Concluding remarks

We have characterized an intrathermocline anticyclonic eddy in terms of its main diapycnal mixing processes. These mixing process acting over the eddy can be well explained across three depth layers (Figure 5.7), thereby revealing the depth variability of the mixing states within an anticyclonic eddy. The main conclusion of this chapter may be summarized as:

- Surface diapycnal mixing within the anticyclonic eddy is mainly driven by the combined effect of nighttime convection, vertical current shear, and wind stirring, and this should be integrated into entrainment parameterizations.
- Mixing layer depths were deeper than mixed layers depth over the whole sampled transect, indicating active mixing associated with the eddy which might favor the redistribution of tracers into the photic layer by entrainment. Hence the importance in considered both mixed and mixing layer depths in bulk mixed layer models. In turn, the entrainment rates are related to a mixing rather than a mixed layer depth, and this is likely conditioned by the shape of the isopycnals within the intrathermocline eddy.
- At the surface and interfacial layers of the eddy edges, an enhancement of diapycnal mixing and high TKE-dissipation rates agrees with a slight increase of entrainment velocities. This suggests that turbulent diapycnal mixing is linked with the dynamics of mesoscale structures that interact with the implicated TKE sources.
- The behavior of diapycnal mixing through K_ε is opposite in the deeper layers of the eddy, being more intense at the eddy core. The pattern is also observed when comparing with a KPP-based diffusivity coefficient K_{kpp}, although these were two orders of magnitude higher than K_ε. This enhancement is consistent with an increase in vertical shear and dissipation rates, as well as near-critical Ri_g, suggesting that this may be the result of near-inertial waves that are trapped inside anticyclonic eddies of the Canary Eddy Corridor.

6

Vertical Velocities in Mesoscale Eddies: A Numerical Experiment[*]

6.1 Introduction

As indicated in Chapter 5, mesoscale eddies represent an "oases" of marine life that populates the whole ocean. Knowledge of their dynamics, vertical mixing, horizontal advection and vertical eddy fluxes is constantly growing, driven in partly by their impact on biogeochemical cycles and potential role in the modulation of the global climate system. However, the study of mesoscale and submesoscale structures in a rotating framework often represents a challenge due the short spatio-temporal scales involved in their dynamics. In particular, the study of vertical mixing and vertical velocity inside eddies must be conducted synoptically in order to maintain consistence in the results. In this regard, numerical models have proved to be useful tools on which to set the bases for key issues to be addressed in subsequent observational studies. Contrary to the classical view, anticyclones are not oligotrophic areas. Recent studies have reported clear enhancements in primary production within these structures (e.g., McGillicuddy et al., 2007; Ledwell et al., 2008; Gaube et al., 2015). This is also the case of the observed eddy of Chapter 5 for example. The generation of vertical velocity inside mesoscale structures is related to a variety of process such as frontogenesis, eddy-wind interaction and eddy-pumping by linear and nonlinear Ekman effects (e.g., Martin and Richards, 2001; McGillicuddy et al., 2007; Capet et al., 2008b; Mahadevan et al., 2008; Calil and Richards, 2010). There is still some controversy about the physical-biological impact of these processes in the vertical velocity (w) field of mesoscale and submesoscale features. Some studies have pointed out that eddy-wind interactions have a dominant influence on the vertical fluxes of nutrients in the context of eddy Ekman pumping theory (Martin and Richards, 2001; Gaube et al., 2015). Others such as McGillicuddy et al. (2007) propose that such interaction leads to upwelling at the centers of anticyclones, increasing the primary production within these regions. The latter is discussed by Mahadevan et al. (2008), who suggest that eddy-wind interaction takes place at the eddy periphery, recirculating towards the eddy center through ageostrophic secondary cells (Nagai et al., 2006; Capet et al., 2008b). In addition, modeling (Viúdez and Dritschel, 2003; Koszalka et al., 2009; Cardona and Bracco, 2012) and observational studies (Chavanne et al., 2010; Nardelli, 2013) suggest that vortex Rossby waves (VRWs) may also be contributors to the vertical velocity patterns seen inside mesoscale vortices. VRWs are disturbances of potential vorticity (PV) with a slow outward propagation from the vortex core, while they are being sheared by the differential of the vortex angular velocity. With a time scale comparable to the advective scale (Graves et al., 2006) (here of the order of $2\pi LV^{-1} \approx 9.09$ days), and frequencies lower than the planetary vorticity f, VRWs can feel the earth rotation thus being largely geostrophically balanced (Montgomery and Kallenbach, 1997; McWilliams et al., 2003).

---

[*] Estrada-Allis, S., Mason, E., Barceló-Llull, B., Pallàs-Sanz, E., Sangrà, P., and Rodríguez-Santana, Á. Vertical Velocities Dynamics in Anticyclonic Eddies: A Numerical Experiment. *In preparation to be submitted to an international refereed journal.*

Only a few studies have emphasized the effects of mixing on vertical motions due to high order derivatives, nonlinear effects, and the large dependence on mixing parameterizations that must be included in the general formulations. The observational study of Pallàs-Sanz et al. (2010) includes a parameterization of the vertical mixing in the Quasi-Geostrophic (QG) omega equation, and shows that the effect of mixing is constrained in the upper 100 m, leading to an intensification of w. This finding is consistent with other observational (Johnston et al., 2011) and modeling studies (Giordani et al., 2006; Nagai et al., 2006; Koszalka et al., 2010). Furthermore, Ponte et al. (2013) suggest that surface vertical mixing within the mixed layer tends to destroy thermal wind balance by smoothing the vertical profiles of the total horizontal motions. Subsequently, thermal wind balance is restored by the development of vertical circulation. However, their formulation is only valid at small Rossby numbers and by using a constant value for the diapycnal diffusivity coefficient (see Chapter 5).

The vertical velocity within anticyclonic eddies is itself a complex structure that can depend on several factors for its source (e.g., Viúdez and Dritschel, 2003; Koszalka et al., 2009; Calil and Richards, 2010; Cardona and Bracco, 2012; Nardelli, 2013; Ponte et al., 2013). Hence, the mechanisms that explain the structure of the vertical velocity in anticyclonic eddies are not well understood and still need to be clarified. Following on from Chapter 5, this study focus on analyzing the vertical structure in terms of vertical velocities inside anticyclonic eddies and the influence of diapycnal mixing on the w-field. The vortices analyzed here are generated by flow perturbation at the Canary Islands (Arístegui et al., 1994; Sangrà et al., 2005; Mason et al., 2011) within a high resolution numerical model simulation (ROMS) (Chapter 3). The model configuration is from the thesis of Mason, E. (Mason, 2009). The high horizontal resolution of ~ 1 km allows us to study mesoscale and associated submesoscale structures (Capet et al., 2008b; Cardona and Bracco, 2012) inside anticyclonic eddies.

This chapter is organized as follows. In section 6.2 we describe the vertical velocity field associated with a pair of anticyclonic eddies generated by the Canary Islands as obtained from numerical simulations. Then in section 6.3 the forcings of the w-field are examined in terms of the instantaneous divergence of the flow. In the same section 6.3 the relevance of nonlinear Ekman effects and the presence of VRWs as forcing mechanisms are also discussed. The impact of surface diapycnal mixing is examined in section 6.4. In section 6.5 we focus our attention on a subsurface dipolar vertical velocity pattern, ubiquitous for most of the simulated vortices, where Lagrangian numerical experiments are carried out to elucidate changes in axisymmetry of the vortices. A comparison of the simulated sub-surface w field with those obtained using the omega equation is done in section 6.6. Finally, a discussion and principal conclusions are presented in section 6.7.

6.2 Model outputs and selected eddies

A high resolution model is used in order to examine the role of the vertical velocity field inside mesoscale anticyclonic eddies in the lee of the Canary Islands. The model set-up (L2) has been successfully validated (Mason et al., 2010; 2011) and is a nested solution from a 7.5 km resolution parent model for the whole Canary Basin, which was briefly described in Chapter 3. Detailed information as well as an extensive validation of this solution can be found in Mason (2009). The L2 numerical configuration has a spatial horizontal resolution of $\sim$ 1 km, with 60 sigma layers in the vertical. The numerical model domain, which is centered on the Canary Archipelago, is shown in 6.1. The model solution used here corresponds to three simulated years with daily averaged outputs of the 3D velocity field, salinity, temperature and turbulent diapycnal coefficients derived from the KPP parameterization (Large et al., 1994). The vertical velocity as obtained each time step from the model output will be referred as w_{ROMS}. As depicted in Figure 6.1a the model is able to reproduce the rich mesoscale variability observed south of the Canary Islands and represented by anticyclonic and cyclonic mesoscale island-induced eddies. Notice also that the fine resolution reveals the submesoscale variability associated with these structures, such as submesoscale filaments. The eddy field is characterized by moderately high Rossby numbers ($Ro = \zeta_r/f$), with maxima up to $|Ro| \sim 0.7$, indicating that ageostrophy and thus vertical velocities may be important. As shown in Figure 6.1b the signal of the corresponding vertical velocity field is complex and is associated with mesoscale eddies and related submesoscale filaments.

For a description of the w_{ROMS} field inside an anticyclonic eddy we have selected the anticyclone annotated $A2$ in Figure 6.1a. This eddy was spun off from Tenerife and, as we will see, experienced changes in its orbital shape. For further analysis, we will also compare $A2$ with another anticyclonic vortex, newly formed in the passage between Tenerife and Gran Canaria islands ($A1$ in Figure 6.1a). Our observations of the $A2$ simulated eddy can be extrapolated to the rest of the anticyclonic eddies that populate the model domain, whose characteristic relative vorticity and vertical velocity fields compare well (Figures 6.1a and b). The $A2$ vortex has relatively high Ro numbers with strong negative ζ_r at the eddy core (Ro = -0.7), wrapped by a positive ζ_r ring, suggesting that ageostrophic velocities dominate in the eddy interior, while being controlled

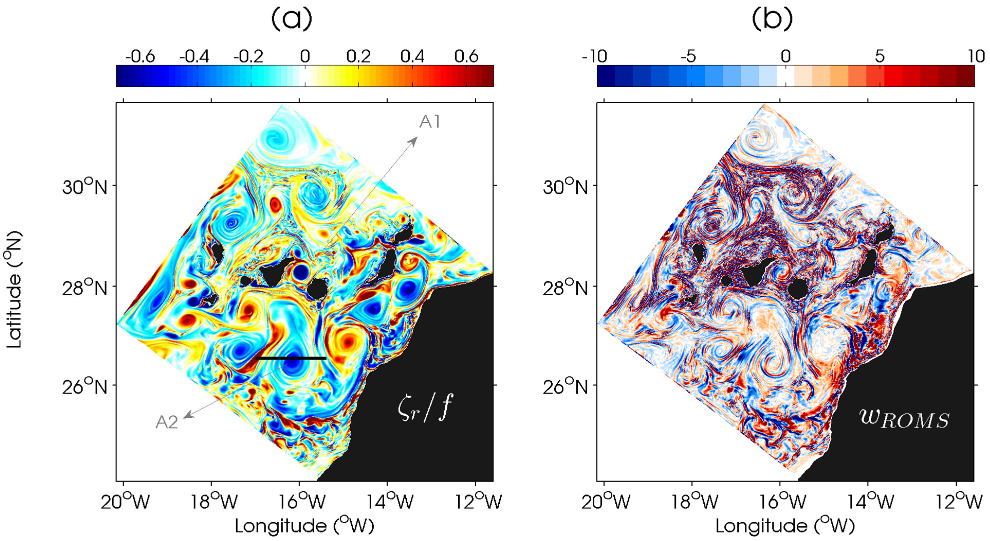

Figure 6.1: Horizontal fields of the simulated day 29 of month 08, of (a) vertical component of relative vorticity normalized by the Coriolis parameter, $Ro = \zeta_r/f$, at 1 m depth, and (b) surface vertical velocity, w (m d^{-1}), at 10 m depth. The arrows marked the two vortex analyzed in this study, $A1$ and $A2$. Black horizontal line indicates zonal sections.

by geostrophic dynamics at the edges.

The vertical structure of the $A2$ vortex is shown in Figure 6.2. As expected from a typical anticyclonic eddy, the isopycnals deepen at the eddy center until ≈ 800 m where they flatten, indicating the base of the eddy. At the eddy periphery the isopycnals outcrop at the surface. This eddy is elliptical with a mean radii of 35.56 ± 7.10 km and experiences changes in its aspect ratio whilst it propagates westward following the CEC (Sangrà et al., 2009). The deepening of the isopycnals at the center influences the depth of the mixed layer (Chapter 5), here computed by the KPP parameterization (Large et al., 1994) which usually refers to the upper boundary layer (h_{ubl}, continuous line in Figure 6.2). This would result in a strong subsurface stratified fluid delimited by the maximum vertical gradient of N^2 (dashed line in Figure 6.2) as suggested in Chapter 4. The simulated h_{ubl} mainly changes seasonally with mean values of $h_{ubl} =$ 65.22 m ±29.88. In particular, the $A2$ vortex has a mean $h_{ubl} = 35m$ at the edges and deepens in the core with mean values of $h_{ubl} = 80m$.

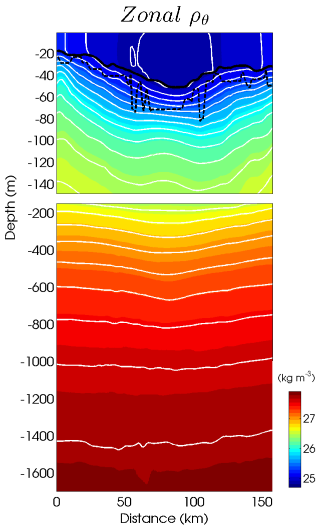

Figure 6.2: Zonal vertical section of potential density, ρ_θ (kg m^{-3}), from -15.4 to -17 °W, at a fixed latitude of 26.55 °N, denoted in Figure 6.1a as a black line, for $A2$ vortex (day 29 of month 8). White contours are isopycnals plotted every 0.15 kg m^{-3}. Continuous black line is h_{ubl}. Dashed line is the surface maximum gradient of N^2.

6.3 Forcing mechanisms of the w-field

6.3.1 Decomposition of the vertical velocity field

As indicated above, the simulated w-field is complex and its detailed description as well as its forcing mechanisms need to be investigated. In this regard, and motivated by the study of Koszalka et al. (2009), we have implemented the same approach suggested by Vallis (2006) and implemented in Koszalka et al. (2009) that is based on the instantaneous divergence of the flux to examine the different forcing mechanisms that control the total w-field inside anticyclonic eddies. The main difference in our model in comparison with the idealized configuration of Koszalka et al. (2009) lies in the model forcing: variable wind conditions and the implementation of surface flux climatologies. The presence of rough bathymetry and land obstacles to the flow (i.e., the Canary Islands and the African coast) also contribute to a more realistic regional ocean.

Following Vallis (2006) and Koszalka et al. (2009), the w_{ROMS} field is examined through its contributions as follows,

$$
\begin{aligned}
w(x,y,z) = \; & D\eta_r/Dt + \int_z^{\eta_r} [\\
& - \underbrace{[\alpha_1(D\zeta_r^1/Dt) - \alpha_2(D\zeta_r^2/Dt)]}_{\textbf{Ageo}} \\
& - \underbrace{[\alpha_1(\partial_x u\zeta_r^1) - \alpha_2(\partial_y v\zeta_r^2)]}_{\textbf{Str}} \\
& - \underbrace{[\alpha_1(\partial_x w\partial_z v) + \alpha_2(\partial_y w\partial_z u)]}_{\textbf{Tilt}} \\
& + \underbrace{[\alpha_2\rho_o^{-1}(-\partial^2_{yz}\tau^x) + \alpha_1\rho_o^{-1}(\partial^2_{xz}\tau^y)]}_{\textbf{Wstr}} \\
& + \underbrace{[A_H\alpha_1(\partial^4_{x^4}\zeta_r^1 + \partial^4_{y^4}\zeta_r^1) + A_H\alpha_2(\partial^4_{x^4}\zeta_r^2 + \partial^4_{y^4}\zeta_r^2)]}_{\textbf{Hmix}} \\
& + \underbrace{[\alpha_1\partial^2_{xz}(Kv\partial_z v) - \alpha_2\partial^2_{yz}(Kv\partial_z u)]}_{\textbf{Vmix}}]dz
\end{aligned}
\tag{6.1}
$$

where D/Dt denotes the material derivative, A_H is the constant biharmonic horizontal diffusion with a value of 10^6 m^{4}s^{-1}. The diapycnal diffusivity coefficient is given by the KPP parameterization of Large et al. (1994). All terms are modulated by the inverse of the absolute vorticity $1/(\zeta_r + f)$, where $\zeta_r^1 = \partial_y u$, $\zeta_r^2 = \partial_x v$, $\alpha_1 = (f + \zeta_r^1)^{-1}$ and $\alpha_2 = (f + \zeta_r^2)^{-1}$.

The first right hand side (r.h.s) term formulates the free surface elevation of the sea surface (η_r) variability. The second r.h.s. is the ageostrophic term (***Ageo***) and represents instantaneous vorticity changes and advection of ζ_r. The third r.h.s is the stretching term (***Str***) of w inside the vortex. Vertical velocities related to the effect of the wind are included in the wind stress (***Wstr***) term and w due the tilting of the vortex is described by ***Tilt***. Finally, the last two r.h.s terms account for the influence of mixing on the w field and are separated into two components, namely horizontal mixing (***Hmix***) and vertical or diapycnal mixing (***Vmix***).

The diagnostic from the flow divergence through eq. (6.1) permits the inclusion of sources such as the mixing terms, that can be treated more fully in modeling configurations where all fields are provided by the model outputs. Other forcing terms, such as the non-zero vertical advection, stretching and tilting terms in eq. (6.1) are new with respect to the QG approximation (Koszalka et al., 2009). However, it is important to note that QG can be useful to also explore the physics behind w forcing, and this will be addressed later.

In order to conduct a more detailed examination of the w-field and related forcing mechanisms of the $A2$ vortex we have selected three depths: 20, 300 and 1000 m. Note that although the analyses are focused on the $A2$ eddy, similar results were obtained for other anticyclonic eddies with similar Ro and divergence fields, using this model configuration.

i. Surface depth: 20 m. At the surface layers, the w_{ROMS} field reveals a complex submesoscale wave-like pattern (Figure 6.3a), in which cells of downwelling and upwelling alternate around the vortex core, being more intense at the eddy periphery, achieving w up to 31 m d^{-1}. This can also be observed over the whole domain in Figure 6.1b, and is in good agreement with the suggestion that the most intense vertical transport is associated with fronts and at the edges of mesoscale eddies (Capet et al., 2008b; Mahadevan et al., 2008).

The decomposition of w_{ROMS} by eq. (6.1) also shows that the ***Ageo*** term exerts a major control on the vertical velocity at the surface, along with ***Str*** (Figures 6.3b and c). The ***Vmix*** forcing (Figure 6.3g) has a secondary role in the magnitude of the vertical velocity, although its wave-like pattern seems to match with the spiral structure of the total w_{ROMS} pattern. The contributions of the vertical mixing effects are analyzed in the next section. The ***Tilt*** term shows a similar wave-like shape with alternating cells of vertical velocity (Figure 6.3d). Following Koszalka et al. (2009), the ***Tilt*** and ***Vmix*** terms are related to wave movement, being less intense than ***Ageo*** or ***Str*** by an order of magnitude. In our case, all the forcing terms at the surface levels have the same order of magnitude with slight variations. The main differences between these forcing terms are related to the distribution of the vertical velocity inside the vortex.

The ***Wstr*** forcing also has important contributions, although it does not explain the wave-like pattern of w_{ROMS} (Figure 6.3e). Finally, less influence is attributed to the ***Hmix*** forcing (Figure 6.3f) which shows w magnitudes five times less than the overall w_{ROMS}. However, its spiral like wave pattern resembles the w_{ROMS} structure. Vertical velocities due to η_r were on average an order of magnitude less than w_{ROMS}.

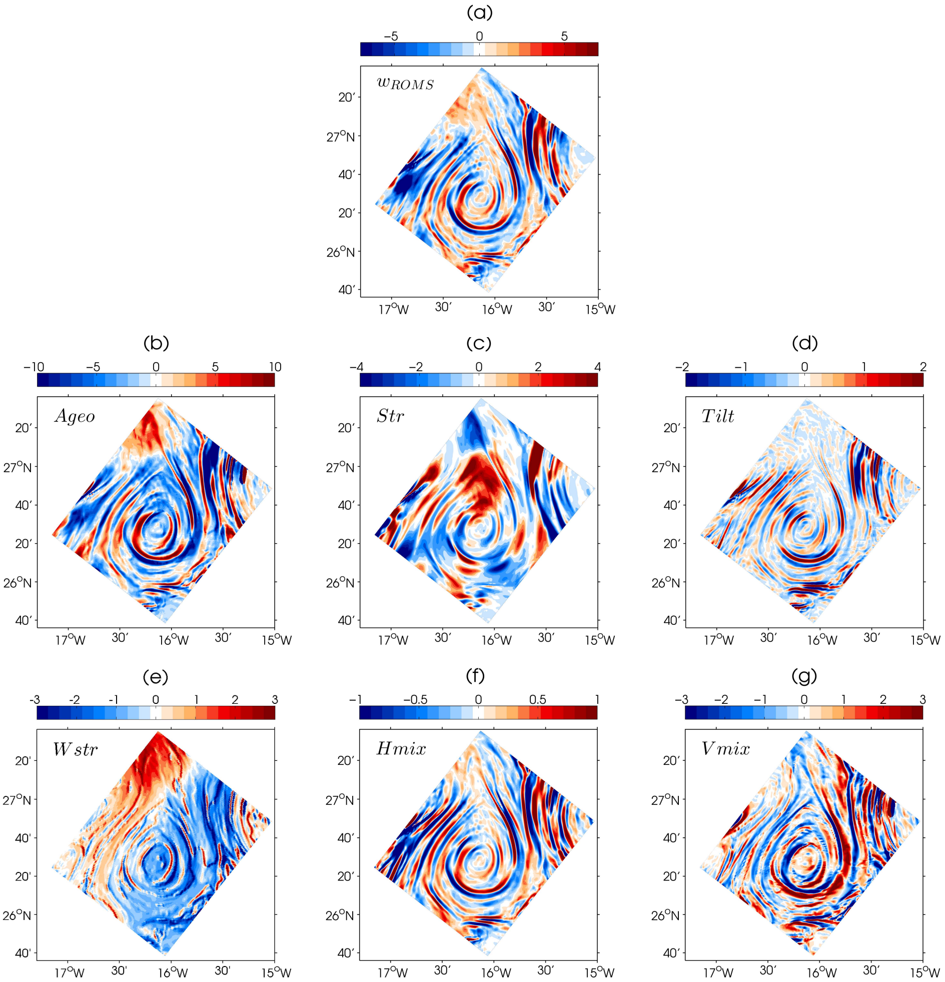

Figure 6.3: Horizontal fields, at 20 m depth, corresponding to each forcing term of the overall vertical velocity, w_{ROMS}. (a) w_{ROMS}, (b) Ageostrophic term, ***Ageo***, (c) Stretching term, ***Str***, (c) Tilting term, ***Tilt***, (d) Wind stress term, ***Wstr***, (e) Horizontal mixing term, ***Hmix***, and (f) Vertical mixing term, ***Vmix***. Note changes in the scale of color-bar. The simulated date corresponds to the day 29 of month 08.

ii. Intermediate depth: 300 m. The choice of this depth was motivated by the appearance of an isolated dipole of vertical velocity (Figure 6.4) that is intensified at intermediate depths below the mixed layer. The dipole consists of two cells of upwelling-downwelling vertical velocities located at the eddy core extending vertically down to $\approx$ 800 m (see Figures 6.11b and c), which is near the base of the anticyclonic vortex. The magnitude of w_{ROMS} at intermediate depths reaches maximum values of 85 m d^{-1}, being largely linked to the presence of the w-dipole. A subsequent analysis of this dipolar structure is examined in more detail in section 6.5.

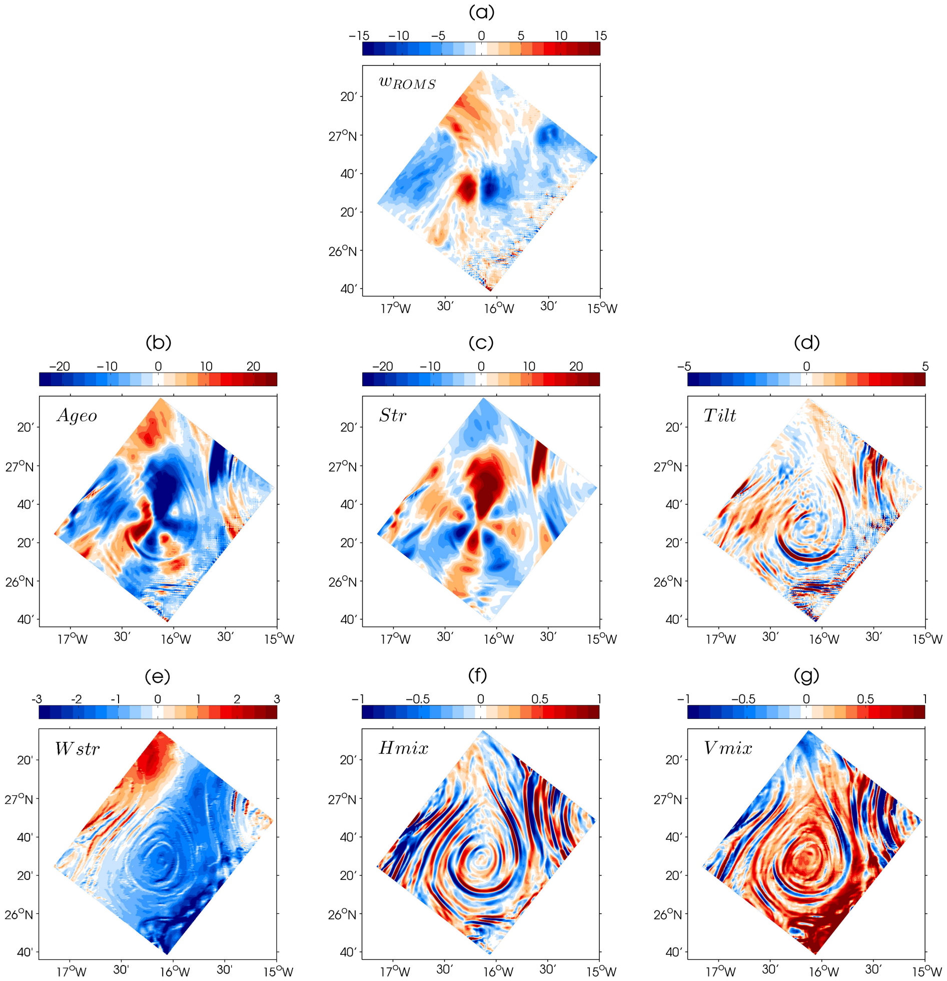
(a)
−15 −10 −5 0 5 10 15
w_{ROMS}
(b)
−20 −10 0 10 20
Ageo
(c)
−20 −10 0 10 20
Str
(d)
−5 0 5
Tilt
(e)
-3 -2 -1 0 1 2 3
Wstr
(f)
−1 −0.5 0 0.5 1
Hmix
(g)
−1 −0.5 0 0.5 1
Vmix
20′
27°N
40′
20′
26°N
40′
17°W
30′
16°W
30′
15°W

Figure 6.4: Same than Figure 6.3 but at 300 m depth.

The decomposition of w_{ROMS} suggests again that the ageostrophic and stretching terms are the most intense forcing mechanisms (Figures 6.4b and c). Both forcing terms exhibit shapes of an azimuthal wave of wavenumber of order 4, but out of phase, thus largely cancelling each other out as also observed by Koszalka et al. (2009). In their model, they found that a cancellation between ***Ageo*** and ***Str*** allows for a complete dominance of the tilting term over w_{ROMS}. Despite the fact that in this study we also observe a cancellation between these terms, the overall pattern and magnitude of w_{ROMS} can not be solely explained by the ***Tilt*** term (Figure 6.4d). Certainly, when the ***Ageo*** and ***Str*** terms do not cancel each other, the dipole structure arises, suggesting that the imbalances between both contributions act as forcing mechanisms to maintain the dipolar structure of the vertical velocity below the mixed layer. Moreover, the azimuthal wavenumber four of the ageostrophic and stretching terms may be related to the presence of VRWs, where the spiral pattern of w_{ROMS} reveals their outward propagation (Graves et al., 2006; Koszalka et al., 2009; Chavanne et al., 2010). The presence of these waves is examined below.

iii. Deep depth: 1000 m. From the base of the $A2$ vortex at 800 m down to 3000 m depth (near the ocean bottom $\approx$ 3500 m), the vertical velocity field has no clear pattern (Figure 6.5a). Simulated patches of w are concentrated in different regions and can reach w up to 162 m d^{-1} in some regions. Both the ***Ageo*** and ***Str*** forcing terms try to cancel each other out, as in the case of the intermediate depths (*ii*), and still carry an azimuthal wavenumber of four (Figures 6.5b and c). The distribution of the vertical velocity of ***Tilt***, ***Vmix*** and ***Hmix*** seems to resemble the shape of the vortex (Figure 6.5d, f and g). Therefore, one can think that the degree of influence of the eddies in the velocity field may be extended beyond the region where vorticity is significant. This can be possible by considering the non-local velocity field of the vortex, largely influenced by the degree of vortex baroclinicity (Bracco et al., 2004; Pasquero et al., 2007). Therefore, the more barotropic is the eddy the higher will be the influence in the vertical of the vortex velocity field. As expected, at deeper depths there is little influence of surface generated terms such as the mixing and wind stress forcing components (Figures 6.5e, f and g).

6.3.2 Influence of eddy-wind interaction and nonlinear Ekman effects

The interaction of the wind field with the background geostrophic currents (eddy-wind interaction) through Ekman pumping/suction may be partly responsible for the w field inside the eddies. Linear Ekman pumping may lead to upwelling at the eddy center (Martin and Richards, 2001; McGillicuddy et al., 2007) and nonlinear Ekman pumping to secondary circulation vertical cells at the periphery for submesoscale variability, or to a dipolar cell for mesoscale variability (Mahadevan et al., 2008; McGillicuddy et al.,

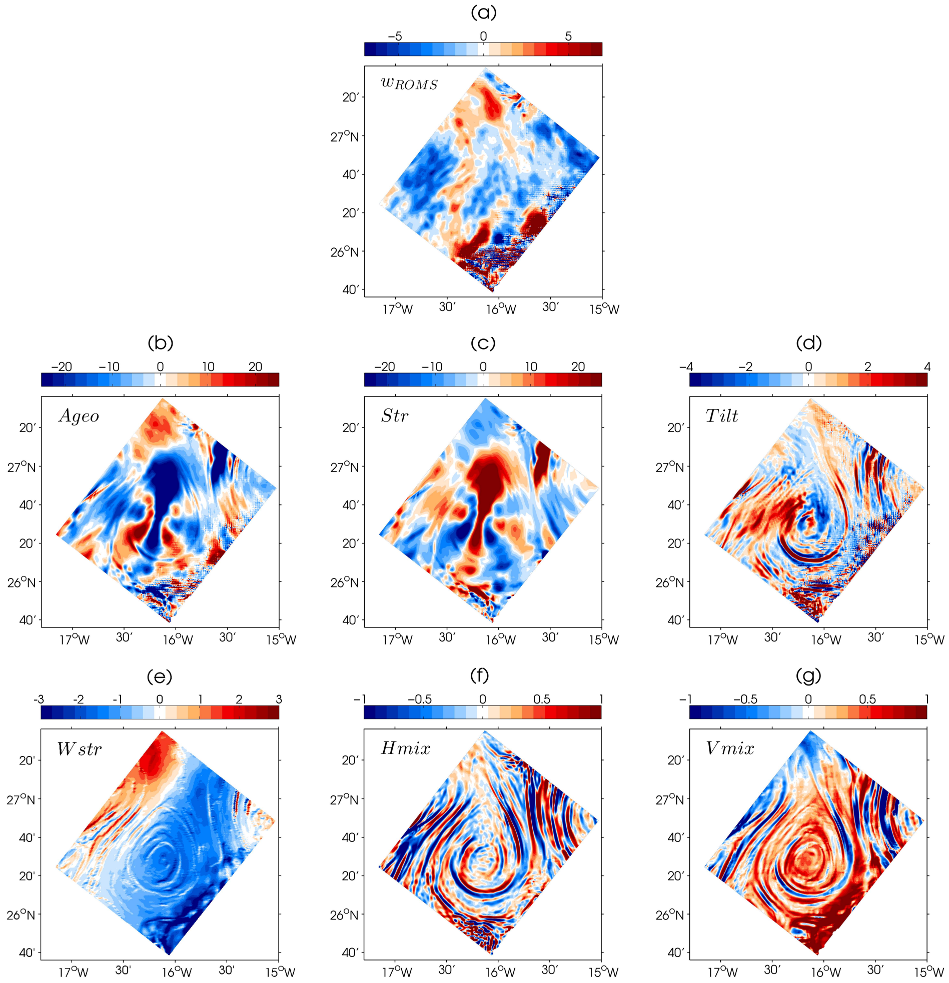
(a)
−5
0
5
w_{ROMS}
20′
27°N
40′
20′
26°N
40′
17°W
30′
16°W
30′
15°W
(b)
−20
−10
0
10
20
Ageo
(c)
−20
−10
0
10
20
Str
(d)
−4
−2
0
2
4
Tilt
(e)
-3
-2
-1
0
1
2
3
Wstr
(f)
−1
−0.5
0
0.5
1
Hmix
(g)
−1
−0.5
0
0.5
1
Vmix

Figure 6.5: Same than Figure 6.3 but at 1000 m depth.

2008). Eq. (6.1) includes wind stress effects as a forcing mechanism for w_{ROMS} (see e.g., Figures 6.4d) including implicitly linear and nonlinear Ekman effects (Koszalka, 2008). However, to explicitly examine the role of the interaction between the eddy current and the wind field we have also computed the total Ekman pumping/suction velocity (w_{EkT}), splitting their linear (w_{EkL}) and nonlinear (w_{EkNL}) contributions (Stern, 1965):

$$w_{EkT} = w_{EkL} + w_{EkNL} \tag{6.2}$$

where the linear contribution w_{EkL} is,

$$w_{EkL} = \frac{1}{\rho_o(f+\zeta_g)}(\partial_x \tau^y - \partial_x \tau^x) \tag{6.3}$$

This linear contribution is the classical one where a wind curl field induces a divergence of the Ekman transport and thus a vertical velocity. The nonlinear term w_{EkNL} is related to the advection of surface relative geostrophic vorticity (ζ_g) by the wind-induced Ekman transport in the mixed layer (e.g., Niiler, 1965; Thomas and Rhines, 2002; Mahadevan and Tandon, 2006). This w_{EkNL} becomes important in strongly sheared submesoscale regions where the Rossby number regime is high ($Ro \sim 1$). It can be formulated

$$w_{EkNL} = \frac{1}{\rho_o(f+\zeta_g)^2}[\boldsymbol{\tau}^x \partial_y(\zeta_g + f) - \boldsymbol{\tau}^y \partial_x(\zeta_g + f)] \tag{6.4}$$

where $\rho_o = 1026$ kg m^{-3} is the mean eddy density. Note that even a uniform wind stress field will lead to nonlinear Ekman vertical velocities.
Eddy wind interaction must also be included in the wind stress computation as

$$\begin{aligned} \tau^x &= \rho_a C_d(u_{rel})|u_{rel}| \\ \tau^y &= \rho_a C_d(v_{rel})|v_{rel}| \end{aligned} \tag{6.5}$$

where $\rho_a = 1.22$ kg m^{-3} is the air density and C_d is the drag coefficient as a function of the wind velocity (Yelland et al., 1998). The velocity components associated with the eddy-wind interaction are $u_{rel} = u_{wind} - u_g$ and $v_{rel} = v_{wind} - v_g$, where u_{rel} and v_{rel} denotes relative velocities, u_{wind} and v_{wind} are wind speed components and u_g and v_g are geostrophic eddy current components. Notice that the effective wind stress will be larger when geostrophic current and wind are in opposing directions and viceversa. Total Ekman pumping resulting from eddy wind interaction is compared for three cases in 6.6. First a uniform wind blowing over an analytical mesoscale Gaussian vortex is considered. Second non-uniform Trade winds blowing over eddy $A1$ is explored. As it is at its young stage it still preserves its axisymmetric shape (Figure 6.6d, e and f). Finally, the case of our elliptical eddy $A2$ is shown, also for non-uniform Trade winds (Figure 6.6g, h and i) where submesoscale variability is important.

Eddy wind interaction for the Gaussian vortex leads to a dipole of the w_{EkT} field consisting of an upwelling and a downwelling cell (Figure 6.6c). The more realistic

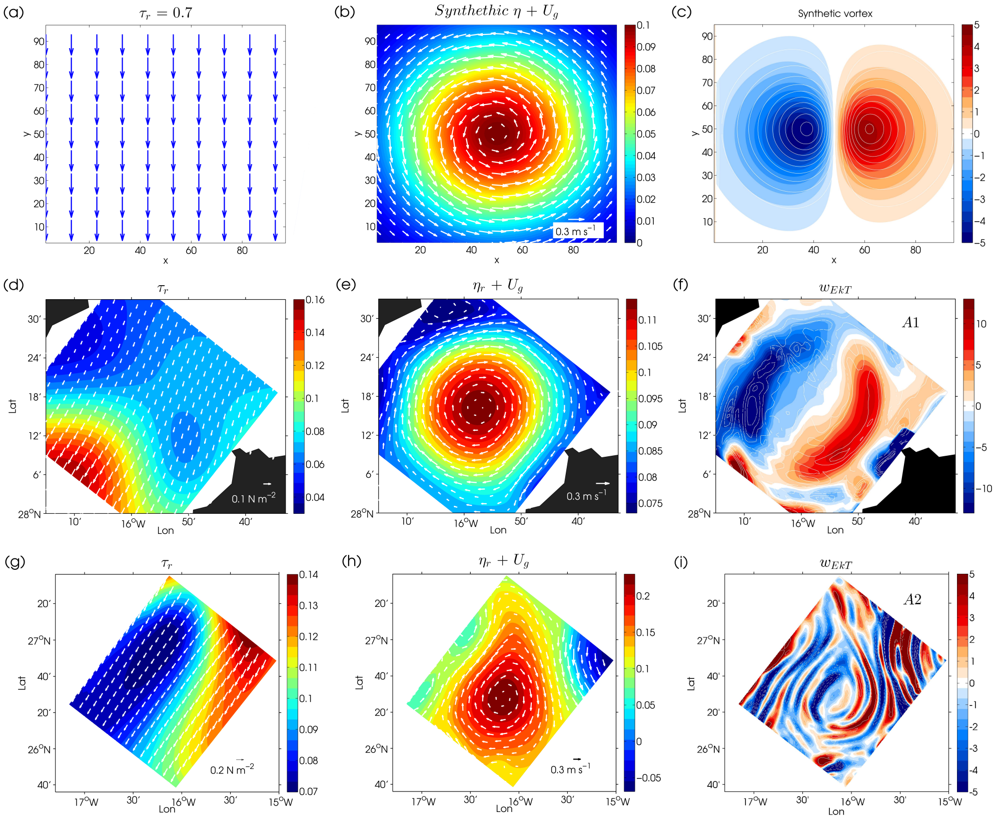

Figure 6.6: Fields derived from eq. (6.2) for three different vortices. For a synthetic Gaussian vortex: (a) Uniform wind stress field, $\boldsymbol{\tau}_r$, (b) η_r with superimposed geostrophic currents vectors u_g and v_g and (c) total Ekman pumping w_{EkT}. For an asymmetric vortex $A1$: (d) climatological $\boldsymbol{\tau}_r$, (e) η_r and vectors of u_g and v_g, and (f) w_{EkT}. The lowest panels: (g), (h) and (i) are analogous to (d), (e) and (f), but for an elliptical vortex $A2$. Both $A1$ and $A2$ are highlighted in Figure 6.1a.

configuration of eddy $A1$ also leads to a dipole of the w_{EkT} field but is clearly distorted with respect to the idealized configuration of the Gaussian vortex, with a clear increase of the w_{EkT} field toward the eddy periphery where strong gradients of absolute geostrophic vorticity are most likely expected (Figure 6.6f). For our case study eddy $A2$, the pattern of the w_{EkT} field is much more complex (Figure 6.6i). We still observe a dipolar cell clustered at the inner core, but it is now surrounded by narrow filaments of the w_{EkT} field which are most likely related to submesoscale variability of the absolute vorticity field at the eddy periphery.

Regarding the contribution of nonlinear pumping, the w_{EkNL} field mirrors the w_{EkT}

field, with downwelling on the western flank and upwelling on the eastern flank for the two vortices $A1$ and $A2$ (Figure 6.7a, b and also e and f). This indicates the dominance of nonlinear effects which are related to the ageostrophic dynamics of the eddies that exhibit finite Ro, causing the Ekman transport divergence to vary inversely with absolute rather than planetary vorticity (Niiler, 1965; Stern, 1965; Thomas and Rhines, 2002). The averaged linear Ekman pumping field for both $A1$ and $A2$ shows an inverted normal distribution rather than a Gaussian distribution as theorized by McGillicuddy et al. (2008), likely due to a nonuniform northwestward wind field.

It is noteworthy, that by applying a uniform wind-stress ($\boldsymbol{\tau}_r$ = 0.7 N m^{-2}) an Ekman pumping at the eddy center is observed for the lineal case w_{EkL} (not shown) as predicted by Martin and Richards (2001). However, this upwelling is an order of magnitude less ($|w| \sim 0.2$ m d^{-1}) than the simulated vertical velocities ($|w_{ROMS}| \sim 10$ m d^{-1}) (Martin and Richards, 2001; McGillicuddy et al., 2007).

An important issue to address is whether the interaction of the current eddy field with the wind field has some contribution in the total w_{ROMS}. This is envisaged by comparing the above results of w_{EkT} with the classical Ekman velocities given by $w_{Ek} = \boldsymbol{k} \cdot \boldsymbol{\nabla} \times (\boldsymbol{\tau_r}/f\rho_o)$, where now the eddy current interaction is not included in the wind stress formulation neither non lineal term is considered. Results depicted in Figures 6.7a and b, indicate that when the feedback between eddy current and wind fields is suppressed, Ekman pumping/suction velocities resemble the behavior of a lineal Ekman circulation. Therefore, w_{Ek} is similar to w_{EkL} and in turn it is consistent with the forcing term $\boldsymbol{Wstr}$ from eq. (6.1). In contrast, the general magnitude/pattern of w_{ROMS} is in agreement with w_{EkNL}, being larger than w_{EkL} and w_{Ek}, and hence $\boldsymbol{Wstr}$. However, this agreement between w_{EkNL} and w_{ROMS} is met only at surface layers of the eddy, since as will be further described in section 6.5, w_{ROMS} dynamic below h_{ubl} displays a quite different pattern.

6.3.3 Influence of vortex Rossby waves

Other processes in addition to eddy wind interaction through Ekman pumping may be implicated in vertical transport inside eddies. One such process is the growth and related straining by vortex Rossby waves. These waves are excited by the energy transfer of the wind in the deeper layers of the eddy. The numerical study of Koszalka et al. (2010) suggests that VRWs and near-inertial motions trapped inside anticyclonic

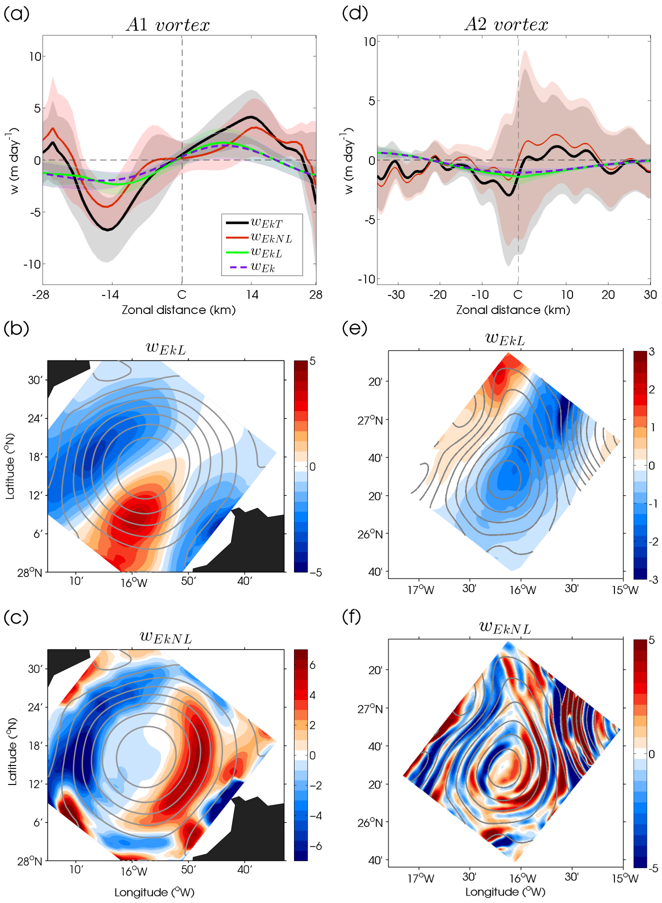

Figure 6.7: Latitudinal averages of total w_{EkT}, lineal w_{EkL}, nonlinear w_{EkNL} and classic w_{Ek} Ekman suction/pumping for the case of: (a) vortex $A1$, and (d) vortex $A2$. Shaded areas denote the standard deviation error. Vertical dashed lines show vortices centers. The distance from the eddy center in km is shown at the bottom. Instantaneous snapshots of (b) w_{EkL} and (c) w_{EkNL} are depicted for vortex $A1$, whereas (e) and (f) are analogous to (b) and (c), for vortex $A2$.

vortices may explain increases of near surface vertical transport through mixing below 150 m for weakly stratified flows. They also discuss the interactions of VRWs with the Ekman circulation that lead to more intense and complex w patterns in the layers close to the surface. Moreover, they observed dipole and quadrupole patterns of the w field that they associated with the propagation of these waves at the periphery of the vortex (Koszalka et al., 2009; Nardelli, 2013). Although analysis of VRWs influence is not straightforward, the wave-like surface spiral and deep dipole-like patterns that dominate our observed vertical velocity field in eddy $A2$ suggests that VRWs may play a role in modulating w_{ROMS}.

VRWs were first investigated by Montgomery and Kallenbach (1997) who established its dispersion relationship and showed the outward propagation of these features. Some years later McWilliams et al. (2003) extended the study of Montgomery and Kallenbach (1997) to finite Rossby number regimes. In Appendix B of this thesis we give the local dispersion relation for these waves as obtained by Nardelli (2013) for an Aghulas Current ring. Periods for VRWs as computed from this dispersion relationship give us periods from 1.25 to 5 days for the inner core of the $A2$ vortex. For outer VRWs, the period increases to almost $\sim$ 40 days. This frequency range is similar to those reported in other numerical (Koszalka et al., 2009) and observational studies (Chavanne et al., 2010; Nardelli, 2013). Frequencies lower than the inertial frequency (max. $f = 6.7354{\times}10^{-5}$ rad sec^{-1} $\equiv$ 1.16 days) were found only at the inner core of the vortex. Similar frequencies were found for radial and azimuthal velocities for different time evolution of the vortex. The spatial distribution of wave frequencies inside the vortex is largely dependent on the spatial distribution of the vortex azimuthal velocity as formulated in the dispersion relation (see Appendix B). Furthermore, the period decreases with depth, reaching inertial frequencies at the inner core of the vortex.

In order to obtain a more general time-dependent view, the frequency spectra of w_{ROMS} field is analyzed at three different depths for the whole numerical domain. To isolate the signature of anticyclonic eddies, only those vortices with $\zeta_r/f < 0$ were averaged (Figure 6.8a). Figure 6.8 clearly shows spectral peaks of lower frequency than the inertial frequency (shaded bands in Figures 6.8b and c). These peaks are matches with the most recurrent range of frequencies given by the dispersion relation for VRWs, in particular for those waves that radiate from the inner vortex cores (up to $\sim$ 5 days).

Despite the possibility that the frequency spectra peaks could be related to other processes, we can rule out the wave-like structure being due to other types of waves, such as inertial or gravitational waves, whose presence cannot be reproduced by this model configuration due to the climatological wind forcing (Cardona and Bracco, 2012). Accordingly, the analysis presented here should serve as an indication of the existence of VRWs in PE numerical eddying flows. Although our results are consistent with other related studies they must be taken with care since the determination of VRWs is

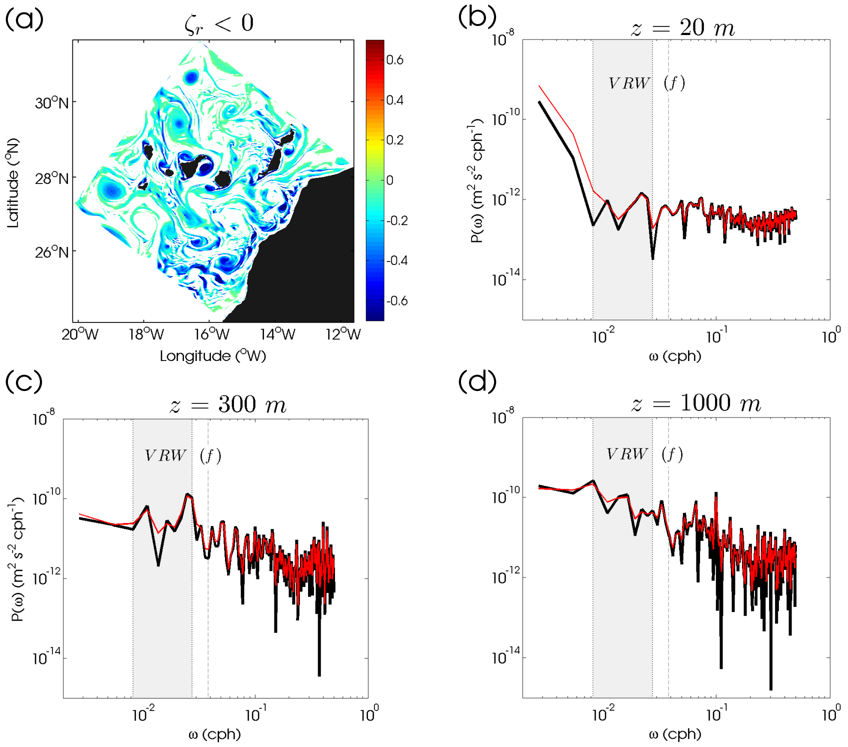

Figure 6.8: (a) An example of horizontal snapshot (day 27 of month 06) of ζ_r/f. Negative relative vorticity fields are isolated in order to only considers anticyclonic eddies. The frequency spectra of vertical velocity is computed at three different depths: (b) 20 m; (c) 300 m and (d) 1000 m. Thin red lines are smoothed signals by using a Hanning filter. The inertial frequency (f) is indicated by vertical lines, while shaded areas denote the frequency range for vortex Rossby waves from 0.0083 to 0.0278 cph (1.5 to 5 days).

extremely sensitive to their control parameters* (Nardelli, 2013).

Forcing controls on surface and deeper w_{ROMS}

Having stated the different sources that dominate the vertical velocity field inside mesoscale anticyclonic eddies, we now explore the implications of these forcing terms. Similarly to Chapter 5, the $A2$ eddy will be divided into surface and subsurface layers as explained in the next two sections.

---

[*] And also due the lack of quantitative arguments which makes their impact on the vertical velocity field to be still poorly explored.

6.4 Surface role of diapycnal mixing in w

As shown in Figure (Figure 6.9a) the strongest diapycnal mixing regions in our numerical domain are related to the occurrence of mesoscale eddies away from coastal areas. For the particular case of the $A2$ vortex, a slight enhancement of K_v is shown in Figure 6.9a at the eddy periphery, consistent with the observed enhancement of diapycnal mixing found for the anticyclonic intrathermocline eddy described in Chapter 5. This enhancement of mixing is higher on the eastern flank of the eddy (red line in Figure 6.9c). In this case, Ekman transport related to a southwestward wind direction may advect the far field denser water westward over the lighter eddy water, setting up conditions for the triggering of convective mixing.

A slight increase of K_v on the northern flank can also be appreciated (blue line in Figure 6.9c) for $A2$, although this is lower than the eastern K_v increase and may be related to an interaction with its linked submesoscale filament located on the northern edge. In fact, for the case of the more axisymmetric vortex $A1$, K_v enhancement only takes place from the eddy center to the eastern flank (Figure 6.9d). On the other hand, below the mixed layer the diapycnal coefficient acquires an almost constant value of $K_v = 10^{-6}$ m^2 s^{-2} given by the ocean interior parameterization of KPP (Large et al., 1994). This constant value was included in order to parameterize the effect of the background turbulence, such that related to the breaking of internal waves. Only two vortices exhibit non-constant K_v in the stratified thermocline, namely $A2$ and the more axisymmetric case of $A1$ vortex (Figure 6.9b), which in turn also exhibit the highest Ro inside their centers (see Figure 6.1a).

As described in section 6.3, vertical mixing contributes to the overall magnitude of surface w_{ROMS} and in a similar way to the tilting or stretching forcing terms at the surface (see Figures 6.3). However, the spiral w pattern from ***Vmix*** resembles the surface w_{ROMS} shape (Figures 6.3a and g) but with opposite sign, as can be seen in the vertical sections of Figures 6.10b and c.

Our results also indicate that, although the ***Vmix*** forcing influence is constrained at the surface (Nagai et al., 2006; Koszalka et al., 2010; Pallàs-Sanz et al., 2010), it may indirectly control the w_{ROMS} field by influencing the ***Ageo*** term in the surface layers (Figure 6.10a). When this happens, the ageostrophic component is enhanced, breaking the thermal-wind balance, especially at the eddy periphery. To restore thermal-wind

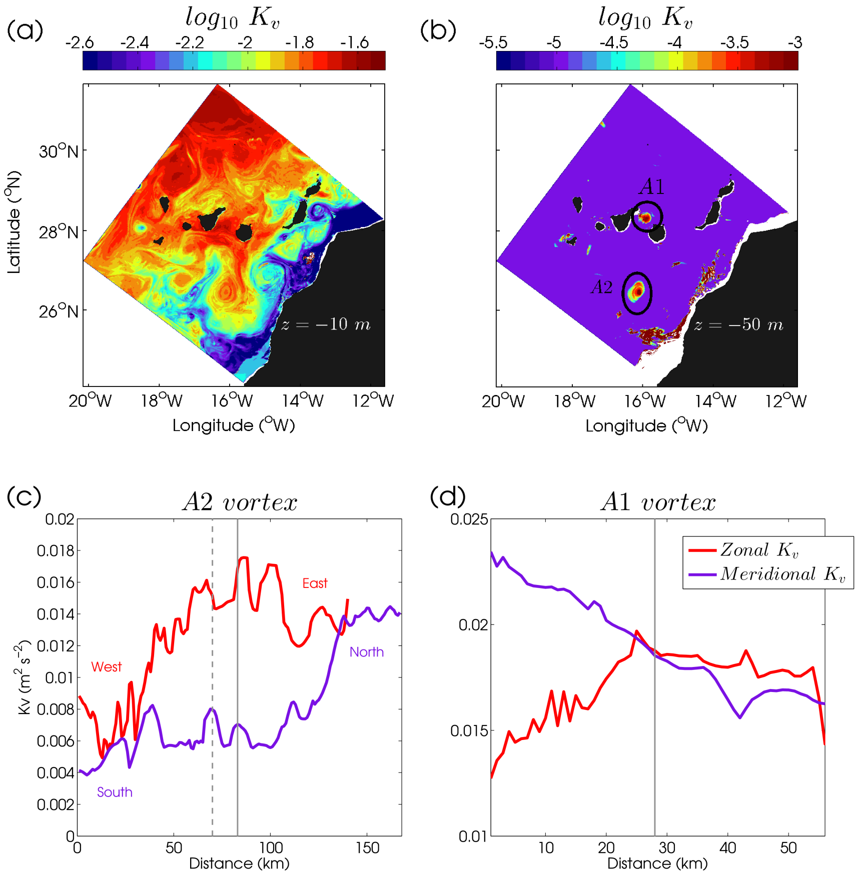

Figure 6.9: Snapshots of diapycnal coefficients, K_v (m^2 s^{-2}) in logarithmic scale, for two depths: (a) 10 m and (b) 50 m, covering the whole model domain. Note the differences in color-bar scales. Zonal (red) and meridional (blue) horizontal K_v profiles tied to the eddy center, shown for (c) vortex $A2$, and (d) vortex $A1$. Vertical continuous and dashed lines denote the eddy center for zonal and meridional sections, respectively.

balance a vertical circulation begins (Ponte et al., 2013), leading to a maximum in ***Ageo*** and hence in the overall w_{ROMS} profile at the surface, as is shown by the root mean square (r.m.s) of each $wROMS$ contribution for $A2$ (Figure 6.10a). Although Figure 6.10a represents the horizontal average for a snapshot of the $A2$ vortex, similar results were found at different model time steps. The differences are associated with seasonal changes of h_{ubl} and the surface maximum gradient of N^2, thus being dependent of the seasonal variability of the stratification and the upper boundary layer depth.

In our case, the strong stratification below the upper boundary layer seems to

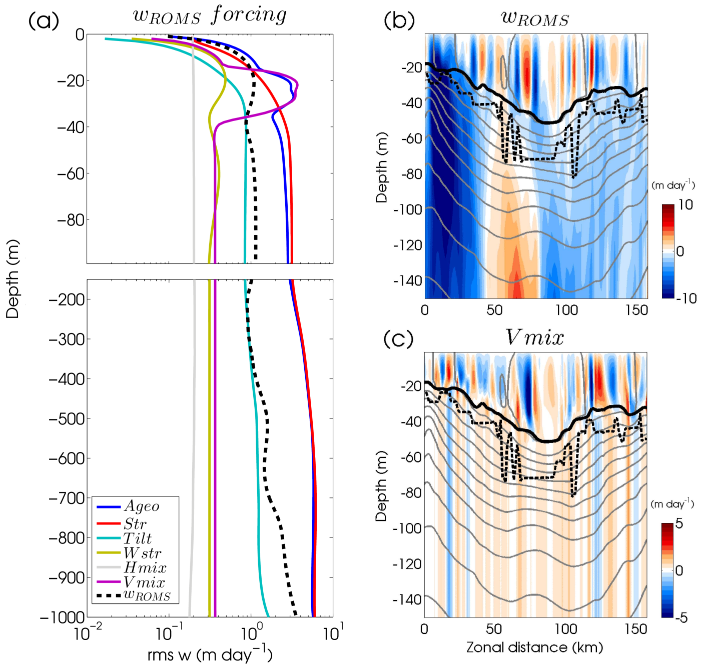

Figure 6.10: (a) Root mean square of each forcing term for $A2$ vortex, in logarithmic scale. Surface zonal vertical sections of the $A2$ vortex with (b) overall vertical velocity w_{ROMS}, and (c) vertical mixing forcing term, ***Vmix***. Horizontal continuous and dashed lines denote h_{ubl} and the surface maximum gradient of N^2, respectively. Superimposed gray contours are isopycnals plotted every 0.15 (kg m^{-3}).

impose a barrier to the extension of the vertical velocity bands which drastically fade at the base of h_{ubl} (Figures 6.10b and c).

6.5 Sub-surface w-dipole

We now focus our discussion on the examination of w below the h_{ubl} where recurrent w-dipoles are observed. The meridional vertical section of w_{ROMS} for vortex $A2$ does not show a clear signature of this structure (Figure 6.11a), whereas it is well represented in the zonal section (Figure 6.11b). The horizontal and vertical extensions of these w-cells largely coincide with $\zeta_r < 0$ values at the eddy core (Figure 6.11c), and fade at the eddy base (i.e., 800 m). Between both vertical velocities cells, null or minimum w values are found, in agreement with recent observational findings of Barceló-Llull et al. (in prep.). w-dipoles are located around the vortex centers, although they are tilted with respect to the vortex inner core (Figure 6.11). Moreover, they are ubiquitous for all the mesoscale eddies (both cyclones and anticyclones) of our numerical domain, varying in intensity over time.

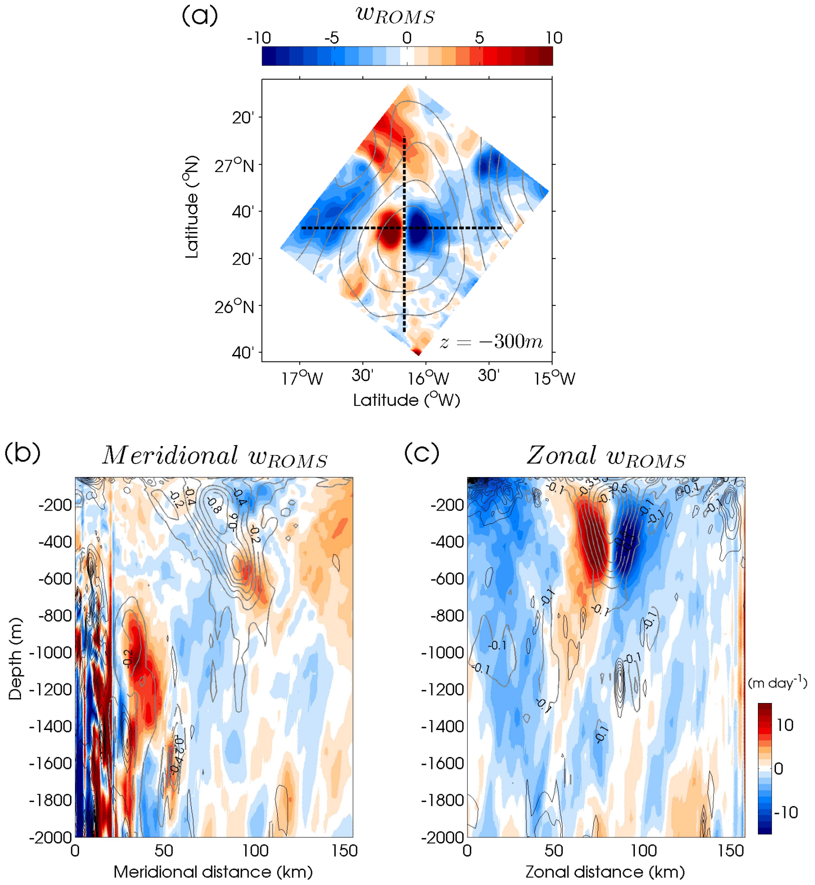

Figure 6.11: Horizontal w_{ROMS} at 300 m depth for vortex $A2$ in m d^{-1}. Contours of η_r are superimposed in gray. Lower panels are sub-surface vertical sections of w_{ROMS} with (b) a zonal section and (c) a meridional section. Isolines of ζ_r are superimposed in gray for negative and black for positive values. Dashed black lines in (a) denote coordinates for both meridional and zonal sections.

6.5.1 Temporal w-dipole evolution

In this section the temporal evolution of w-dipoles and their relationship to vortex shape will be discussed. Eddies can be near-circular structures which experience changes in axisymmetrization during their lifetimes (Sangrà et al., 2005; 2007; 2009). Figure 6.12

shows time series of w-dipoles for several selected vortices of our numerical model illustrating their evolution at five day intervals. The mean rotation rate of the vortices as obtained from a wavelet analysis of virtual buoys (not shown) was ∼ 6 days. These rotation rates match rather well with those observed by Sangrà et al. (2005; 2007) from drifters deployed inside Canary Island eddies. It can be also noticed that the aspect ratio of the vortices and dipoles rotates in the sense of the eddy motion. Temporal animation shows that dipolar structures rotate more slowly than the rotational period of the vortices, taking around ∼ 30 days to complete a cycle (see supplementary material), which is also partially shown in the snapshots of Figure 6.12.

Regarding the intensity of the $A2$ dipole, Figures 6.12 show that it weakens on day 10 of month 9 (Figure 6.12c), but is then reinforced ten days later (Figure 6.12e) and maintains its intensity for several days more (Figure 6.12h). Similarly, the weakening/strengthening of the $A2$ dipole can be seen in Figures 6.13.

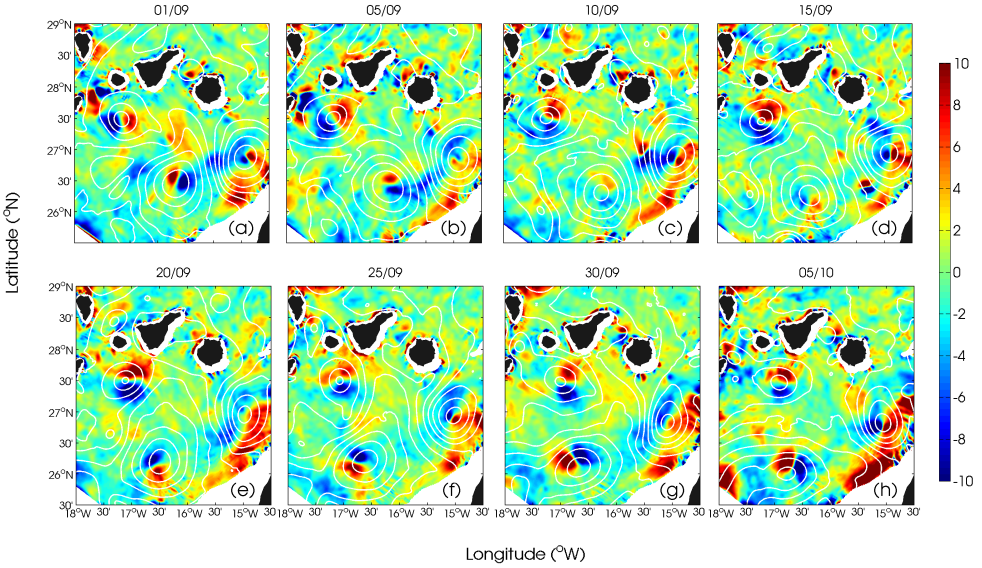

Figure 6.12: Temporal evolution of the w-dipoles for various vortices south of the Canary Islands. Snapshots correspond to horizontal maps of w_{ROMS} at 300 m depth in m d^{-1}, plotted every 5 days from day 01 of month 09. The date is shown at the top. Contours of η_r are superimposed in white in order to highlight the shape of each vortex.

Some issues arise from these numerical observations. The first is whether weaker stages of the w-dipoles imply a decrease of the vertical velocity, or should be attributed to a shallow vertical range of the dipole in the water column. The second issue is whether the intensity of the dipoles can be related to the vortex axisymmetric state. The first question can be easily addressed by examining the vertical extension of the vortex over time. An example can be seen on three different dates for the $A2$ w-dipole of Figure 6.13, where the w-dipole weakens from day 23 of month 8 (Figure 6.13a) to day 9 of month 9 (Figure 6.13b). After ≈ 14 days, the w-dipole strengthens again on day 23 (Figure 6.13c), keeping this intensity for 30 more days.

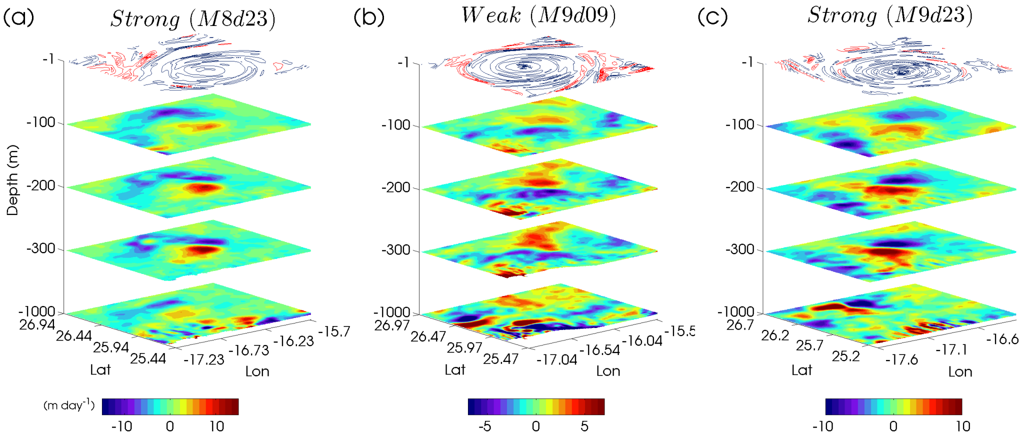

Figure 6.13: Horizontal maps of w_{ROMS} (in m d^{-1}) for vortex $A2$ at four different depths: 100, 200, 300 and 1000 m. To show variations of the w-dipole magnitude, three dates are taken into account: (a) day 23 of month 08, (b) day 09 of month 09, and (c) day 23 of month 09. Contours of ζ_r are also represented in red for $\zeta_r > 0$ and blue for $\zeta_r < 0$.

Although the dipole experiences changes in its intensity its vertical extension appears to be constant along the lifespan of the vortex, being strongly dependent on the ζ_r vertical extension.

6.5.1.1 Lagrangian release of passive tracers

A Lagrangian particle release experiment was carried out in order to investigate if the intensity of dipoles can be related to the vortex axisymmetric state. This leads us to also investigate the related effects on vortex filamentation and rotation rate variability. Details of the Lagrangian numerical tool are indicated in Chapter 3. After several tests, a total of 5000 particles were released at 20 m depth inside the $A2$ eddy, at the beginning of month 8 until month 9 (Figure 6.14a).

The particles were time integrated using a time step of 6 hours. They are transported passively by the horizontal current field and thus not allowed to experience vertical migrations as w was is set to 0. Particles were released within the eddy core, defined as the region with negative Okubo-Weiss (OW) parameter (Okubo, 1970; Weiss, 1991):

$$OW = \underbrace{(\partial_x u - \partial_y v)^2}_{\text{normal strain}} + \underbrace{(\partial_x v + \partial_y u)^2}_{\text{shear strain}} - \underbrace{(\partial_x v - \partial_y u)^2}_{\text{vorticity}} \tag{6.6}$$

In this regard, hyperbolic or vorticity-dominated regions are those where $OW < 0$ and strain-dominated regions where $OW > 0$. OW analysis shows that most of the simulated anticyclonic vortices are vorticity-dominated in their cores and strain-dominated at the periphery. Snapshots of particle positions over vorticity-dominated regions are shown in Figure 6.14.

As expected, in general virtual floats show loop-like trajectories that closely resemble the observations for the region (Sangrà et al., 2005; 2007; 2009). The results from the Lagrangian run indicate that the vortices experience cycles of axisymmetrization followed by unstable periods with elliptical shapes as observed in the temporal evolution of the virtual floats of Figure 6.14.

The mechanisms for the w-dipole intensity changes may be related to a combination of various factors, in which axisymmetrization can have an important role. In an elliptic vortex such as in our case, the density field is not axisymmetric, hence the gradient-wind balance cannot be satisfied and strong vertical circulation develops in order to restore the gradient-wind balance. Furthermore, because ageostrophic effects are dominant forcing terms for the w-field, a decreasing of ageostrophy would be linked to w weakening. However, further analysis is needed in order to establish a relationship between a weakening w-dipole and vortex axisymmetrization phases.

On the other hand, virtual tracer experiments also show an interesting submesoscale filament-like feature at the northern vortex edge (Figure 6.14), which seems to maintain the coherence of the vortex along its lifetime (Koumoutsakos, 1997). The filament may be related to the re-axisymmetrization process suggested by Graves et al. (2006), which is largely conditioned by the existence of VRWs. Through ejection of PV filaments, VRWs transfer their energy back to the vortex while propagating outwards, thus the filaments tend to encircle the vortex making it more axisymmetric (Graves et al., 2006)

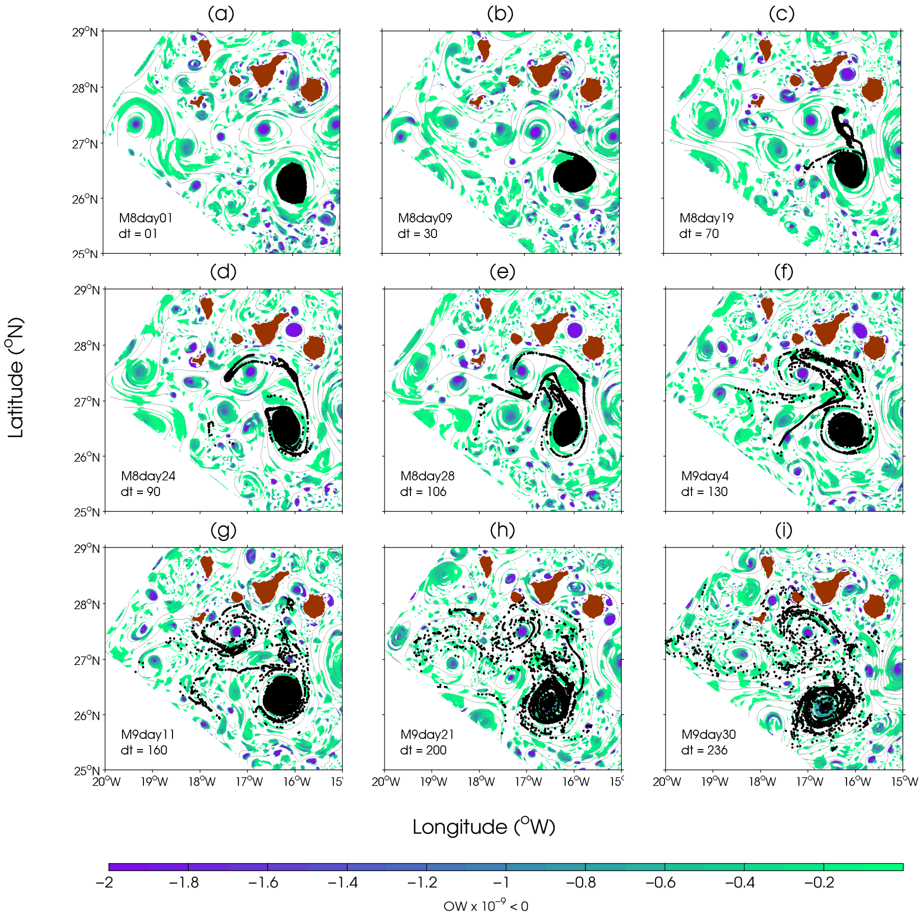
(a)
(b)
(c)
(d)
(e)
(f)
(g)
(h)
(i)
M8day01
dt = 01
M8day09
dt = 30
M8day19
dt = 70
M8day24
dt = 90
M8day28
dt = 106
M9day4
dt = 130
M9day11
dt = 160
M9day21
dt = 200
M9day30
dt = 236
29°N
28°N
27°N
26°N
25°N
20°W
19°W
18°W
17°W
16°W
15°W
Latitude (°N)
Longitude (°W)
−2
−1.8
−1.6
−1.4
−1.2
−1
−0.8
−0.6
−0.4
−0.2
OW x 10⁻⁹ < 0

Figure 6.14: Time sequence from a Lagrangian particle experiment, where (a) shows the release area of the Lagrangian experiment corresponding to the $A2$ vortex core. Color scale for negative OW denotes vorticity-dominated regions. Month, day and time-step (dt) of each snapshot is shown in the lower left corner.

and subsequently reinforcing the eddy*. Additionally, a low proportion of particles are expelled far away from the eddy through the vortex filament (Figure 6.14c), indicating that strong gradients of ζ_r can act as barriers to tracers (Provenzale, 1999; Samuelsen et al., 2012). After a period of re-axisymmetrization ($\sim$ 30 days), the particles tend to migrate towards the vortex inner core (Figure 6.14f and animation in supplementary material) forming clusters. This is consistent with the real buoys released in the observational study of Sangrà et al. (2005), and can be the result of the anticyclonic vortex dynamics itself and their vertical velocity field due to divergent motion (Koszalka, 2008; Samuelsen et al., 2012).

---

*This effect seems to be stronger for anticyclones and may help to the dominance of anticyclones over cyclones (Graves et al., 2006).

6.6 A Comparison with the generalized omega equation

Unfortunately, the direct measurement of vertical velocity is very difficult in the ocean. This is mainly due to the lower values of vertical velocities when compared to horizontal ones $[w(10^{-3}\text{–}10^{-4})U]$. Therefore, several diagnostic formulations have been developed in order to indirectly infer the w field from common hydrographic variables such as the density field (Hoskins et al., 1978). In addition, eq. (6.1) is very difficult to achieve at synoptic scales and a large data base is needed in order to diagnose w from this approach. For the case when only the density field is available, indirect theoretical methods have been developed to estimate w. One of the most successful formulations is to solve the adiabatic QG ω-equation (e.g., Hoskins et al., 1978; Pollard and Regier, 1992; Pinot et al., 1996). Viúdez and Dritschel (2004) proposed an approximation of the generalized ω-equation first derived by Viúdez et al. (1996), valid when density and horizontal velocity fields are available, which was reexamined by Pallàs-Sanz and Viúdez (2005) to obtain w in the Alborán Sea. In this section we diagnose w form the generalized ω-equation (w_{OMEGA}, hereafter) in order to compare it with w diagnosed from the flux divergence discussed in section 6.3 (i.e., w_{ROMS}) and to complete our physical interpretation of the w field.

In terms of the $\boldsymbol{Q}$ vector, the generalized ω-equation from Viúdez et al. (1996) can be read as follows:

$$N^2\boldsymbol{\nabla}_h^2(w) + f(f+\zeta_r)\frac{\partial^2 w}{\partial z^2} = \underbrace{2\boldsymbol{\nabla}_h \cdot \boldsymbol{Q}_h}_{F_{QT}} + \underbrace{f\boldsymbol{\zeta}_{ph}^a \cdot \boldsymbol{\nabla}_h^2 \boldsymbol{u}_h}_{F_{PSE}} \tag{6.7}$$

with $\boldsymbol{Q}_h$ being the horizontal vector

$$\boldsymbol{Q}_h = \frac{g}{\rho_o}(\partial_x u \partial_x \rho + \partial_x v \partial_y \rho, \partial_y u \partial_x \rho + \partial_y v \partial_y \rho) \tag{6.8}$$

where the subscript h denotes horizontal components and superscript a indicates the

ageostrophic vector component. The generalized ω-equation (eq. 6.7) was solved by an iterative relaxation method (Press et al., 1993) with Dirichlet boundary conditions for total velocities and density fields. Refer to Viúdez et al. (1996) and Pallàs-Sanz and Viúdez (2005) for further details. Notice that in eq. (6.7) the effects of diapycnal mixing are not included. Hence, results from this analysis will be presented only for stratified fluid below the surface maximum gradient of N^2 (see Figure 6.2).
The first r.h.s. term in eq. (6.7) can be seen as the temporal change of the horizontal density gradient induced by the total horizontal current field (i.e., the divergence of the $\boldsymbol{Q_h}$ vector; F_{QT}). The second r.h.s is the horizontal ageostrophic pseudo-vorticity forcing (F_{PSE}), where $\boldsymbol{\zeta}^a_{ph} = (-\partial_z v^a, \partial_z u^a)$, with u^a and v^a ageostrophic velocities components. F_{PSE} represents reorientation by the horizontal velocity total field of a pre-existing pseudo-vorticity horizontal and ageostrophic field (Viúdez and Dritschel, 2004; Giordani et al., 2006). One of the advantages of the generalized ω-equation is that it explicitly includes both geostrophic and ageostrophic quantities in the divergence of the $\boldsymbol{Q_h}$ vector (Viúdez et al., 1996; Pallàs-Sanz and Viúdez, 2005), where $F_{QG} = 2\boldsymbol{\nabla}_h \cdot \boldsymbol{Q}^g_h$ is the divergence of the geostrophic velocity field and $F_{QA} = 2\boldsymbol{\nabla}_h \cdot \boldsymbol{Q}^a_h$ is its ageostrophic counterpart. Consequently, vertical velocities from the four forcing terms due to the generalized ω-equation will be: w_{QT}, w_{QG}, w_{QA} and w_{QPSE} which, in sum, give the overall diagnosed vertical velocity w_{OMEGA}.
As illustrated in Figures 6.15a and b, w_{ROMS} and w_{OMEGA} match very well and one field mirrors the other field. Both show a dipolar shape of the w field centered at the eddy center. The order of magnitude of w is also surprisingly similar, which contrasts with the finding by Koszalka et al. (2009). In their numerical model, they show that w_{OMEGA}, despite having a similar w pattern to w_{ROMS}, had velocities an order of magnitude lower than those diagnosed by expression eq. (6.1). Other studies (Pinot et al., 1996; LaCasce and Mahadevan, 2006) also found an underestimation of the w-field when using QG-approximation theory. However, our results suggest that the use of the generalized *omega*-equation leads to consistent estimations of the w-field inside mesoscale eddies.

Figure 6.15c shows that w_{OMEGA} is mainly induced by the total deformation of the density gradient (F_{QT}). Calil and Richards (2010), in their ROMS model of a mesoscale eddy near the Hawaii coast, also found that the divergence of the $\boldsymbol{Q_h}$-vector is consistent with the simulated w_{ROMS} field, especially in regions of intense w. An

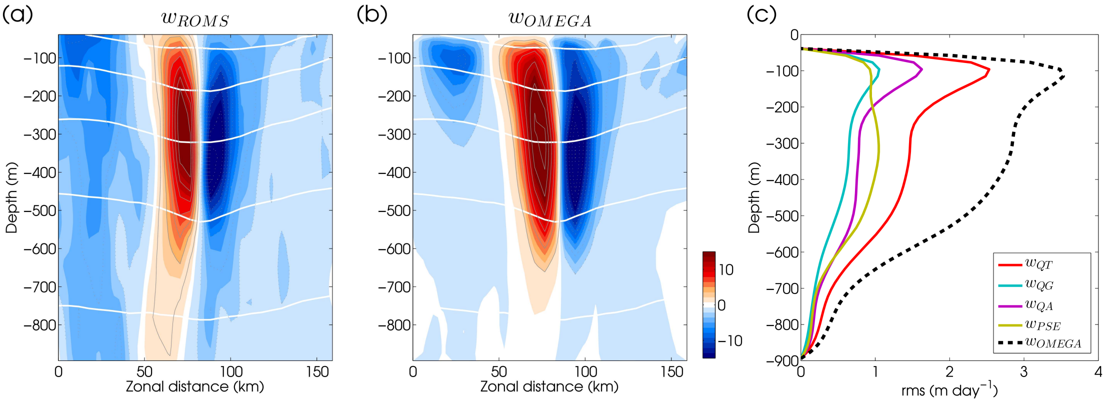

Figure 6.15: Zonal vertical sections of vortex $A2$ with (a) w_{ROMS} and (b) w_{OMEGA} (in m d^{-1}). White contours are isopycnals plotted every 0.25 kg m^{-3}. Both vertical velocities have an horizontal resolution of 5 km. The rms of the forcing terms computed from eq. (6.7) are shown in (c), including the diagnosed w_{OMEGA}.

interesting contribution of our modeling study is that a preponderance of ageostrophic forcing is found at subsurface levels of the water column (Figure 6.15c). The dominance of the ageostrophic vertical velocity term w_{QA}, is also obtained by diagnosing w from eq. (6.1) through ***Ageo***. Albeit that we use different approaches, both analyses suggest that ageostrophic effects are relevant forcings for the vertical dynamics of mesoscale eddies. On the other hand, the w induced by the pseudo-vorticity forcing w_{PSE}, represents a minor contribution to the total w-field (Figure 6.15c), although it also has a similar dipolar pattern.

Despite of the consistence of the above results, it should be noted that comparisons between w_{ROMS} and w_{OMEGA} were made by decreasing the resolution of the model to 5 km for the horizontal fields and to 20 m depth cells in the vertical. Insignificant variations were found by using finer vertical resolutions (that greatly increase the computational cost). On the other hand, an underestimation of about one order of magnitude in the diagnosed w_{OMEGA} is produced when the equation is forced the with original horizontal model fields ($\sim$ 1 km), although the w-dipole may still be appreciated. This can be attributed to high submesoscale variability of the forcing (r.h.s of eq. 6.7), which introduces strong gradients in the elliptic equation to solve w_{OMEGA}, where the relaxation method would act to smooth the velocity field by successive iterations. In consequence, special care must be taken in the treatment of modeled mesoscale structures using the QG-approximation at fine resolutions.

6.7 Summary and discussion

The main results of this study indicate that the vertical velocity inside anticyclonic eddies is strongly linked to ageostrophic and stretching effects. Eddy-wind interactions (Ekman pumping mechanism) do not explain the overall w-pattern inside the anticyclonic simulated eddies. Moreover, the presence of VRWs may impact the w field by controlling the axisymmetrization process. The main forcing mechanisms of the vertical velocity field in the two layered structure of the numerical eddy under study are detailed below.

6.7.1 The role of diapycnal mixing in surface w

The first layer is constrained between the surface and the base of the upper boundary layer h_{ubl}, in which w exhibits a wave-like pattern with alternating spirals of downwelling/upwelling cells around the eddy core. This spiraling wave like shape was also imprinted on the tilting term field as well as on the horizontal and vertical mixing term fields. Vertical or diapycnal mixing in this layer was linked to the occurrence of mesoscale structures, such as in our case study eddy and related submesoscale variability. Mixing is often intensified at the edges of mesoscale anticyclonic eddies.

Another noteworthy result of this work is related to the role of diapycnal mixing in the surface w field. Vertical mixing in the mixed layer indirectly controls w by enhancing the ageostrophic forcing terms that subsequently induce a surface maximum of w by restoring thermal-wind balance supporting the suggestions of Ponte et al. (2013). Consequently, the lack of deep diapycnal mixing would also help to maintain the dipolar w pattern seen below the upper boundary layer.

In this regard, below h_{ubl}, diapycnal mixing is inhibited by strong steady stratification, where there are no extra sources of turbulent kinetic energy. In addition, although the KPP configuration permits the generation of near inertial internal waves, these are not resolved in this model configuration. This is likely due to the use of monthly climatological winds, that preclude the generation of near-inertial waves trapped inside anticyclonic eddies, which in turn act as precursors of deep diapycnal mixing as is evidenced in Chapter 5 of this thesis.

6.7.2 The subsurface w-dipole

The second layer is located below the mixed layer where a recurrent dipole-like structure dominates the center of all the mesoscale eddies in the numerical model domain. The dipole structure rotates in the same sense as the eddy but with a lower rotation rate. The intensity of both w cells of the dipole varies with time. Weakening states of the w-dipole may be related to periods of axisymmetrization and decreasing of ageostrophic effects. However, further studies are needed in order to investigate the underlying causes of these changes in w intensity.

w-dipoles are mainly induced when the ageostrophic and stretching terms do not cancel each other out. At these places, the strongest w values are exhibited by the model. Consequently, the mechanism behind the formation of this dipolar pattern could be related to an imbalance in the gradient-wind equation produced by the lack of axisymmetrization of the vortex (Koszalka et al., 2009). This causes a rearrangement between Coriolis, pressure gradient, and centrifugal forces inside the eddy that induces secondary circulations by frontogenesis (Capet et al., 2008b).

Under a QG framework, the w dipole is also observed when the generalized ω-equation from Viúdez et al. (1996) is computed. The comparisons show a large degree of correspondence between w_{ROMS} and w_{OMEGA} below h_{ubl}. Moreover, analysis of the ω-equation forcing shows that the divergence of the $\boldsymbol{Q}_h$-vector dominates the vertical velocity. Interestingly, the deformation of the density gradient is mainly induced by the ageostrophic horizontal current field that strains the horizontal density gradient. In sum, both the QG-approximation (given by w_{OMEGA} analysis) and the instantaneous divergence of the flux (given by w_{ROMS} analysis) indicate that ageostrophic effects are strongly implicated in the formation of w-dipoles in stratified fluids.

6.7.3 Influence of VRWs on the total w field

The occurrence of VRWs is examined and evidenced through changes in eddy shape, filamentation towards re-axisymmetrization, and wave-like structures in the forcing terms of the overall w_{ROMS} field. Although characterization of VRWs is not trivial due to the lack of quantitative analysis and sensitivity to different parameters of the dispersion relation (Appendix B), our results reveal that VRWs can occur in this model configuration with periods between 1.5 and 40 days.

Simulated vortices experience variations in their aspect ratio with periods of axisymmetrization, as is the case for real buoys deployed in the same region. Eddies also develop submesoscale filaments which represent a barrier to passive tracers. At the mature stages of the eddy, particles can either migrate to the inner vortex core or are driven through the filament far from the eddy center. This may be explained because VRWs act as restoring mechanisms towards vortex re-axisymmetrization, expelling potential vorticity outward from the eddy core after a strain-induced perturbation. Furthermore, the propagation of these potential vorticity perturbations may also drive changes in vertical transport inside the eddies, producing upwelling/downwelling patches according to variations in vorticity. Therefore, it is suggested that VRWs could modulate w patterns.

7

Conclusions and Future Research

7.1 Main conclusions

The main conclusions are now summarised. These include our main findings and are organized according to the corresponding chapter.

Chapter 4: Diapycnal entrainment in an Eastern-boundary upwelling filament

In a one-dimensional sense, the entrainment parameterization serves as a proxy to examine the different sources of turbulent kinetic energy that control the upper ocean layer. The entrainment phenomenon is particularly important inside strong dynamical systems such as the Cape Ghir upwelling filament where turbulent kinetic energy dissipation rates were measured, leading to the following conclusions:

- Vertical shear-induced mixing at the base of the mixed layer should not be simply neglected in turbulent kinetic energy bulk mixed layer models, as suggested by the observed increase of entrainment rates, in turn related with enhancement of vertical shear levels in waters influenced by the Cape Ghir upwelling filament.

- The vertical extension of the region of active mixing, identified by positive entrainment zones, along with an enhancement of turbulent kinetic energy dissipation rates, creates optimal conditions for the occurrence of entrainment, especially in filament waters where the pycnocline is close to the surface and turbulent mixing can act more efficiently. The latter also suggests a relationship between the filament and enhancement of turbulent mixing.
- Parameterized turbulent kinetic energy dissipation rates differ from those observed by one order of magnitude, leading to an underestimation of entrainment rates. In consequence, this may produce overheating of SST in numerical models that include such parameterizations.
- The lack of consensus between different parameterizations encourages the development of a more accurate entrainment formulation based on the parameterization suggested here, where wind-stirring mixing, surface as well as interfacial buoyancy fluxes, and vertical current shear at the base of the mixed layer are included into a single equation. Such a formulation takes account of the extension of the active mixing layer and observed dissipation rates.

Chapter 5: Turbulent diapycnal mixing within an intrathermocline anticyclonic eddy

Through hydrographic and turbulent microstructure measurements at synoptic scales, a detailed characterization of the principal mixing process inside an intrathermocline eddy shed by the Canary archipelago in the northeast Atlantic have been analyzed. A summary of the major results of this chapter is:

- The turbulent kinetic energy source of surface and interfacial diapycnal mixing inside the intrathermocline anticyclonic eddy is a result of a combined effect of nighttime convection, vertical current shear, and peaks in wind speed, and must be integrated into entrainment parameterizations. This supports the findings from the Cape Ghir filament observations.
- The mixing layer depth extended deeper than the mixed layer over the entire eddy, independently of air sea heat flux cycles, and leads to favorable entrainment conditions. The entrainment rates are largely related to mixing rather than a mixed

layer which is dependent on the shape of the isopycnals of the intrathermocline eddy. This also highlights the importance of including mixing layer depths in bulk mixed layer models.

- At the eddy periphery, the surface and interfacial increase of turbulent kinetic energy dissipation rates is consistent with an enhancement of diapycnal diffusivity and a relative increase in entrainment rates. At the eddy core, the diffusivity was an order of magnitude lower. In contrast, the diapycnal diffusivity in the eddy center is enhanced at intermediate depths in agreement with diffusivities derived from the KPP parameterization, and is consistent with increased vertical current shear, high dissipation rates, and near-critical Richardson numbers, suggesting that it may be the result of deep mixing enhancement by near-inertial waves trapped inside anticyclonic eddies in the Canary Eddy Corridor.

Chapter 6: Vertical velocities in mesoscale eddies. A numerical experiment

Using a high resolution numerical model, the sources that govern the vertical velocity field inside anticyclonic eddies, including the role of vertical mixing, were analyzed. The principal conclusions of this study are:

- In the first surface layer, from the surface to the upper boundary layer, the numerical vertical velocity field exhibits a spiral wave-like pattern associated with both the tilting and vertical mixing terms. This vertical mixing is related to mesoscale structures often being intensified at the periphery of the eddies. Moreover, vertical mixing can indirectly control the surface vertical velocity field by modifying the ageostrophic forcing terms. A noticeable effect is the surface vertical velocity maximum observed in the numerical domain that results from the tendency to restore the thermal-wind balance. The diapycnal mixing is inhibited by strong stratification below the upper boundary layer. The lack of sources of kinetic energy at these depths is the result of a climatological wind forcing that precludes the generation of near-inertial waves.
- In the second subsurface layer, below the upper boundary layer, the numerical vertical velocity pattern shows a recurrent dipole-like structure at the center of

all mesoscale eddies within the numerical domain. These dipole are strongly related with vorticity. The vertical velocity dipoles slowly rotate in the sense of the eddy and variations in their intensity may be related to changes in the axisymmetrization of the eddies. The occurrence of these dipoles cannot be explained by eddy-wind interactions through Ekman pumping mechanism. The imbalance between the ageostrophic and stretching terms indicates that the breaking of the gradient-wind balance is implicated in the generation of these dipoles.

- Comparisons of vertical velocities given by the model with diagnosed vertical velocities from the omega equation show a large degree of correspondence between both vertical velocities. The analysis of a generalized omega equation shows that the divergence of the $\boldsymbol{Q}_h$ vector dominates the vertical velocity and, in particular, that the horizontal ageostrophic current field that strains the horizontal density gradient is the main forcing mechanism for the vertical velocity field at subsurface depths. The latter is consistent with the finding by the analysis from the instantaneous flux divergence.

- The occurrence of vortex Rossby waves is examined through filamentation towards the re-axisymmetrization and wave-like vertical velocity patterns. Periods from the dispersion relation are between 1.5 and 40 days. These waves represent a restoring mechanism in the axisymmetrization process by expelling potential vorticity outward from the eddy core. In turn, the axisymmetrization is related to submesoscale eddy filaments that act as barriers to passive tracers and also drive particles away from the eddy center. Vortex Rossby waves may also modulate the vertical velocity pattern through the propagation of these potential vorticity perturbations, leading to variations in vorticity and hence driving changes in vertical transport.

7.2 Future research

Next, we outline some remaining open questions arising from the results of this thesis.

1. Other sources of turbulent kinetic energy, such as radiating energy from breaking interfacial waves that impinge upon the entrained interface, and Langmuir

turbulent circulation, should be investigated for inclusion into the proposed entrainment parameterization of Chapter 4. In addition, because our suggested entrainment formulation depends on observed dissipation rates, a well correlated parameterization of the TKE-dissipation rate is needed. The wide range of existent dissipation parameterizations must be tested and validated with this aim.

2. Better algorithms are needed to determine the depth of the active mixing layer. Recent studies highlight the relevance of the mixing layer depth in the modulation of the upper ocean layer, and in the critical depth hypothesis of Sverdrup (1953) (Franks, 2014; Sutherland et al., 2014). An alternative measure of turbulence can be provided by Thorpe scales that, although dependent on the accuracy of the density profiles, may serve as good indicators of turbulent overturns.

3. An issue to be addressed is the relationship between the entrainment and frontogenesis processes. As pointed out by Capet et al. (2008b), the role of the entrainment process in maintaining or enhancing the ageostrophic secondary circulation, for example at the eddy periphery, remains unknown.

4. Previous studies should be conducted by an appropriate spatial and temporal sampling. For example, through submarine gliders with coupled turbulent microstructure sensors.

5. Further studies can be conducted in order to investigate the underlying causes of the changes in vertical velocity intensity, as well as the physical mechanisms behind the generation of the vertical velocity dipole, and the role of deep vertical mixing in their intensification. In this regard, a high resolution model solution including inter-annual surface wind forcing may help to corroborate if deep vertical mixing can disrupt/enhance the dipolar vertical velocity structure.

6. Motivated by the axisymmetrization process of Chapter 6, future studies should be conducted to corroborate whether there exists a direct relationship between intensification of vertical velocities and intermittence of the eddies deformation rate. In this regard, the implication of vortex Rossby waves in the process of axisymmetrization and subsequent intensification of the vertical velocity field must be also addressed

7. Elucidate whether isopycnal or diapycnal vertical velocities dominate the total vertical transport within mesoscale structures. In addition, the degree of influence of both diapycnal and epipycnal mixing must also be investigated. This can be done by considering an isopycnal reference frame, included into a Quasi- or Semi-geostrophic approximation. Under this framework, turbulent mixing processes would also be examined.

In general, the role of diapycnal mixing and associated turbulent processes in the ocean still needs to be resolved. Several mixing processes, including the entrainment phenomenon and diapycnal diffusivity, are often parameterized independently of the dynamic of the area under study and its physical flow characteristics. This thesis encourages future related studies where the main aim should be simplification of parameterizations to be included into high resolution models and a delineation of the role of diapycnal mixing in the vertical transport within mesoscale structures.

8

Resumen en Español

8.1 Capítulo 1: Introducción

La complejidad del estudio del océano radica en que una amplia variedad de procesos pueden tener lugar interactuando entre sí en diferentes escalas espacio-temporales. En las últimas décadas, una gran proporción de estudios han sido enfocados hacia procesos que ocurren en la mesoescala y submesoescala, cuyo impacto en la modulación del clima parece ganar cada vez más importancia (e.g., Smith et al., 2000; Capet et al., 2008c; Lévy et al., 2010; Sasaki et al., 2014; Sheen et al., 2014; Callies et al., 2015). Aunque las técnicas para medir y examinar la mesoescala y microescala han mejorado notablemente en estos últimos años (Chelton et al., 2007; Xu and Fu, 2012; Ponte et al., 2013), el principal esfuerzo de investigación se centra en enfoques más teóricos y modelos numéricos de alta resolución (e.g., Siegel et al., 2001; Mahadevan and Tandon, 2006; Capet et al., 2008b; Klein et al., 2008; Thomas et al., 2008; Ponte et al., 2013).

8.1.1 Proceso de intrusión (*entrainment*) diapicno turbulento

Desde los primeros experimentos de laboratorio de Rouse and Dodu (1955), se define al proceso de intrusión diapicna o *entrainment*[*] diapicno, como fluido turbulento dentro de una capa de mezcla débilmente estratificada que incorpora fluido adyacente desde la picnoclina altamente estratificada (Turner, 1979). Esto lo hace mediante una velocidad de *entrainment* denominada w_e. Los principales efectos de este proceso son un incremento de la capa de mezcla, el transporte de propiedades físicas y biológicas entre las capas superficiales fóticas y océano interior (e.g., Deardorff, 1983; Kolodziejczyk et al., 2015), así como la modulación de la temperatura superficial del mar y flujos de calor (e.g., Price et al., 1986; Alexander et al., 2000; Jacob and Shay, 2003; Wada et al., 2009). Además, algunos estudios teorizan que el *entrainment* diferencial podría estar implicado en el refuerzo de la circulación secundaria inducida por frontogénesis (Dewey and Moum, 1990; Capet et al., 2008b).

Sin embargo, la determinación del proceso de *entrainment* diapicno resulta en un desafío debido al enmascaramiento de estas pequeñas velocidades por movimientos a gran escala. En los modelos de capa de mezcla, se requiere la parametrización del proceso de *entrainment* para resolver y cerrar las ecuaciones unidimensionales de momento, salinidad y flujos de calor. La principal suposición de estos modelos es que la capa de mezcla no debe contener gradientes. Esto nos permite integrar el balance de la energía cinética turbulenta (ECT) desde la superficie hasta la profundidad de la capa de mezcla (h_ρ) resultando en la clásica expresión de Niiler and Kraus (1977):

$$\frac{1}{2}w_e(q^2+\delta b h_\rho-\overline{\boldsymbol{u}_h^2}) = m u_*^3+\frac{1}{2}h_\rho J_b^o + J_o(\frac{h_\rho}{2}-\frac{1}{\gamma})+\frac{1}{3}C|\overline{\boldsymbol{u}_h^3}| - \int_{-h_\rho}^{0}\varepsilon(dz) \qquad (8.1)$$

donde $q^2 = \overline{w'2} + \overline{\boldsymbol{u}_h'^2}$ es el promedio específico de ECT, $\overline{\boldsymbol{u_h}} = (u, v)$ es el campo horizontal total de la corriente, y las primas denotan desviaciones turbulentas de las velocidades totales, siendo su producto promedio el flujo vertical de momento horizontal a partir de la descomposición de Reynolds, $\overline{w'\boldsymbol{u}_h'}$. La mezcla inducida por el viento vendrá representada por la fricción del viento u_* formulada más adelante, m es una constante empírica, y $\delta b = b_1 - b_2$ es el salto de flotabilidad entre la capa 1 (en la base de la capa de mezcla) y la capa 2 (debajo de la capa de mezcla), donde $b = g(\rho_o - \rho)/\rho_o)$ y γ es el coeficiente de atenuación. El flujo superficial de flotabilidad (J_b^o) será descrito en el Capítulo 3 y $J_o \equiv (g\alpha/\rho C)I_o$ es el flujo de flotabilidad por radiación con I_o como el flujo superficial de penetración solar, $g \approx 9.81$ m s^{-2} es la constante de aceleración gravitacional, α °C^{-1} el coeficiente de expansión termal, ρ la densidad de referencia del agua de mar y C el coeficiente de dragado. Finalmente, el principal sumidero de energía en el balance vendrá dado por la tasa de disipación de energía cinética turbulenta mediante ε (Niiler and Kraus, 1977).

---

[*] En la literatura se le atribuyen diversos nombres, tales como: intrusión, entrañamiento e incluso arrastre. Sin embargo, ninguno de ellos parece englobar el real significado de la entrada de fluido no turbulento dentro de la capa de mezcla. Debido a esto, de ahora en adelante preferimos recurrir al término anglosajón del proceso denominado como *entrainment*.

Así, el sistema de la ecuación integrada (8.1) puede ser cerrado cuando se acude a una parametrización de w_e. Principalmente existen tres fuentes de ECT, las cuales a través de sus escalas de velocidad controlan el proceso de *entrainment*. Estas son: la agitación mecánica del viento inducida por la velocidad de fricción $u_* = \boldsymbol{\tau}_o/(\rho_o)^{1/2}$, donde la tensión del viento es $\boldsymbol{\tau}_o = (\tau^x, \tau^y)$. El flujo superficial de flotabilidad, cuya velocidad de escala viene dada por la convección libre de Deardorff (1970) $w_* = (J_b^o h_\rho)^{1/3}$. El último es la cizalla vertical inducida por las corrientes horizontales en la base de la capa de mezcla, cuya escala de velocidad es el salto de velocidad desde la capa 2 a la capa 1 $\delta V = \boldsymbol{u}_h^2 - \boldsymbol{u}_h^1$. Basado en este clausura de Niiler and Kraus (1977) (ec. 8.1), las parametrizaciones de w_e variarán de acuerdo a las escalas de velocidad que se tengan en cuenta en el balance.

Una forma alternativa de determinar w_e se basa en un argumento dependiente del número de Richardson global $Ri_b = (h_\rho \delta b)/v_{ECT}^2$, donde v_{ECT} puede ser cualquier fuente de ECT (u_*, w_* o δV). Esta forma alternativa subyace en la ley de *entrainment* (e.g., Ellison and Turner, 1959; Kato and Phillips, 1969; Khanta et al., 1977; Strang and Fernando, 2001), la cual puede ser vista como la relación entre el coeficiente de *entrainment* diapicno (E) y los parámetros que lo gobiernan. En consecuencia, dicha ley de *entrainment* puede tomar la forma de $E = \frac{w_e}{v_{ECT}} = \gamma_e Ri_b^{-k}$, donde γ_e y $-k$ son constantes. Dado que existen diferentes mecanismos que pueden activar el *entrainment* diapicno, varias leyes de *entrainment* han sido publicadas, no existiendo por lo tanto una ley universal unificada (Deardorff, 1983; Price et al., 1986; Fernando, 1991; Pelegrí and Richman, 1993; Strang and Fernando, 2001; Nagai et al., 2005). En consecuencia, todas estas incertidumbres hacen que el proceso de *entrainment* diapicno permanezca aún sin clarificar (Jonker et al., 2013).

8.1.2 Velocidades verticales en la mesoescala

Mientas que w_e es una velocidad diapicna que tiene lugar en la microescala, el transporte vertical neto incluye ambas componentes diapicnas y epipicnas. Ambas velocidades verticales comprenden el campo total de velocidad vertical (w).

En la mesoescala, las velocidades verticales pueden ser generadas principalmente por dos procesos: a través del mecanismo de transporte vertical de Ekman (e.g., Martin and Richards, 2001; Gaube et al., 2015) o por procesos de frontogénesis (e.g., Pollard and Regier, 1992; Nagai et al., 2006; Capet et al., 2008b). En remolinos mesoescalares, el campo de w puede estar también influenciado por patrones de ondas, las cuales son probablemente inducidas por ondas cuasi-inerciales que resultan de las interacciones del remolino con el flujo medio (e.g., Koszalka et al., 2009; 2010; Cardona and Bracco, 2012; Nardelli, 2013). Como se verá en el Capítulo 6, esas ondas son análogas a las ondas planetarias de Rossby, solo que con el gradiente radial del vorticidad vertical sirviendo como mecanismo restaurador (Montgomery and Kallenbach, 1997).

A pesar de que las velocidades verticales en el océano son pequeñas cantidades comparadas con las grandes escalas horizontales, estas pueden tener un enorme impacto en los sistemas biogeoquímicos y climáticos supliendo de nutrientes a las capas fóticas, transportando calor sal y momento, e intercambiando gases con la atmósfera. Sin embargo, similar al caso de las velocidades de *entrainment* diapicno, las velocidades verticales w son difíciles de medir y determinar debido a la falta de técnicas observacionales precisas (e.g., Vélez-Belchí and Tintoré, 2001). Hasta el momento, las estimaciones más precisas de w pueden ser llevadas a cabo mediante métodos indirectos tales como la ecuación omega en aproximación cuasi-geostrófica (Hoskins et al., 1978). La consideración de los procesos de mezcla dentro del diagnóstico de w, por otra parte, representa también un desafío, incluyendo derivadas de alto orden y parametrizaciones que dependen de Ri_b. En consecuencia, cuestiones como la influencia de la mezcla en el transporte vertical dentro de estructuras de mesoescala y su asociada submesoescala, necesitan ser investigadas con más detalle.

8.2 Capítulo 2: Motivación y Objetivos

En esta tesis, se investigan los procesos de fina y microescala turbulenta y las velocidades de submesoescala dentro de dos estructuras de mesoescala del Atlántico norte:

(i).- El filamento de afloramiento de Cabo Ghir y (ii).- Remolinos anticiclónicos del corredor de remolinos de Canarias. A continuación se detallan las principales cuestiones a ser analizadas en este trabajo.

1. Elucidar cuales son las principales fuentes de energía cinética turbulenta que controlan la capa superficial oceánica dentro de estructuras de mesoescala altamente dinámicas, tales como el filamento de Cabo Ghir. Basándonos en el balance unidimensional de la energía cinética turbulenta, establecer el estado del arte de las diferentes parametrizaciones de *entrainment* diapicno e investigar cuestiones sobre ¿cómo se ve afectado el proceso de *entrainment* al considerar la cizalla vertical inducida por corrientes horizontales en la picnoclina? ¿y por la diferencia entre la capa de mezcla y la capa de mezcla activa ?

2. Inspeccionar ambos procesos de *entrainment* y de mezcla diapicna dentro de remolinos anticiclónicos, prestando particular atención a las fuentes que conducen a un aumento de mezcla turbulenta. Enfatizando en los mecanismos de mezcla diapicna no solo en capas superficiales sino también en capas intermedias y profundas, proporcionando así una imagen completa de la mezcla diapicna dentro de remolinos anticiclónicos.

3. Investigar numéricamente los mecanismos responsables del campo de velocidades verticales dentro de remolinos anticiclónicos de mesoescala. Usando para ello un enfoque de diagnóstico doble a través de la divergencia instantánea del flujo y de la ecuación omega. Las principales cuestiones a ser tratadas son: (i) ¿Cuál es la estructura tridimensional del campo de velocidades verticales y cuáles son los mecanismos que la fuerzan? (ii) ¿Cuál es la contribución de la mezcla vertical en modular el campo de velocidad vertical? (iii) ¿Cuál es la importancia de las interacciones remolino-viento a través de los mecanismos de la succión y bombeo de Ekman? (iv) ¿Están las ondas de vórtice de Rossby presentes en el modelo? en tal caso, ¿cuál es su papel en el forzamiento del campo de velocidades verticales?

8.3 Capítulo 3: Material y Metodología

8.3.1 Datos *in situ*

Los datos tratados en esta tesis fueron adquiridos durante dos campañas oceanográficas en el marco de los proyectos: (1).- Procesos de Mezcla en la Cuenca Canaria (PROMECA) y (2).- Estudio de la bomba vertical oceánica en remolinos de mesoescala (PUMP). PROMECA fue llevada a cabo en la región de Cabo Ghir, en la costa del noroeste de África, cuyo detallado estudio del filamento de afloramiento se incluye en el Capítulo 4. La campaña PUMP fue realizada al suroeste de las Islas Canarias para el muestreo de un remolino anticiclónico intratermoclina en el Capítulo 5. Adicionalmente, también se describe el estudio de velocidades verticales dentro de remolinos anticiclónicos del Corredor de Remolinos Canario (Sangrà et al., 2009, CRC) mediante un modelo de alta resolución numérica en el Capítulo 6. En la Figura 8.1 se representan ambas áreas de estudio a través del mapa de energía cinética de remolinos (EKE, por sus siglas en inglés).

En ambas campañas, se utilizó una sonda de conductividad, temperatura y profundidad (CTD por sus siglas en nglés) SBE911+, para adquirir perfiles verticales de temperatura (T), salinidad (S) y densidad (ρ) promediados a 1 dbar previa calibración. Durante ambos cruceros, las velocidades de la corrientes fueron también continuamente registradas mediante un perfilador de corriente doppler (SADCP por sus siglas en inglés). Los datos del SADCP fueron procesados de acuerdo a Firing et al. (1995) operando a 75 KHz. El procesado para ambas campañas fue usado para obtener tamaños de celdas verticales de 10 m en el caso de PROMECA y de 8 m para PUMP, todos promediados en intervalos de 2 horas. Solamente para la campaña PUMP, se adquirieron datos de corrientes adicionales a través de un ADCP montado en la roseta junto con el CTD (LADCP). Estos perfiles fueron también promediados a 8 m para mantener la consistencia con los datos del SADCP y fueron procesados mediante el método de velocidad de cizalla descrito en Firing and Gordon (1990) y Fischer and Visbeck (1993).

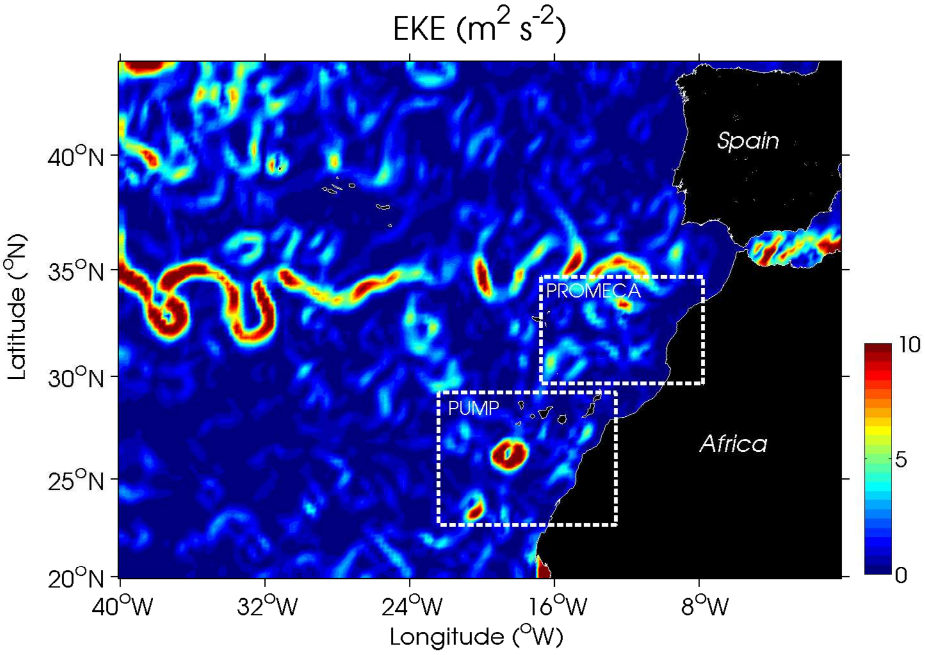

Figure 8.1: Mapa de energía cinética de remolinos, EKE (m^2 s^{-2}), derivado de los productos de altimetría de AVISO. La instantánea corresponde a la fecha 01 de enero de 2014. Los recuadros blancos delimitan las áreas de estudio comprendidas en esta tesis. El recuadro superior muestra la región del filamento de Cabo Ghir estudiada en el proyecto PROMECA del Capítulo 4. El recuadro inferior delimita el inicio del corredor de remolinos canario (Sangrà et al., 2009), como parte del proyecto PUMP examinado en los Capítulos 5 y 6.

8.3.2 Cantidades meteorológicas y flujos superficiales

Los parámetros meteorológicos estándar fueron continuamente registrados por las estaciones meteorológicas montadas en ambos buques *R/V García del Cid* de la campaña PROMECA y *BIO Hespérides* para la campaña PUMP. Estas estaciones consisten en ocho sensores de velocidad promedio e instantánea del viento, dirección del viento, temperatura del aire (T_{air}) y del agua de mar (T_{sw}), humedad relativa, presión del aire y radiación solar a intervalos de 2 minutos. Para mantener consistencia temporal con las medidas hidrográficas, estos parámetros meteorológicos fueron promediados en intervalos de 2 horas, siendo esta la resolución temporal de cada perfil de CTD.

Los datos meteorológicos fueron usados para calcular el flujo neto superficial de calor (J_q^o) como la suma de cuatro componentes: $J_q^o = J_q^{Sw} + J_q^{Lw} + J_q^{Se} + J_q^{La}$, donde J_q^{Sw} es la radiación de onda corta directamente obtenida de la estación meteorológica. J_q^{Se} y J_q^{La} son los flujos superficiales de calor sensible y latente, respectivamente. La radiación de onda larga (J_q^{Lw}) es estimada siguiendo la expresión de Berliand and Berliand (1952):

$$J_q^{Lw} = E_{Lw}\sigma T_{air}^4(0.39 - 0.5\sqrt{e}_a)F_c - 4E_{Lw}\sigma T_{air}^3(T_{sw} - T_{air}) \tag{8.2}$$

donde $E_{Lw} = 0.985$ es la emisión de onda larga de Dickey et al. (1994), $\sigma = 5.67 \times 10^{-8}$ m^{2}K^{-4} es la constante de Stefan-Boltzman, e_a es la presión del vapor y F_c es el factor de corrección debido a la nubosidad. Los flujos superficiales de calor sensible y latente son determinados a través del código *TOGA-COARE*[*] por sus siglas en inglés, que se describe en Fairall et al. (1996).

Una vez obtenidos los flujos superficiales de calor, se obtienen los flujos superficiales de flotabilidad

$$J_b^o = \frac{g}{\rho_o}\left(\frac{\alpha J_q^o}{C_p}\right) + g\beta(E - P)So \tag{8.3}$$

donde C_p es la capacidad de calor específico del agua de mar, α y β son los coeficientes de contracción termales y salinos respectivamente. El primer término corresponde al flujo de flotabilidad termal (J_b^T), mientras que el segundo término da cuenta de la contribución salina (J_b^S) (Dorrestein, 1979), donde So es la salinidad superficial y $(E - P)$ es la diferencia entre tasas de evaporación y precipitación.

8.3.3 Procesamiento de datos de microestructura

En ambas campañas se usó un perfilador de microestructura TurboMAP-L (Wolk et al., 2002) para adquirir tasas de disipación de energía cinética turbulenta (ε_o). Este perfilador contiene sensores de microestructura que incluyen dos sondas de cizalla y un termistor FP07, además de sensores de CTD, y acelerómetros montados internamente. El instrumento cae en caída libre a una velocidad media de $\sim$ 0.7 m s^{-1} a la vez que muestrea a una tasa de 512 Hz. Todos los datos fueron promediados en celdas verticales de 8 m a partir de los 16 m hasta $\sim$ 500 m de profundidad y al menos cada perfil se repitió tres veces en el mismo lugar.

---

[*] Mediante las rutinas Matlab AirSea toolbox (versión 3.0; http://sea-mat.whoi.edu)

Las ε_o son obtenidas, previo filtrado, a partir de multiplicar el espectro de frecuencia por la velocidad vertical del perfil, obteniendo así el espectro de número de onda $\psi(k)$, siendo k el número de onda. Bajo la suposición de turbulencia isotrópica (Hinze, 1979), el observado perfil de ε_o se estima integrando el espectro de número de onda dentro de un rango apropiado de número de onda según Oakey (1982):

$$\varepsilon_o = \frac{15}{2}\nu \int_{k_1}^{k_2} \psi(k)dk \tag{8.4}$$

donde $\nu = 1\times10^{-6}$ m^2 s^{-1} es el coeficiente de viscosidad molecular, el número de onda de corte más bajo es $k_1 = 1$ cpm, mientras que el límite superior de integración es k_2 usualmente tomado como el número de onda de Kolmogorov $k_c = (2\pi)^{-1}(\varepsilon\nu^{-3})^{1/4}$. Seguidamente, el espectro de cizalla es ajustado al espectro universal para la turbulencia de Nasmyth (Oakey, 1982; Wolk et al., 2002).

8.3.4 Datos de satélite

Con el objetivo de discernir la localización, evolución y cobertura del filamento de afloramiento de Cabo Ghir durante la campaña PROMECA, se obtuvieron imágenes de temperatura superficial del mar y de clorofila, mediante el espectro-radiómetro de resolución moderada (MODIS), a bordo de los satélites AQUA y TERRA. Las imágenes fueron descargadas de la página `http://oceancolor.gsfc.nasa.gov` para su posterior análisis. Un ejemplo puede verse en la Figura 8.3 del Capítulo 4.

Por otro lado, la señal de las estructuras de mesoescala es claramente detectable en datos de anomalía del nivel del mar, debido a que encuentran en balance geostrófico. Estos datos son proporcionados por los productos de altimetría de AVISO a una resolución espacial de 1/4° × 1/4°, descargados vía OpenDAP desde la página web de AVISO (`http://www.aviso.altimetry.fr/en/home.html`). Un ejemplo de los productos derivados de estos mapas puede observarse en la Figura 8.9a del Capítulo 5.

8.3.5 Modelo numérico: ROMS

Los resultados y análisis del Capítulo 6, se basan en las salidas de un modelo de alta resolución numérico: ROMS, en el marco del proyecto PUMP. ROMS es un modelo de ecuaciones primitivas, de superficie libre con aproximación de Boussinesq y balance de momento hidrostático vertical, el cual usa un sistema de coordenadas ortogonales

curvilíneas en la horizontal y coordenadas sigma en la vertical (Haidvogel and Beckmann, 1999). La densidad ρ es una variable diagnóstico en ROMS calculada por la ecuación de estado del agua de mar, y la velocidad vertical w es también diagnosticada a partir de la divergencia del flujo $\boldsymbol{\nabla} \cdot \boldsymbol{u}_h + \partial_z w = 0$.
Los procesos de mezcla vertical a escala de sub-celda son parametrizados usando una formulación de capa límite no local "non-local K-profile planetary" (KPP, por sus siglas en inglés) cuya detallada explicación se encuentra en Large et al. (1994).

Table 8.1: Características de la configuración del modelo ROMS de (Mason, 2009) usado en esta tesis, así como los forzamientos iniciales y condiciones de frontera interpoladas en el grillado del modelo.

Configuración del Modelo	
Resolución horizontal	1 km
Tiempo	3 años
Dimensiones de la grilla	592 × 612
Capas sigma	60
Profundidad mínima	0.08 m
Forzamientos iniciales	
Condiciones de frontera lateral y condiciones iniciales	NEAClim 0.1° climatología[a]
Flujos superficiales atmosféricos (E-P)	COADS 1° climatología[b]
Tensión del viento superficial	SCOW 0.25° climatología[c]
Temperatura superficial del mar	Mensual 4-km Global producto de NOAA/NASA AVHRR[d]
Altura de la superficie del mar	15-años climatología de AVISO SLA AVISO data
Topografía	GEBCO[e]

[a] DIVA climatología de Troupin et al. (2010)
[b] Set de datos Comprehensive Ocean-Atmosphere (da Silva et al., 1994; Worley et al., 2005)
[c] Climatología de escaterómetro (8-años) de Scatterometer Climatology of Ocean Winds, basado en QuickSCAT (Risien and Chelton, 2008)
[d] de Kilpatrick et al. (2001)
[e] Batimetría de General Bathymetric Chart of the Ocean dataset (Hunter and Macnab, 2003)

Las salidas del modelo ROMS usadas en esta tesis fueron configuradas por Evan Mason como parte de su tesis de doctorado (Mason, 2009), mediante el uso de la variante del núcleo de ROMS de UCLA (Shchepetkin and McWilliams, 2005; 2009). Detalles de su validación se encuentran en Mason (2009) y en sus artículos relacionados (Mason et al., 2010; 2011; 2012). La Tabla 8.1 provee un resumen de las principales características relacionadas con esta configuración

8.4 Capítulo 4: Velocidades de *Entrainment* en un Filamento de Afloramiento de Margen Este

8.4.1 Introducción

Uno de los principales mecanismos por el cual la capa superficial del océano débilmente estratificada es controlada, es mediante el fenómeno de *entrainment* diapicno. Este proceso está implicado en el incremento temporal de la capa de mezcla y en el transporte de trazadores y propiedades biológicas. A pesar del considerable esfuerzo en clarificarlo (e.g., Deardorff, 1983; Dewey and Moum, 1990; Fernando, 1991; Pelegrí and Richman, 1993; Anis and Moum, 1994; Jacob and Shay, 2003; Nagai et al., 2005; Sun and Wang, 2008; Jackson and Rehmann, 2014), solo unos pocos observacionales estudios han llevado a cabo la comparación de las diferentes parametrizaciones de *entrainment* diapicno propuestas en la literatura. Por ejemplo, Anis and Moum (1994), mediante el uso de perfiles turbulentos de microestructura en condiciones convectivas, observan que diversas parametrizaciones de *entrainment* difieren en un factor de dos. Nagai et al. (2005) sugiere incluso que la ley de *entrainment* no puede ser representada como una simple suma de sus contribuciones.

La determinación de w_e es a su vez necesaria para cerrar los modelos de energía cinética turbulenta uni-dimensionales. De esta forma, su parametrización puede ayudar a examinar el papel de las diferentes fuentes de ECT que modulan la capa superior oceánica, particularmente en áreas altamente dinámicas tales como los filamentos de afloramiento. En dichas áreas, varias fuentes y escalas espacio-temporales pueden coexistir. Sin embargo, pocos estudios relacionan el aumento de ECT en regiones de filamento a través de este enfoque. Por ejemplo, Dewey and Moum (1990) muestran que el *entrainment* diapicno inducido por el viento es más eficiente en el lado frío del frente, donde la picnoclina se levanta hacia la superficie. Ellos también sugieren que el *entrainment* diapicno podría ser un proceso mediante el cual se mantiene la señal superficial fría de los filamentos de afloramiento. Recientemente, Grodsky et al. (2008) relaciona el aumento de *entrainment* diapicno con una extrema floración fitoplanctónica en el afloramiento del Atlántico Ecuatorial.

En este capítulo nos centramos en la cizalla vertical inducida por las corrientes horizontales como fuente de ECT, la cual puede jugar un importante papel en áreas frontales tales como los filamentos de afloramiento. Esto se debe a que dentro de los filamentos, la baroclinicidad puede incrementar los niveles de cizalla vertical en la base de la capa de mezcla. El aumento de cizalla vertical, podría estar asociado con un acrecentamiento de la mezcla turbulenta dentro de la termoclina (Schafstall et al., 2010), así como con regiones de alta difusión vertical (Barton et al., 2001).
A través de las primeras observaciones de ε_o para esta región, el grado en el que la mezcla turbulenta afecta a los filamentos y su relación con el proceso de *entrainment* diapicno podrán ser también determinados. Algunos estudios observacionales de perfiles turbulentos de microestructura apuntan a un incremento de ε_o debajo de la capa de mezcla, asociados a frentes y filamentos (Dewey et al., 1993; Nagai et al., 2009; Johnson et al., 2012). Sin embargo, el efecto de la cizalla vertical no se encuentra integrada dentro de la mayoría de las parametrizaciones de w_e. Adicionalmente, el efecto de ε_o[*] podría ser significativo dentro de aguas de filamento. En consecuencia, se requiere una investigación de las contribuciones de tales parámetros en la zona de *entrainment* diapicno dentro de frentes termohalinos.

8.4.2 Caso estudio: Filamento de afloramiento de Cabo Ghir

Los datos hidrográficos utilizados en este estudio corresponden al muestreo realizado en el marco del proyecto PROMECA, llevado a cabo en la región de Cabo Ghir al noroeste de África (Figura 8.2). Los datos constan de perfiles verticales de CTD, XBT y SADCP, y perfiles de microestructura muestreados cada $\sim$ 10 km entre el 18 y el 29 de octubre de 2010[†].

8.4.3 Parametrizaciones de *entrainment* diapicno

A lo largo de las últimas décadas se han propuesto diferentes formulaciones para el cálculo de w_e. Este estudio se centra en dos enfoques principales. En el primero, w_e es derivada a partir de un balance de ECT, siguiendo el modelo de capa de mezcla de Niiler and Kraus (1977) (Capítulo 1, ec. 8.1). En el segundo enfoque, w_e puede ser obtenida a través de la relación entre el número de Richardson global y el coeficiente

---

[*] En varios modelos de capa de mezcla, ε_o es considerado como una cantidad constante

[†] ver Capítulo 3

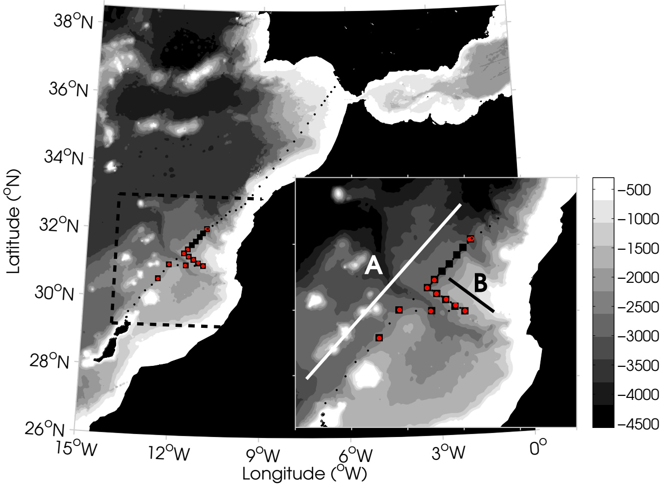

Figure 8.2: Batimetría de la región de estudio en intervalos de 500 m. Se muestran las estaciones hidrográficas medidas en las vecindades del filamento de afloramiento de Cabo Ghir al noroeste de África en octubre de 2010. La región englobada dentro del recuadro de líneas discontinuas delimita las estaciones hidrográficas utilizadas en esta tesis. La región de estudio se amplifica para su mejor visualización en la figura superpuesta de la esquina izquierda inferior. Los cuadrados negros muestran las estaciones CTD, junto con las medidas de ADCP; los puntos en rojo denotan estaciones de microestructura; mientras que los pequeños puntos en negro son perfiles de XBT no utilizados en este resumen pero sí en el Capítulo 4 de esta tesis en inglés. Los transectos A, y B son también indicados.

de *entrainment* diapicno (e.g., Khanta et al., 1977; Strang and Fernando, 2001) (ver definición de Ri_b y E en Capítulo 1).

Para el primer enfoque, la parametrización de w_e utilizada en este estudio es originaria del modelo de capa de mezcla de Gaspar (1988) (de ahora en adelante w_e^G), donde la evolución temporal de la capa de mezcla puede ser calculada a partir de

$$w_e^G = \frac{(m_1 + m_2)u_*^3 + 0.5h_\rho J_b^o - \overline{\varepsilon_p}h_\rho}{0.5(\delta b h_\rho)} \tag{8.5}$$

donde $m_1 = 2.6$ y $m_2 = 1.9$ son constantes empíricas y ε_p es la parametrización de la tasa de disipación de ECT. Añadiendo el término de inestabilidad dinámica, $DIT = 0.5w_e(\delta u^2 + \delta v^2)$, a w_e^G (eq. 8.5), es posible incluir el efecto de la cizalla vertical al cuadrado, $Sh^2 = (\partial_z u)^2 + (\partial_z v)^2$, como una fuente de ECT, obteniendo así:

$$w_e^{GS2} = \frac{(m_2 + m_3)u_*^3 + 0.5h_\rho J_b^o - \overline{\varepsilon_p} h_\rho}{0.5[(\delta b h_\rho) - (\delta u^2 + \delta v^2)]} \tag{8.6}$$

La ec. (8.6) (de ahora en adelante w_e^{GS2}), ha sido previamente implementada en el modelo de Samson et al. (2009) para examinar la respuesta de la capa de mezcla durante el paso de un huracán sobre el océano.

Para el segundo enfoque, se obtiene w_e a partir de un método alternativo basado en la ley de *entrainment* diapicno (e.g., Ellison and Turner, 1959; Kato and Phillips, 1969; Khanta et al., 1977; Strang and Fernando, 2001). Se ha considerado que una comparación con una parametrización de w_e basada en dicha ley de *entrainment* diapicno, podría ayudar a discernir si el flujo de cizalla ejerce un papel relevante en la dinámica de la capa de mezcla en aguas de filamento. La parametrización de w_e elegida es la propuesta por Strang and Fernando (2001) (de ahora en adelante w_e^{SF}). En su experimento de laboratorio, ellos discriminan tres regímenes de w_e basándose en un número de Richardson de cizalla, $Ri_v = h_\rho \delta b(\delta V)^{-2}$, tal que:

$$\begin{aligned} E_v &= 0.024 && si && Ri_v < 1.5 \\ E_v &= 0.22 Ri_v^{-2.6} && si && 1.5 < Ri_v < 5 \\ E_v &= 0.02 Ri_v^{-1.3} && si && Ri_v > 5 \end{aligned} \tag{8.7}$$

De acuerdo a esta relación, w_e tomarán la simple forma de $w_e^{SF} = E_v \delta V$.

8.4.4 Hidrografía del filamento

Se describe a continuación las características generales hidrográficas del filamento para los días del muestreo.

La estructura en forma de meandro se identifica como una señal fría con alta concentración de clorofila que cruza ambos transectos A y B (Figura 8.3). Las aguas del filamento tiene una diferencia de ∼ 2°C con respecto a las aguas circundantes, y están altamente condicionados por la dinámica de mesoescala del área, tal y como se observa en las corrientes geostróficas superpuestas en la Figura 8.3.

La señal del filamento se intensifica después de la última estación de CTD número 50, cuando se registra una fuerte intensidad del viento. La descripción general de

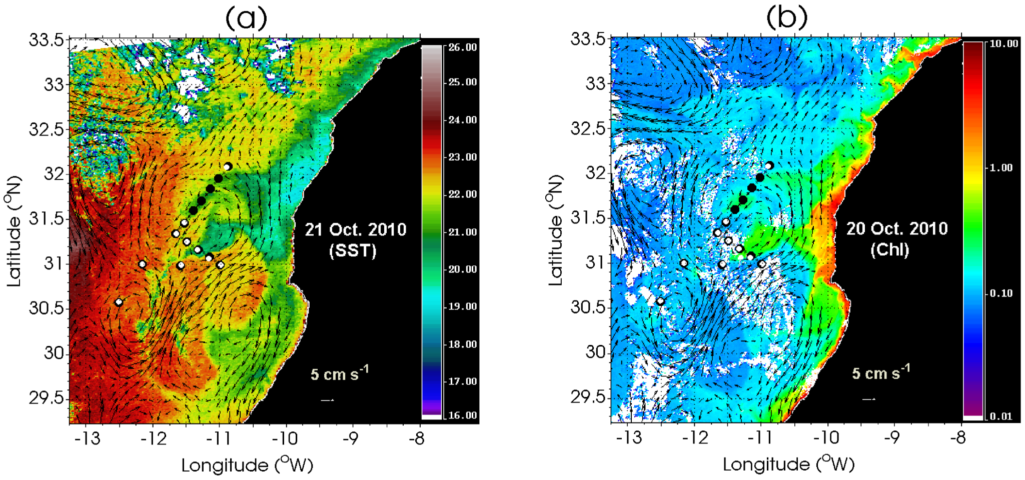

Figure 8.3: Mapas instantáneos de (a) temperatura superficial del mar de MODIS-Terra en °C para el 21 de octubre de 2010 a las 14:25 pm y (b) Clorofila de MODIS-Aqua para el 21 de octubre de 2010 a las 13:45 pm. Los vectores superpuestos denotan la magnitud y dirección del campo de velocidades geostróficas derivados de datos de altimetría de AVISO, a una resolución horizontal de 1/4°. Las estaciones CTD+ADCP son mostradas como puntos en negro. Las estaciones de microestructura son representadas mediante puntos en blanco.

este filamento coincide con anteriores estudios observacionales de los filamentos de afloramiento africano (e.g., Barton et al., 2001; Hagen, 2001), especialmente con el estudio de Pelegrí et al. (2005b), llevado a cabo en el mismo filamento y estación del año, pero durante los años 1995 y 1997.

Las secciones verticales de salinidad y anomalía de la densidad potencial (σ_θ), en la Figura 8.4, muestran un levantamiento de las isohalinas e isopicnas en las estaciones situadas más hacia el noreste del transecto A (Figuras 8.4a y b). Esta estructura en forma de domo de las isopicnas parece coincidir con las estaciones afectadas por el filamento, de acuerdo a las imágenes de satélite (Figuras 8.3a y b).

El transecto B, más cercano a la costa africana, muestra una abrupta subida de las isopicnas e isohalinas (Figuras 8.4c y d) desde la estación 44 a la 48. En general, parece que este ascenso de las isopicnas afecta a los primeros 200 m de la columna de agua, particularmente en las estaciones localizadas en aguas de filamento. Este resultado,

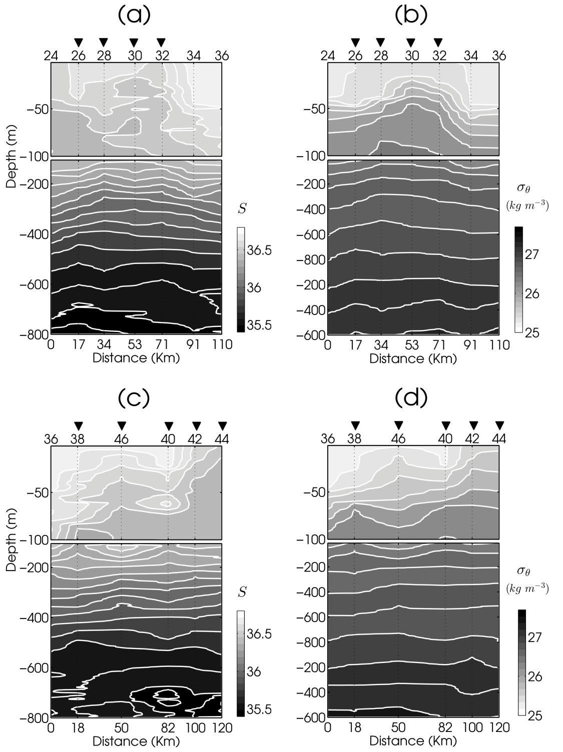

Figure 8.4: Secciones vertical hidrográficas derivadas de los perfiles de CTD de salinidad, S, y (b) anomalía de la densidad potencial, σ_θ (kg m^{-3}), para el transecto A. De forma análoga, (c) S, y (d) σ_θ lo son para el transecto B. Contornos de S son trazados en intervalos de 0.5, mientras que los contornos de σ_θ son representados cada 0.1 kg m^{-3}. La distancia acumulativa entre las estaciones en km se muestra en la parte inferior. En la parte superior de la figura se muestran los correspondientes números de las estaciones hidrográficas. Los triángulos invertidos muestran las estaciones influenciadas por las aguas de filamento.

concuerda con lo encontrado por Pelegrí et al. (2005b), quienes sugieren el origen del filamento en niveles someros de la columna de agua.

Mediante las imágenes de satélite y secciones verticales hidrográficas, se concluye que las estaciones pueden ser separadas en dos grupos. El primer grupo comprende aquellas estaciones influenciadas por el filamento de afloramiento desde la estación 26 a la 32 del transecto A y desde la estación 38 a la 46 del transecto B, al cual se le denomina grupo-F. El segundo grupo cubre el resto de estaciones que no están directamente influenciadas por la estructura de mesoescala, denominado como grupo-nF. Estas son la estación 24 y de la 34 a la 36 de la sección A, y de la 48 a la 50 de la sección B. Un estudio relacionado de Arcos-Pulido et al. (2014), el cual usa la misma base de datos que en este trabajo, muestra que el primer grupo-F experimenta un incremento en la concentración de nutrientes debajo de la capa de mezcla.

8.4.5 Condiciones meteorológicas

Los flujos superficiales de calor y flotabilidad muestran un ciclo regular diurno donde ambos son positivos durante condiciones nocturnas (Figuras 8.5a y b)*. Los flujos superficiales de flotabilidad debidos a la contribución salina fueron siempre menores a la contribución termal, difiriendo en un orden de magnitud. Durante la noche, las mayores aportaciones al flujo de calor neto superficial vienen dadas por los flujos calor latente y por la radiación de onda larga (Figura 8.5a).

Débiles vientos del noreste prevalecieron durante el crucero, con un aumento en los días finales del muestreo (Figura 8.5d). Este patrón de vientos es característico de esta estación en la cual los vientos Alisios son menos intensos.

Debido a que tanto $\boldsymbol{\tau_o}$ como J_q^o pueden actuar como mecanismos de forzamiento para el aumento de mezcla en la capa de mezcla, se investiga la relación de ambos acudiendo a la escala de Monin-Obukhov (L_{mo}, Figura 8.5e). Esta escala indica la profundidad a la cual ambos forzamientos mecánicos y convectivos son comparables: $L_{mo} = -\frac{u^{*3}}{\kappa J_b^o}$, donde $\kappa = 0.4$ es la constante de von Kármán. Escalas $L_{mo} > 0$ (Figura 8.5e) indican que la turbulencia generada por la agitación del viento se suprime por una estratificación estable, que ocurre durante tiempos diurnos. Mientras que $L_{mo} < 0$ tiene lugar durante condiciones inestables de convección nocturna. Además, se observa que $|L_{mo}|$ es generalmente más somero que la capa de mezcla (Figura 8.5e), sugiriendo que la mezcla inducida por el viento no podría ser una fuente de energía suficiente para controlar la profundidad total de la capa de mezcla.

8.4.6 Mezcla activa en aguas de filamento

Varios autores han reportado la necesidad de considerar una región de frontera de elevada y activa mezcla en la base de la capa de mezcla (e.g., Dewey and Moum, 1990; Brainerd and Gregg, 1995; Nagai et al., 2005; Inoue et al., 2010; Sutherland et al., 2014),

---

*Los flujos netos de calor y flotabilidad fueron calculados como se describe en el Capítulo 3

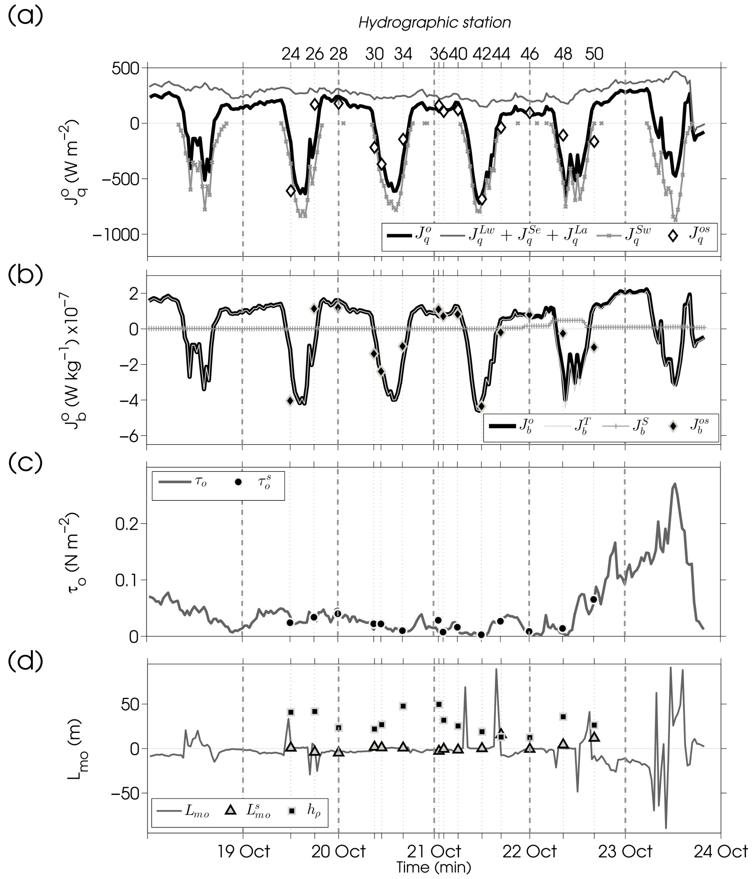

Figure 8.5: Datos meteorológicos promediados en intervalos de media hora. (a) flujo neto superficial de calor, J_q^o (positivo desde océano hacia atmósfera), y sus componentes relacionados: radiación de onda corta, J_q^{Sw}, flujo de calor de onda larga J_q^{Lw}, flujo de calor latente, J_q^{La}, y flujo de calor sensible, J_q^{Se}; (b) flujo neto superficial de flotabilidad, J_b^o, definido como la suma de sus contribuciones termales, J_b^T, y salinas J_b^S; (c) tensión del viento $\boldsymbol{\tau}_o$; (d) escala de Monin-Obukhov, L_{mo}, y profundidad de la capa de mezcla, h_ρ. Los símbolos sobre las series temporales denotados con el superíndice s representan el valor exacto de cada cantidad meteorológica, calculada a partir de los datos de cada perfil de CTD. Las líneas finas verticales muestran cada estación hidrográfica. Las líneas verticales gruesas indican el final de cada día muestreado.

usualmente referida como capa de mezcla activa (h_ε). La diferencia con la clásica capa de mezcla h_ρ, radica en que h_ε es la profundidad a la cual los procesos turbulentos son activos y trabajan para mezclar los flujos de calor de la capa superficial en un momento dado. Mientras, h_ρ representa la profundidad a la cual esos flujos superficiales han sido mezclados en un pasado reciente, por lo que puede verse como la historia integrada de dichos eventos de mezcla activa. Por lo tanto, dependiendo de la escala de tiempo y de la resolución espacial de estudio, h_ε podría ser más apropiada que h_ρ (Brainerd and Gregg, 1995; Franks, 2014; Sutherland et al., 2014).

A veces, la capa de mezcla activa se extiende a mayor profundidad que la capa de mezcla (Dewey and Moum, 1990; Brainerd and Gregg, 1995; Inoue et al., 2010). El incremento de la turbulencia debajo de h_ρ podría estar relacionado con inestabilidades de cizalla provocada por ondas internas como resultado de plumas convectivas incidiendo en el fondo de la h_ρ (Moum et al., 1989). Algunos autores han reportado que el proceso de *entrainment* diapicno solo puede tener lugar cuando h_ε excede h_ρ (Dewey and Moum, 1990; Inoue et al., 2010), es decir, cuando la mezcla es lo suficientemente intensa para sobreponerse a los efectos de la estratificación en la picnoclina. En este estudio, se considera que la zona de *entrainment* diapicno Δh, cuando positiva, dará lugar a $w_e > 0$. Esta zona se define como $\Delta h = h_\varepsilon - h_\rho$.

La base de la capa de mezcla, se determina siguiendo el algoritmo de Holte and Talley (2009), y coincide además con el máximo gradiente superficial de la frecuencia de flotabilidad, $N^2 = -g/\rho_o \partial_z \rho$. La base de la capa de mezcla activa se determina cuando el perfil de disipación desciende en dos órdenes de magnitud desde la superficie. Sin embargo, los perfiles de ε_o no siempre muestran una clara transición energética. Por lo tanto, una escala turbulenta, tal como la escala de Ozmidov L_o (Ozmidov, 1965), podría ayudarnos a clarificar la extensión de la mezcla activa, donde $L_o = \sqrt{\varepsilon_o/N^3}$.

Un ejemplo puede verse en la Figura 8.6, donde $h_\varepsilon > h_\rho$ para la estación 42 del grupo-F (Figuras 8.6a y b). En contraste, la estación 48 del grupo-nF (Figuras 8.6c y d) muestra que tanto h_ε como h_ρ son comparables en profundidad. Ambas estaciones fueron medidas durante condiciones diurnas. Además, el débil régimen de vientos y las escalas de L_{mo} (Figura 8.5d y e), indican que la generación de turbulencia dentro del filamento podría deberse a otras fuentes a parte de la del viento. Por ejemplo, a turbulencia generada por cizalla vertical y flujos de flotabilidad en la base de h_ρ.

La Figura 8.7 muestra este resultado de forma más general, indicando que las estaciones de grupo-F (8.7) tienen Δh positivos. Esto sugiere que solo esas estaciones son susceptibles de experimentar *entrainment* diapicno (Dewey and Moum, 1990). Los elevados niveles de ε_o en las estaciones del grupo-F, junto con capas de mezcla someras

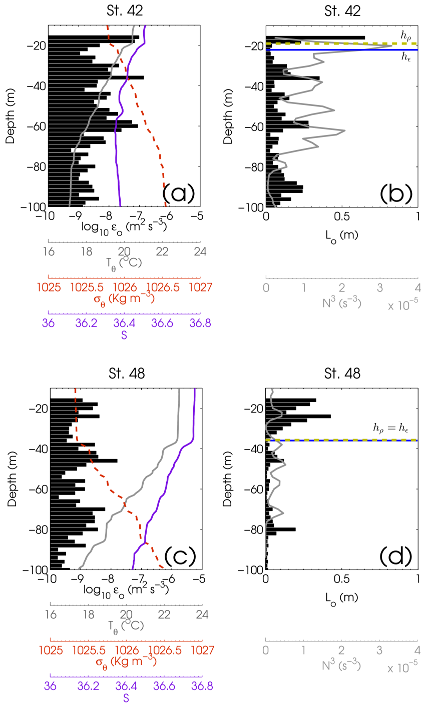

Figure 8.6: Perfiles verticales hidrográficos y de microestructura. Las figuras de la izquierda muestran T_θ (gris), σ_θ (rojo) y S (violeta), superpuestas a perfiles de ε_o (barras negras) correspondientes a: (a) estación 42 del grupo-F; y (c) la estación 48, del grupo-nF. Ambas estaciones fueron medidas durante estables condiciones diurnas. Las figuras de la derecha muestran las escalas de Ozmidov, L_o (barras negras), y los perfiles de N^{-3} (gris) para (b) la estación 42 y (d) la estación 48. Las líneas horizontales amarillas y azules denotan h_ρ y h_ε, respectivamente.

como resultado del levantamiento de las isopicnas, podrían explicar el aumento de mezcla activa en esas estaciones.

8.4.7 Cizalla vertical como forzamiento de w_e

Parece razonable pensar que la cizalla vertical en la base de la capa de mezcla juega un relevante papel en el proceso de *entrainment* diapicno (Price et al., 1978; Jacob and Shay, 2003; Wada et al., 2009), particularmente en las estructuras de filamento, donde los efectos baroclinos podrían ser importantes (Pelegrí et al., 2005b; Troupin et al., 2012). Sin embargo, este término de cizalla no es tenido en cuenta en la mayoría de los

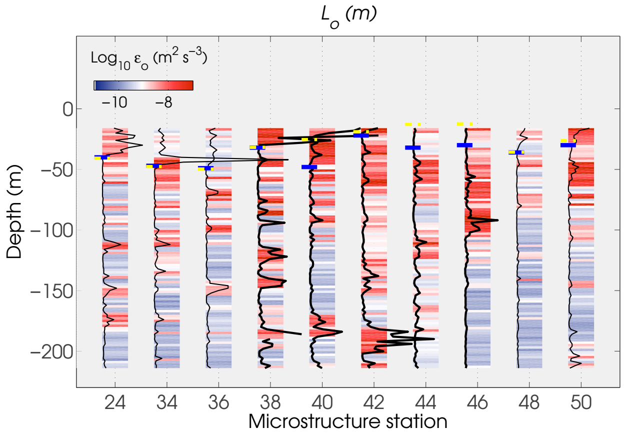

Figure 8.7: Perfiles verticales de las escalas de Ozmidov L_o para cada estación de microestructura. En el fondo se muestran perfiles de ε_o. El máximo valor de L_o corresponde a 5.18 m para la estación 34 a 42 m de profundidad, y el mínimo valor de L_o de 0.0045 m fue registrado en la estación 38 a 66 m de profundidad. Las estaciones del grupo-F se destacan de las del grupo-nF a través de perfiles verticales gruesos. Las líneas horizontales verdes y azules indican la profundidad de h_ρ y h_ε, respectivamente.

modelos de capa de mezcla (Gaspar, 1988).

A este respecto, para examinar el papel de la mezcla impulsada por la cizalla en la base de la capa de mezcla, se lleva a cabo un análisis comparativo entre tres parametrizaciones de *entrainment*: w_e^G, w_e^{GS2} y w_e^{SF}, anteriormente descritas. Como se esperaba, w_e^{GS2} somete un aumento de w_e en todas las estaciones cuando se compara con w_e^G. El aumento es más pronunciado en las estaciones del grupo-F: 28, 44 y 46, con diferencias de $\sim 4 \times 10^{-4}$ m s^{-1}. La última estación 50, también muestra elevados w_e, probablemente debido a la influencia de una estructura ciclónica de mesoescala* observada en las imágenes de satélite (Figuras 8.3a y b).

En estaciones medidas durante condiciones diurnas, w_e^G exhibe velocidades negativas (Figura 8.8a), resultando en una ausencia de w_e o retroceso de la capa de mezcla (Gaspar, 1988). Esto indica que el forzamiento del viento por sí solo es ineficiente para inducir mezcla debajo de la capa de mezcla. Por otro lado, w_e^{SF} siempre arroja velocidades diapicnas positivas debido a su dependencia con Ri_v, mostrando un aumento de w_e en la mayoría de las estaciones del grupo-F (Figura 8.8a).

---

*La influencia del *entrainment* diapicno en un remolino de mesoescala será posteriormente analizada en el Capítulo 4.

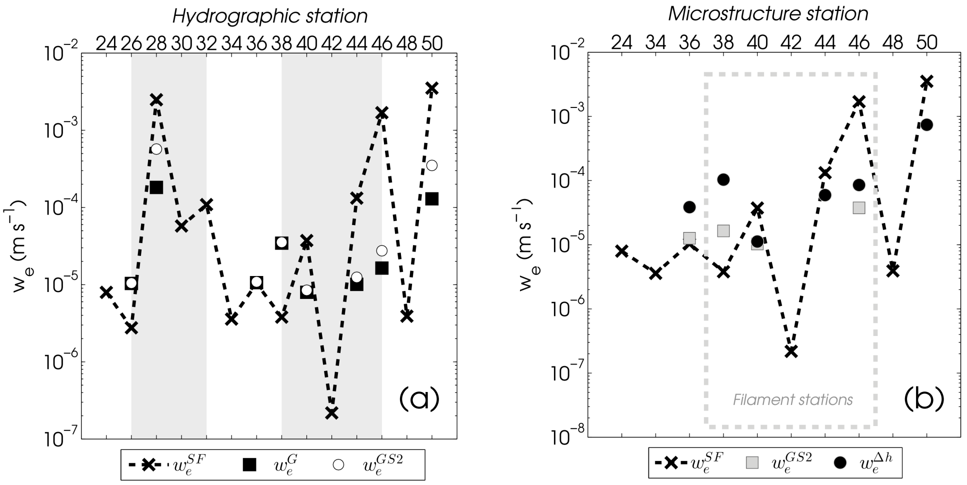

Figure 8.8: (a) Velocidades diapicnas w_e obtenidas mediante tres parametrizaciones: w_e^G, en la cual el efecto de la cizalla vertical no es tenido en cuenta en su parametrización. w_e^{GS2}, en cuya formulación viene incluido el término DIT de cizalla vertical. w_e^{SF}, basada en un enfoque dependiente de Ri_v. Las áreas sombreadas indican aquellas estaciones pertenecientes al grupo-F. (b) Comparación entre velocidades diapicnas w_e dadas por las parametrizaciones de w_e^{SF}, w_e^{GS2}, y $w_e^{\Delta h}$. Las estaciones de microestructura potencialmente influenciadas por el filamento son destacadas en el rectángulo de líneas discontinuas.

8.4.8 Nuevo enfoque del *entrainment* diapicno

De acuerdo con Dewey and Moum (1990), Inoue et al. (2010), y medidas directas de h_ε, se restringe el análisis a aquellas estaciones donde se satisfacen ambas condiciones de disponibilidad de ε_o y $\Delta h > 0$.

De forma que también se considere la aportación del flujo diapicno turbulento de flotabilidad ($\overline{w'b'}$) en la zona de *entrainment* diapicno se integra la parametrización de Osborn (1980) sobre Δh, de manera que,

$$\int_{-h_\varepsilon}^{-h_\rho} \overline{w'b'}(dz) = (J_b^{\Delta h})_I = -\int_{-h_\varepsilon}^{-h_\rho} 0.2\varepsilon_o(dz) \tag{8.8}$$

donde $(J_b^{\Delta h})_I$ es el flujo de flotabilidad integrado sobre la zona de *entrainment*. Así, este término representará un sumidero de ECT en la zona de *entrainment* solamente cuando $\Delta h > 0$, dado que se está consumiendo energía en romper la estratificación.

Así, nos aseguramos que las contribuciones de $(J_b^{\Delta h})_I$ son producidas en la zona de *entrainment* como un sumidero de ECT solo cuando $\Delta h > 0$. Siguiendo este razonamiento, se integra el término de disipación sobre la profundidad de la capa de mezcla activa $\int_{-h_\varepsilon}^{0} \varepsilon_o(dz) = \overline{\varepsilon_o} h_\varepsilon$. Añadiendo esas modificaciones a w_e^{GS2}, la parametrización de w_e puede tomar la siguiente forma:

$$w_e^{\Delta h} = \frac{(m_2 + m_3)u_*^3 + 0.5h_\rho J_b^o + (J_b^{\Delta h})_I - \overline{\varepsilon_o} h_\varepsilon}{0.5[(\delta b h_\rho) - (\delta u^2 + \delta v^2)]} \tag{8.9}$$

A diferencia de otras parametrizaciones, la ec. (8.9) permite la consideración de la mezcla debida a la agitación mecánica del viento, la cizalla vertical en la zona de *entrainment*, los flujos de flotabilidad en superficie y en la zona de *entrainment* diapicno, así como la disipación de ECT a través de la capa donde opera la mezcla activa h_ε. En la Figura 8.8b se observa un aumento de w_e en las estaciones de filamento considerando este nuevo enfoque. Estos resultados son consistentes con el incremento de los niveles de disipación mostrados en la Figura 8.7.

Nuestra formulación de w_e difiere en aproximadamente un orden de magnitud respecto de la original w_e^G. Algunas velocidades calculadas a partir de w_e^{SF} alcanzaron valores similares a los de $w_e^{\Delta h}$, con correlaciones de $r^2 = 0.81$. Este resultado está probablemente relacionado con la inclusión del término DIT y refuerza nuestra suposición de que para un mejor entendimiento del flujo estratificado debe considerarse Ri_v en lugar de $Ri_\tau = h_\rho \delta b (u_*)^{-2}$ (Pollard et al., 1973; Price, 1979; Jonker et al., 2013).

8.4.9 Parametrización de ε_p

Desde nuestro conocimiento, los perfiles de microestructura obtenidos en este estudio representan los primeros adquiridos para esta región. Hasta la fecha, no se han reportado previos análisis cualitativos/cuantitativos comparando las parametrizaciones de ε_p incluidas dentro de las formulaciones de w_e, las cuales han probado ser un sumidero dominante en el balance de ECT (e.g., Deardorff, 1983; Gaspar, 1988; Wada et al., 2009). Asumiendo una capa superior oceánica bien mezclada, el promedio de ε_o desde la superficie hasta h_ε es entonces comparado con la parametrización de ε_p derivada en el modelo de Gaspar (1988) (Apéndice A), e incluida en las expresiones de w_e^G y w_e^{GS2}. Los resultados de la Tabla 4.2 indican que ε_p derivada a partir de Gaspar (1988) es

Table 8.2: Términos de disipación de un balance de ECT (m^3 s^{-3}), promediados espacialmente para ambos transectos A y B. Las tasas de disipación de ECT son también promediadas verticalmente hasta profundidades de h_ρ para el caso de ε_p y hasta h_ε para ε_o y ε_{LG}.

Término de disipación	**Transecto A**	**Transecto B**
$\overline{\varepsilon_o}\ h_\varepsilon$	0.23×10^{-6}	0.18×10^{-6}
$\overline{\varepsilon_p}\ h_\rho$	2.66×10^{-6}	1.76×10^{-6}
$\overline{\varepsilon_{LG}}\ h_\varepsilon$	3.25×10^{-6}	2.17×10^{-6}

sobrestimada en un orden de magnitud. Comparaciones con el escalado de Lombardo and Gregg (1989), $\varepsilon_{LG}(z) = 1.76\varepsilon_w(z) + 0.58J_b^{o*}$ también indican una sobrestima de los valores de ε_{LG} con respecto a ε_o (Tabla 4.2).

En el contexto de un balance unidimensional de ECT, la mayoría de la energía transferida a la interfase es disipada por viscosidad. La energía restante, es almacenada en forma de energía potencial que será consecuentemente transformada en energía cinética por *entrainment* diapicno. La sobrestimación de ε_o provoca w_e menores de lo esperado. Esto se observa en la Tabla 8.2, donde $w_e^{\Delta h}$, la cual incluye ε_o, aumenta con respecto a w_e^G.

Adicionalmente, la mayoría de las parametrizaciones de w_e basadas en el modelo de Niiler and Kraus (1977), asumen que la disipación es simplemente una fracción constante del balance de ECT que principalmente depende de u_*. Otros como Gaspar (1988), parametrizan el término de disipación en función de parámetros de estabilidad y rotación y no dependen solamente de la velocidad de fricción. Sin embargo, esta parametrización no tiene en cuenta el término DIT (Apéndice A), por lo tanto una posible causa del desacuerdo entre ε_o y ε_p puede deberse al papel que juega la cizalla vertical en la zona de *entrainment*, el cual debe ser analizado en más detalle mediante apropiadas medidas de series temporales de microestructura.

8.4.10 Conclusiones

En este capítulo se ha analizado el proceso de *entrainment* diapicno en el filamento de afloramiento de Cabo Ghir, mediante el uso de imágenes de satélite, medidas

---

[*] Donde $\varepsilon_w = u_*^3/\kappa z$, es la denominada «Ley de Muro»(e.g., Oakey and Elliott, 1982)

hidrográficas y perfiles de microestructura medidos por primera vez en esta región.

La ausencia de fuertes vientos nos permite resaltar otras fuentes de ECT envueltas en el fenómeno de *entrainment* diapicno. Por lo tanto, cuando el efecto de la cizalla vertical es incluido en un modelo de capa de mezcla, se observa un esperado incremento de w_e. Este aumento es especialmente alto en aguas de filamento, sugiriendo que la mezcla inducida por la cizalla vertical en la base de la capa de mezcla no debería ser descuidada en la mayoría de los modelos de capa de mezcla.

Uno de los resultados más relevantes de este estudio sugiere que la mezcla activa, determinada por la extensión de h_ε, es capaz de crear condiciones óptimas para la existencia de *entrainment* diapicno cuando esta excede la capa de mezcla. Esta teoría es apoyada por el hecho de que Δh es positiva en aquellas áreas afectadas por el filamento, donde la picnoclina es más cercana a superficie. En tales casos, la mezcla turbulenta puede actuar de forma más eficiente en un pequeño volumen de agua. De ahí la importancia en diferenciar h_ρ de h_ε. Los resultados también mostraron un aumento de ε_o en el frente de filamento, concordando con el aumento de w_e y altos niveles de cizalla vertical. Esto destaca la dependencia del proceso de *entrainment* diapicno con la dinámica de la estructura de mesoescala y su relación con la mezcla turbulenta.

La parametrización del término de disipación dentro de la formulación de w_e, difiere de las tasas de ε_o observadas, indicando una subestima de w_e. El impacto de anómalas velocidades verticales podría causar un sobrecalentamiento de la temperatura superficial del mar en modelos numéricos que incluyan tales parametrizaciones. Una posible explicación de esta discrepancia en las tasas de disipación podría estar ligado a la omisión del efecto de la cizalla vertical.

En vistas de los anteriores resultados, se propone un nuevo enfoque para w_e, en el cual se incluye la disipación integrada desde la superficie hasta h_ε, la mezcla mecánica, la cizalla vertical, flujos de flotabilidad en superficie y en la interfase así como la condición de que el proceso de *entrainment* diapicno solo tiene lugar cuando Δh es positiva.

8.5 Capítulo 5: Mezcla Turbulenta Diapicna en un Remolino Intratermoclino Anticiclónico

8.5.1 Introducción

El estudio de la mezcla diapicna turbulenta superficial es crucial para entender el transporte vertical de salinidad, calor, momento y propiedades biogeoquímicas (e.g., Sverdrup, 1953; Lewis et al., 1986; Klein and Lapeyre, 2009; Stramma et al., 2013), siendo particularmente importante en regiones altamente oligotróficas (Cuypers et al., 2012) como la cuenca del noreste Atlántico subtropical.
Además de los procesos de convección y agitación del viento (e.g., Gaspar, 1988; Nagai et al., 2005), la capa superficial oceánica depende en gran medida de otros procesos que ocurren en la interfase entre la termoclina estacional y la capa estratificada que se encuentra por debajo. Estos procesos abarcan el incremento local de la cizalla vertical en la base de la picnoclina, la cual representa una fuente de ECT que podría incrementar las tasas de *entrainment* diapicno (Strang and Fernando, 2001; Samson et al., 2009; Estrada-Allis et al., under review). Como ha sido previamente examinado en el Capítulo 4, las fuentes que gobiernan el proceso de *entrainment* diapicno también dependen de la zona de *entrainment* diapicno (Brainerd and Gregg, 1995; Sutherland et al., 2014). De acuerdo a la formulación propuesta en la ec. (8.9), solo zonas positivas de *entrainment* provocarán velocidades $w_e > 0$ (Dewey and Moum, 1990; Inoue et al., 2010), ayudando así a la redistribución de trazadores físico-biológicos hacia capas fóticas (Kolodziejczyk et al., 2015), entre otros efectos.
Bajo la capa de mezcla, el océano profundo se encuentra principalmente mezclado por la propagación hacia abajo de energía de la tensión del viento y mareas (Wunsch and Ferrari, 2004). Adicionalmente, estudios teóricos y numéricos predicen que los remolinos anticiclónicos podrían jugar un importante papel en el aumento de mezcla diapicna profunda por atrapar ondas cuasi-inerciales (e.g., Kunze, 1985; Zhai et al., 2005; Ferrari and Wunsch, 2009; Stanley and Saenko, 2014; Zhang et al., 2015). Esto ocurre dado que la frecuencia local inercial de las ondas inerciales son reducidas dentro del remolino anticiclónico (Lueck and Osborn, 1986). Las ondas inerciales, se vuelven subinerciales a medida que viajan hacia abajo por los bordes del remolino. Se llega a un punto crítico, donde la frecuencia de las ondas se iguala con la frecuencia inercial local. El

vector de número de onda se vuelve vertical y las ondas se reflejan de nuevo dentro del remolino, quedando por lo tanto, atrapadas. Debido a que las ondas no se pueden reflejar hacia arriba, la amplitud de las mismas debe crecer para conservar su flujo de momento hacia abajo. Esto da lugar a efectos no lineales que eventualmente actúan para extraer y disipar energía de las ondas. De esta manera, la mezcla diapicna está ligada a una fuerte cizalla introducida por ondas inerciales atrapadas en la base del remolino. Aunque existen crecientes evidencias de este proceso (e.g., Danioux et al., 2008; Cuypers et al., 2012; Forryan et al., 2012; Joyce et al., 2013; Sheen et al., 2014), hay una falta de observaciones en la literatura. Esto se debe en gran parte, a la dificultad en el desarrollo de un muestreo sinóptico de alta resolución del fenómeno con perfiladores de microestructura.

Tanto en superficie como en el océano interior, los procesos de mezcla descritos anteriormente pueden ser particularmente activos en remolinos de mesoescala y su asociada submesoescala (Capet et al., 2008b; Klein and Lapeyre, 2009). En este contexto, nuestra región de estudio, el Corredor de Remolinos de Canarias sugerido por Sangrà et al. (2009) (de ahora en adelante CRC), es la principal vía de propagación de remolinos hacia el oeste del Atlántico noreste (Mason et al., 2014), representando así una fuente relativamente constante de mezcla turbulenta (Sangrà et al., 2009).

A pesar de la importancia de los procesos de mezcla que actúan sobre las estructuras de mesoescala, el discernimiento sobre cuáles son las fuentes de ECT que controlan la capa de mezcla dentro de remolinos de mesoescala y cuál es la proporción de energía que es disipada o usada para incrementar la mezcla oceánica profunda, siguen siendo preguntas abiertas. Esto se debe a la falta de observaciones directas de los procesos de mezcla y de medidas de ε_o, las cuales son aún escasas.

El principal objetivo de este estudio es la caracterización de la mezcla diapicna en un típico remolino intratermoclino anticiclónico del CRC en el noreste Atlántico subtropical. La estructura de mesoescala fue muestreada durante la campaña PUMP en Setiembre de 2014 (Capítulo 3).

8.5.2 Caso estudio: Remolino intratermoclina PUMP

El remolino muestreado* fue formado por la perturbación del flujo de la corriente de Canarias con la Isla de Tenerife. Para este estudio se seleccionó un transecto meridional cruzando el centro del remolino, el cual consta de 25 estaciones de CTD y SADCP, 24 de LADCP cada 5 millas náuticas, datos continuos de la estación meteorológica del buque y 13 estaciones de TurboMAP cada 10 millas náuticas. La señal de vorticidad relativa geostrófica ($\zeta_g = \partial_x v - \partial_y u$) normalizada con el parámetro de Coriolis (f), así como la localización de las estaciones hidrográficas se presentan en la Figura 8.9a.

El perfil vertical de la anomalía de densidad potencial a lo largo del transecto indica que el remolino tiene 110 km de diámetro y su base podría encontrarse a 600 m de profundidad (Figura 8.9b). El abombamiento de las isopicnas en las capas superficiales y su depresión en las capas más profundas son características típicas de un remolino intratermoclina. La capa de estratificación máxima, dada por N^2, se localiza cerca de la superficie hacia los 120 m en la periferia del remolino mientras que decrece hacia los 80 m de profundidad en el centro del remolino (Figura 8.9c). También se observa un mínimo de N^2 en el núcleo del remolino (entre 200 y 400 m de profundidad), sugiriendo condiciones favorables para el desarrollo de mezcla diapicna.

8.5.3 Capas de mezcla activa y de mezcla

Después de una comparación entre diferentes métodos, h_ρ es determinada a través del algoritmo propuesto por Holte and Talley (2009). A su vez h_ε, esencial para el establecimiento de la zona Δh, es determinada a través del método propuesto en el capítulo anterior. Los resultados de la Figura 8.10 muestran que h_ε es más profunda que h_ρ, por lo tanto Δh es siempre positiva en cada estación de microestructura, incluso con débiles vientos. El comportamiento de Δh parece ser también independiente de las condiciones nocturnas de convección. Una plausible explicación podría estar relacionada con la poca profundidad de la capa de mezcla, resultado de la baja transferencia de momento por relativamente débiles vientos Alisios y bajos flujos de flotabilidad. Eventos de mezcla superficial intermitentes, debidos por ejemplo al aumento repentino de la velocidad

---

*Al momento de muestreo, el remolino se encontraba en un estado maduro con cuatro meses de vida.

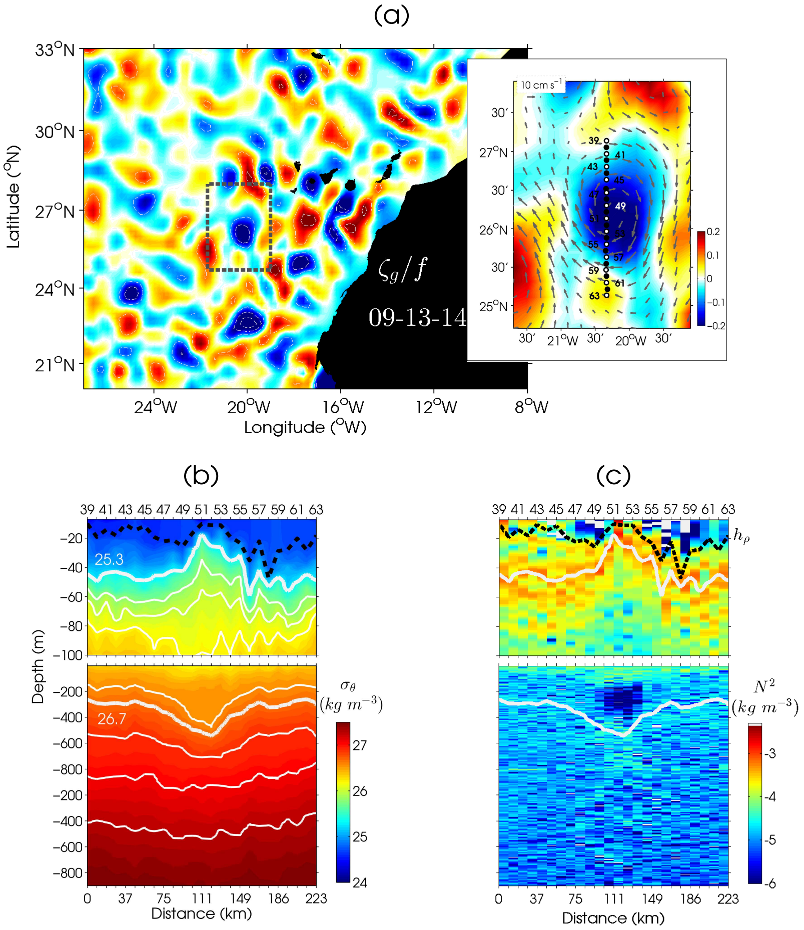

Figure 8.9: (a) Componente vertical de la vorticidad relativa geostrófica normalizada por la vorticidad planetaria, $Ro = \zeta_g/f$. A la izquierda, se amplifica la zona muestreada del remolino donde se denotan las estaciones hidrográficas y de ADCP con puntos en negro. Los puntos blancos muestran las estaciones de microestructura. Las estaciones 39 a la 47 se denominan estaciones norte; desde la 48 a la 51 estaciones del centro del remolino y las estaciones sur comprenderán desde la estación 52 a la 63. Los vectores representan la corriente geostrófica calculada a través de datos de altimetría. Las figuras inferiores representan las secciones verticales meridionales del remolino donde (b) anomalía de la densidad potencial, σ_θ (km m^{-3}), y (b) frecuencia de flotabilidad al cuadrado, N^2 (s^{-2}). Las líneas negras punteadas representan la profundidad de la capa de mezcla, h_ρ, y los contornos blancos denotan las isopicnas.

del viento, podrían extenderse fácilmente debajo de una capa de mezcla somera conduciendo a $\Delta h > 0$ y en consecuencia a $w_e > 0$ (Estrada-Allis et al., under review).

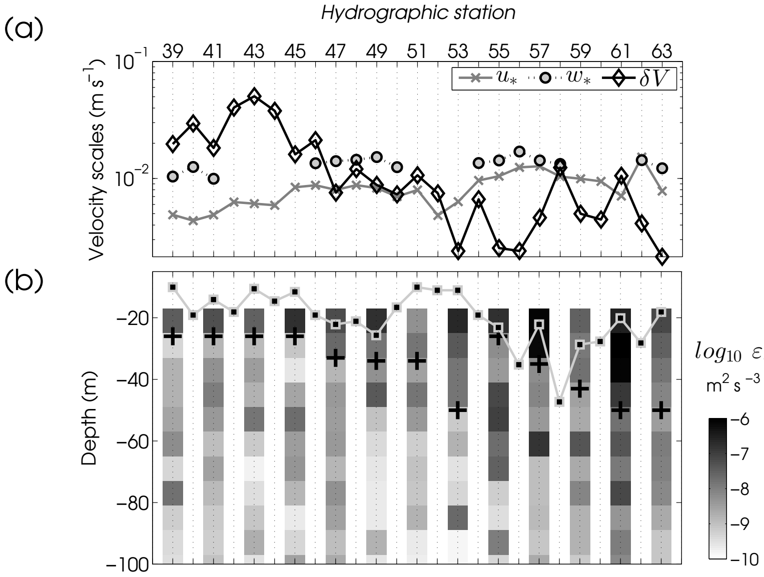

Figure 8.10: (a) Escalas de velocidad de las tres fuentes de ECT implicadas en el proceso de *entrainment* diapicno, donde u_* es la velocidad de fricción, w_* es la convección libre, y δV es el salto de velocidad a través de h_ρ. (b) Perfiles verticales de ε_o observados. Los símbolos cuadrados muestran valores de h_ρ y las cruces negras indican h_ε. Para una mejor visualización solo se muestra el número de las estaciones impares en la parte superior del gráfico.

El incremento de la velocidad del viento en los últimos días de muestreo da como resultado un aumento de u_*, como se observa en la Figura 8.10a. Este incremento conlleva a una ligera profundización de h_ρ y h_ε, y está relacionado con un aumento de la disipación dada por ε_o (Figure 8.10b). Además, δV se muestra como uno de los mayores contribuyentes de ECT en las estaciones situadas más al norte (desde la 37 a la 47), reforzando los resultados del Capítulo 4. Por el contrario, desde la estación 48 a la 63 situadas al sur, todas las fuentes de ECT son comparables en magnitud, lo que sugiere que las tres fuentes son esenciales en la modulación de la capa de mezcla dentro del remolino.

8.5.4 Mezcla en la zona de *entrainment* diapicno

Las velocidades w_e analizadas a través de la parametrización propuesta en Estrada-Allis et al. (under review), $w_e^{\Delta h}$ (ec. 8.9), tienden a incrementar en la periferia del remolino. En el centro del remolino, por el contrario, $w_e^{\Delta h}$ es ligeramente reducida como se observa en la Figura 8.11.

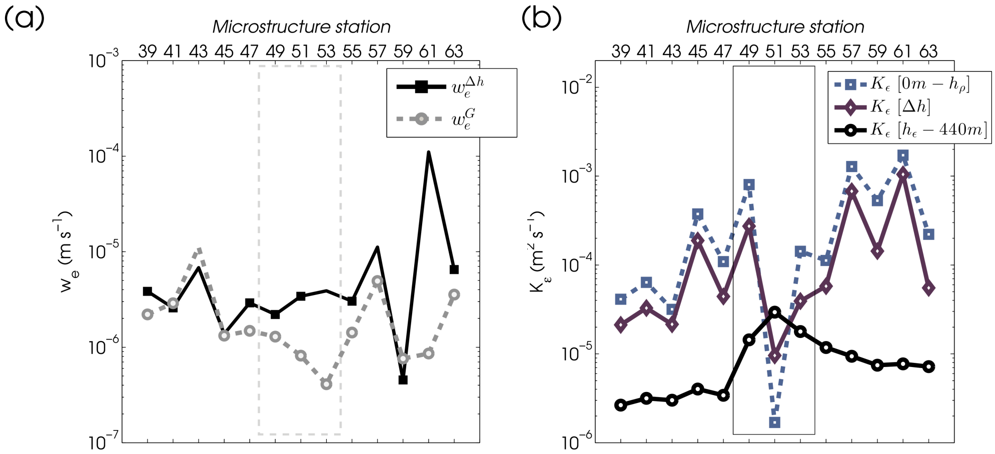

Figure 8.11: (a) Tasas de *entrainment* diapicno turbulento w_e calculadas a partir de la clásica parametrización de Gaspar (1988) w_e^G (ec. 8.5), y a partir del nuevo enfoque propuesto por Estrada-Allis et al. (under review) $w_e^{\Delta h}$ (ec. 8.9). Las líneas punteadas muestran la tendencia de los valores absolutos de w_e, mientras que solamente valores positivos de w_e son denotados con símbolos. (b) Promedio vertical de los coeficientes de difusividad diapicna, K_ε (m^2 s^{-1}), para las tres profundidades en las que se divide el análisis de mezcla del remolino. Los recuadros punteados dentro de ambas figuras remarcan aquellas estaciones localizadas en el centro del remolino.

Las diferencias entre $w_e^{\Delta h}$ y w_e^G fueron menores de las esperadas, existiendo un gran acuerdo entre ambas w_e. Esto contrasta con las grandes diferencias encontradas para el caso del filamento de Cabo Ghir (Capítulo 4) y son probablemente debidas a la inclusión del término DIT y a la sobrestima de las tasas de disipación de ECT con respecto a las observadas ε_o (Estrada-Allis et al., under review).

Simultáneamente, la forma de las isopicnas del remolino intratermoclina, podrían también afectar a la magnitud de w_e. La depresión de las isopicnas en los primeros metros de la columna de agua en los bordes del remolino daría lugar a capas de mezcla más profundas que en el centro del mismo. Por el contrario, la capa de mezcla activa debajo de h_ρ se comporta de forma contraria, siendo más profunda en el centro del remolino y viceversa en la periferia. Los resultados de la Figura 8.11a muestran que w_e parece seguir la tendencia de h_ε en lugar de la de h_ρ.

8.5.5 Aumento de mezcla diapicna profunda

En lo que concierne a la mezcla diapicna profunda, estudios teóricos puntualizan que los remolinos anticiclónicos podrían atrapar ondas cuasi inerciales en sus base, representando una fuente de mezcla diapicna extra en los niveles más profundos de la base de los remolinos (e.g., Kunze, 1985; Cuypers et al., 2012; Stanley and Saenko, 2014). Gracias a la alta resolución espacial de la sección TurboMAP usada en este estudio, se puede proveer nuevas evidencias de tales eventos de mezcla profunda.

En la Figura 8.12 se puede observar un notable aumento de ε_o subsuperficial en las estaciones de microestructura 51 y 53, localizadas en el núcleo del remolino. Este máximo local profundo de ε_o coincide con una región de gran cizalla vertical extendiéndose justo debajo de la base del núcleo del remolino hasta el valor más profundo muestreado por el LADCP a 900 m. Martínez-Marrero et al. (in prep.) han atribuido esta fuerte columna de cizalla vertical a la presencia de ondas inerciales atrapadas en la base del remolino. En consecuencia, los resultados anteriores sugieren que el aumento de mezcla turbulenta a medias y grandes profundidades podría ser debido a la rotura de ondas cuasi-inerciales, previamente atrapadas por el remolino anticiclónico Martínez-Marrero et al. (in prep.).

Otro indicativo de mezcla diapicna turbulenta en fluidos estratificados viene dado por los coeficientes de difusividad diapicna (K_ε). Calculados a partir de la expresión de Osborn (1980), en la Figura 8.11b se observa un aumento de K_ε en los bordes y una disminución en el centro del remolino tanto en superficie como en la zona de *entrainment* diapicno. Por el contrario, el promedio vertical de K_ε desde h_ε hasta aproximadamente 450 m, es un orden de magnitud mayor en el núcleo que el promedio en los bordes.

8.5.6 Conclusiones

Los principales procesos de mezcla actuando sobre el remolino son representados a través de tres capas de profundidad (Figura 8.11b), las cuales revelan la variabilidad del estado de la mezcla con la profundidad dentro de un remolino anticiclónico.

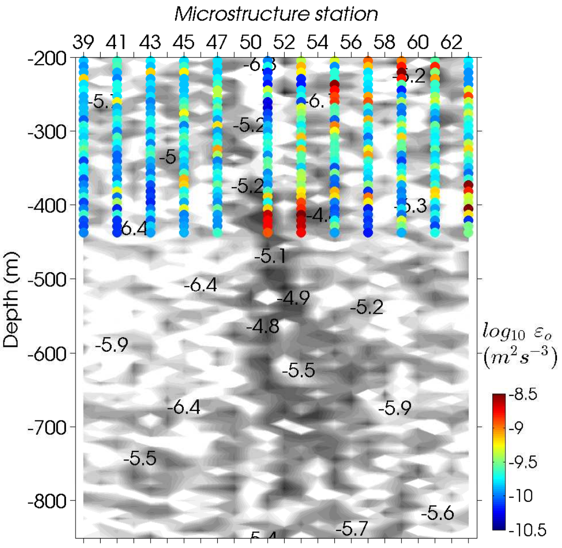

Figure 8.12: Sección vertical subsuperficial meridional de la cizalla vertical inducida por corrientes horizontales, Sh^2, en escala logarítmica, calculada a partir de los perfiles de LADCP. Los símbolos de colores superpuestos indican valores de ε_o para cada estación de microestructura y cada profundidad en la que fue promediada. Note que la ausencia de la estación 49 de LADCP impide la representación del perfil de ε_o para dicha estación.

Las principales conclusiones de este capítulo pueden ser resumidas como: (i).- La mezcla diapicna superficial dentro del remolino anticiclónico es conducida principalmente por el efecto combinado de la convección nocturna, la cizalla vertical y la agitación por el viento, las cuales deben ser integradas dentro de las parametrizaciones de w_e. (ii).- Las profundidades de h_ε fueron más profundas que h_ρ a lo largo de todo el transecto muestreado, favoreciendo así la redistribución de trazadores dentro la capa fótica mediante *entrainment* diapicno. A su vez, las tasas de w_e parecen estar más relacionadas con la capa de mezcla activa más que con la capa de mezcla, y están probablemente condicionadas por la forma de las isopicnas superficiales del remolino intratermoclina. (iii).- En las capas superficiales y en la interfase del borde del remolino, el aumento de ε_o y de los coeficientes de difusividad diapicna mediante K_ε concuerdan con un incremento de w_e. Esto sugiere que la mezcla turbulenta diapicna está fuertemente ligada a la dinámica de mesoescala que interacciona con las fuentes de ECT implicadas. (iv).- El comportamiento de la mezcla diapicna es inverso en las capas más profundas del remolino, siendo más intenso en el núcleo del remolino. Este incremento es consistente con un aumento de la cizalla vertical y de la disipación de energía cinética turbulenta, sugiriendo que podría ser el resultado de ondas cuasi-inerciales atrapadas dentro de remolinos anticiclónicos del CRC.

8.6 Capítulo 6: Velocidades Verticales en Remolinos Mesoescalares (Experimento Numérico)

8.6.1 Introducción

El estudio de la mezcla vertical y velocidades verticales dentro de remolinos de mesoescala a menudo representan un reto, esto se debe en parte a que debe llevarse a cabo guardando la escala sinóptica del muestreo, para así mantener la consistencia de los resultados. A este respecto, los modelos numéricos han demostrado ser una herramienta útil para establecer las bases de cuestiones claves, que posteriormente podrán ser abordadas en estudios observacionales.

Recientes estudios han reportado que los anticiclones no son áreas oligotróficas (e.g., McGillicuddy et al., 2007; Ledwell et al., 2008; Gaube et al., 2015), tal es el caso del remolino observado en el anterior Capítulo 5. La generación de velocidad vertical dentro de estructuras de mesoescala está relacionada con una variedad de procesos tales como la frontogénesis, la interacción remolino-viento y la succión/bombeo de Ekman por efectos lineales y no lineales (e.g., Martin and Richards, 2001; McGillicuddy et al., 2007; Capet et al., 2008b; Mahadevan et al., 2008; Calil and Richards, 2010). El impacto físico-biológico de estos procesos en el campo de velocidad vertical es aún cuestión de debate. Adicionalmente, estudios de modelos numéricos (Viúdez and Dritschel, 2003; Koszalka et al., 2009; Cardona and Bracco, 2012) y observacionales (Chavanne et al., 2010; Nardelli, 2013), sugieren que las ondas de vórtice de Rossby (VRWs, por sus siglas en inglés), podrían también contribuir al patrón de w dentro de los vórtices de mesoescala. Las VRWs son perturbaciones de la vorticidad potencial que se propagan lentamente desde el núcleo del remolino hacia afuera, a la vez que son sesgadas por el diferencial de la velocidad angular del propio remolino. Con un tiempo de escala comparable al de la escala advectiva (Graves et al., 2006)[*] y frecuencias menores a la vorticidad planetaria, las VRWs pueden sentir la rotación de la tierra siendo en gran medida geostróficamente balanceadas (Montgomery and Kallenbach, 1997; McWilliams et al., 2003).

---

[*] El tiempo de escala advectiva de los remolinos estudiados en este modelo es del orden de $2\pi LV^{-1}$ $\approx$ 9.09 días

Solo unos pocos estudios han enfatizado los efectos de la mezcla en los movimientos verticales. La falta de estudios observacionales a este respecto es probablemente debido a las derivaciones de alto orden, efectos no lineales y a la gran dependencia de las parametrizaciones de mezcla que deben ser incluidas dentro de formulaciones más generales. Estudios observacionales y de modelización numérica indican que los efectos de la mezcla se concentran principalmente en los primeros 100 metros de la columna de agua, conduciendo a una intensificación de w (Giordani et al., 2006; Nagai et al., 2006; Koszalka et al., 2010; Pallàs-Sanz et al., 2010; Johnston et al., 2011). Ponte et al. (2013), sugiere que la mezcla vertical superficial dentro de la capa de mezcla tiende a destruir el balance de viento termal mediante el suavizado de los perfiles vertical de los movimientos horizontales totales. Posteriormente, este equilibrio es restaurado a través del desarrollo de una fuerte circulación vertical. Sin embargo, sus formulaciones solo son válidas a bajos números de Rossby y manteniendo un valor constante de K_v.

El campo de velocidades verticales dentro de remolinos anticiclónicos es en sí mismo, una compleja estructura que puede depender de tantos factores como fuentes implicadas (e.g., Viúdez and Dritschel, 2003; Koszalka et al., 2009; Calil and Richards, 2010; Cardona and Bracco, 2012; Nardelli, 2013; Ponte et al., 2013), y que por consiguiente necesita aún ser clarificado. Motivado por el anterior Capítulo 5, este estudio se centra en el análisis de la estructura vertical en términos de velocidades verticales, así como en la influencia que ejerce la mezcla vertical dentro del campo de w en remolinos anticiclónicos. Dichos remolinos son generados por la perturbación del flujo de la corriente con las Islas Canarias (Arístegui et al., 1994; Sangrà et al., 2005; Mason et al., 2011), y son modelizados a partir de un modelo de alta resolución ROMS, cuya configuración y validación forma parte de la tesis de (Mason, 2009). La alta resolución espacial de $\sim$ 1 km, y 60 capas verticales sigma, permite de este modo el estudio de estructuras de mesoescala y su submesoescala asociada dentro de remolinos anticiclónicos.

Resultados

8.6.2 Descomposición del campo de w

La fina resolución del modelo permite la reproducción de la rica variabilidad de mesoescala caracterizada por altos números de Rossby, $Ro = \zeta_r/f$ (Figura 8.13a), indicando que la ageostrofía podría ser importante en la dinámica de los remolinos. La señal del correspondiente campo de w superficial es compleja y está generalmente asociada con remolinos mesoescalares y sus filamentos submesoescalares como se verá más adelante. Para la descripción del campo de velocidades verticales numéricas (de ahora en adelante denominadas como w_{ROMS}), hemos seleccionado un remolino anticiclónico denotado como $A2$ en la Figura 8.13a, el cual fue escindido de la Isla de Tenerife. También se comparará el remolino $A2$ con otro anticiclónico más joven y de forma más circular denotado en la Figura 8.13a como $A1$.

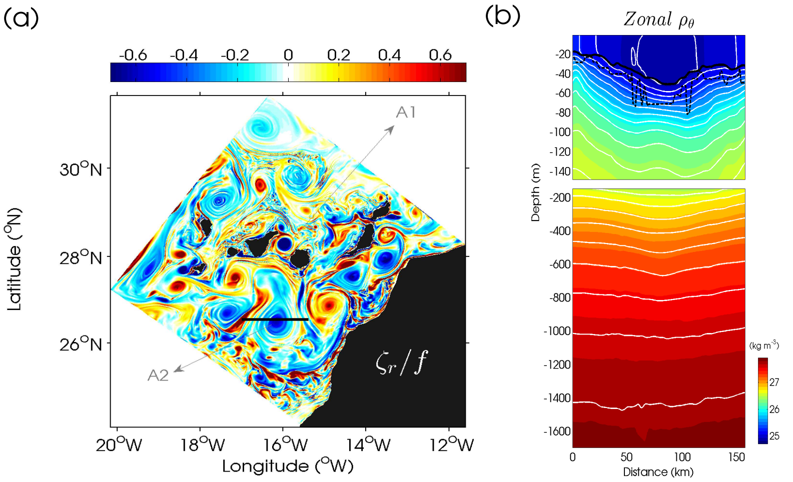

Figure 8.13: (a) Campo horizontal simulado del día 29, mes 8 de la vorticidad relativa normalizada por la vorticidad planetaria, $Ro = \zeta_r/f$, a 1 m de profundidad. Las flechas delimitan los dos vórtices analizados en este estudio $A1$ y $A2$. La barra horizontal negra indica el corte para las secciones zonales verticales posteriores. (b) Sección zonal vertical de la densidad potencial, ρ_θ (kg m^{-3}), de $A2$ para la misma fecha que (a). Los contornos blancos son isopicnas trazadas cada 0.15 kg m^{-3}. La línea continua negra denota la capa de frontera superior, h_{ubl}, mientras que la línea discontinua muestra el máximo gradiente superficial del cuadrado de la frecuencia de flotabilidad, N^2.

La estructura vertical del vórtice $A2$ se muestra en la Figura 8.13b. Las isopicnas se profundizan en el centro del remolino hasta ≈ 800 m donde se encuentra presumiblemente su base. Este remolino tiene un radii medio de 35.56 ± 7.10 km y experimenta variaciones en su forma elíptica a medida que se propaga siguiendo el CRC (Sangrà et al., 2009). La profundización de las isopicnas en el centro influencian la profundidad de la capa de mezcla (Capítulo 5), que aquí es computada mediante la parametrización KPP de Large et al. (1994) (Figura 8.13b), y se denomina capa de frontera superior (h_{ubl}).

Motivado por el estudio de remolinos numéricos ideales de Koszalka et al. (2009), se ha implementado el mismo enfoque para la descomposición del campo de w_{ROMS}. Este enfoque se basa en la divergencia instantánea del flujo propuesta por Vallis (2006). De esta forma, el campo de w_{ROMS} puede descomponerse en los principales campos que lo fuerzan de acuerdo a:

$$
\begin{aligned}
w(x,y,z) = \; & D\eta_r/Dt + \int_z^{\eta_r} [\\
& - \underbrace{[\alpha_1(D\zeta_r^1/Dt) - \alpha_2(D\zeta_r^2/Dt)]}_{\textbf{Ageo}} \\
& - \underbrace{[\alpha_1(\partial_x u\zeta_r^1) - \alpha_2(\partial_y v\zeta_r^2)]}_{\textbf{Str}} \\
& - \underbrace{[\alpha_1(\partial_x w\partial_z v) + \alpha_2(\partial_y w\partial_z u)]}_{\textbf{Tilt}} \\
& + \underbrace{[\alpha_2\rho_o^{-1}(-\partial_{yz}^2\tau^x) + \alpha_1\rho_o^{-1}(\partial_{xz}^2\tau^y)]}_{\textbf{Wstr}} \\
& + \underbrace{[A_H\alpha_1(\partial_{x^4}^4\zeta_r^1 + \partial_{y^4}^4\zeta_r^1) + A_H\alpha_2(\partial_{x^4}^4\zeta_r^2 + \partial_{y^4}^4\zeta_r^2)]}_{\textbf{Hmix}} \\
& + \underbrace{[\alpha_1\partial_{xz}^2(Kv\partial_z v) - \alpha_2\partial_{yz}^2(Kv\partial_z u)]}_{\textbf{Vmix}}]dz
\end{aligned}
\tag{8.10}
$$

donde D/Dt es derivada material y $A_H = 10^6$ m^{4}s^{-1} es la constante biarmónica de difusión horizontal. El coeficiente de difusividad diapicna (K_v), viene dado por la parametrización de KPP (Large et al., 1994). Todos los términos son modulados por la inversa de la vorticidad absoluta $1/(\zeta_r + f)$, donde $\zeta_r^1 = \partial_y u$, $\zeta_r^2 = \partial_x v$, $\alpha_1 = (f + \zeta_r^1)^{-1}$ y $\alpha_2 = (f + \zeta_r^2)^{-1}$.

Los términos del lado derecho de la ecuación representan: el primero la elevación libre del mar (η_r). El segundo término es el forzamiento ageostrófico ($\boldsymbol{Ageo}$) que denota los cambios instantáneos de vorticidad y advección de ζ_r. El tercer y cuarto término describen el estiramiento e inclinación de w_{ROMS} dentro del vórtice ($\boldsymbol{Str}$ y $\boldsymbol{Tilt}$, respectivamente). La componente de w_{ROMS} relacionada con el efecto del viento está englobada en el término de la tensión del viento ($\boldsymbol{Wstr}$). Finalmente, los últimos dos términos dan cuenta de la influencia de la mezcla horizontal y vertical en el campo de velocidades verticales dentro del remolino ($\boldsymbol{Hmix}$ y $\boldsymbol{Vmix}$, respectivamente).

En las capas superficiales (desde superficie hasta h_{ubl}), el campo de w_{ROMS} revela un complejo patrón de ondas submesoescalares (Figura 8.14a), en el cual celdas de afloramiento y hundimiento se alternan al rededor del núcleo del remolino, con w_{ROMS} más intensas en la periferia (Capet et al., 2008b; Mahadevan et al., 2008).

La descomposición de w_{ROMS} mediante la ec. (8.10) también muestra que el forzamiento $\boldsymbol{Ageo}$ ejerce un control mayoritario, seguido por el término $\boldsymbol{Str}$ (Figuras 8.14b and c). El término de $\boldsymbol{Tilt}$ muestra un patrón de onda similar al de w_{ROMS}, aunque con magnitudes menores (Figura 8.14d). El forzamiento $\boldsymbol{Wstr}$ (Figura 8.14e) también tiene una contribución secundaria, pero no es capaz de explicar el patrón de espiral del campo general de w_{ROMS}. Seguidamente, la componente $\boldsymbol{Hmix}$ tiene una contribución minoritaria a pesar de que su patrón se ajusta al observado en w_{ROMS} (Figura 8.14f), al igual que la contribución de η_r. Por último, el forzamiento $\boldsymbol{Vmix}$ parece coincidir con la distribución de w_{ROMS} de forma secundaria[*] (Figura 8.14g).

Por debajo de h_{ubl}, el patrón de espiral es reemplazado por dos celdas de afloramiento y hundimiento (Figura 8.15a), que se intensifican a profundidades intermedias (~ 300 m). Este dipolo de w_{ROMS} se extiende verticalmente hasta ≈ 800 m (ver Figura 8.22a) coincidiendo con la base del remolino. La magnitud de w_{ROMS} en estas profundidades tiene una media de 85 m d^{-1}. La dinámica del dipolo de velocidad vertical, será examinada en las próximas secciones.

La descomposición de w_{ROMS} a 300 m de profundidad sugiere nuevamente que los términos $\boldsymbol{Ageo}$ y $\boldsymbol{Str}$ dominan el campo de w (Figuras 8.15b y c). Ambos forzamientos exhiben formas de ondas azimutales de número de onda de orden 4. Sin embargo, estas ondas se encuentran en desface, siendo por lo tanto en gran medida canceladas como también observa Koszalka et al. (2009). A diferencia del estudio de Koszalka et al.

---

[*] Su papel será analizado en detalle más adelante

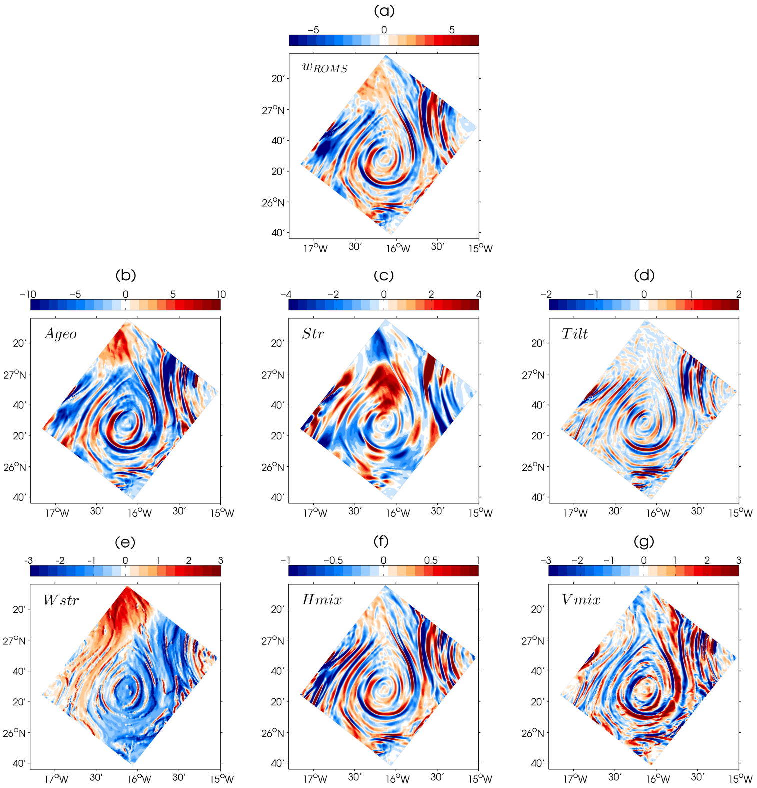
(a)
−5
0
5
w_{ROMS}
(b)
−10
−5
0
5
10
Ageo
(c)
−4
−2
0
2
4
Str
(d)
−2
−1
0
1
2
Tilt
(e)
-3
-2
-1
0
1
2
3
Wstr
(f)
−1
−0.5
0
0.5
1
Hmix
(g)
−3
−2
−1
0
1
2
3
Vmix
20'
27°N
40'
20'
26°N
40'
17°W
30'
16°W
30'
15°W

Figure 8.14: Campo horizontal a 20 m de profundidad, para cada uno de los términos en los que se descompone w_{ROMS} a través de la ec. (8.10). (a) w_{ROMS} total, (b) término ageostrófico ***Ageo***, (c) término de estiramiento ***Str***, (c) término de inclinación ***Tilt***, (d) término de tensión del viento ***Wstr***, (e) mezcla horizontal ***Hmix*** y (f) mezcla vertical ***Vmix***. Note las variaciones en la escala de colores. El campo simulado corresponde al día 29 del mes 08.

(2009), la cancelación de ambos término en este modelo no da lugar a la predominancia de la componente ***Tilt*** (Figura 8.15d). Por el contrario, cuando ***Ageo*** y ***Str*** no se cancelan entre sí, surge la estructura de dipolo de w, lo que los sugiere como los principales candidatos para su formación. Además, el número de onda azimutal de orden 4 de ambos términos, podría estar relacionado con la presencia de VRWs, donde el patrón de espiral de w_{ROMS} revelaría la propagación de tales ondas (Graves et al., 2006; Koszalka et al., 2009; Chavanne et al., 2010).

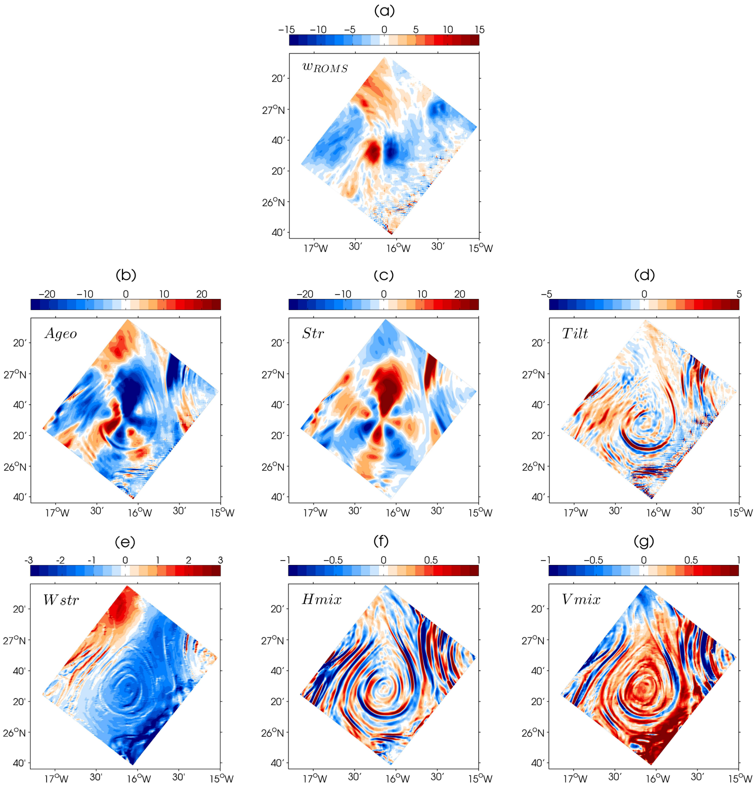
(a)
−15 −10 −5 0 5 10 15
w_{ROMS}
(b)
−20 −10 0 10 20
Ageo
(c)
−20 −10 0 10 20
Str
(d)
−5 0 5
Tilt
(e)
-3 -2 -1 0 1 2 3
Wstr
(f)
−1 −0.5 0 0.5 1
Hmix
(g)
−1 −0.5 0 0.5 1
Vmix
20'
27°N
40'
20'
26°N
40'
17°W
30'
16°W
30'
15°W

Figure 8.15: Igual que en la Figura 8.14, pero a -300 m.

8.6.3 Influencia de la interacción remolino-viento y de los efectos no lineales de Ekman

La circulación vertical de Ekman podría conducir a un afloramiento en el centro del remolino (Martin and Richards, 2001; McGillicuddy et al., 2007), y los efectos no lineales de Ekman a una celda de dipolo (Mahadevan et al., 2008; McGillicuddy et al., 2008). A pesar de que la ec. (8.10) incluye los efectos de Ekman lineal y no lineal de forma implícita, se examina explícitamente el papel de la interacción entre la corriente geostrófica superficial del remolino con el campo de vientos. Para esto, se calcula la succión/bombeo de Ekman total (w_{EkT}) dividiendo sus contribuciones lineales (w_{EkL}) y no lineales (w_{EkNL}) de acuerdo a como se describe en Stern (1965). El término no lineal w_{EkNL} se encuentra relacionado con la advección de vorticidad relativa superficial geostrófica, por el transporte de Ekman inducido por el viento (e.g., Niiler, 1965; Thomas and Rhines, 2002; Mahadevan and Tandon, 2006).

El caso del remolino $A1$ más circular conduce a un esperado dipolo de w_{EkT}, con un claro incremento de w hacia la periferia del remolino donde se encuentran los gradientes de vorticidad relativa geostrófica más fuertes (Figura 8.16c). Para nuestro caso estudio $A2$, el patrón del campo de w_{EkT} es mucho más complejo (Figura 8.16f), donde aún pueden observarse el dipolo de w_{EkT} pero en una pequeña región concentrada en el núcleo interior del remolino, rodeada a su vez por estrechos filamentos del campo de w_{EkT}.

La contribución de w_{EkNL} es el reflejo del campo de w_{EkT} con un hundimiento en el flanco oeste y un afloramiento en el flanco este de los dos vórtices $A1$ y $A2$ (Figuras 8.16a, b, c y f). Esto indica la predominancia de los efectos no lineales relacionados con la dinámica ageostrófica de los remolinos, causando que la divergencia del transporte de Ekman varíe inversamente con la vorticidad absoluta más que con la vorticidad planetaria (Niiler, 1965; Stern, 1965; Thomas and Rhines, 2002).

Mediante la comparación de w_{EkT} con la clásica formulación de las velocidades de Ekman dadas por $w_{Ek} = \boldsymbol{k} \cdot \boldsymbol{\nabla} \times (\boldsymbol{\tau_r}/f\rho_o)$, es posible discernir el grado de implicación de los efectos que acarrea la interacción remolino-viento. Los resultados mostrados en las Figuras 8.16a y d, indican que cuando se suprime la retroalimentación entre la corriente del remolino y el campo de viento, las velocidades de Ekman simulan el comportamiento de una circulación vertical de Ekman lineal. En consecuencia, w_{Ek} es similar a w_{EkL} y a su vez es consistente con el forzamiento $\boldsymbol{Wstr}$ de la ec. (8.10). Todas estas velocidades son menores en magnitud que el término w_{EkT} y por consiguiente que el campo general de w_{ROMS} (Figuras 8.16a, b, d y e).

8.6.4 Influencia de las ondas de vórtice de Rossby

Otro proceso que podría estar implicado en el transporte vertical dentro de remolinos, es la deformación relacionada con el crecimiento de las ondas de vórtice de Rossby (VRWs). Las VRWs podrían explicar el incremento del transporte vertical cerca de la superficie para un flujo débilmente estratificado (Koszalka et al., 2010). La interacción de estas ondas con la circulación de Ekman conduciría a patrones de w más intensos y complejos en las capas superficiales (Koszalka et al., 2010). Koszalka et al. (2010) observan patrones en forma de cuádruplo y de dipolo en el campo de w relacionado con la propagación de esas ondas (Nardelli, 2013). El campo de w_{ROMS} aquí simulado con patrones de ondas en espiral y dipolos, sugieren que las VRWs podrían jugar un

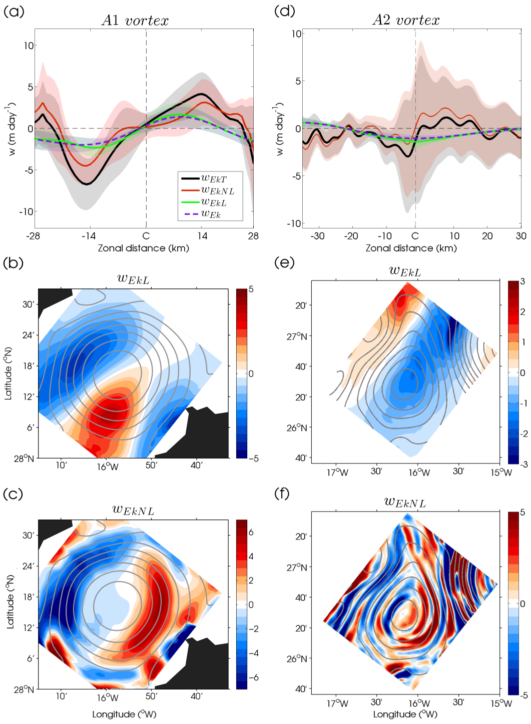

Figure 8.16: Promedio latitudinal de succión de Ekman total, w_{EkT}, lineal, w_{EkL}, no lineal, w_{EkL} y succión de Ekman clásico, w_{Ek}, para el caso de (a) vórtice $A1$ y (d) vórtice $A2$ donde las áreas sombreadas denotan la desviación estándar y las líneas verticales muestran el centro de los vórtices. La distancia desde el centro del remolino en km se muestra en la parte inferior de las figuras. Mapas instantáneos de (b) w_{EkL} y (c) w_{EkNL} para el vórtice $A1$, mientras que de forma análoga (e) y (f) lo son para el vórtice $A2$.

certero rol en la modulación de w_{ROMS}.

En el Apéndice B de esta tesis, se describe la relación de dispersión local de esas ondas derivada por McWilliams et al. (2003) en su estudio teórico y aplicada por Nardelli (2013) en anillos de la corriente de Agulas. La relación de dispersión para las VRWs del remolino $A2$ arroja periodos que comprenden desde los 1.25 a los 5 días para núcleo más interior del vórtice. El periodo incrementa hasta casi alcanzar los 40 días para ondas alejadas del núcleo del remolino. Este rango de periodos/frecuencias es similar al reportado en otros estudios numéricos (Koszalka et al., 2009) y observacionales (Chavanne et al., 2010; Nardelli, 2013). El análisis espectral del campo de w_{ROMS} de todos los remolinos anticiclónicos del dominio numérico, para tres profundidades diferentes a lo largo de 1 año de simulación (Figura 8.17), indica picos espectrales a frecuencias menores que la frecuencia inercial (bandas sombreadas en Figuras 8.17b y c). Estos picos coinciden con el rango de frecuencias más recurrente del núcleo interior del remolino dadas por la relación de dispersión para las VRWs.

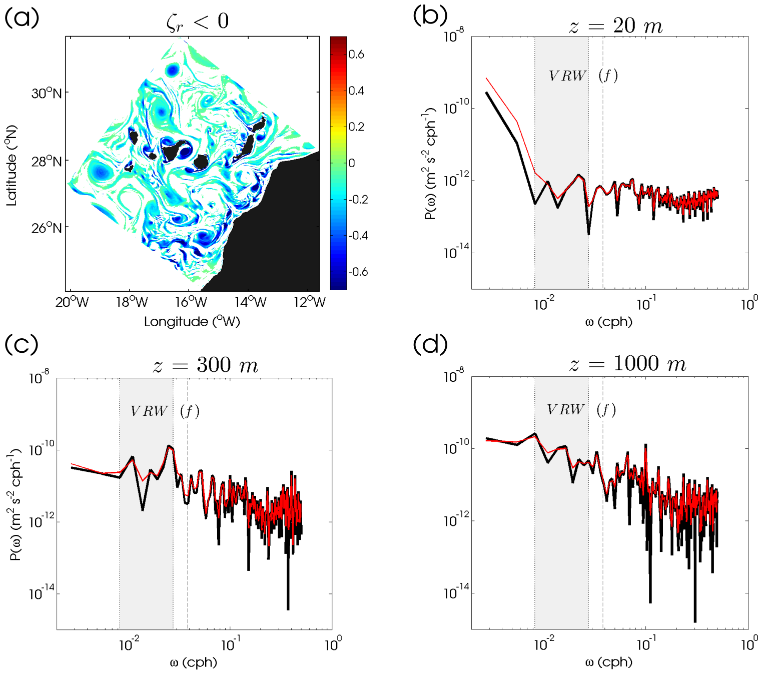

Figure 8.17: (a) Ejemplo de una instantánea horizontal $\zeta_r < 0$ normalizada con f del día 27 y mes 06, cribando así solamente aquellos remolinos anticiclónicos en los que se realiza el promedio para el análisis espectral. La frecuencia espectral de la velocidad vertical se calcula para tres profundidades: (b) 20 m; (c) 300 m y (d) 1000 m. Las líneas rojas finas denotan el filtrado de las señales mediante un filtro de Hanning. La frecuencia inercial f es también indicada por la línea vertical negra, mientras que las áreas sombreadas muestran el rango de frecuencias desde 0.0083 a 0.0278 cph (1.5 a 5 días).

8.6.5 Papel de la mezcla diapicna en el campo superficial de w

La mezcla vertical más intensa está relacionada con los remolinos mesoescalares lejos de las zonas costeras (Figura 8.18a). Se observa un ligero aumento de K_v en la periferia este de ambos remolinos $A1$ y $A2$ (Figura 8.18a), resultado que concuerda con el aumento de mezcla diapicna observado en el caso del remolino intratermoclina del Capítulo 5.

La mezcla vertical contribuye al patrón general de w_{ROMS} en superficie de forma similar a como lo hacen los términos de estiramiento e inclinación del vórtice (ver

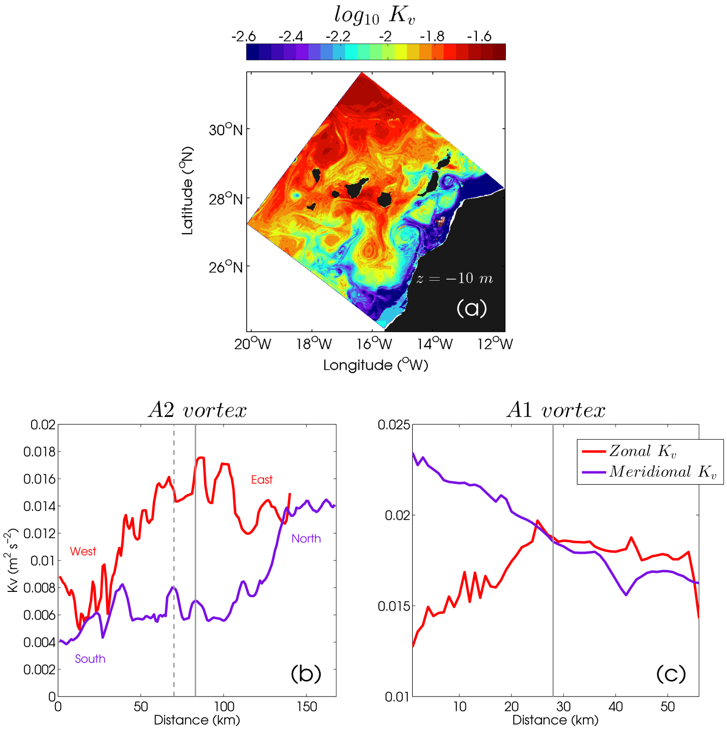

Figure 8.18: Campo instantáneo de K_v ($\mathrm{m}^2\ \mathrm{s}^{-2}$) a 10 m de profundidad cubriendo todo el dominio numérico, generado por la parametrización de KPP incluida en ROMS. Las figuras inferiores son perfiles zonales (rojo) y meridionales (azul) de K_v centrados en el núcleo de ambos remolinos (b) $A2$ y (c) $A1$. Las líneas verticales continuas y discontinuas denotan el centro del remolino para las secciones zonales y meridionales respectivamente.

Figuras 8.14). Sin embargo, de estos tres términos solo ***Vmix*** se asemeja al patrón en espiral de w_{ROMS} en superficie (Figuras 8.14a y g).

Nuestros resultados también indican que, aunque la influencia de ***Vmix*** esté restringida a la capa de frontera superior (Nagai et al., 2006; Koszalka et al., 2010; Pallàs-Sanz et al., 2010), podría controlar indirectamente el campo general w_{ROMS} mediante la influencia que ejerce en el término ***Ageo*** en superficie (Figura 8.19a). Cuando esto ocurre, la componente ageostrófica es realzada, destruyendo el balance de viento termal, especialmente en la periferia del remolino. Para restaurar el balance, se origina una circulación vertical (Ponte et al., 2013) que conduce a un máximo superficial de ***Ageo*** y por lo tanto también de w_{ROMS} como se observa en los perfiles verticales de la Figura 8.19a.

Es este caso, la fuerte estratificación debajo de las capas superficiales parece imponer una barrera para la extensión de la mezcla vertical, la cual se desvanece drásticamente en la base de h_{ubl} (Figuras 8.19b y c).

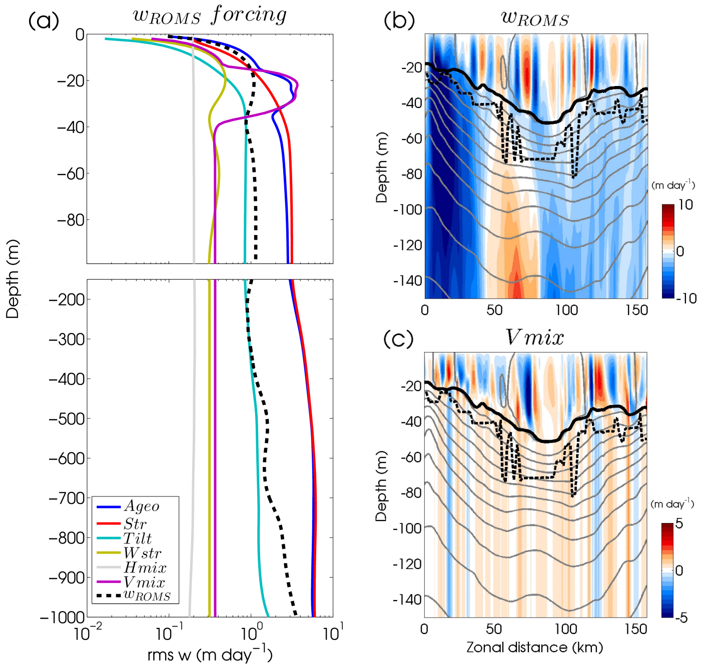

Figure 8.19: (a) Error cuadrático medio (rms por sus siglas en inglés) de cada término en los que se descompone w_{ROMS} para el remolino $A2$. Note la escala logarítmica. Secciones zonales verticales donde (b) w_{ROMS}, y (c) término $\boldsymbol{Vmix}$. Las líneas horizontales continuas y discontinuas denotan h_{ubl} y el máximo gradiente de N^2, respectivamente. Los contornos en gris son isopicnas cada 0.15 (kg m^{-3}).

8.6.6 Dipolo subsuperficial de w

Mientras que por encima de h_{ubl} el campo de w se encuentra dominado por un patrón de onda en forma de espiral, debajo de esta capa se desarrollan dipolos de w en todos los remolinos del dominio numérico, tanto ciclónicos como anticiclónicos. Las secciones verticales del dipolo de w para nuestro caso particular del vórtice $A2$ (Figura 8.22a), muestra que este se extiende hasta la base del remolino (800 m). Entre ambas celdas de velocidad vertical, se encontraron w nulas o extremadamente débiles, concordando con recientes observaciones de Barceló-Llull et al. (in prep.)*. Los dipolos de w se

---

[*] Los resultados de su estudio son además concernientes al remolino del Capítulo 5.

encuentran centrados en el núcleo de los remolinos y están inclinados con respecto al centro superficial de estos (Figura 8.22a).

A través de el seguimiento lagrangiano de partículas virtuales lanzadas en el centro del remolino, se observa que los dipolos de w rotan en el mismo sentido que el remolino que lo contiene. Sin embargo, su periodo de rotación es más lento que el del remolino ($\sim$ 6 días), tomando alrededor de $\sim$ 30 días en completar un ciclo completo (Figura 8.20 y animación en material complementario). El dipolo del remolino $A2$, experimenta cambios en su intensidad con el tiempo, debilitándose el día 10 del mes 09 (Figura 8.20c) y reforzándose 10 días después (Figura 8.20e).

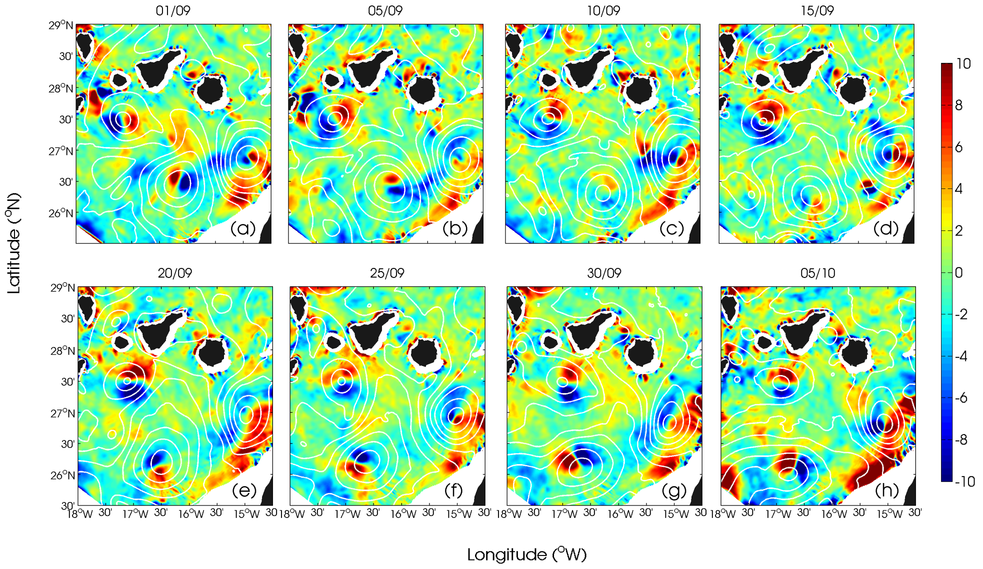

Figure 8.20: Evolución temporal de los dipolos de w para varios vórtices al sur de las Islas Canarias. Las instantáneas corresponden a los mapas horizontales del campo de w_{ROMS} a 300 m de profundidad trazadas cada 5 días desde el día 01 del mes 09. En la parte superior de los mapas se muestra la fecha correspondiente a cada instantánea. Los contornos blancos denotan valores de superficie libre, η_r, a modo de resaltar la forma de cada vórtice.

Trazadores pasivos lagrangianos

A fin de investigar el proceso de axisimetrización de los vórtices, formación de filamentos, periodo de rotación y su relación con la intensidad de los dipolos de w, se lleva a cabo un experimento de liberación de partículas virtuales lagrangianas usando los campos tridimensionales $\boldsymbol{u} = (u, v, w)$ del modelo. La herramienta numérica utilizada para este fin es ROMS OFline Floats (Roff, versión 2.0.1) (Carr et al., 2008)[*]. Después de varios test, se liberaron un total de 5000 partículas a 20 m de profundidad dentro del remolino $A2$, desde el mes 08 al 09 (Figura 8.21a). Las partículas fueron integradas usando un tiempo de paso de 6 horas y transportadas pasivamente por la corriente horizontal sin experimentar migraciones verticales mediante el establecimiento de $w = 0$. La región inicial de liberación de partículas se define como aquella región dominada por la vorticidad, también llamada hiperbólica, dada por el parámetro de Okubo-Weiss (OW) (Okubo, 1970; Weiss, 1991) cuando este es negativo (Figura 8.21).

Los resultados del experimento lagrangiano muestran que el vórtice $A2$ experimenta ciclos de axisimetrización seguidos por periodos inestables de formas elípticas observadas en la evolución temporal de la Figura 8.21.

La causa por la cual los dipolos de w experimentan cambios en su intensidad podría estar relacionada a una combinación de varios factores, en la que la axisimetrización puede tener un importante papel. En un vórtice elíptico como este, el campo de densidad no es axisimétrico impidiendo que se satisfaga el balance de viento gradiente. En consecuencia, se genera una fuerte circulación vertical para restaurar el balance viento gradiente. Además, debido a que los efectos ageostróficos son términos dominantes del campo de w, un decrecimiento de la ageostrofía podría estar ligado a un debilitamiento del dipolo de w. Sin embargo, se necesita un análisis más exhaustivo para establecer las relaciones entre el debilitamiento de los dipolos y las fases de axisimetrización de los vórtices.

Por otro lado, se observa una interesante estructura submesoescalar en forma de filamento a raíz de los experimentos lagrangianos (Figura 8.21). Este filamento en el borde norte del vórtice $A2$ parece mantener la coherencia del remolino a lo largo de su ciclo de vida (Koumoutsakos, 1997). El desarrollo del filamento submesoescalar podría estar relacionado con el proceso de re-axisimetrización propuesto por Graves et al. (2006), el cual a su vez se encuentra condicionado por la existencia de VRWs. A través de la eyección de filamentos de vorticidad potencial, las VRWs transfieren su energía nuevamente hacia el vórtice a medida que se propagan hacia afuera, así, los filamentos tienden a rodear el vórtice haciéndolo más circular (Graves et al., 2006) y por lo tanto

---

[*] Roff es básicamente la modificación del módulo lagrangiano de ROMS para usar archivos netcdf del modelo de forma “offline”, es decir, una vez finalizada la simulación.

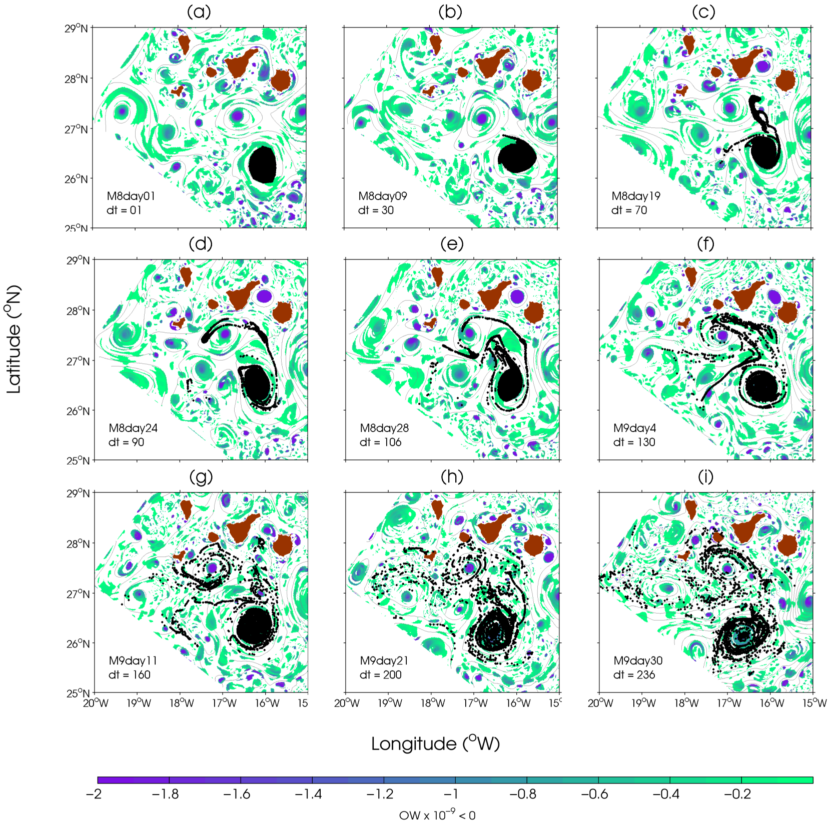
(a)
(b)
(c)
(d)
(e)
(f)
(g)
(h)
(i)
M8day01
dt = 01
M8day09
dt = 30
M8day19
dt = 70
M8day24
dt = 90
M8day28
dt = 106
M9day4
dt = 130
M9day11
dt = 160
M9day21
dt = 200
M9day30
dt = 236
29°N
28°N
27°N
26°N
25°N
20°W
19°W
18°W
17°W
16°W
15°W
Latitude (°N)
Longitude (°W)
−2
−1.8
−1.6
−1.4
−1.2
−1
−0.8
−0.6
−0.4
−0.2
OW x 10^−9 < 0

Figure 8.21: Secuencia temporal del experimento de liberación de partículas lagrangianas. (a) Área de vertido de las partículas correspondiente al centro del vórtice $A2$. La escala de colores denota OW negativos indicando solamente regiones dominadas por la vorticidad. El mes, día y tiempo de paso (dt) de cada instantánea se muestra en la esquina inferior izquierda.

reforzándolo. Adicionalmente, una baja proporción de partículas son expelidas lejos del remolino a través de estos filamentos (Figura 8.21c), indicando que fuertes gradientes de ζ_r pueden actuar como barreras para los trazadores (Provenzale, 1999; Samuelsen et al., 2012). Después de un periodo de re-axisimetrización ($\sim$ 30 días), las partículas tienden a migrar hacia el centro del remolino agrupándose (Figura 8.21f y animación en material suplementario). Esto es consistente con la liberación de boyas reales en el estudio observacional de Sangrà et al. (2005) y puede ser el resultado de la propia dinámica de los remolinos y de su campo de velocidad debido a movimientos divergentes (Koszalka, 2008; Samuelsen et al., 2012).

8.6.7 Comparación con la ecuación omega generalizada

La obtención de medidas directas de velocidad vertical en el océano representan un desafío, en gran parte debido a los bajos valores de w cuando se compara con escalas horizontales. En consecuencia, se han desarrollado formulaciones diagnóstico en orden de inferir indirectamente el campo de w a partir de variables hidrográficas comunes tales como el campo de densidad (Hoskins et al., 1978). La ec. (8.10) es por otro lado difícil de diagnosticar manteniendo las escalas sinópticas de las medidas. Para el caso cuando se dispone de campos de densidad y velocidades horizontales Viúdez and Dritschel (2004) proponen una aproximación a la ecuación omega generalizada, derivada por Viúdez et al. (1996).

La w_{ROMS} dada por la ecuación de divergencia instantánea del flujo (ec. 8.10), es comparada con la w diagnosticada por la ecuación omega generalizada de Viúdez et al. (1996) (de ahora en adelante denominada w_{OMEGA}).

En términos del vector $\boldsymbol{Q}$, dicha ecuación omega generalizada se lee tal que:

$$N^2\boldsymbol{\nabla}_h^2(w) + f(f+\zeta_r)\frac{\partial^2 w}{\partial z^2} = \underbrace{2\boldsymbol{\nabla}_h \cdot \boldsymbol{Q}_h}_{F_{QT}} + \underbrace{f\boldsymbol{\zeta}_{ph}^a \cdot \boldsymbol{\nabla}_h^2 \boldsymbol{u}_h}_{F_{PSE}} \tag{8.11}$$

siendo el vector horizontal $\boldsymbol{Q}_h$

$$\boldsymbol{Q}_h = \frac{g}{\rho_o}(\partial_x u \partial_x \rho + \partial_x v \partial_y \rho, \partial_y u \partial_x \rho + \partial_y v \partial_y \rho) \tag{8.12}$$

donde el subíndice h denota la componente horizontal y el superíndice a indica la componente del vector ageostrófico. Referirse a Viúdez et al. (1996) y Pallàs-Sanz and Viúdez (2005) para mayores detalles de la implementación de esta ecuación. Note que en la ec. (8.11), los efectos de la mezcla diapicna no son incluidos y que por lo tanto, la comparación se restringe a profundidades debajo de la capa límite superior.

De los términos a la derecha de la ec. (8.11), el primero corresponde al cambio temporal del gradiente horizontal de densidad inducido por el campo de corrientes horizontales totales cuyo forzamiento es F_{QT} (es decir, la divergencia del vector $\boldsymbol{Q_h}$). El segundo término de forzamiento es la pseudovorticidad ageostrófica horizontal (F_{PSE}), donde $\boldsymbol{\zeta}_{ph}^a = (-\partial_z v^a, \partial_z u^a)$ y representa la reorientación por el campo total de velocidad horizontal de una pseudovorticidad horizontal y ageostrófica (Viúdez and Dritschel, 2004; Giordani et al., 2006). Una de las ventajas de la ecuación omega generalizada es que incluye de forma explícita ambas cantidades geostróficas y ageostróficas en la divergencia del vector $\boldsymbol{Q_h}$ (Viúdez et al., 1996; Pallàs-Sanz and Viúdez, 2005), donde $F_{QG} = 2\boldsymbol{\nabla}_h \cdot \boldsymbol{Q}_h^g$ es la divergencia del campo de velocidades geostrófico y $F_{QA} = 2\boldsymbol{\nabla}_h \cdot \boldsymbol{Q}_h^a$ es su contrapartida ageostrófica. En consecuencia, las velocidades verticales forzadas por estas cuatro componentes serán: w_{QT}, w_{QG}, w_{QA} y w_{QPSE}, donde en suma darán la velocidad vertical total diagnosticada w_{OMEGA}.

Como se ilustra en las Figuras 8.22a y b, w_{ROMS} y w_{OMEGA} tienen un alto grado de coincidencia donde una es el reflejo del campo de la otra. Ambas muestran una forma de dipolo en el campo de w centrado en el núcleo del remolino. El orden de magnitud de w es también sorprendentemente similar, en contraste con lo encontrado por Koszalka et al. (2009). En su modelo ROMS idealizado, Koszalka et al. (2009) muestran que w_{OMEGA} es sobrestimada en relación al campo de w diagnosticado mediante la teoría cuasi-geostrófica* (Pinot et al., 1996; LaCasce and Mahadevan, 2006). Sin embargo, nuestros resultados sugieren que el uso de la ecuación omega generalizada da lugar a estimaciones coherentes del campo de w dentro de remolinos mesoescalares.

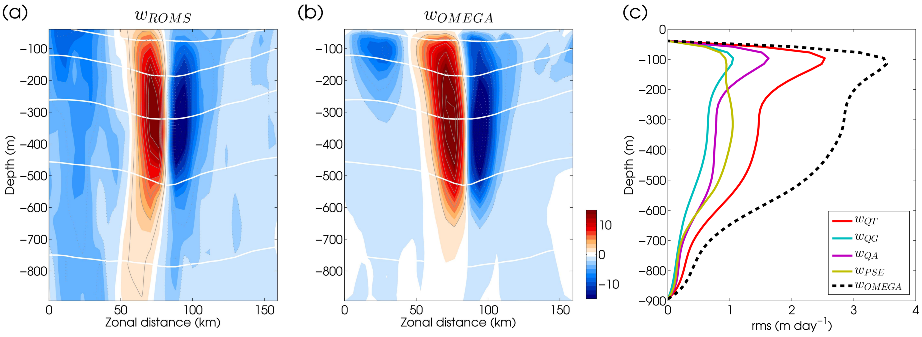

Figure 8.22: Secciones verticales zonales del vórtice $A2$ para el día 29 del mes 08 de (a) w_{ROMS} y (b) w_{OMEGA} (m d^{-1}). Las isopicnas trazadas cada 0.25 kg m^{-3} son trazadas mediante contornos blancos. Ambas w tienen una resolución horizontal de 5 km. El error cuadrático medio (rms por sus siglas en inglés) de cada componente de w_{OMEGA} se muestra en la figura (c).

La Figura 8.22c muestra que w_{OMEGA} se encuentra principalmente inducida por la deformación total del gradiente de densidad F_{QT} (Calil and Richards, 2010). Una interesante contribución de este estudio numérico es que hay una preponderancia del

---

[*] No obstante, Koszalka et al. (2009) también observan similares distribuciones de la velocidad vertical entre w_{ROMS} y w_{OMEGA}.

forzamiento F_{QA} en las capas superficiales de la columna de agua (Figura 8.22c). El predominio del término de velocidad vertical ageostrófica w_{QA}, también es destacado mediante el diagnóstico de w dado por la ec. (8.10) a través del forzamiento $\boldsymbol{Ageo}$. A pesar de encontrarnos bajo diferentes enfoques, ambos análisis (divergencia del flujo y ecuación omega) sugieren que los efectos ageostróficos son forzamientos relevantes para la dinámica vertical de los remolinos mesoescalares. Por otro lado, la w inducida por el forzamiento de pseudovorticidad F_{PSE}, representa una contribución menor al campo general de w (Figura 8.22c), aunque también exhibe un patrón de dipolo semejante.

8.6.8 Discusión y conclusiones

Los principales resultados de este capítulo destacan que la velocidad vertical dentro de remolinos anticiclónicos de mesoescala está fuertemente ligada a los efectos ageostróficos y de estiramiento del vórtice. Las interacciones remolino-viento, así como los términos de Ekman no lineales asociados no explican el patrón general del campo de w. Los principales forzamientos del campo de w de remolinos anticiclónicos de este estudio numérico son detallados a continuación

Papel de la mezcla diapicna en la w superficial

El campo de w entre la superficie y h_{ubl}, exhibe un patrón de onda en forma de espiral donde se alternan celdas de hundimiento y afloramiento al rededor del núcleo de los remolinos. Esta distribución del campo de w también es reproducida por el término de forzamiento de inclinación del vórtice y por el de mezcla vertical. La mezcla vertical o diapicna en esta capa superficial se encuentra vinculada a la presencia de estructuras de mesoescala como remolinos y su relacionada variabilidad de submesoescala. A menudo, es intensificada en los bordes de los remolinos anticiclónicos mesoescalares.

La mezcla vertical de la capa de mezcla ejerce un control indirecto sobre el campo de w mediante su influencia en el forzamiento ageostrófico reforzándolo. En respuesta de este reforzamiento, se induce un máximo superficial de w para restaurar el balance de viento termal (Ponte et al., 2013).

Por debajo de h_{ubl}, la mezcla diapicna es inhibida por una fuerte estratificación, donde no se observan fuentes extra de energía cinética turbulenta como en el caso del remolino anticiclónico intratermoclina del Capítulo 5. A pesar de que la configuración de KPP permite la generación de ondas inerciales como precursoras de mezcla interior, estas no son simuladas en este modelo numérico debido al forzamiento inicial de un campo de vientos climatológicos.

Dipolo de w subsuperficial

En la parte subsuperficial del remolino, se desarrolla una recurrente estructura de dipolo en el campo de w. Esta estructura domina el centro de todos los remolinos mesoescalares del dominio numérico. El dipolo de w rota en el sentido del remolino experimentando cambios en su intensidad a medida que se propaga. Los periodos de debilitamiento del dipolo de w podrían estar relacionado con fases de axisimetrización y decrecimiento de efectos ageostróficos. Estos dipolos de w son principalmente provocados cuando los términos ageostróficos y de estiramiento no se cancelan mutuamente. En consecuencia, el mecanismo detrás de su formación podría estar relacionado con un desequilibrio en las ecuaciones de viento-gradiente producidas por la falta de axisimetrización del remolino (Koszalka et al., 2009). Esto causaría un desajuste entre Coriolis, el gradiente de presión y la fuerza centrífuga en el vórtice, induciendo fuertes circulaciones secundarias por frontogénesis Capet et al. (2008b).
Los dipolos de w también son observados cuando se diagnostica w a través de la ecuación omega generalizada de Viúdez et al. (1996). Las comparaciones arrojan un buen grado de correspondencia entre w_{ROMS} y w_{OMEGA} debajo de h_{ubl}. El análisis de los forzamientos de la ecuación omega generalizada muestra que la divergencia del vector $\boldsymbol{Q}_h$ domina la velocidad vertical. La deformación del gradiente de densidades es principalmente inducido por el campo de corrientes horizontales ageostróficas. En suma, ambos análisis, indican que los efectos ageostróficos están fuertemente implicados en la formación del dipolo de w en fluido estratificado.

Influencia de VRWs en el campo de w

Los cambios en la forma superficial del remolino, la formación de filamentos hacia estados de axisimetrización y las estructuras en forma de onda del campo de w_{ROMS} y de sus forzamientos, indican la posible presencia de ondas de vórtice de Rossby. Los resultados revelan que estas ondas pueden tener lugar en esta configuración numérica con periodos entre 1.5 y 40 días.
Los vórtices simulados experimentan variaciones en su relación de aspecto, con fases de axisimetrización. También se desarrollan filamentos de submesoescala asociados a los

remolinos, representando una barrera para los trazadores pasivos. En estados maduros del remolino, las partículas pueden migrar hacia el núcleo interior o ser conducidas lejos del remolino utilizando a estos filamentos como vía principal. La explicación de esto subyace en que las VRWs actúan como un mecanismo restaurador hacia la re-axisimetrización del vórtice, expeliendo vorticidad potencial desde el centro del remolino hacia afuera después de una perturbación inducida por la deformación. Adicionalmente, la propagación de esas perturbaciones de vorticidad potencial también pueden conducir a cambios en el transporte vertical dentro de los remolinos, produciendo parches de hundimiento y afloramiento de acuerdo con las variaciones en vorticidad (Koszalka et al., 2009; Cardona and Bracco, 2012; Nardelli, 2013). Por lo tanto, se sugiere también que las VRWs podrían estar modulando el patrón espacial del campo de w general.

8.7 Capítulo 7: Conclusiones Finales y Líneas Futuras

A continuación se detallan las principales conclusiones extraídas de esta tesis.

Capítulo 4

- El aumento de las tasas de *entrainment* diapicno en aguas influenciadas por el filamento de afloramiento está relacionado con un incremento de la cizalla vertical y altas tasas de disipación turbulenta.

- La extensión vertical de la mezcla activa, dada por zonas de *entrainment* positivas, junto con un aumento de las tasas de disipación de energía cinética turbulenta, crean condiciones óptimas para la generación de procesos de *entrainment* diapicno. Esto es especialmente importante en aguas de filamento donde la picnoclina es cercana a la superficie y la mezcla puede actuar de forma más eficiente.

- La sobrestima de las tasas de disipación turbulenta parametrizadas conducen a débiles tasas de *entrainment*. En consecuencia, esto podría producir un sobrecalentamiento de la temperatura superficial del mar en modelos que incluyan tales formulaciones.

- La falta de consenso entre las diferentes parametrizaciones animan al desarrollo de una formulación de *entrainment* diapicno más precisa, basada en la formulación sugerida en este trabajo, donde la agitación del viento, los flujos de flotabilidad superficiales y en la interfase, la corriente de cizalla vertical en la base de la capa de mezcla, sean incluidas como fuentes de *entrainment* diapicno dentro de una sola formulación.

Capítulo 5

- La fuente de energía cinética turbulenta en la superficie e interfase de un remolino anticiclónico intratermoclina resulta de un efecto combinado de convección nocturna, cizalla vertical de la corriente y picos en la tensión del viento, los cuales deben ser integrados dentro de las parametrizaciones de *entrainment* diapicno.

- La capa de mezcla activa se extiende debajo de la capa de mezcla a lo largo del transecto del remolino, y es independiente de los ciclos de flujos de calor y flotabilidad. Esto puede dar lugar a condiciones favorables para la generación de velocidades de *entrainment* diapicno positivas. Las tasas de *entrainment* se encuentran relacionadas en gran medida con la capa de mezcla activa, la cual a su vez muestra una dependencia con la forma de las isopicnas del remolino intratermoclina.

- En la periferia del remolino, el incremento de las tasas de disipación turbulenta en superficie e interfase es consistente con un aumento de la difusividad diapicna y un ligero incremento de las tasas de *entrainment*. En el núcleo del remolino, la difusividad es un orden de magnitud menor que en los bordes. Por el contrario, la difusividad diapicna es realzada en profundidades intermedias en el núcleo del remolino. Además, este incremento se ve favorecido por un aumento en los niveles de cizalla vertical y altas tasas de disipación a estas profundidades. Esto último sugiere que el aumento de mezcla interna podría ser el resultado de ondas cuasi-inerciales atrapadas por el remolino anticiclónicos del corredor de remolinos de Canarias.

Capítulo 6

- La velocidad vertical superficial de un remolino numérico anticiclónico exhibe un patrón de onda en espiral, asociado con la inclinación del vórtice y mezcla vertical. Esta última está relacionada con estructuras de mesoescala, siendo a menudo intensificada en la periferia de los remolinos. La mezcla vertical puede indirectamente controlar el campo de velocidades vertical mediante la modificación de los términos de forzamiento ageostróficos. Una consecuencia notable, es el máximo superficial de la velocidad vertical resultado de la tendencia de restaurar el balance de viento termal. La mezcla diapicna es inhibida por una fuerte estratificación debajo de la capa límite superior.

- El patrón de velocidad vertical subsuperficial muestra una recurrente estructura en forma de dipolo en el centro de todos los remolinos del dominio numérico. La velocidad vertical del dipolo rota lentamente en el sentido del remolino y sus variaciones en intensidad podrían estar relacionadas con cambios en la axisimetrización de los remolinos. La creación de esos dipolos no puede ser explicada por las interacciones remolino-viento a través de los mecanismos de Ekman no lineal. El desequilibrio entre los términos de forzamiento ageostrófico y de estiramiento del vórtice indican que la interrupción del balance viento gradiente está implicado en el mecanismo de generación de esos dipolos.
- Las comparaciones de las velocidades verticales dadas por el modelo numérico con las diagnosticadas mediante la ecuación omega, muestra que existe un gran grado de correspondencia entre ambas. La divergencia del vector $\boldsymbol{Q}_h$ domina el campo de velocidad vertical, y en particular el campo de corrientes horizontales ageostróficos es el principal forzamiento de la velocidad vertical en profundidades subsuperficiales de los remolinos. Este resultado es consistente con el encontrado mediante la divergencia del flujo.
- La presencia de ondas de vórtice Rossby es evidenciada mediante los patrones de onda de la velocidad vertical. Los periodos de dispersión para estas ondas se encuentran en el rango de 1.5 a 40 días. Las ondas de vórtice de Rossby representan un mecanismo restaurador en el proceso de axisimetrización dado que expelen vorticidad potencial hacia afuera del remolino. A su vez, la axisimetrización se encuentra relacionada con los filamentos de submesoescala de los remolinos que actúan como una barrera para los trazadores pasivos y también como vía de escape de las mismas fuera de la estructura. Las ondas de vórtice de Rossby podrían estar modulando el patrón de velocidades verticales a través de la propagación

de esas perturbaciones de vorticidad potencial conduciendo a variaciones en la vorticidad y en última instancia a cambios en el transporte vertical.

8.7.1 Líneas futuras de investigación

Finalmente, se enumeran algunas cuestiones que surgen a raíz de los resultados obtenidos en esta tesis y que en consecuencia pueden ser exploradas en trabajos futuros.

1. Otras fuentes de energía cinética turbulenta, tales como la radiación de energía de la rotura de ondas en la interfase y la circulación de Langmuir, deberían ser investigadas con el fin de incluirlas dentro de la parametrización propuesta del Capítulo 4. Al mismo tiempo, debido a que nuestra formulación sugerida depende de observaciones de tasas de disipación, se requiere una parametrización de la misma que sea coherente con la disipación observada.

2. Se precisan algoritmos más precisos para determinar la profundidad de la capa de mezcla activa. Estudios recientes indican la relevancia de la capa de mezcla activa en la modulación de la capa superficial del océano y en la hipótesis de la profundidad crítica de Sverdrup (1953) (Franks, 2014; Sutherland et al., 2014). Una forma alternativa de obtención de esta capa puede ser proporcionada por las escalas de Thorpe, las cuales, aunque dependen de la resolución vertical de los perfiles de densidad, pueden servir como un buen indicador de parches turbulentos.

3. Una cuestión a ser tratada es la relación que existe entre los procesos de *entrainment* diapicno y frontogénesis (Capet et al., 2008b). El papel del proceso de *entrainment* en mantener o magnificar la circulación secundaria ageostrófica, por ejemplo en la periferia de un remolino, sigue sin ser clarificado.

4. Los anteriores estudios deben ser llevados a cabo mediante un apropiado muestreo espacio-temporal. Por ejemplo, a través de submarinos teledirigidos no tripulados (*gliders*), equipados con sensores de microestructura.

5. Explorar los mecanismos físicos que subyacen detrás de la generación de dipolos de velocidad vertical dentro de remolinos de mesoescala, así como las causas de sus cambios de intensidad con el tiempo. Modelos numéricos de alta resolución, incluyendo forzamientos atmosféricos interanuales, podrían ayudar a corroborar si la mezcla vertical profunda puede interrumpir o reforzar la estructura de dipolo.

6. Corroborar si existe una relación directa entre la intensificación de las velocidades verticales y la intermitencia de la tasa de deformación de los remolinos. A este respecto, se debe examinar la implicación de las ondas de vórtice de Rossby en el proceso de axisimetrización y la consecuente intensificación del campo de velocidades verticales.

7. Examinar la predominancia de velocidades diapicnas e isopicnas en el campo total de velocidades, dentro de estructuras de mesoescala. Esto puede llevarse a cabo mediante la consideración de un sistema de referencia isopicno, incluido dentro de una aproximación cuasi- o semi-geostrófica. Bajo este marco teórico, los procesos de mezcla turbulenta podrán ser también investigados.

En general, el papel de la mezcla diapicna y los procesos turbulentos asociados en el océano debe aún ser esclarecido. Varios procesos de mezcla, incluyendo el fenómeno de *entrainment* diapicno y la difusividad diapicna, son a menudo parametrizados independientemente de la dinámica de la región oceánica y de las condiciones físicas del flujo. Esta tesis anima a la realización de futuros estudios enfocados en la simplificación de las parametrizaciones de mezcla y en la delineación del papel de la mezcla diapicna en el transporte vertical dentro de estructuras de mesoescala.

A

Parameterization of ε_p

Bulk mixed layer based entrainment parameterizations included in Chapters 4 and 5 depend on a parameterized form of the turbulent kinetic energy dissipation rates (ε_p) given by Gaspar (1988), which is briefly described below.

Based on the parameterization of (Kolmogorov, 1942), the dissipation ε_m appropriately extended for the use in mixed layer models takes the form:

$$\varepsilon_m = \sigma_e^3/l \tag{A1}$$

where σ_e is a characteristic value for the turbulent velocity within the mixed layer and l is a dissipation integration length which should depend on:

$$l = F(h_\rho, L, \lambda, L_\Delta) \tag{A2}$$

with

F = a function to be determined

$L = u_*^3/J_b^o(h_\rho)$, a bulk Monin-Obukhov length, where J_b^o is the surface net buoyancy flux, u_* the friction velocity and h_ρ is the depth of the mixed layer.

$\lambda = u_*/f$, the Ekman length scale.
$L_\Delta = (\delta u^2 + \delta v^2)/\delta b$, a Monin-Obukhov lenght appropiated to the entrainment zone (DIT term).
As the DIT term is neglected in eq. (4.1), it is subsequently omitted in the ε_p parameterization (i.e., L_Δ is avoided). After a dimensional analysis, eq.(A1) can be rewritten as

$$h_\rho \varepsilon_m = h_\rho \sigma_e^3/l = \sigma_e^3 G(h_\rho/L_{mo}, h_\rho/\lambda) \tag{A3}$$

where G is a dimensionless function of the Monin-Obukhov stability parameter (h_ρ/L), and the Rossby rotation parameter (h_ρ/λ). Subscripts m of all parameters denote averages over the mixed layer. Most of the parameterizations assume that $\sigma_e = u_*$ is inappropriate in convective conditions, for example Deardorff (1983). Consequently, Gaspar (1988) suggests that the best choice for σ_e is

$$\sigma_e^2 = q_m = \frac{1}{h_\rho}\int_{h_\rho}^{0} \overline{q}(dz) \tag{A4}$$

yielding the natural extension of the Kolmogorov relation of $\varepsilon = \overline{q_m}^{3/2}/l_m$ for depth integrated models, where q_m is the turbulent kinetic energy averaged over the mixed layer.
Atmospheric observations of the upper boundary layer suggest that l decreases while the stability parameter increases (Louis et al., 1983). It is also argued that rotation limits the vertical size of the eddies and, hence, l. Accordingly, it is required that the ratio h_ρ/l is an increasing function for both the stability and rotation parameters:

$$\begin{gathered}\frac{\partial G}{\partial(h_\rho/L_{mo})} \geq 0 \\ \frac{\partial G}{\partial(h_\rho/\lambda)} \geq 0\end{gathered} \tag{A5}$$

Gaspar (1988) proposes to use a definition for h_ρ/l such as:

$$\begin{aligned} h_\rho/l &= G(h_\rho/Lmo, h_\rho/\lambda) \\ &= a_1 + a_2 max[1, h_\rho/(0.4\lambda)] exp(h_\rho/L_{mo}) \end{aligned} \tag{A6}$$

where a_1 and a_2 are positive constants. Expression A6 assumes that when h_ρ exceeds the neutral height scale (0.4λ), this height will become the main dissipation length instead of h_ρ. Similarly, A6 is also consistent with conditions A3 and A5.

In brief, the equation for the prediction of h_ρ in the model of Gaspar (1988) is simply the turbulent kinetic energy budget in which the dissipation is parameterized using equations A3, A4 and A6:

$$0.5h_\rho \delta b w_e = (m_1 + m_2)u_*^3 + 0.5h_\rho J_b^o(h_\rho) - (h_\rho/l)q_m^{3/2} \tag{A7}$$

where q_m in eq.(A7) is finally obtained as

$$q_m = \overline{\varepsilon_p} h_\rho = (h_\rho/l)^{-2/3}(S_p - 0.5X)^{2/3} \tag{A8}$$

with $S_p = (m_1 + m_2)u_*^3 - 0.5J_b^o h_\rho > 0$; and
$X = h_\rho \delta b w_e$.

B

Local dispersion relation for vortex Rossby waves

The local dispersion relation for quasigeostrophic Vortex Rossby Waves (VRW) was first obtained by Montgomery and Kallenbach (1997) and some years later was extended by McWilliams et al. (2003). This relation is formulated through a Wenzel-Kramers-Brillouin analysis of the shallow water equations on the f-plane. McWilliams et al. (2003) generalized both the wave amplitude and wave phase coordinate dependencies, and followed a different derivation path of the asymmetric balance model used. Here, the local dispersion relation for VRWs used in Chapter 6 is summarized according to the observational study of Nardelli (2013) who examine VRWs by using synthetic satellite observations.

After transforming actual model coordinates to a cylindrical coordinate system tied to the eddy center, the dimensional form of the local dispersion relation for VRWs can be read as:

$$\omega_v = k_A\overline{\Omega} + \frac{k_A}{r}\frac{\overline{G}}{(k_r^2 + (\frac{\overline{\varphi} k_A}{r})^2 + \gamma^2)} \tag{B1}$$

where ω_v is the wave angular frequency and k_A the azimuthal wavenumber. In the study of Chapter 6, k_A is taken to be 2 which prevails in the vertical velocity field because of the vertical mixing and tilting terms (Koszalka et al., 2009). $k_r = 2\pi/\lambda_w$ is the radial wavenumber, where $\lambda_w \approx 15$ km, since it is the mean wavelength found for the vertical velocity disturbances of the simulated vortex field (Koszalka et al., 2009). $\overline{\Omega}$ is the angular velocity of the vortex and r the radial distance. $\overline{G}$ is the normalized mean-vortex potential vorticity radial gradient

$$\overline{G} = \overline{\xi}\frac{\partial(ln\overline{q_{pv}})}{\partial r} \tag{B2}$$

being $\overline{\xi} = f + 2\Omega$ the modified Coriolis frequency and $\overline{q_{pv}}$ the potential vorticity

$$\overline{q_{pv}} = \frac{f + \overline{\zeta}}{g\overline{h}} \tag{B3}$$

and the relative vorticity

$$\overline{\zeta} = \frac{1}{r}\frac{\partial(r\overline{v})}{\partial r} \tag{B4}$$

Then, γ^2 is the square inverse local deformation radius

$$\gamma^2 = \frac{\overline{\xi}\overline{\eta}}{g\overline{h}} \tag{B5}$$

$\overline{\eta} = \overline{\zeta} + \overline{\xi}$ being the absolute vorticity and $\overline{h}$ is the fluid depth. Finally, g is the vertical gravitational acceleration, and $\overline{\varphi}$ is given by the ratio:

$$\overline{\varphi} = \frac{2\overline{\xi} - \overline{\eta}}{\overline{\eta}} \tag{B6}$$

References

A

Alexander, M. A., Scott, J. D., and Deser, C. Processes that influence sea surface temperature and ocean mixed layer depth variability in a coupled model. *Journal of Geophysical Research*, 105(C7):16823–16842, 2000. 5, 124

Anis, A. and Moum, J. Prescriptions for heat flux and entrainment rates in the upper ocean during convection. *Journal of Physical Oceanography*, 24(C10):2142–2155, 1994. doi: 10.1175/1520-0485(1994)024⟨2142:PFHFAE⟩2.0.CO;2. 33, 75, 133

Arcos-Pulido, M., Rodríguez-Santana, A., Emelianov, M., Paka, V., Arístegui, J., Benavides, M., Sangrà, P., Machín, F., García-Weil, L., and Estrada-Allis, S. Diapycnal nutrient fluxes on the northern boundary of Cape Ghir upwelling region. *Deep-Sea Research Part I*, 84: 100–109, 2014. doi: 10.1016/j.dsr.2013.10.010. 14, 15, 41, 42, 139

Arístegui, J., Sangrà, P., Hernádez-León, S., Cantón, M., Hernández-Guerra, A., and Kerling, J. L. Island-induced eddies in the Canary Island. *Deep Sea Research Part I*, 41:1509–1525, 1994. 16, 87, 157

B

Barceló-Llull, B., Pallàs-Sanz, E., and Sangrà, P. On the nature of a subtropical mode water eddy Part II: vertical velocities. in prep. 105, 167

Barton, E., Inall, M., and Sherwin, T. J. Vertical structure, turbulent mixing and fluxes during Lagrangian observations of an upwelling filament system off Northwest Iberia. *Progress in Oceanography*, 51(1):249–268, 2001. 34, 40, 134, 137

Barton, E. D., Arístegui, J., Tett, P., Cantón, M., García-Braun, J., Hernández-León, S., Nykjaer, L., Almeida, C., Almunia, J., Ballesteros, S., Basterretxea, G., Escánez, J., García-Weil, L., Hernández-Guerra, A., López-Laatzen, F., Molina, R., Montero, M. F., Navarro-Pérez, E., Rodríguez, J. M., vanLenning, K., Vélez, H., and Wild, K. The transition zone of the Canary Current upwelling region. *Progress in Oceanography*, 41(455–504), 1998. 14, 39

Belcher, S. E., Grant, A. L. M., Hanley, K. E., Fox-Kemper, B., Van Roekel, L., Sullivan, P. P., Large, W. G., Brown, A., Hines, D. A.and Calvert, Rutgersson, A., Pettersson, H., Bidlot, J.-R., Janssen, P. A. E. M., and Polton, J. A. A global perspective on Langmuir turbulence in the ocean surface boundary layer. *Geophysical Research Letters*, 39(18), 2012. ISSN 1944-8007. doi: 10.1029/2012GL052932. 65

Berliand, M. E. and Berliand, T. G. Measurement of the effective radiation of the earth with varying cloud amounts. *Izvestiya Akademii Nauk SSSR, Seriya Geofiz 1*, 1952. 25, 130

Blanke, B., Speich, S., Madec, G., and Mauge, R. A global diagnostic of interior ocean ventilation. *Geophysical Research Letters*, 29(8):1267, 2002. URL `10.1029/2001GL013727`. 65

Boussinesq, J. Thorie de lcoulement Tourbillant. *Mem. Prsents par Divers Savant Acad. Sci. Inst. Fr.*, 23:pp. 46–50, 1877. 3

Bracco, A., von Hardenberg, J., Provenzale, A., Weiss, J., and McWilliams, J. Dispersion and mixing in quasigeostrophic turbulence. *Physical Review Letters*, 92(084501), 2004. 95

Brainerd, K. E. and Gregg, M. C. Surface mixed and mixing layer depths. *Geophysical Research Letters*, 42(9):1521–1543, 1995. doi: 10.1016/0967-0637(95)00068-H. 46, 47, 48, 66, 73, 139, 141, 148

Brochier, T., Mason, E., Moyano, M., Berraho, A., Colas, F., Sangrà, P., Hern´ andez León, S., Ettahiri, O., and Lett, C. Ichthyoplankton transport from the African coast to the Canary Islands. *Journal of Marine Systems*, 87(2):109–122, 2011. 16

Burchard, H., Peter, D. C., Gemmrich, J. R., van Haren, H., Pierre-Philippe, M., Markus, M., M., A., Smith, N., Prandke, H., Rippeth, T. P., Skyllingstad, E. D., Smyth, W. D., Welsh, D. J. S., and Wijesekera, H. W. Observational and numerical modeling methods for quantifying coastal ocean turbulence and mixing. *Progress in Oceanography*, 76(4):399 – 442, 2008. ISSN 0079-6611. doi: http://dx.doi.org/10.1016/j.pocean.2007.09.005. 3, 36, 65, 75

C

Calil, P. H. R. and Richards, K. J. Transient upwelling hot spots in the oligotrophic North Pacific. *Journal of Geophysical Research: Oceans*, 115(C2):n/a–n/a, 2010. ISSN 2156-2202. doi: 10.1029/2009JC005360. URL `http://dx.doi.org/10.1029/2009JC005360`. C02003. 17, 86, 87, 112, 156, 157, 172

Callies, J., Ferrari, R., Klymak, J. M., and Gula, J. Seasonality in submesoscale turbulence. *Nature Communications*, 6(6862), 2015. doi: 10.1038/ncomms7862. 1, 123

Capet, A., Mason, E., Rossi, V., Troupin, C., Faugère, Y., Pujol, I., and Pascual, A. Implications of refined altimetry on estimates of mesoscale activity and eddy-driven offshore transport in the Eastern Boundary Upwelling Systems. *Geophysical Research Letters*, 41 (21):7602–7610, 2014. ISSN 1944-8007. doi: 10.1002/2014GL061770. 29

Capet, X., Campos, E. J., and Paiva, A. M. Submesoscale activity over the Argentinian shelf. *Geophysical Research Letters*, 35(L15605), 2008a. 32

Capet, X., McWilliams, J. C., Molemaker, M. J., and Shchepetkin, A. F. Mesoscale to submesoscale transition in the California Current System. Part II: Frontal processes. *Journal of Physical Oceanography*, 38:44–64, 2008b. doi: http://dx.doi.org/10.1175/2007JPO3672.1. 2, 6, 11, 58, 67, 86, 87, 92, 115, 121, 123, 124, 126, 149, 156, 160, 174, 178

Capet, X., McWilliams, J. C., Molemaker, M. J., and Shchepetkin, A. F. Mesoscale to submesoscale transition in the California Current system. Part III: Energy balance and flux. *Journal of Physical Oceanography*, 38:2256–2269, 2008c. 1, 3, 123

Cardona, Y. and Bracco, A. Enhanced vertical mixing within mesoscale eddies due to high frequency winds in the South China Sea. *Ocean Modelling*, 42:1–15, 2012. doi: 10.1016/j.ocemod.2011.11.004. 11, 16, 18, 86, 87, 101, 126, 156, 157, 175

Carr, S. D., Capet, X. J., Mcwilliams, J. C., Pennington, J. T., and Chavez, F. P. The influence of diel vertical migration on zooplankton transport and recruitment in an upwelling region: estimates from a coupled behavioral-physical model. *Fisheries Oceanography*, 17:1–15, 2008. doi: 10.1111/j.1365-2419.2007.00447.x. 31, 169

Chavanne, C. and Klein, P. Can oceanic submesoscale processes be observed with satellite altimetry? *Geophysical Research Letters*, 37(L22602), 2010. doi: http://dx.doi.org/10.1029/2010GL045057. 30

Chavanne, C. P., Flament, P., Luther, D. S., and Gurgel, K.-W. Observations of vortex Rossby waves associated with a mesoscale cyclone. *Journal of Physical Oceanography*, 40:2333–2340, 2010. doi: http://dx.doi.org/10.1175/2010JPO4495.1. 17, 86, 95, 101, 156, 161, 164

Chelton, D. Report of the high-resolution ocean topography science working group meeting. Technical Report Reference 2001-4, College of Oceanic and Atmospheric Sciences, Oregon State University, Corvallis, Oregon, October 2001. 224p. xvii, 2

Chelton, D. B., Schlax, M. G., Samelson, R. M., and de Szoeke, R. A. Global observations of large oceanic eddies. *Geophysical Research Letters*, 34(15), 2007. doi: 10.1029/2007GL030812. 1, 123

Csanady, G. T. *Turbulent Diffusion in the Environment, Geophysics and Astrophysics Monographs*, volume pp.248. D. Reidel Publishing Company, 1973. 81

Cuypers, Y., Bouruet-Aubertot, P., Marec, C., and Fuda, J. L. Characterization of turbulence from a fine-scale parameterization and microstructure measurements in the Mediterranean Sea during the BOUM experiment. *Biogeosciences*, 9:3131–3149, 2012. doi: 10.5194/bg-9-3131-2012. 16, 65, 67, 78, 148, 149, 154

D

da Silva, A. M., Young, C. C., and Levitus, S. Atlas of surface marine data 1994, Vol. 4: Anomalies of fresh water fluxes. *NOAA Atlas, NESDIS*, 9, 1994. 32, 132

Danioux, E., Klein, P., and Riviere, P. Propagation of wind energy into the deep ocean through a fully turbulent mesoscale eddy field. *Journal of Physical Oceanography*, 38:2224–2241, 2008. 67, 149

D'Asaro, E., Lee, C. M., Rainville, L., Harcourt, R., and Thomas, L. N. Enhanced turbulence and energy dissipation at ocean fronts. *Science*, 332:318–332, 2011. doi: 10.1126/science.1201515. 58, 59, 60

de Boyer Montégut, C., Madec, G., Fischer, A. S., Lazar, A., and Iudicone, D. Mixed layer depth over the global ocean: An examination of profile data and a profile-based climatology. *Journal of Geophysical Research*, 109(C12003), 2004. doi: 10.1029/2004JC002378. xx, 46, 47, 73

Deardorff, J. W. A multi-limit mixed-layer entrainment formulation. *Journal of Physical Oceanography*, 13(6):988–1002., 1983. 5, 10, 33, 53, 54, 60, 61, 124, 125, 133, 145, 182

Deardorff, J. W. Preliminary results from numerical integrations of the unstable boundary layer. *Journal of Atmospheric Science*, 27:1209–1231, 1970. 8, 125

Dewey, R. K. and Moum, J. N. Enhancement of fronts by vertical mixing. *Journal of Geophysical Research*, 95(C6):9433–9445., 1990. 6, 14, 33, 34, 35, 46, 47, 48, 55, 56, 62, 66, 73, 77, 124, 133, 139, 141, 144, 148

Dewey, R. K., Moum, J. N., and Caldwell, D. R. Microstructure activity within a minifilament in the coastal transition zone. *Journal of Geophysical Research*, 98(C8):14457–14470, 1993. 34, 35, 57, 58, 134

Dickey, T. C., Manov, D. V., Weller, R. A., and Seigel, D. Determination of longwave heat flux at the airsea interface using measurements from buoy platforms. *Journal of Atmospheric and Oceanic Technology*, 11:1057–1078, 1994. 25, 130

Dong, S., Sprintall, J., Gille, S. T., and Talley, L. Southern Ocean mixed-layer depth from Argo float profiles. *Journal of Geophysical Research*, 113(C06013), 2008. doi: 10.1029/2006JC004051. xx, 46, 47

Dorrestein, R. On the vertical buoyancy flux below the sea surface as induced by atmospheric factors. *Journal of Physical Oceanography*, 9:229–231, 1979. 26, 69, 130

E

Ellison, T. H. and Turner, J. S. Turbulent entrainment in stratified flow. *Journal of Fluid Mechanics*, 6(3):423–448, 1959. 10, 39, 125, 136

Endoh, T., Matsuno, T., Yoshikawa, Y., Tatsuyama, Y., and Ishizaka, J. Observations of wind-driven deepening of the surface mixing layer in the Tsushima strait. *Journal of Oceanography*, 62(2):273–279, 2009. doi: 10.1007/s10872-013-0215-3. 36

Estrada-Allis, S., Rodríguez-Santana, A., Naveira Garabato, A. C., García-Weil, L., Arcos-Pulido, M., and Emelianov, M. Diapycnal entrainment in an Eastern-Boundary upwelling filament. under review. xxiii, xxx, 15, 66, 72, 75, 76, 77, 148, 152, 153

F

Fairall, C. W., Bradley, E. F., Rogers, D. P., Edson, J. B., and Young, G. S. Bulk parameterization of airsea fluxes for Tropical OceanGlobal Atmosphere CoupledOcean Atmosphere Response Experiment. *Journal of Geophysical Research*, 101(C2):3747–3764, 1996. doi: 10.1029/2010JC006884. 25, 130

Fernando, H. J. Turbulent mixing in stratified fluids. *Annual Review of Fluid Mechanics*, 23 (1):455–493, 1991. 10, 33, 125, 133

Ferrari, R. and Wunsch, C. Ocean circulation kinetic energy: Reservoirs, sources, and sinks. *Annual Review of Fluid Mechanics*, 41:253–282, 2009. doi: 10.1146/annurev.fluid.40.111406.102139. 3, 4, 66, 148

Ferron, B., Mercier, H., Speer, K., Gargett, A., and Polzin, K. Mixing in the Romanche Fracture Zone. *Journal of Physical Oceanography*, 28(10):1929–1945, 1998. 4

Firing, E. and Gordon, R. Deep ocean acoustic Doppler current profiling. *Proc. IEEE Fourth Working Conf. on Current Measurements, Clinton, MD, Institute of Electrical and Electronics Engineers*, pages 192–201, 1990. 24, 128

Firing, E., Ranada, J., and Caldwell, P. Processing ADCP Data with the CODAS Software System Version 3.1. *Joint Institute for Marine and Atmospheric Research/NODC*, 1995. 24, 128

Fischer, J. and Visbeck, M. Deep velocity profiling with self-contained ADCPs. *Journal of Atmospheric and Oceanic Technology*, 10:764–773, 1993. 24, 128

Flór, J. B., Hopfinger, E. J., and Guyez, E. Contribution of coherent vortices such as Langmuir cells to winddriven surface layer mixing. *Journal of Geophysical Research*, 115(C10031), 2010. doi: 10.1029/2009JC005900. 37

Forryan, A., Allen, J. T., Edhouse, E., Silburn, B., Reeve, K., and Tesi, E. Turbulent mixing in the eddy transport of Western Mediterranean Intermediate Water to the Alboran Sea. *Journal of Geophysical Research*, 117(C09008), 2012. doi: 10.1029/2012JC008284. 67, 149

Franks, P. J. Has Sverdrups critical depth hypothesis been tested? Mixed layers vs. turbulent layers. *ICES Journal of Marine Science*, 72(6):1897– 1907, 2014. doi: 10.1093/icesjms/fsu175. 46, 48, 121, 141, 178

G

García-Weil, L., Nykjaer, L., Tejera-Cruz, A., and Cantón, M. Cálculo de velocidades oceánicas superficiales en el área del afloramiento del NW de África mediante imágenes del sensor AVHRR. *Rev. Teledetección*, 3:37–41, 1994. 15

Gaspar, P. Modeling the seasonal cycle of the upper ocean. *Journal of Physical Oceanography*, 18(2):161–180, 1988. xxiii, xxx, 10, 37, 38, 53, 54, 55, 60, 61, 62, 65, 75, 76, 77, 135, 143, 145, 146, 148, 153, 181, 182, 183

Gaube, P., Chelton, D. B., Samelson, R. M., Schlax, M. G., and ONeill, L. W. Satellite observations of mesoscale eddy-induced Ekman pumping. *Journal of Physical Oceanography*, 45(1):104–132, 2015. doi: http://dx.doi.org/10.1175/JPO-D-14-0032.1. 11, 86, 126, 156

Giordani, H., Prieur, L., and Caniaux, G. Advanced insights into sources of vertical velocity in the ocean. *Ocean Dynamics*, 56:513–524, 2006. 12, 86, 112, 157, 171

Graves, L. P., McWilliams, J. C., and Montgomery, M. T. Vortex evolution due to straining: A mechanism for dominance of strong, interior anticyclones. *Geophysical and Astrophysical Fluid Dynamics*, 100(3):151–183, 2006. doi: 10.1080/03091920600792041. 17, 86, 95, 109, 110, 156, 161, 169

Grodsky, S. A., Carton, J. A., and McClain, C. R. Variability of upwelling and chlorophyll in the equatorial Atlantic. *Geophysical Research Letters*, 35(L03 610), 2008. doi: 10.1029/2007GL032466. 34, 133

H

Hagen, E. Northwest African upwelling scenario. *Oceanology Acta*, 24:113–128, 2001. 14, 39, 40, 137

Hagen, E., Zülicke, C., and Feistal, R. Near surface structures in the Cape Ghir filament off Morocco. *Oceanology Acta*, 19:577–598, 1996. 14, 15

Haidvogel, D. B. and Beckmann, A. *Numerical Ocean Circulation Modeling.* 1999. 31, 132

Hernández-Guerra, A. and Nykjaer, L. Sea surface temperature variability off North-West Africa: 19811989. *International Journal of Remote Sensing*, 18:2539–2558, 1997. doi: 10.1080/014311697217468. 15

Hinze, J. O. Turbulence, second ed. *New York*, p. 790, 1979. 27, 131

Holte, J. and Talley, L. A new algorithm for finding mixed layer depths with applications to argo data and subantarctic mode water formation. *Journal of Atmospheric and Oceanic Technology*, 26:1920–1939, 2009. doi: 10.1175/2009JTECHO543.1. xx, 46, 47, 72, 73, 141, 150

Hoskins, B. J. The mathematical theory of frontogenesis. *Annual Review of Fluid Mechanics*, 14:131–151, 1982. 57

Hoskins, B. J., Draghici, I., and Davies, H. A. C. A new look at the infinite equation. *Quarterly Journal of the Royal Meteorological Society*, 104:31–38, 1978. 12, 111, 126, 171

Howard, L. Note on a paper of John W. Miles. *Journal of Fluid Mechanics*, 10:509–512, 1961. 52

Huffman, G. D. and Radshaw, B. P. A note on von Kármáns constant in low Reynolds number turbulent flows. *Journal of Fluid Mechanics*, 53:45–60, 1972. 44

Hunter, P. and Macnab, R. The GEBCO Digital Atlas published by the British Oceanographic Data Centre on behalf of IOC and IHO. North Atlantic region. Available from: http://www.gebco.net, 2003. URL `http://www.gebco.net`. 32, 132

I

Ikeda, M. and Emery, W. J. Satellite observations and modeling of meanders in the California Current system off Oregon and Northern California. *Journal of Physical Oceanography*, 14:1434–1450, 1984. doi: 10.1175/1520-0485(1984)014⟨1434:SOAMOM⟩2.0.CO;2. 15

Inoue, R., Gregg, M. C., and Harcourt, R. R. Mixing rates across the Gulf Stream, part 1: On the formation of eighteen degree water. *Journal of Marine Research*, 68(5):643–671, 2010. doi: 10.1357/002224011795977662. 5, 46, 47, 48, 55, 66, 73, 139, 141, 144, 148

J

Jackson, P. R. and Rehmann, C. R. Experiments on differential scalar mixing in turbulence in a sheared, stratified flow. *Journal of Physical Oceanography*, 44:2661–2680, 2014. doi: http://dx.doi.org/10.1175/JPO-D-14-0027.1. 33, 133

Jacob, S. D. and Koblinsky, C. J. Effects of precipitation on the upper-ocean response to a hurricane. *Monthly Weather Review*, 135:2207–2225, 2007. 37

Jacob, S. D. and Shay, L. K. The role of oceanic mesoscale features on the tropical cyclone-induced mixed layer response: A case study. *Journal of Physical Oceanography*, 33(4):649–676, 2003. doi: 10.1175/1520-0485(2003)332.0.CO;2. 5, 33, 37, 53, 56, 124, 133, 142

Jia, F., Wu, L., and Qiu, B. Seasonal modulation of eddy kinetic energy and Its formation mechanism in the Southeast Indian Ocean. *Journal of Physical Oceanography*, 41(4):657–665, 2011. doi: 10.1175/2010JPO4436.1. 29

Jiménez, B., Sangrà, P., and Mason, E. A numerical study of the relative importance of wind and topographic forcing on oceanic eddies shedding by deep water islands. *Ocean Modelling*, 22:146–157, 2008. 17

Jiménez, J. Oceanic turbulence at millimeter scales. *Scientia Marina*, 61(Supl. 1):47–56, 1997. 3

Johnson, G. C., Schmidtko, S., and Lyman, J. M. Relative contributions of temperature and salinity to seasonal mixed layer density changes and horizontal density gradients. *Journal of Geophysical Research*, 117(C4), 2012. doi: 10.1029/2011JC007651. 35, 134

Johnston, T. M. S., Rudnick, D. L., and Pallàs-Sanz, E. Elevated mixing at a front. *Journal of Geophysical Research*, 116(C11033), 2011. doi: 10.1029/2011JC007192. 86, 157

Jonker, H. J., van Reeuwijk, M., Sullivan, P. P., and Patton, E. G. On the scaling of shear-driven entrainment: a DNS study. *Journal of Fluid Mechanics*, 732:150–165, 2013. doi: 10.1017/jfm.2013.394. 10, 56, 125, 145

Joyce, T. M., Toole, J. M., Klein, P., and Thomas, L. N. A near-inertial mode observed within a Gulf Stream warm-core ring. *Journal of Geophysical Research*, 118:1797–1806., 2013. 67, 149

K

Kang, Y. J., Noh, Y., and Yeh, S. W. Processes that influence the mixed layer deepening during winter in the North Pacific. *Journal of Geophysical Research*, 115(C12004), 2010. doi: 10.1029/2009JC005833. 36

Kara, A., Wallcraft, A. J., Metzger, E. J., and Gunduz, M. Impacts of freshwater on the seasonal variations of surface salinity and circulation in the Caspian Sea. *Continental Shelf Research*, 30:1211–1225, 2010. doi: doi:10.1016/j.csr.2010.03.011. 70

Kara, A. B., Rochford, P. A., and Hurlburt, H. E. An optimal definition for ocean mixed layer depth. *Journal of Geophysical Research*, 105(16):803–1682, 2000. xx, 46, 47, 72

Kato, H. and Phillips, O. M. On the penetration of a turbulent layer into stratified fluid. *Journal of Fluid Mechanics*, 37(4):643–655, 1969. 10, 39, 125, 136

Khanta, L. H., Phillips, O. M., and Azadp, R. S. On turbulent entrainment at a stable density interface. *Journal of Fluid Mechanics*, 79(4):753–768, 1977. 10, 39, 125, 135, 136

Kilpatrick, K., Podesta, G. P., and Evans, R. Overview of the NOAA/NASA Advanced Very High Resolution Radiometer Pathfinder algorithm for sea surface temperature and associated matchup database. *Journal of Geophysical Research*, 106(C5):9179–9197, 2001. 32, 132

Klein, P. and Lapeyre, G. The oceanic vertical pump induced by mesoscale and submesoscale turbulence. *Annual Review of Marine Science*, 1:351–375, 2009. doi: 10.1146/annurev.marine.010908.163704. 65, 67, 148, 149

Klein, P., Hua, B. L., Lapeyre, G., Capet, X., Le Gentil, S., and Sasaki, H. Upper ocean turbulence from high-Resolution 3D simulations. *Journal of Physical Oceanography*, 38: 1748–1763, 2008. doi: http://dx.doi.org/10.1175/2007JPO3773.1. 2, 3, 123

Klein, P., Isern-Fontanet, J., Lapeyre, G., Roullet, G., Danioux, E., Chapron, B., Le Gentil, S., and Sasaki, H. Diagnosis of vertical velocities in the upper ocean from high resolution sea surface height. *Geophysical Research Letters*, 36(12), 2009. ISSN 1944-8007. doi: 10.1029/2009GL038359. L12603. 11, 30

Kolmogorov, A. N. Equations of turbulent motion in an incompressible fluid. *Izv. Akad. Nauk. SSSR ser. Fiz.*, 6:56–58, 1942. 181

Kolmogorov, A. N. Dissipation of energy in isotropic turbulence. *Dokl. Akad. Nauk. SSSR,*, 32:19–21, 1941. 2, 3

Kolodziejczyk, N., Reverdin, G., and Lazar, A. Interannual variability of the mixed layer winter convection and spice injection in the Eastern Subtropical North Atlantic. *Journal of Physical Oceanography*, 45:504–525, 2015. doi: http://dx.doi.org/10.1175/JPO-D-14-0042.1. 5, 66, 124, 148

Koszalka, I. *Mesoscale vortices, Lagrangian transport and marine ecosystem dynamics.* PhD thesis, Politecnico di Torino, Torino, Italy, 104 pp. 2008. 96, 111, 170

Koszalka, I., Bracco, A., McWilliams, J. C., and Provenzale, A. Dynamics of wind-forced coherent anticyclones in the open ocean. *Journal of Geophysical Research: Oceans*, 114(C8), 2009. ISSN 2156-2202. doi: 10.1029/2009JC005388. 11, 12, 16, 17, 18, 86, 87, 90, 92, 94, 95, 100, 101, 112, 115, 126, 156, 157, 159, 160, 161, 164, 172, 174, 175, 186

Koszalka, I., Ceballos, L., and Bracco, A. Vertical mixing and coherent anticyclones in the ocean: the role of stratification. *Nonlinear Processes in Geophysics*, 17(1):37–47, 2010. doi: 10.5194/npg-17-37-2010. 11, 17, 18, 87, 99, 103, 126, 157, 163, 166

Koumoutsakos, P. Inviscid axisymmetrization of an elliptical vortex. *Journal of Computational Physics*, 138(2):821–857, 1997. ISSN 0021-9991. doi: http://dx.doi.org/10.1006/jcph.1997.

5749. URL http://www.sciencedirect.com/science/article/pii/S0021999197957491. 109, 169

Kraus, E. B. and Turner, J. S. A one-dimensional model of the seasonal thermocline II. The general theory and its consequences. *Tellus*, 19:98–106, 1967. 6, 55

Kunze, E. Near-inertial wave propagation in geostrophic shear. *Journal of Geophysical Research*, 14:544–565., 1985. 66, 78, 148, 154

Kunze, E., Williams, A., and Briscoe, M. G. Observations of shear and stability from a neutrally buoyant float. *Journal of Geophysical Research*, 95(C10):1812718142, 1990. doi: 10.1029/JC095iC10p18127. 82

Kunze, E., Firing, E., Hummon, J. M., Chereskin, T. K., and Thurnherr, A. M. Global abyssal mixing inferred from lowered ADCP shear and CTD strain profiles. *Journal of Physical Oceanography*, 36(8):1553–1576., 2006. 4

L

LaCasce, J. H. and Mahadevan, A. Estimating subsurface horizontal and vertical velocities from sea-surface temperature. *Journal of Marine Research*, 64:695–721, 2006. 112, 172

Large, W. G. and Pond, S. Open ocean momentum flux measurements in moderate to strong winds. *Journal of Physical Oceanography*, 11(3):324–336, 1981. 8, 26

Large, W. G., McWilliams, J. C., and Doney, S. Oceanic vertical mixing: A review and a model with a nonlocal boundary layer parameterization. *Reviews of Geophysics*, 32:363–403, 1994. xxiv, 31, 36, 81, 82, 88, 89, 91, 103, 132, 159

Le Traon, P., Klein, P., Hua, B. L., and Dibarboure, G. Do altimeter data agree with interior or surface quasi-geostrophic theory. *Journal of Physical Oceanography*, 38:11371142, 2008. doi: http://dx.doi.org/10.1175/2007JPO3806.1. 11

Lea, D., Drecourt, J.-P., Haines, K., and Martin, M. Ocean altimeter assimilation with observational-and model-bias correction. *Quarterly Journal of the Royal Meteorological Society*, 134(636):1761–1774, 2008. doi: 10.1002/qj.320. 30

Ledwell, J. R., Montgomery, K., Polzin, K. L., St. Laurent, L., Schmitt, R., and Toole, J. M. Evidence for enhanced mixing over rough topography in the abyssal ocean. *Nature*, 403 (6766):179–182, 2000. 4

Ledwell, J. R., McGillicuddy, D. J., and A.Anderson, L. Nutrient flux into an intense deep chlorophyll layer in a mode-water eddy. *Deep Sea Research Part II*, 55:1139–1160, 2008. doi: doi:10.1016/j.dsr2.2008.02.005. 16, 86, 156

Lévy, M., Klein, P., Tréguier, A.-M., Iovino, D., Madec, G., Masson, S., and Takahashi, K. Modifications of gyre circulation by sub-mesoscale physics. *Ocean Modelling*, 34(1):1–15, 2010. doi: 10.1016/j.ocemod.2010.04.001. 1, 3, 123

Lewis, M. R., Harrison, W. G., Oakey, N. S., Herbert, D., and Platt, T. Vertical nitrate fluxes in the oligotrophic ocean. *Science*, 234(4778):870–872, 1986. 65, 148

Liu, Y., Lee, S. K., Muhling, B. A., Lamkin, J. T., and Enfield, D. B. Significant reduction of the Loop Current in the 21st century and its impact on the Gulf of Mexico. *Journal of Geophysical Research*, 117(C05039), 2012. doi: 10.1029/2011JC007555. 36

Lombardo, C. P. and Gregg, M. C. Similarity scaling of viscous and thermal dissipation in a convecting surface boundary layer. *Journal of Geophysical Research*, 94:6273–6284, 1989. 61, 146

Louis, J. F., Weill, A., and Vidal-Madjar, D. Dissipation length in stable layers. *Boundary-Layer Meteorology*, 25(3):229–243, 1983. 182

Lueck, R. and Osborn, T. The dissipation of kinetic energy in a warm-core ring. *Journal of Geophysical Research: Oceans*, 91(C1):803–818, 1986. ISSN 2156-2202. doi: 10.1029/JC091iC01p00803. 66, 148

M

MacKinnon, J. A. and Gregg, M. C. Spring mixing: Turbulence and internal waves during restratification on the New England shelf. *Journal of Physical Oceanography*, 35(12):2425–2443, 2005. doi: 10.1175/JPO2821.1. 47, 73

Mahadevan, A. Eddy effects on biogeochemistry. *Nature*, 506:168–169, 2014. doi: 10.1038/nature13048. 16

Mahadevan, A. and Tandon, A. An analysis of mechanisms for submesoscale vertical motion at ocean fronts. *Ocean Modelling*, 14:241–256, 2006. 2, 97, 123, 162

Mahadevan, A., Thomas, L. N., and Tandon, A. Comment on "Eddy/wind interactions stimulate extraordinary mid-Ocean plankton blooms". *Science*, 320(5875):448, 2008. doi: 10.1126/science.1152111. URL `http://www.sciencemag.org/content/320/5875/448.2.abstract`. 86, 92, 95, 156, 160, 162

Martin, A. and Richards, K. Mechanisms for vertical nutrient transport within a North Atlantic mesoscale eddy. *Deep Sea Research Part II*, 48:757–773, 2001. 11, 16, 86, 95, 99, 126, 156, 162

Martínez-Marrero, A., Sangrà, B. P. Barceló-Llull, and Gordo, C. Near-inertial waves trapping by anticyclonic eddies in the Canary eddy Corridor. in prep. 78, 83, 154

Mason, E. High-resolution modelling of the Canary Basin oceanic circulation. Ph.D. thesis. *Universidad de Las Palmas de Gran Canaria*, page 235 pp., 2009. xxxiii, 21, 31, 87, 88, 132, 157

Mason, E., Molemaker, J., Shchepetkin, A. F., Colas, F., McWilliams, J. C., and Sangrà, P. Procedures for offline grid nesting in regional ocean models. *Ocean Modelling*, 35(12):1–15, 2010. ISSN 1463-5003. doi: http://dx.doi.org/10.1016/j.ocemod.2010.05.007. 31, 88, 132

Mason, E., Colas, F., Molemaker, J., Shchepetkin, A. F., Troupin, C., McWilliams, J., and Sangrà, P. Seasonal variability of the Canary Current: a numerical study. *Journal of Geophysical Research*, 116(C06001), 2011. doi: 10.1029/2010JC006665. 31, 87, 88, 132, 157

Mason, E., Pascual, A., and McWilliams, C. A new sea surface heightbased code for oceanic mesoscale eddy tracking. *Journal of Atmospheric and Oceanic Technology*, 31:1181–1188, 2014. doi: http://dx.doi.org/10.1175/JTECH-D-14-00019.1. 17, 67, 149

Mason, E., Colas, F., and Pelegrí, J. L. A Lagrangian study tracing water parcel origins in the Canary Upwelling System. *Scientia Marina*, 76(S1):79–94, 2012. 31, 32, 132

McGillicuddy, D. J. Formation of intrathermocline lenses by eddywind interaction. *Journal of Physical Oceanography*, 45:606–612, 2015. doi: http://dx.doi.org/10.1175/JPO-D-14-0221.1. 16, 68

McGillicuddy, D. J., Anderson, L. A., Bates, N. R., Bibby, T., Buesseler, K. O., Carlson, C. A., Davis, C. S., Ewart, C., Falkowski, P. G., Goldhwait, S. A., Hansell, D. A., Jenkins, W. J., Johnson, R., Kosnyrev, V. K., Ledwell, J. R., Li, Q. P., Siegel, D. A., and D. K. Steinberg, D. K. Eddy/wind interactions stimulate extraordinary mid-ocean plankton blooms. *Science*, 316:1021–1026, 2007. doi: 10.1126/science.1136256. 16, 86, 95, 99, 156, 162

McGillicuddy, D. J., Ledwell, J. R., and Anderson, L. A. Response to comment on "Eddy/wind interactions stimulate extraordinary mid-ocean plankton blooms". *Science*, 320(5875):448, 2008. doi: 10.1126/science.1148974. 95, 99, 162

McWilliams, J. C., Graves, L., and Montgomery, M. A formal theory for vortex Rossby waves and vortex evolution. *Geophysical and Astrophysical Fluid Dynamics*, 97(4):275–309, 2003. 17, 86, 101, 157, 164, 185

McWilliams, J. The emergence of isolated coherent vortices in turbulent flow. *Journal of Fluid Mechanics*, 146:21–43, 1984. 3

Miles, J. W. On the stability of heterogeneous shear flows. *Journal of Fluid Mechanics*, 10: 496–508, 1961. 52, 82

Montgomery, T. M. and Kallenbach, R. J. A theory for vortex Rossby-waves and its application to spiral bands and intensity changes in hurricanes. *Quarterly Journal of the Royal Meteorological Society*, 123:435–465, 1997. 11, 17, 86, 101, 126, 157, 185

Mooers, C. and Robinson, A. Turbulent jets and eddies in the California current and inferred cross-shore transports. *Science*, 223:51–53, 1984. doi: 10.1126/science.223.4631.51. 15

Moum, J. N. and Smyth, W. D. *Upper ocean mixing processes, in Encyclopedia of Ocean Sciences*, volume 6. Elsevier, New York., 2001. 5

Moum, J. N., Caldwell, D. R., and Paulson, C. A. Mixing in the equatorial surface layer and thermocline. *Journal of Geophysical Research*, 94(C2):2005–2022, 1989. 47, 73, 141

Moum, J. N., Farmer, D. M., Smyth, W. D., Armi, L., and Vagle, S. Structure and generation of turbulence at interfaces strained by internal solitary waves propagating shoreward over the continental shelf. *Journal of Physical Oceanography*, 33:2093–2112, 2003. doi: http://dx.doi.org/10.1175/1520-0485(2003)033⟨2093:SAGOTA⟩2.0.CO;2. xvii, 4

Muench, R., Padman, L., Howard, S., and Fahrbach, E. Upper ocean diapycnal mixing in the northwestern Weddell Sea. *Deep Sea Research Part II: Topical Studies in Oceanography*, 49(21):4843 – 4861, 2002. ISSN 0967-0645. doi: http://dx.doi.org/10.1016/S0967-0645(02)00162-5. URL `http://www.sciencedirect.com/science/article/pii/S0967064502001625`. 82, 84

Munk, W. Abyssal recipes. *Deep Sea Research*, 13:707–730, 1966. 4

Munk, W. and Wunsch, C. Abyssal recipes ii: energetics of tidal and wind mixing. *Deep Sea Research Part I: Oceanographic Research Papers*, 45(12):1977–2010, 1998. 4, 16

N

Nagai, T., Yamazaki, H., Nagashima, H., and Kantha, L. H. Field and numerical study of entrainment laws for surface mixed layer. *Deep-Sea Research Part II*, 52(9):1109–1132, 2005. doi: 10.1016/j.dsr2.2005.01.011. 10, 33, 34, 36, 46, 48, 65, 75, 125, 133, 139, 148

Nagai, T., Tandon, A., and Rudnick, D. L. Twodimensional ageostrophic secondary circulation at ocean fronts due to vertical mixing and largescale deformation. *Journal of Geophysical Research*, 111(C09038), 2006. doi: 10.1029/2005JC002964. 11, 12, 86, 87, 103, 126, 157, 166

Nagai, T., Tandon, A., Yamazaki, H., and Doubell, M. J. Evidence of enhanced turbulent dissipation in the frontogenetic Kuroshio Front thermocline. *Geophysical Research Letters*, 36(L12609), 2009. doi: 10.1029/2009GL038832. 34, 134

Nagai, T., Tandon, A., Yamazaki, H., Doubell, M. J., and Gallager, S. Direct observations of microscale turbulence and thermohaline structure in the Kuroshio Front. *Journal of Geophysical Research*, 117(C8):1978–2012, 2012. doi: 10.1029/2011JC007228. 35

Nardelli, B. B. Vortex waves and vertical motion in a mesoscale cyclonic eddy. *Journal of Geophysical Research: Oceans*, 118(10):5609–5624, 2013. ISSN 2169-9291. doi: 10.1002/jgrc.20345. 11, 18, 30, 86, 87, 100, 101, 102, 126, 156, 157, 163, 164, 175, 185

Naveira Garabato, A. C., Polzin, K. L., King, B. A., Heywood, K. J., and Visbeck, M. Widespread intense turbulent mixing in the Southern Ocean. *Science*, 303:210–213, 2004. doi: 10.1126/science.1090929. 4, 81

Niiler, P. P. On the Ekman divergence in an oceanic jet. *Journal of Geophysical Research*, 74: 7048–7052, 1965. 97, 99, 162, 163

Niiler, P. P. and Kraus, E. B. One-dimensional model ofthe upper ocean. Modelling and prediction of the upper layers of the ocean. *E. B. Kraus, Ed., Pergamon Press.*, pages 143–172, 1977. 6, 7, 9, 37, 53, 55, 60, 74, 124, 125, 134, 146

Nilsen, J. and Falck, E. Variations of mixed layer properties in the Norwegian Sea for the period 19481999. *Progress in Oceanography*, 70(1):58–90, 2006. doi: 10.1016/j.pocean.2006.03.014. 62

O

Oakey, N. S. Determination of the rate of dissipation of turbulent energy from simultaneous temperature and velocity shear microstructure measurements. *Journal of Physical Oceanography*, 12:256–271, 1982. 27, 131

Oakey, N. S. and Elliott, J. A. Dissipation within the surface mixed layer. *Journal of Physical Oceanography*, 12:171–185, 1982. 61, 146

Okubo, A. Horizontal dispersion of floatable particles in the vicinity of velocity singularity such as convergences. *Deep Sea Research*, 17:445–454, 1970. 109, 169

Osborn, T. R. Estimates of the local rate of vertical diffusion from dissipation measurements. *Journal of Physical Oceanography*, 10:83–89, 1980. xxiv, 55, 79, 82, 144, 154

Ozmidov, R. V. On the turbulent exchange in a stably stratified ocean. *Atmospheric and Oceanic Physics*, 8:853–860, 1965. 48, 141

P

Pacheco, M. and Hernández-Guerra, A. Seasonal variability of recurrent phytoplankton pigment patterns in the Canary Islands area. *International Journal of Remote Sensing*, 20:1408–1495., 1999. 15, 16

Pallàs-Sanz, E. and Viúdez, A. Diagnosing mesoscale vertical velocity from horizontal velocity and density data. *Journal of Physical Oceanography*, 35:1744–1762, 2005. 111, 112, 171, 172

Pallàs-Sanz, E., Johnston, T. M. S., and Rudnick, D. L. Frontal dynamics in a California Current System shallow front: 2. Mesoscale vertical velocity. *Journal of Geophysical Research*, 115(C12068), 2010. doi: 10.1029/2010JC006474. 11, 12, 86, 103, 157, 166

Pasquero, C., Annalisa, B., Antonello, P., and Weiss, J. B. Particle motion in a sea of eddies. In Griffa, A., A. D. Kirwan, J., Mariano, A. J., zgkmen, T., and Rossby, H. T., editors, *Lagrangian Analysis and Prediction of Coastal and Ocean Dynamics*, pages 89–118. Cambridge University Press, 2007. ISBN 9780511535901. URL `http://dx.doi.org/10.1017/CBO9780511535901.005`. Cambridge Books Online. 95

Pelegrí, J. L. and Richman, J. G. On the role of shear mixing during transient coastal upwelling. *Continental Shelf Research*, 13(12):1363–1400, 1993. doi: 10.1016/0278-4343(93)90088-F. 10, 33, 52, 53, 54, 56, 125, 133

Pelegrí, J. L., Arístegui, J., Cana, L., González-Dávila, M., Hernández-Guerra, A., Hernández-León, S., Marrero-Díaz, A., Montero, M., Sangrà, P., and Santana-Casiano, M. Coupling between the open ocean and the coastal upwelling region off Northwest Africa: water recirculation and offshore pumping of organic matter. *Journal of Marine Systems*, 54(14):3 – 37, 2005a. ISSN 0924-7963. doi: http://dx.doi.org/10.1016/j.jmarsys.2004.07.003. URL `http://www.sciencedirect.com/science/article/pii/S0924796304002027`. 14, 15, 16

Pelegrí, J. L., Marrero-Díaz, A., Ratsimandresy, A., Antoranz, A., Cisneros-Aguirre, J., Gordo, C., Grisolía, D., Hernndez-Guerra, A., Laíz, I., Martínez, A., Parrilla, G., Pérez-Rodríguez, P., Rodríguez-Santana, A., and Sangrà, P. Hydrographic cruises off Northwest Africa: the canary current and the Cape Ghir region. *Journal of Marine Systems*, 54:39–63, 2005b. doi: 10.1016/j.jmarsys.2004.07.001. 14, 15, 16, 24, 39, 40, 41, 46, 54, 137, 138, 142

Peliz, A., Santos, A., Oliveira, P., and Dubert, J. Extreme cross-shelf transport induced by eddy interactions southwest of iberia in winter 2001. *Geophysical Research Letters*, 31(L08301), 2004. doi: 10.1029/2004GL019618. 15

Pham, H. T., Sarkar, S., and Winters, K. B. Intermittent patches of turbulence in a stratified medium with stable shear. *Journal of Turbulence*, 13:1–17, 2012. doi: 10.1080/14685248.2012.686666. 52

Piedeleu, M., Sangrà, P., Sánchez-Vidal, A., Fabrs, J., Gordo, C., and Calafat, A. An observational study of oceanic eddy generation mechanisms by tall deep-water islands (Gran Canaria). *Geophysical Research Letters*, 36(14), 2009. ISSN 1944-8007. doi: 10.1029/2008GL037010. URL `http://dx.doi.org/10.1029/2008GL037010`. L14605. 17

Pinot, J. M., Tintore, J., and Wang, D. P. A study of the omega equation for diagnosing vertical motions at ocean fronts. *Journal of Marine Research*, 54:239–259, 1996. 12, 111, 112, 172

Pollard, R. T. and Regier, L. A. Vorticity and vertical circulation at an ocean front. *Journal of Physical Oceanography*, 22:609–625, 1992. 11, 111, 126

Pollard, R. T., Rhines, P. B., and Thompson, R. O. The deepening of the wind-mixed layer. *Geophysical Fluid Dynamics*, 3:381–404, 1973. 53, 56, 145

Ponte, A., Klein, P., Capet, X., Le Traon, P., Bertrand, Y. C., and Lherminier, P. Diagnosing surface mixed layer dynamics from high resolution satellite onservations: Numerical isurface. *Journal of Physical Oceanography*, 43(7):1345 – 1355., 2013. doi: http://dx.doi.org/10.1175/JPO-D-12-0136.1. 1, 2, 87, 104, 114, 123, 157, 166, 173

Press, W. H., Flannery, B. P., Teukolsky, S. A., and Vetterling, W. T. *Numerical Recipes in FORTRAN 77*, volume 2nd ed. of *992 pp.* Cambridge, U. K, 1993. 112

Price, J. F. On the scaling of stress-driven entrainment experiments. *Journal of Fluid Mechanics*, 90:509–529, 1979. 52, 56, 145

Price, J. F., Mooers, C., and Leer, C. V. Observation and simulation of storm-induced mixed layer deepening. *Journal of Physical Oceanography*, 8:582–599, 1978. 53, 142

Price, J. F., Weller, R. A., and Pinkel, R. Diurnal cycling: Observations and models of the upper ocean response to diurnal heating, cooling, and wind mixing. *Journal of Geophysical Research*, 91:8411–8427, 1986. 5, 10, 124, 125

Provenzale, A. Transport by coherent barotropic vortices. *Annual Review of Fluid Mechanics*, 31:55–93, 1999. 110, 170

R

Ravindran, P., Wright, D. G., Platt, T., and Sathyendranath, S. A generalized depth-integrated model of the oceanic mixed layer. *Journal of Physical Oceanography*, 29(4):791–806, 1999. 46

Reynolds, O. *On the dynamical theory of incompressible viscous fluids and the determination of the criterion*, volume 186. Philosophical Transactions of the Royal Society of London, 1895. 3

Risien, C. and Chelton, D. B. A global climatology of surface wind and wind stress fields from eight years of QuikSCAT scatterometer data. *Journal of Physical Oceanography*, 38: 2379–2413, 2008. 32, 132

Rouse, H. and Dodu, J. Turbulent diffusion across a density discontinuity. *Rouille Blanche*, 10: 522–532, 1955. 5, 124

S

Samson, G., Giordani, H., Caniaux, G., and Roux, F. Numerical investigation of an oceanic resonant regime induced by hurricane winds. *Ocean Dynamics*, 59(4):565–586, 2009. doi: 10.1007/s10236-009-0203-8. 39, 66, 136, 148

Samuelsen, A., Hjøllo, S. S., Johannessen, J. A., and Patel, R. Particle aggregation at the edges of anticyclonic eddies and implications for distribution of biomass. *Ocean Science*, 8 (3):389–400, 2012. doi: 10.5194/os-8-389-2012. 110, 111, 170

Sangrà, P., Pelegrí, J., Hernández-Guerra, A., Arregui, I., Martin, J., Marrero-Díaz, A., Martinez, A., Ratsimandresy, A., and Rodríguez-Santana, A. Life history of an anticyclonic eddy. *Journal of Geophysical Research: Oceans (1978–2012)*, 110(C3), 2005. doi: 10.1029/2004JC002526. 17, 87, 106, 107, 109, 111, 157, 170

Sangrà, P., Auladell, M., Marrero-Díaz, A., Pelegrí, J., Fraile-Nuez, E., Rodríguez-Santana, A., Martín, J., Mason, E., and Hernández-Guerra, A. On the nature of oceanic eddies shed by the Island of Gran Canaria. *Deep Sea Research Part I: Oceanographic Research Papers*, 54 (5):687–709, 2007. doi: doi:10.1016/j.dsr.2007.02.004. 17, 106, 107, 109

Sangrà, P., Pascual, A., Rodríguez-Santana, A., Machín, F., Mason, E., McWilliams, J. C., Pelegrí, J. L., Dong, C., Rubio, A., Arístegui, J., Marrero-Díaz, A., Hernández-Guerra, A., Martínez-Marrero, A., and Auladell, M. The Canary Eddy Corridor: A major pathway for long-lived eddies in the subtropical North Atlantic. *Deep Sea Research Part I*, 56:2100–2114, 2009. doi: http://dx.doi.org/10.1016/j.dsr.2009.08.008. xviii, xxvii, 13, 16, 17, 30, 67, 89, 106, 109, 128, 129, 149, 159

Sangrà, P., Troupin, C., Barreiro-Gonzlez, B., Barton, D. E., Abdellatif, O., and Arístegui, J. The Cape Ghir filament system in August 2009 (NW Africa). *Journal of Geophysical Research: Oceans*, 120(6):4516–4533, 2015. ISSN 2169-9291. doi: 10.1002/2014JC010514. URL `http://dx.doi.org/10.1002/2014JC010514`. 14, 15

Sasaki, H. and Klein, P. Ssh wavenumber spectra in the north pacific from a high-resolution realistic simulation. *Journal of Physical Oceanography*, 42:1233–1241, 2012. doi: http://dx.doi.org/10.1175/JPO-D-11-0180.1. 3

Sasaki, H., Klein, P., Qiu, B., and Sasai, Y. Impact of oceanic-scale interactions on the seasonal modulation of ocean dynamics by the atmosphere. *Nature Communications*, 5(5636), 2014. doi: 10.1038/ncomms6636. 1, 3, 30, 123

Schafstall, J., Dengler, M., Brandt, P., and Bange, H. Tidal induced mixing and diapycnal nutrient fluxes in the Mauritanian upwelling region. *Journal of Geophysical Research*, 115 (C10):1978–2012, 2010. doi: 10.1029/2009JC005940. 34, 134

Shchepetkin, A. F. and McWilliams, J. C. The Regional Oceanic Modeling System (ROMS): a split-explicit, free-surface, topography-following-coordinate oceanic model. *Ocean Modelling*, 9(4):347–404, 2005. 31, 132

Shchepetkin, A. F. and McWilliams, J. C. Correction and commentary for Ocean forecasting in terrain-following coordinates: Formulation and skill assessment of the regional ocean modeling system" by Haidvogel et al. J. Comp. Phys. 227, pp. 3595-3624. *Journal of Computational Physics*, 228:8985–9000, 2009. 31, 132

Sheen, K. L., Naveira Garabato, A. C., Brearley, J. A., Meredith, M. P., Polzin, K. L., Smeed, D. A., Forryan, A., King, B., Sallee, J.-B., St. Laurent, L., Thurnherr, A. M., Toole, J. M., Waterman, S. N., and Watson, A. J. Eddy-induced variability in Southern Ocean abyssal mixing on climatic timescales. *Nature Geoscience*, 7:577–582, 2014. doi: 10.1038/ngeo2200. 1, 16, 17, 67, 81, 123, 149

Siegel, A., Weiss, J., Toomre, J., McWilliams, J. C., Berloff, P., and Yavneh, I. Eddies and vortices in ocean basin dynamics. *Geophysical Research Letters*, 28:3183–3186, 2001. 2, 123

Small, R. J., Carniel, S., Campbell, T., Teixeira, J., and Allard, R. The response of the Ligurian and Tyrrhenian Seas to a summer Mistral event: A coupled atmosphereocean approach. *Ocean Modelling*, 48:30–44, 2012. doi: 10.1016/j.ocemod.2012.02.003. 34

Smith, R. D., Maltrud, M. E., Bryan, F. O., and Hecht, M. W. Numerical simulation of the North Atlantic Ocean at 1/10. *Journal of Physical Oceanography*, 30:15321561, 2000. 1, 123

Smyth, W. D. and Moum, J. N. Length scales of turbulence in stably stratified mixing layers. *Physics of Fluids*, 12:1327–1342, 2000. 56

St. Laurent, L. and Garrett, C. The role of internal tides in mixing the deep ocean. *Journal of Physical Oceanography*, 32:2882–2899., 2002. 4

Stanley, G. J. and Saenko, O. A. Bottom-enhanced diapycnal mixing driven by mesoscale eddies: Sensitivity to wind energy supply. *Journal of Physical Oceanography*, 44(1):68–85, 2014. doi: http://dx.doi.org/10.1175/JPO-D-13-0116.1. 16, 66, 78, 81, 148, 154

Stern, M. Interaction of a uniform wind stress with a geostrophic vortex. *Deep Sea Research*, 12:355–367, 1965. 96, 99, 162, 163

Stramma, L., Bange, H. W., Czeschel, R., Lorenzo, A., and Frank, M. On the role of mesoscale eddies for the biological productivity and biogeochemistry in the eastern tropical Pacific Ocean off Peru. *Biogeosciences,*, 10:72937306, 2013. doi: 10.5194/bg-10-7293-2013. 65, 148

Strang, E. J. and Fernando, H. J. S. Entrainment and mixing in stratified shear flows. *Journal of Fluid Mechanics*, 428:349–386, 2001. doi: 10.1017/S0022112000002706. 10, 37, 38, 39, 52, 63, 66, 73, 82, 125, 135, 136, 148

Strub, P., Kosro, P., and Huyer, A. The nature of cold filaments in the California current system. *Journal of Geophysical Research*, 96:14743–14768, 1991. 15

Sun, J. and Wang, Y. Effect of the entrainment flux ratio on the relationship between entrainment rate and convective Richardson number. *Boundary-Layer Meteorology*, 126(2):237–247, 2008. doi: 0.1007/s10546-007-9231-4. 33, 133

Sutherland, G., Reverdin, G., Marié, L., and Ward, B. Mixed and mixing layer depths in the ocean surface boundary layer under conditions of diurnal stratification. *Geophysical Research Letters*, 41:8469–8476, 2014. doi: 10.1002/2014GL061939. 46, 48, 66, 121, 139, 141, 148, 178

Sverdrup, H. U. On conditions for the vernal blooming of phytoplankton. *Journal du Conseil International pour lExploration de la Mer*, 18(3):287–295, 1953. 65, 121, 148, 178

T

Thomas, L. N. Formation of intrathermocline eddies at ocean fronts by wind-driven destruction of potential vorticity. *Dynamics of Atmospheres and Oceans*, 45(34):252 – 273, 2008. ISSN 0377-0265. doi: http://dx.doi.org/10.1016/j.dynatmoce.2008.02.002. 16

Thomas, L. N. and Rhines, P. B. Nonlinear stratified spin up. *Journal of Fluid Mechanics*, 473:211–244, 2002. 97, 99, 162, 163

Thomas, L. N., Tandon, A., and Mahadevan, A. Submesoscale processes and dynamics. *Ocean Modeling in an Eddying Regime, Geophys. Monogr. Ser*, 177:17–38, 2008. 2, 123

Thomas, L. N., Taylor, J. R., Ferrari, R., and Joyce, T. M. Symmetric instability in the Gulf Stream. *Deep-Sea Research Part II*, 91:96–110, 2013. doi: 10.1016/j.dsr2.2013.02.025. 58, 59

Thorpe, S. A. *The Turbulent Ocean*. Cambridge University Press, 2005. ISBN 9780511819933. URL `http://dx.doi.org/10.1017/CBO9780511819933`. Cambridge Books Online. 5

Tintore, J., Gomis, D., Alonso, S., and Porrilla, G. Mesoscale dynamics and vertical motion in the Alboran Sea. *Journal of Physical Oceanography*, 21:811–823, 1991. 12

Troupin, C., Machín, F., Ouberdous, M., Sirjacobs, D., Barth, A., and Beckers, J.-M. High-resolution climatology of the northeast Atlantic using Data-Interpolating Variational Analysis (Diva). *Journal of Geophysical Research: Oceans*, 115(C8), 2010. ISSN 2156-2202. doi: 10.1029/2009JC005512. 32, 132

Troupin, C., Mason, E., Beckers, J. M., and Sangrà, P. Generation of the Cape Ghir upwelling filament: A numerical study. *Ocean Modelling*, 41:1–15, 2012. doi: 10.1016/j.ocemod.2011.09.001. 15, 54, 142

Turner, J. S. *Buoyancy effects in fluids*. Number pp. 368. Cambridge University Press., London, 1979. doi: http://dx.doi.org/10.1017/CBO9780511608827. 5, 6, 124

V

Vallis, G. K. *Atmospheric and Oceanic Fluid Dynamics*. Cambridge University Press, Cambridge, U.K., 2006. 12, 90, 159

Van Camp, L., Nykjaer, L., Mittelstaed, E., and Schlittenhard, P. Upwelling and boundary circulation off Northwest Africa as depicted by infrared and visible satellite observations. *Progress in Oceanography*, 26:357–402, 1991. doi: 10.1016/0079-6611(91)90012-B. 15

Vélez-Belchí, P. and Tintoré, J. Vertical velocities at an ocean front. *Scientia Marina*, 65: 291–300, 2001. 11, 126

Viúdez, A. and Dritschel, D. G. Vertical velocity in mesoscale geophysical flows. *Journal of Fluid Mechanics*, 483:199–223, 2003. 16, 86, 87, 156, 157

Viúdez, A. and Dritschel, D. G. Potential vorticity and the quasi-geostrophic and semi-geostrophic mesoscale vertical velocity. *Journal of Physical Oceanography*, 34:865–887, 2004. 12, 111, 112, 171

Viúdez, A., Tintoré, J., and Haney, R. L. About the nature of the generalized omega equation. *Journal of Atmospheric Science*, 53:787–795, 1996. 12, 111, 112, 115, 171, 172, 174

W

Wada, A., Niino, H., and Nakano, H. Roles of vertical turbulent mixing in the ocean response to Typhoon Rex (1998). *Journal of Oceanography*, 65(3):373–396, 2009. doi: 10.1007/s10872-009-0034-8. 5, 10, 53, 60, 61, 124, 142, 145

Wallcraft, A. J., Kara, A. B., Hurlburt, H. E., and Rochford, P. A. The NRL Layered Global Ocean Model (NLOM) with an embedded mixed layer submodel: Formulation and tuning. *Journal of Atmospheric and Oceanic Technology*, 20(11):1601–1615, 2003. doi: 10.1175/1520-0426(2003)020⟨1601:TNLGOM⟩2.0.CO;2. 36

Weiss, J. The dynamics of enstrophy transfer in two dimensional hydrodynamics. *Physica D: Nonlinear Phenomena*, 48:273–294, 1991. 109, 169

Wolk, F., Yamazaki, H., Seuront, L., and Lueck, R. G. A new free-fall profiler for measuring biophysical microstructure. *Journal of Atmospheric and Oceanic Technology*, 19(5):780–793, 2002. 26, 27, 130, 131

Worley, S., Woodruff, S. D., Reynolds, R. W., and adnd N. Lott, S. J. L. 2005. ICOADS release 2.1 data and products. *International Journal of Climatology*, 25:823–842, 2005. 32, 132

Wunsch, C. and Ferrari, R. Vertical mixing, energy, and the general circulation of the oceans. *Annual Review of Fluid Mechanics*, 36:281–314, 2004. doi: 10.1146/annurev.fluid.36.050802.122121. 16, 66, 148

X

Xu, Y. and Fu, L. L. The effects of altimeter instrument noise on the estimation of the wavenumber spectrum of sea surface heigh. *Journal of Physical Oceanography*, 42:22292233, 2012. doi: http://dx.doi.org/10.1175/JPO-D-12-0106.1. 1, 123

Y

Yelland, M., Moat, B. I., Taylor, P. K., Pascal, R. W., Hutchings, J., and Cornell, V. C. Wind stress measurements from the open ocean corrected for airflow distortion by the ship. *Journal of Physical Oceanography*, 28(7):1511–1526, 1998. 97

Z

Zaron, E. D. and Moum, J. N. A new look at Richardson number mixing schemes for equatorial ocean modeling. *Journal of Physical Oceanography*, 39(10):2652–2664, 2009. doi: 10.1175/2009JPO4133.1. 52, 81, 82

Zhai, X., Greatbatch, R. J., and Zhao, J. Enhanced vertical propagation of storm induced near-inertial energy in an eddying ocean channel model. *Geophysical Research Letters*, 32 (L18602), 2005. doi: 10.1029/2005GL023643. 66, 148

Zhang, Y., Liu, Z., Zhao, Y., and Liang, J. L. X. Effect of surface mesoscale eddies on deep-sea currents and mixing in the northeastern South China Sea. *Deep Sea Research Part II: Topical Studies in Oceanography*, in press:–, 2015. ISSN 0967-0645. doi: http://dx.doi.org/10.1016/j.dsr2.2015.07.007. 66, 148

Zhurbas, V. *Introduction to Turbulence: Lectures on Oceanography.* P.P. Shirshov Institute of Oceanology of the Russian Academy of Sciences, 2001. 57